Modelling the Excited State Properties of TiO_2 Nanoparticles

Enrico Berardo

Supervised by

Dr. Martijn Zwijnenburg

Department of Chemistry

Thesis submitted for the degree of Doctor of Philosophy

March 2015

I, Enrico Berardo, confirm that the work presented in this thesis is my own. Where information has been derived by other sources, I confirm that this has been indicated in the thesis.

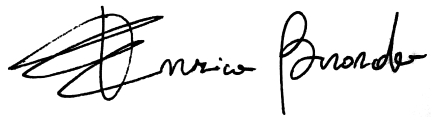

Enrico Berardo

March 2015

Abstract

Since the discovery in 1972 of photocatalytic water splitting on TiO_2 electrodes, there has been a worldwide research effort focused on the study of this material. Recently, it was shown that the use of nanosized systems could overcome the usual TiO_2 limitations, e.g. a too large band gap, and increase its efficiency in photocatalytic applications.

This thesis involves the computational modelling of excited state properties of TiO_2 nanoparticles in order to provide atomic scale insights into the optical and photocatalytic properties of these materials. In the first part of this thesis, accurate correlated wave function benchmarks (i.e. EOM-CC) are defined for the calculation of excited states of small TiO_2 nanoparticles (< 1 nm in size). These results are then employed for the evaluation of the accuracy of different Time Dependent DFT (TD-DFT) exchange-correlation (XC) potentials. The main conclusion is that standard TD-DFT XC energy functionals (e.g. PBE, B3LYP) tend to underestimate charge transfer excitations, whereas long-range corrected (e.g. CAM-B3LYP) potentials accurately describe optical properties of TiO_2 nanoparticles. Following this study, in an effort to close the gap between simple theoretical models and systems of experimental relevance, TD-DFT is used for the investigation of a range of optical and excited state properties for a rutile bulk-like particle with a diameter of approximately 2 nm. These studies reveal that this or smaller rutile nanoparticles are predicted to be thermodynamically unable to drive photocatalytic water splitting because of the strong self-trapping of free electrons and holes generated during the excitation process in these particles. Finally, the excited state lifetimes and the photo-reactivity of a small hydrated TiO_2 particle were investigated by employing TD-DFT non-adiabatic excited state molecular dynamics (NAMD). This study corresponds to a first attempt of using TD-DFT to

uncover the initial steps of the photochemical water-splitting reaction catalysed by TiO_2 nanoparticles. The results from this thesis suggest that in the case of the TD-B3LYP trajectories, the first steps of the water splitting reaction mechanism are found to be heterolytic in character.

Contents

ABSTRACT ..... **III**
CONTENTS ..... **V**
LIST OF ABBREVIATIONS ..... **IX**
LIST OF TABLES ..... **XII**
LIST OF FIGURES ..... **XIII**

CHAPTER 1: *TiO_2 A MATERIAL FOR RENEWABLE ENERGY APPLICATION* **18**
1.1 INTRODUCTION 19
1.2 TITANIUM DIOXIDE 20
1.3 TiO_2 AS A PHOTOCATALYST 22
1.3.1 Excited state processes in semiconductors *22*
1.3.2 Water Splitting *26*
1.3.3 Methodologies to improve the electronic properties of bulk TiO_2 ..... *28*
1.4 SCALABILITY OF THE ELECTRONIC PROPERTIES OF TiO_2 30
1.5 EXPERIMENTAL LIMITATIONS AND COMPUTATIONAL STUDIES ABOUT TiO_2 NANOPARTICLES 32
1.6 OBJECTIVES OF THIS PHD 34
1.7 REFERENCES 35

CHAPTER 2: THEORETICAL BACKGROUND **38**
2.1 FOUNDATIONS OF QUANTUM CHEMISTRY 39
2.1.1 Schrödinger equation *39*
2.1.2 The variational principle *40*
2.1.3 Basis sets *40*

2.1.4 The Hartree-Fock Approximation *43*
2.1.5 Electron correlation *45*
2.2 POST HF METHODS 47
2.2.1 CC and EOM-CC methods *49*
2.3 DENSITY FUNCTIONAL THEORY 55
2.3.1 XC energy functional *56*
2.4 TIME DEPENDENT DENSITY FUNCTIONAL THEORY 59
2.4.1 Formal background of TD-DFT *59*
2.4.2 Calculation of forces in TD-DFT *62*
2.4.3 Limitations of the TD-DFT approach and possible solutions *63*
2.5 EINSTEIN EQUATION 65
2.6 SOLVATION METHODS 66
2.7 EXCITED STATE MOLECULAR DYNAMICS 68
2.7.1 Fewest switches Surface Hopping *70*
2.8 GLOBAL MINIMUM OPTIMISATION 72
2.9 REFERENCES 74

CHAPTER 3: *EOM-CC CALCULATIONS ON TIO_2 NANOCLUSTERS* **76**
3.1 INTRODUCTION 77
3.2 METHODOLOGY 79
3.2.1 Equation of Motion Coupled Cluster Theory *79*
3.2.2 Computational Details *80*
3.3 RESULTS 83
3.3.1 Monomer *83*
3.3.2 Dimer *87*
3.3.3 Trimer *89*
3.4 DISCUSSION 91
3.5 CONCLUSIONS 95
3.6 REFERENCES 96

CHAPTER 4: *MODELLING VERTICAL EXCITED STATES IN TIO_2 WITH TD-DFT* **98**
4.1 INTRODUCTION 99
4.2 METHODOLOGY 101
4.3 RESULTS & DISCUSSION 105
4.3.1 TD-DFT vertical excitations for $(TiO_2)_n$ *105*

4.3.2 TD-DFT vs EOM-CC for naked nanoparticles 110
4.3.3 The charge transfer character of the TD-DFT excitations 115
4.3.4 The microscopic picture 117
4.3.5 Hydrated nanoparticles; TD-DFT vs. EOM-CC 121
4.4 CONCLUSIONS 123
4.5 REFERENCES 124

CHAPTER 5; *MODELLING EXCITED STATES RELAXATIONS IN TiO_2 WITH TD-DFT* 126
5.1 INTRODUCTION 127
5.2 METHODOLOGY 129
5.3 RESULTS 131
5.3.1 Photoluminescence and excited state relaxation 131
5.3.2 Charge-transfer character 134
5.3.3 (Electronic) structure of the predicted S1 minima 136
5.3.4 Hydrated particles 140
5.4 DISCUSSION 146
5.5 CONCLUSIONS 148
5.6 REFERENCES 149

CHAPTER 6: *MODELLING PHOTOCATALYTIC PROPERTIES OF A RUTILE TiO_2 NANOPARTICLE* 150
6.1 INTRODUCTION 151
6.2 THEORETICAL APPROACH 154
6.2.1 Water Splitting 154
6.2.2 Modelling the photocatalyst 155
6.2.3 Redox potentials 157
6.2.4 Computational details 158
6.3 RESULTS AND DISCUSSION 161
6.3.1 Free exciton 161
6.3.2 Exciton self-trapping 163
6.3.3 Free electron and hole 165
6.3.4 Triplet exciton 167
6.3.5 Redox potentials 167
6.4 WATER SPLITTING AND THE EFFECT OF PARTICLE SIZE 171

6.5 CONCLUSIONS 173
6.6 REFERENCES 174

CHAPTER 7: *MODELLING PHOTOCATALYTIC PROPERTIES OF A RUTILE TiO_2 NANOPARTICLE* **177**
7.1 INTRODUCTION 178
7.2 METHODOLOGY 180
7.3 RESULTS & DISCUSSION 182
7.3.1 Ground state BOMD *182*
7.3.2 Vertical Excitation Energies *184*
7.3.3 TD-DFT/FSSH Excited state dynamics *184*
7.3.4 Excited state relaxation lifetime *186*
7.3.5 Excitation-fluorescence spectrum *188*
7.3.6 Analysis of specific interesting TD-DFT/FSSH trajectories *189*
7.4 CONCLUSIONS 195
7.5 REFERENCES 196

CHAPTER 8: SUMMARY AND PERSPECTIVES **197**

APPENDIX A **200**
APPENDIX B **204**

ACKNOWLEDGMENTS **206**
LIST OF PUBLICATIONS **208**

List of Abbreviations

AIMD: Ab initio MD

aug-cc-pVTZ: Dunning's correlation consistent triple zeta basis set, augmented with diffuse functions

B3LYP: hybrid XC energy functional, which incorporates 20 % of HF-like exchange

BHLYP: hybrid XC energy functional, which incorporates 50% of HF-like exchange

BO: Born Oppenheimer approximation

BSE: Bethe Salpether Equation

C-PCM: Conductor-like Polarisable Continuum Model

CAM-B3LYP: long range corrected B3LYP, using the Coulomb-attenuating Method (19% HF-like exchange at short range and 65% HF-like exchange at long range)

CAS-SCF: Complete Active Space SCF

CASPT2: Complete Active Space second order Perturbation Theory

CB: Conduction Band

CC: Coupled Cluster

CGF: Contracted Gaussian Function

COSMO: Conductor-like Screening Model

CR-EOM-CC: Completely Renormalised EOM-CC

CT: Charge Transfer

CX: Conical Intersection

def2-SVP: single zeta split valence basis set developed by Ahlrichs and coworkers

def2-TZVP: triple zeta split valence basis set developed by Ahlrichs and coworkers

DFT: Density Functional Theory

EA: Electron Affinity

EA*: excited state Electron Affinity

EBE: Exciton Binding Energy

EOM-CC: Equation of Motion CC

EOM-CCSD: EOM-CC approach that includes Single and Double excitations

ESSE: Excited State Stabilisation Energy

FCI: Full Configuration Interaction

FSSH: Fewest Switches Surface Hopping, method developed by John Tully

GGA: Generalised Gradient Approximation

GM: Global Minimum

GSDE: Ground State Destabilisation Energy

GTO: Gaussian Type Orbitals

GW: approximate method for the calculation of the self-energy of a many body system of electrons

HER: Hydrogen Evolution Reaction

HF: Hartree Fock

HFLE: HF like exchange

HOMO: Highest Occupied Molecular Orbital

IC: Internal Conversion

IP: Ionisation Potential

IP*: excited state Ionisation Potential

ISC: Intersystem Crossing

KS: Kohn-Sham

LDA: Local Density Approximation

LUMO: Lowest Unoccupied Molecular Orbital

MCTDH: Multiconfiguration Time Dependent Hartree

MD: Molecular Dynamics

MR: Multi Reference

MRCI: Multi Reference Configuration Interaction

NAMD: Non Adiabatic MD

NVE-ensemble: microcanonical ensemble. The energy, composition, and volume are kept constant in all possible states of the system.

OER: Oxygen Evolution Reaction

PBE: pure GGA XC energy functional developed by Perdew, Burke and Ernzerhof

PES: Potential Energy Surface

PLE: Photoluminescence Energy

R-KS: Restricted reference KS

RG: Runge-Gross

S: electronic singlet state

SCF: Self Consistent Field

SHE: Standard Hydrogen Electrode

SR: Single Reference

STO: Slater Type Orbitals

T: electronic triplet state

TCE: Tensor Contraction Engine

TD-DFT: Time Dependent DFT

TDA: Tamm-Dancoff Approximation

U-KS: Unrestricted reference KS

UV-Vis: Ultraviolet-Visible spectroscopy

VB: Valence Band

XC: Exchange Correlation

List of Tables

Table 3.1 Adiabatic excitation energies for the first (1^1B_2) and second (1^1A_2) lowest excited states of the monomer as calculated with EOM-CCSD and EOM-CCSDT.....85

Table 5.1 Lowest vertical excitation energy, photoluminescence energy, excited state stabilisation energy and ground state destabilisation energy values as calculated with different XC-potentials for the $(TiO_2)_n$ particles.....133
Table 5.2 Λ diagnostic values as calculated with TD-B3LYP, TD-CAM-B3LYP and TD-BHLYP both for $S1/S0_{min}$ and $S1/S1_{min}$ minimum energy structures.....135
Table 5.3 Vertical excitation energies, photoluminescence and corresponding Λ diagnostic values as calculated with TD-B3LYP, TD-CAM-B3LYP and TD-BHLYP for the hydrated particles.....144

Table 6.1 Vertical excitation and luminescence energies of the lowest S1 state for the TiO_2 rutile nanoparticle, as calculated with TD-CAM-B3LYP and TD-B3LYP. 162
Table 6.2 Vertical and Adiabatic energies for the EA, IP, EA* and IP* introduced in section 6.2.2. 166

Table 7.1 Excitations energies (ΔE) are in eV. 184

List of Figures

Figure 1.1 Three different polymorphs of titanium dioxide. (a) anatase, (b) rutile and (c) brookite. The figures were taken from ref. [11]. 20
Figure 1.2 Excitation process in a semiconductor.....23
Figure 1.3 Cartoon based description of the ground state and lowest excited state energy surfaces schematically showing processes involved with light absorption and fluorescence.....24
Figure 1.4 Schematic representation of the typical photocatalytic decomposition of water molecules.....26
Figure 1.5 Energy band positions for some selected semiconductors in contact with an aqueous electrolyte at pH 1 with respect to the standard hydrogen electrode (NHE) and the vacuum level as a reference. 27

Figure 2.1 Cartoon showing the principle behind the different active space EOM-CCSDt (I/II/III) approaches.. 53
Figure 2.2 Adiabatic molecular dynamics with Fewest Switches Surface Hopping. Solid black lines represent BO PESs (S0 and S1 states). 70
Figure 2.3 Schematic representation of one-dimensional PES and its relevant points GM (Global minimum) and LM (Local Minimum)……73

Figure 3.1 Structures of the three $(TiO_2)_n$ global minima for $n = 1 – 3$. 79
Figure 3.2 Trend in the four lowest excitation energies of the TiO_2 monomer as calculated with different method combinations. 84
Figure 3.3 Leading single electron HF excitation contributions to the two lowest energy excitations for the monomer calculated with EOM-CCSD and EOM-CCSDT.....87
Figure 3.4 Trend in the four lowest excitation energies of the Ti_2O_4 trans dimer as calculated with different method combinations. 88
Figure 3.5 Leading single electron HF excitation contributions to the two lowest energy excitations for the dimer calculated with EOM-CCSD and EOM-CCSDT.....89
Figure 3.6 Trend in the four lowest excitation energies of the Ti_3O_6 trimer as calculated with different method combinations. 90
Figure 3.7 Leading single electron HF excitation contributions to the two lowest energy singlet A' and A" excitations for the trimer, calculated with EOM-CCSD and EOM-CCSDT. 91
Figure 3.8 Energy ordering of the HF orbitals (occupied and virtuals) for the TiO_2 monomer (black lines), Ti_2O_4 dimer (red lines), and Ti_3O_6 trimer (blue lines).....93

Figure 4.1 Global minimum (GM) atomic configurations for $(TiO_2)_n$ nanoparticles with $n = 1 – 13$.. 102
Figure 4.2 $(TiO_2)_n(H_2O)_m$ hydrated nanoparticles, with n and m ranging between 1 and 3......103
Figure 4.3 Lowest singlet excitation energies calculated with different TD-DFT XC energy functionals for the B3LYP/def2-TZVP optimised ground state $(TiO_2)_n$ GM structures.. 106
Figure 4.4 The TD-B3LYP and TD-BHLYP lowest excitation energies plotted against the TD-CAM-B3LYP values for all the $(TiO_2)_n$ naked nanoparticles investigated in this work.....107
Figure 4.5 Trends for the 2nd (top, A) and 3rd (bottom, B) lowest excited state for the GM nanoparticles calculated with TD-DFT and different XC energy functionals.....108
Figure 4.6 TD-DFT calculated optical spectra (100 lowest excitations, or 50 lowest in the case of TD-CAM-B3LYP for reasons of computational tractability) of (A) $(TiO_2)_3$

GM (B) $(TiO_2)_6$ GM and (C) $(TiO_2)_{10}$ GM optimised structures at the B3LYP/def2-TZVP level. 109
Figure 4.7 Trend in the four lowest excitation energies of the $(TiO_2)_2$ GM dimer as calculated with different method combinations. 112
Figure 4.8 Trend in the five lowest excitation energies of the $(TiO_2)_3$ GM trimer as calculated with different method combinations. 113
Figure 4.9 Comparison of TD-DFT excitation energies with EOM-CC results for a series of selected $(TiO_2)_n$ nanoparticles, with n = 1 - 5. 114
Figure 4.10 Λ values for the three lowest excited states of $(TiO_2)_n$ nanoparticles, with n = 1 – 13, calculated with B3LYP XC energy functional. 116
Figure 4.11 TD-B3LYP lowest singlet excited state density difference and Λ value obtained for (A) the *club* dimer and (B) the GM trimer. 118
Figure 4.12 (A) TD-B3LYP lowest singlet excited state density difference and Λ value obtained for the $(TiO_2)_{10}$ structure. (B) Leading B3LYP orbital contributions to the lowest TD-B3LYP singlet excitation. 119
Figure 4.13 TD-B3LYP calculated excited state density difference for the 1st, 2nd and 3rd lowest singlet states for the $(TiO_2)_4$ and $(TiO_2)_5$ GM nanoparticles. 121
Figure 4.14 Comparison between TD-DFT lowest singlet excitations and EOM-CCSD def2-SV(P) for hydrated $(TiO_2)_n(H_2O)_m$ particles, where n and m range between 1 and 3. 122

Figure 5.1 Cartoon of the ground and lowest excited state energy surfaces and special points there on for the case of absorption followed by photoluminescence (A) and a conical intersection (CX) where the two surfaces touch (B). 128
Figure 5.2 S0 minimum energy geometries for the $(TiO_2)_n(H_2O)_2$ hydrated structures obtained from the addition of a water molecule per singly coordinated oxygen atom in the originally naked particles. 130
Figure 5.3 TD-DFT calculated photoluminescence energies for the naked $(TiO_2)_n$ particles; TD-B3LYP, TD-CAM-B3LYP and TD-BHLYP. 132
Figure 5.4 TD-DFT calculated Stokes' shift for the naked $(TiO_2)_n$ particles. 132
Figure 5.5 Comparison of the geometries of the ground and lowest excited state

minimum energy structures for the tentative $(TiO_2)_2$ GM structure obtained with the different method combinations. 137
Figure 5.6 TD-B3LYP and TD-BHLYP excited state density difference plots obtained for the vertical and PL excitations of the $(TiO_2)_2$ GM structure. 138
Figure 5.7 TD-B3LYP and TD-BHLYP excited state density difference plots obtained for the vertical and PL excitations of the $(TiO_2)_3$ GM structure. 139
Figure 5.8 TD-B3LYP and TD-BHLYP excited state density difference plots obtained for the vertical and PL excitations of the $(TiO_2)_6$ GM structure. 140
Figure 5.9 TD-DFT lowest vertical excitation energies for the hydrated particles obtained with the different XC energy functionals: TD-B3LYP, TD-CAM-B3LYP and TD-BHLYP. 141
Figure 5.10 TD-DFT calculated photoluminescence energies for the hydrated particles. 142
Figure 5.11 TD-DFT calculated Stokes' shift for the hydrated particles. 143
Figure 5.12 TD-B3LYP and TD-BHLYP excited state density difference plots obtained for the vertical and PL excitations of the $(TiO_2)_2(H_2O)_2$ particle. 144
Figure 5.13 TD-B3LYP and TD-BHLYP excited state density difference plots obtained for the vertical and PL excitations of the $(TiO_2)_3(H_2O)_2$ particle. 145
Figure 5.14 TD-B3LYP and TD-BHLYP excited state density difference plots obtained for the vertical and PL excitations of the $(TiO_2)_4(H_2O)_2$ particle. 145

Figure 6.1 Scheme showing how the (standard) reduction potentials (IP, EA and EA* and IP*) of the ideal photocatalyst (nanoparticle) straddle the proton reduction and water oxidation potentials (HER as green and OER as red broken lines, respectively). 155
Figure 6.2 A TiO_2 rutile nanoparticle, defined by 23 TiO_2 units and 34 water molecules, which amount to a total of 171 atoms. 160
Figure 6.3 Leading CAM-B3LYP orbital contributions to the lowest TD-CAM-B3LYP S1 excitation for the TiO_2 rutile nanoparticle. 162
Figure 6.4 Geometry of the TD-CAM-B3LYP relaxed S1 excited state minimum for the TiO_2 rutile nanoparticle. 163

Figure 6.5 (TD-)CAM-B3LYP predicted EA, IP, EA* and IP* vertical and adiabatic potentials of the TiO_2 rutile nanoparticle in water, compared to the water-splitting reduction (green line) and oxidation (red line) potentials at pH = 0 (broken lines) and pH = 7 (dotted lines). 169
Figure 6.6 (TD-)B3LYP predicted EA, IP, EA* and IP* vertical and adiabatic potentials of the TiO_2 rutile nanoparticle in water, compared to the water-splitting reduction (green line) and oxidation (red line) potentials at pH = 0. 170

Figure 7.1 $(TiO_2)(OH)_4(H_2O)_2$ particle, where the two molecularly absorbed waters and the relevant atoms discussed later in the text are labeled explicitly. 180
Figure 7.2 B3LYP (top) and BHLYP (bottom) bond distances (Å) vs time (fs) in a ground state BOMD trajectory at 300 K. 183
Figure 7.3 Bond distances (Å) vs time (fs) for a high temperature (500 K) B3LYP ground state BOMD trajectory. 183
Figure 7.4 Set of 30 FSSH MD trajectories for the TiO_2 particle as calculated with B3LYP (top) and BHLYP (bottom). 186
Figure 7.5 Average S1 population (blue line) vs time (fs) of 30 trajectories for the excited state dynamics of the TiO_2 particle as calculated with B3LYP (top) and BHLYP (bottom). 187
Figure 7.6 B3LYP and BHLYP absorption (black) and emission (red) spectra calculated from 30 TD-DFT/FSSH trajectories of the TiO_2 particle. 189
Figure 7.7 Example of B3LYP trajectory of excited state dynamics in which a –OH rupture is observed in both the molecularly absorbed waters. 191
Figure 7.8 Excited state density difference plots obtained for each relevant molecular structure of the first OH rupture observed during the trajectory shown in Figure 7.7. .. 192
Figure 7.9 Example of BHLYP trajectory of excited state dynamics in which a –OH rupture is observed in one of the molecularly absorbed waters. 194

Chapter 1

TiO_2: a material for renewable energy applications

In this chapter I will first introduce titanium dioxide and its most common polymorphs, its photocatalytic properties and then discuss some of the methodologies used to improve the material's photocatalytic performance. I will subsequently move to discussing the fundamental physical and chemical processes that take place after TiO_2 absorbs light and review part of the literature on previous computational studies on TiO_2. Finally, I will define the open questions that this PhD project is trying to answer.

1.1 Introduction

Titanium dioxide (TiO_2), an inexpensive wide band gap semiconductor with a high refractive index and brightness, has been extensively used as a white pigment for paint, food coloring, sunscreens, biomaterials and cosmetics since its commercial production in the 1920s [1]. Thanks to the pioneering work by Fujishima on the ultraviolet (UV) light-induced photoelectrochemical water splitting on TiO_2 surfaces in the 1970s [2], it has been widely investigated for many more advanced applications. These applications include solar fuel production (e.g. hydrogen and methanol) from water [2], ethanol [3], or through CO_2 reduction [4] and CO oxidation [5], removal of organic pollutants from the environment [6], and uses in dye-synthesised solar cells [7]. The performance of TiO_2-based materials in those applications depends on many factors, such as the material's optical, electronic, structural and surface properties. Worldwide research efforts have been devoted to modify some of these properties in order to improve the photocatalytic efficiency of TiO_2-based materials. Such efforts have been focusing on diverse aspects, ranging from the results of different synthesis conditions, and the experimental/theoretical investigations of fundamental physical and chemical properties of TiO_2 materials [8].

As this thesis consists of a computational study of TiO_2 nanomaterials, my work will mostly focus on the theoretical investigations of the material's chemical/physical properties. However, in this chapter I will try to motivate the need of a computational approach and show how this can be used to solve the numerous controversies coming from experimental studies on photocatalytic processes in TiO_2 materials.

1.2 Titanium dioxide

In nature TiO_2 commonly crystallises in one of three different polymorphs; anatase, rutile and brookite. The three crystal structures of these polymorphs, shown in Figure 1.1, can be described in terms of TiO_6 distorted octahedra, and differ by the degree of distortion of each octahedron and their different assembly patterns.

In anatase (Figure 1.1 a), characterised by a primitive tetragonal cell, four of the eight neighbors of each octahedron share corners and the others share edges. The corner-sharing octahedra form (001) planes, linked through their edges with the octahedra forming the neighbouring parallel (001) planes. In rutile (Figure 1.1 b), characterised by a body centered tetragonal cell, ten neighbors are surrounding each octahedron: eight share corners and only two share edges. The long-range polyhedral connectivity of rutile can be visualised as chains of edge sharing TiO_6 octahedra running along the [110]-type direction. These chains share corners with each other as illustrated in Figure 1.1 b [8]. In brookite (Figure 1.1 c), which has an orthorhombic unit cell, each octahedron shares three edges [1,9,10].

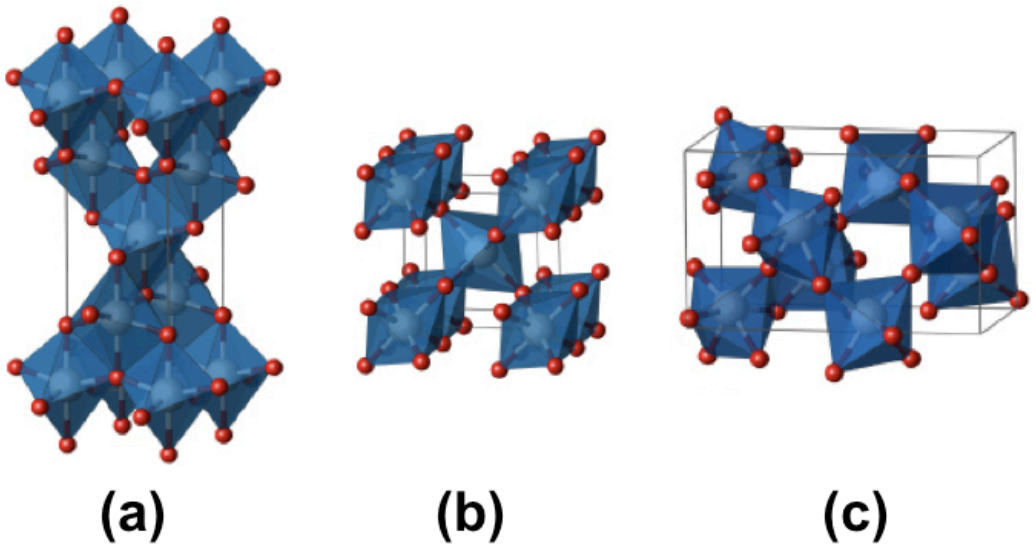

Figure 1.1 Three different polymorphs of titanium dioxide. (a) anatase, (b) rutile and (c) brookite. The small red spheres represent the oxygen atoms, the big grey ones are the titanium atoms, while the blue polyhedral shapes show the orientation in space of the TiO_6 octahedra. The figures were taken from ref. [11].

The coexistence of different TiO_2 polymorphs suggests that one of its crystal phases has a minimal Gibbs free energy, whereas the others are thermodynamically less stable. Calorimetric enthalpy experimental data for bulk TiO_2 predict rutile as the most

thermodynamically stable crystal phase at most temperatures and pressures up to 60 kbar, above which the high-pressure form of TiO_2 (i.e. TiO_2 II) becomes the most relevant polymorph [12-14]. Anatase is the crystal phase generally observed in sol-gel synthesis of TiO_2, whereas brookite is usually found as a by-product when the precipitation is carried out in an acidic medium at low temperature. However, both polymorphs tend to be transformed to rutile when heated [15] (in line with the latter being the thermodynamically preferred phase).

Bulk rutile and anatase have band gaps (energy difference between the top of the valence band and the bottom of the conduction band) of 3.0 and 3.2 eV respectively. In the case of brookite, no precise value of the band gap is known and rather a range of values is reported experimentally (i.e. 3.1-3.4 eV) [10]. This ambiguity arises from the fact that experimentally samples of brookite are generally poorly crystallised. The variations in the band gap between the different TiO_2 polymorphs are naturally attributed to the structural difference in the crystal lattice, both bond length and the stacking of TiO_6 octahedra, which lead to a different orbital mixing between the titanium 3s/3d and oxygen 2p orbitals [4,16].

1.3 TiO_2 as a Photocatalyst

TiO_2 is the quintessential photocatalyst; a material that allows a reaction to happen in the presence of light that otherwise would not take place. Among the different TiO_2 polymorphs, pure anatase is considered the most promising polymorph for photocatalytic applications as it offers higher electron mobility, lower dielectric constant and lower density compared to rutile and brookite [1,17]. Very recently, Maeda [18-20] suggested that also rutile TiO_2, which has always been considered a less efficient photocatalyst than anatase, could be employed in photocatalytic reactions (e.g. water splitting) yielding good performance. In the case of brookite, due to the difficulties encountered in preparing high purity crystals with large surface area, its photocatalytic properties have not been widely investigated, compared to rutile and anatase. Despite the interesting properties exhibited by pure TiO_2 polymorphs, in practice Degussa P25 nanopowder, a mixture of 75% anatase and 25% rutile, is often employed as *reference photocatalyst* in photocatalytic studies and industrial applications. P25 generally displays enhanced photocatalytic performance over pure rutile or anatase nanocrystals [8].

In order to better understand the use of TiO_2 as a photocatalyst, I will first introduce the excited state processes that can take place in semiconducting materials and then discuss their ability to catalyse specific chemical reactions, such as water splitting.

1.3.1 Excited state processes in semiconductors

Semiconductors can be excited by light when a photon, that has an energy higher than the semiconductor band gap, promotes an electron to the conduction band (CB) while at the same time a hole in the top of the valence band (VB) is formed (Figure 1.2 a). This excited electron and hole can either be essentially free charge carriers, where there is negligible interaction between them both (Figure 1.2 b), or form electron-hole pairs bound by their mutual Coulomb interaction (Figure 1.2 c). The latter bound state is referred to as an exciton and is stabilised relative to what would be free carrier states by the exciton binding energy (EBE). A measure of the EBE can be obtained by a comparison between the material's band gap or quasiparticle gap (the energy required to make free charge carriers, experimentally measured indirectly through a combination of normal and inverse photoemission spectroscopy) and the energy of the lowest optical

excitation (the optical gap or optical absorption onset, experimentally measured by UV-Vis absorption spectroscopy).

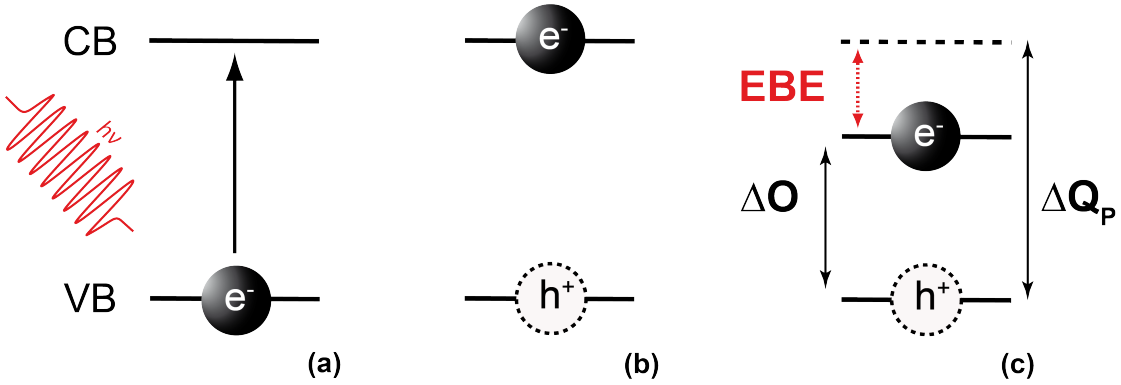

Figure 1.2 Excitation process in a semiconductor, where the absorption of light (a) causes the promotion of an electron (black sphere, e^-) from the VB to the CB, and the creation of a hole (white sphere, h^+) in the VB. (b) The electron and the hole are free charge carriers, with negligible interaction between them both. (c) Exciton, where the electron and hole are bound together by a reciprocal Coulomb interaction. EBE stands for Exciton Binding Energy, while ΔO and ΔQ_P represent the Optical gap and the Quasiparticle gap, respectively.

The exciton generated in this process can then be used in light driven applications; either directly to produce electricity in photovoltaic solar cells or indirectly, to drive chemical processes (photocatalysis). Photocatalytic applications are not strictly considered photochemical in character, as no excited species are directly involved in the reactions. In a photocatalysed reaction, the catalyst is active only in the excited state, but the chemical transformation of the reactants into the products occurs entirely on the ground state surface [21]. For this reason, when investigating the excited state processes involving a photocatalytic material, it is not only important to simply focus on the excitation band gap, but also on the fate of the excited state after the electron occupies the CB. In order to understand these processes better, a simple molecular interpretation can be employed, where the semiconductor in its ground state (assuming it is a close shell singlet, S_0) is approximated by a single Potential Energy Surface (PES). Figure 1.3 displays the most prominent features and processes for a cartoon-like one-dimensional set of PESs. Relevant features are labelled with bold capital letters (**A**-**G**) and the pertinent vertical excitations between the different surfaces by dashed arrows. The first relevant process is the absorption of light by the semiconductor in the ground state minimum energy geometry **A** and the electronic excitation of the system from S_0 to higher excited singlet states S_n (where $n > 0$).

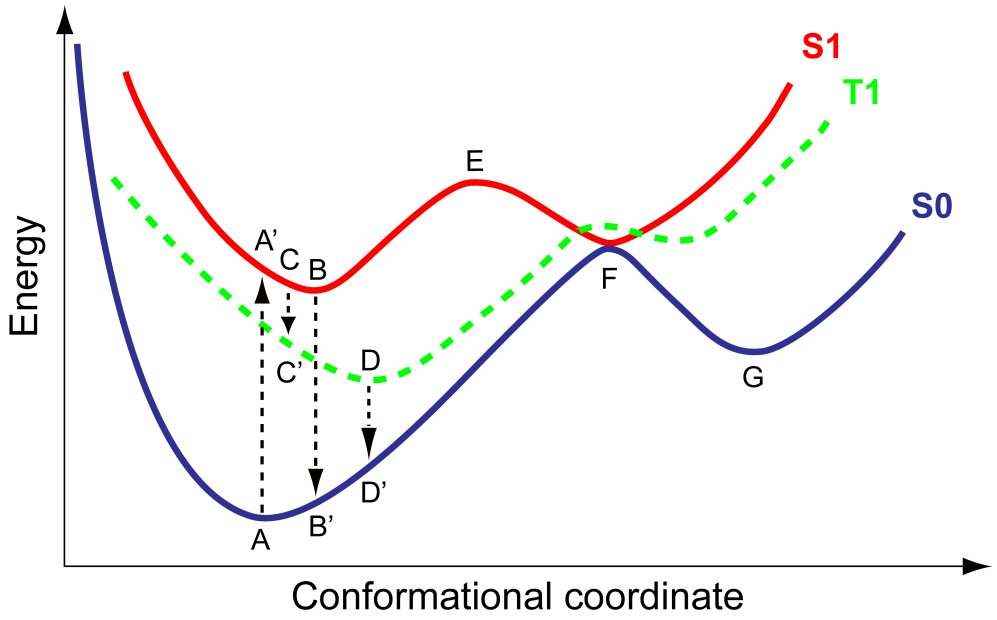

Figure 1.3 Cartoon based description of the ground state (S_0 blue curve) and lowest excited state (singlet, S_1 red and triplet, T_1 green curve) energy surfaces schematically showing processes involved with light absorption and fluorescence.

After absorption of a photon the excited system is generally not in a stationary state and will start to relax and lower its energy. If the semiconductor was initially excited into a higher excited state than the lowest excited state the system will de-excite radiationlessly through *internal conversion* (IC) to the lowest excited state (e.g. from S_n to S_1, for simplicity not shown in Figure 1.3). The system can also lower its energy by nuclear relaxation (also referred at as exciton (self)-trapping) along the excited state surface in the direction of a nearby excited state minimum (e.g. in the case of S_1 in Figure 1.3, relax from **A'** towards **B**). The electronic relaxation from S_n to S_1 through IC is generally very fast compared to nuclear motion so that one can assume that all nuclear relaxation will take place on the S_1 surface. This observation is canonised in Kasha's rule [22], which states that fluorescence or phosphorescence (see below) occur in appreciable yield only from the lowest excited state of a given multiplicity (i.e. S_1 or T_1). The vast majority of systems appear to follow Kasha's rule, though a few experimental examples of non–Kasha behaviour have been reported for specific nanoparticles [23].

Concentrating on the majority of systems that follow Kahsa's rule, nuclear relaxation on the S_1 surface after IC will lead the system to a S_1 excited state minimum (point **B** in Figure 1.3) from which the system can undergo *fluorescence* back to the ground state (**B**

-> **B'**). Alternatively, the system can experience *intersystem crossing* (ISC) from the singlet S_1 to the T_1 triplet surface (**C** -> **C'**), relax to a nearby T_1 minimum (**D**) and display *phosphorescence,* where the system relaxes back to the ground state (**D** -> **D'**). In both cases the system, after de-excitation to the ground state surface (at point **B'** or **D'** respectively), can relax back to the ground state minimum **A**. The energy emitted during fluorescence or phosphorescence is commonly referenced to as the photoluminescence energy (PLE). The PLE signal is the energy at which the excited state system returns to its ground state configuration and it can be easily obtained experimentally through spectroscopy. The PLE by definition is lower in energy than the absorption energy and the difference between the material's optical gap (lowest absorption energy) and the PLE is called the Stokes' shift. As will be discussed in Chapter 3, often experimental studies provide the adiabatic energy, which corresponds to the difference in energy between the excited state minimum and the ground state minimum energies of a specific chemical system (points **B** and **A** in Figure 1.3 respectively).

Other relevant points on the excited state surface are excited state barriers and conical intersections. An excited state barrier (point **E** in Figure 1.3) separates the excited state minimum downhill of the ground state minimum energy structure from other excited state minima or, alternatively, conical intersections (CX, point **F** in Figure 1.3). The latter are points where two excited state surfaces or an excited and ground state surface touch (i.e. are degenerate). At a CX the system can undergo a radiationless transition from one excited state to the other, or, as is the case on point **F**, from the lowest excited state to the ground state.

Finally, the exciton can in principle dissociate, or ionise, into a free electron and a free hole (free charge carriers), which are sufficiently spatially separated that their mutual Coulombic interaction is negligible. This process is generally endothermic as an amount of energy equal to the EBE needs to be provided in order for the exciton to dissociate, either in the form of heat (thermal ionisation) or an electric field (field ionisation). However, the presence of a solvent, which stabilises free charge carriers through screening, and or strong (self-)trapping of the free charge carriers means that exciton dissociation can be spontaneous in specific cases (see Chapter 6). Therefore, depending on the kinetics of a photocatalytic application, the exciton/free charge carriers can either catalyse the specific reaction immediately after excitation or they can first undergo the

different excited state processes discussed above, (self)-trap in the semiconductor (deformation of the ground state geometry) and then finally be transferred to the reactive molecules absorbed on the photocatalytic material.

1.3.2 Water Splitting

Water splitting is an artificial photosynthesis process, which involves the transformation of light into hydrogen and oxygen, from a ubiquitously available source such as water, via electron/hole exchange with an excited photocatalyst [21]. The overall water splitting reaction is shown in (1–a), where water is dissociated to form molecular hydrogen and oxygen. The overall (1–a) reaction can be seen as the combination of the two redox half reactions (1–b) and (1–c), where H_2 is generated via a two electron reduction and O_2 via a four hole oxidation [24].

$$H_2O \rightarrow H_2 + \frac{1}{2}O_2 \qquad (1\text{–a})$$

$$2H^+ + 2e^- \rightleftarrows H_2 \qquad (1\text{–b})$$

$$2H_2O \rightleftarrows O_2 + 4H^+ + 4e^- \qquad (1\text{–c})$$

As already discussed in the introduction, the discovery of the phenomenon of photo-induced splitting of water on a TiO_2 electrode in 1972 by Fujishima *et al.* [2] encouraged research devoted to the use of TiO_2-based materials for the production of hydrogen as a clean and renewable replacement for fossil fuels (see Figure 1.4).

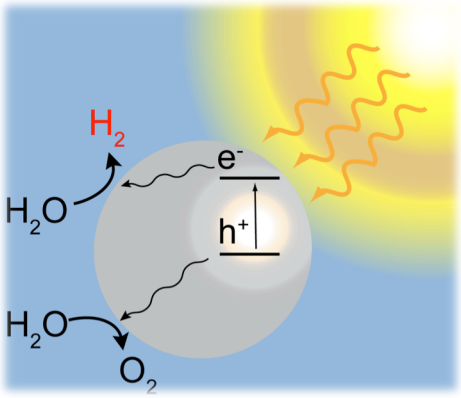

Figure 1.4 Schematic representation of the typical photocatalytic decomposition of water molecules where hydrogen is produced via a reduction process at the conduction band assisted by a generated photoelectron and oxygen is produced via an oxidation process assisted by a photoinduced hole in the valence band of the photocatalyst.

After the discovery of the water splitting phenomenon in TiO_2, many different materials have been identified as photocatalysts (Figure 1.5); nevertheless, TiO_2 is still potentially considered one of the best candidates for the efficient production of molecular hydrogen [7,25].

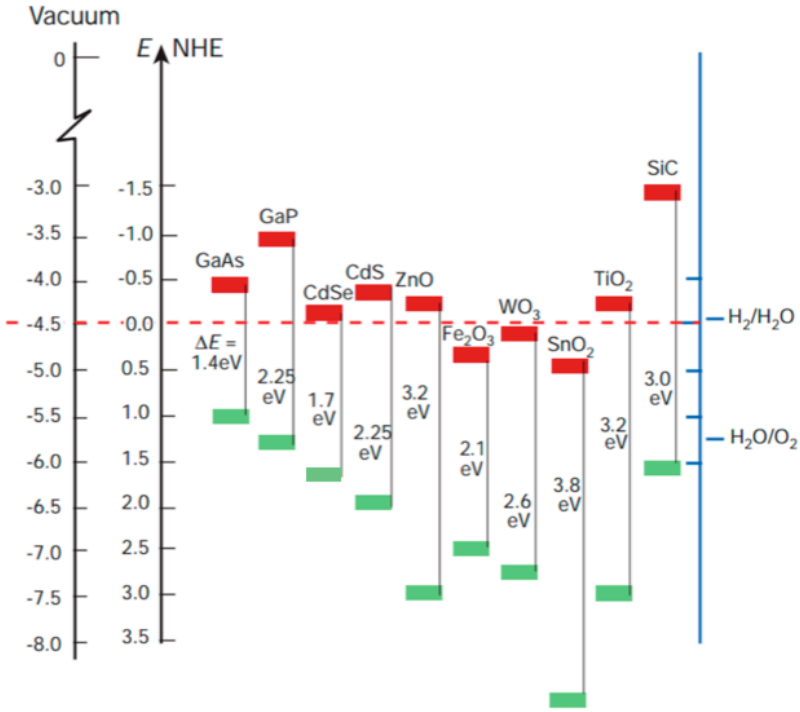

Figure 1.5 Energy band positions (CB in red, VB in green) for some selected semiconductors in contact with an aqueous electrolyte at pH 1 with respect to the standard hydrogen electrode (NHE) and the vacuum level as a reference. For TiO_2 only the anatase level alignments are shown. On the right, the levels of the two water splitting half reactions (reduction and oxidation 0.0 and 1.23 V, respectively) are shown as comparison [7].

The better performance of TiO_2 when compared to other binary semiconductors in converting incident photons into molecular hydrogen depends on several factors [15]. First, excitons inside TiO_2 materials have a lower electron/hole recombination rate, which allows them to move from the bulk to the surface, where they can interact with reactive molecules [15]. Second, as can be observed in Figure 1.5 (only the anatase levels are shown) the position of the CB for TiO_2 is above the energy of the hydrogen redox potential, $E_{red}(H_2/H_2O)$, and the VB is below the water oxidation potential, $E_{ox}(H_2O/O_2)$, therefore both reactions are thermodynamically favoured (however, with a very small overpotential in the case of the water reduction reaction). Furthermore, differently from other semiconductors (e.g. ZnO, CdS and SiC), TiO_2 is an extremely

stable material in the presence of an aqueous electrolyte over a wide range of pH values and applied potentials. However, the main drawback for all the bulk polymorphs of TiO_2 is their large optical gap [26-29], which means that only high-energy UV radiation and that a small part of the solar spectrum (< 10%) can excite electrons to the conduction band. Another important aspect to be considered for the improvement of its photocatalytic properties is the reduction of the rate of recombination processes for the photo-excited electron and holes. As shown in Figure 1.5, the water reduction reaction has only a small overpotential when catalysed by a TiO_2 free electron, and as a result it competes with exciton recombination processes, decreasing the overall photocatalytic efficiency of the material.

Thus, the main goal for improvement of the performance of TiO_2 materials is to increase their photocatalytic activity by shifting the optical gap from the UV to the visible region (highest energy 2.5 eV) [30]. Generally, a larger overall potential than 1.23 V (e.g. 1.8 V) is required to favor the water splitting reaction, where the difference between the effective and equilibrium potentials correspond to the overpotential, the excess energy required to overcome energetic losses and kinetic barriers within the semiconductor [31,32].

1.3.3 Methodologies to improve the electronic properties of bulk TiO_2

Adding impurity ions to semiconductors is a commonly applied method to tune the material's optical and electronic properties. Compared to other semiconductors, TiO_2 polymorphs exhibit a high phase stability and as a result a high solubility of impurity ions in the host lattice [15]. The introduction of impurity ions into the TiO_2 lattice is performed through the substitution of the host anions and or cations. Cation (or metal) doping involves the substitution of Ti ions by other 3d transition metal ions (e.g. Mn, Mo, V, Fe, Cr, Cu) [15]. The crystal field splitting of the transition metal 3d orbitals generates potentially both localised and delocalised impurity states within the TiO_2 band gap. Anion doping of bulk TiO_2 or thin films, especially with B [33], C [34], N [35,36] and S [37], has been shown to be a very efficient way to reduce the semiconductor's band gap, although many dopants yield smaller gaps than the threshold needed for water splitting. This kind of doping causes changes in the electronic structure of the semiconductor, introducing intra band gap impurity energy levels (localised 2p acceptor states), which are located in the proximity of the VB [15]. However, it must be said that

these mid-gap states are of limited use for optical applications, as they don't give rise to strong absorption of light.

In addition to doping the semiconductor's lattice with impurities, in recent years, a considerable research effort focused on morphology and size as another key property to be manipulated in order to tune the photocatalytic performance of TiO_2-based materials [8]. The general interest in nanotechnologies relies on the idea that there exists an optimal size for specific chemical and physical properties between the atomic scale and very large systems [38]. For example, nanomaterials (e.g. nanoparticles, nanowires and nanoflakes) exhibit higher catalytic efficiency as a consequence of the high surface area resulting from the small particle size [39]. In the next section I will try to discuss in more detail the size dependency of the electronic properties of TiO_2-based materials.

1.4 Scalability of the electronic properties of TiO_2

Recent experimental investigations suggest that some electronic and optical properties of TiO_2 particles at the nanolevel are different in character from those of bulk materials [38]. Furthermore, for low dimensional nanostructured materials the movement of electrons and holes is influenced by quantum confinement and the transport properties related to phonons and photons are to a large degree affected by the size of the system [15,30,38].

In the case of large TiO_2 nanoparticles the analysis of X-ray diffraction patterns by Zhang *et al.* [40] suggests that the particle's crystalline phase strongly depends on the temperature at which they are synthesised; at room temperature anatase is generally observed, but as the temperature increases, rutile becomes the predominant polymorph. However, for particles smaller than 14 nm, anatase was found to be thermodynamically the most stable polymorph over a wide range of temperatures. This trend can be linked to the experimental surface enthalpy of each different phase, where rutile has the highest value, brookite intermediate and anatase the lowest [15,16]. As the size and predominant phase of the TiO_2 aggregates strongly depend on the methods of synthesis used, in this section I will first quickly revise which are the techniques employed for the synthesis of TiO_2 nanosystems and then move the discussion on the influence of the size on their optical and photocatalytic properties.

Different methods can be used to produce nanoparticles, nanorods, nanowires and nanotubes of the desired size. During the past decades, various approaches, such as sol-gel [30,41,42], hydrothermal/solvothermal [43], physical/chemical vapour deposition [44,45], electrodeposition and sonication [46] techniques have been successfully employed for making TiO_2 nanomaterials. However, as the size of the material becomes smaller, the bigger become the challenges that have to be faced experimentally in order to obtain kinetically stable nanocrystals with a specific size and morphology (e.g. approximately 10 hours are required for the synthesis of nanoparticles with sizes in the range of 10 nm [47]). Until recently, strict particle size control for TiO_2 was very challenging for particles below 10 nm in size, but recent advances in the use of spherical coordination templates allowed the synthesis of TiO_2 particles smaller than 3 nm and with a controllable shape [48].

Cernuto *et al.* [49], with a total scattering Debye function study, recently found that not

only the size, but also the shape and the exposed facets of the TiO_2 nanoparticles can significantly affect their photoactivity (e.g. photoexcited electron-hole generation and separation), suggesting that certain nanoparticle sizes and shapes might be the optimal key for achieving high photocatalytic activity. Experiments on a range of different TiO_2 nanostructures show that as the size of the TiO_2 particle decreases an increase in the semiconductor band gap is observed which, however, shift the redox potentials of the VB holes and the CB electrons, allowing photochemical reactions, which might not otherwise proceed in bulk materials [16,30]. The observed blue shift in the absorption spectrum of a semiconductor of decreasing size is usually linked to the quantum confinement, where the exciton, being confined in a restricted space (nanoparticle) causes a broadening of the CB-VB energy gap [15]. A similar trend was observed for the particle's PLE signal, for which experimental results showed that the maximum peak of the emitted spectra for TiO_2 nanostructures lies around 2.3 eV and it exhibits a blue shift as the average particle size decreases [16,50].

It may seem that as TiO_2 nanoparticles require the absorption of higher energy light for the generation of the electron/hole pair, decreasing the size of the particle has no positive effects on its overall photocatalytic efficiency. However, in principle, the incorporation of dopants in the nanoparticle could be employed to counterbalance quantum confinement's effects and therefore the semiconductor's properties could be tuned to the specific needs. In nanostructured materials, the overall ability to incorporate impurity ions (both anions and cations) is improved, as the nanoparticle, is more prone to tolerate structural distortion [15]. In addition, doped nanoparticles provide impurity centers near the material's surface, which being close to the surface absorbed molecules (e.g. water molecules, for water splitting applications) could assist in spatially separating the electrons and holes and minimising their recombination.

1.5 Experimental limitations and computational studies about TiO_2 nanoparticles

Experimentally, understanding the fundamental processes involved with photocatalytic applications of inorganic nanoparticles is not a straightforward task. Firstly, most scattering and spectroscopic methods yield only an average picture of the atomic structure of nanoparticles, which often show limited long-range order, and high-resolution structural data is therefore lacking. Secondly, structures relevant to the photochemistry and photophysics often only exist for short times (in the order of picoseconds or femtoseconds), and hence it is very challenging to characterise them in experiment [51].

In the last fifty years, quantum-chemistry approaches, when used in conjunction with experiments, have proven to be very useful techniques as they can provide an atomistic interpretation of complex chemical and physical processes (e.g. excited state processes). With the recent development of efficient computational methodologies and state of the art supercomputers allowing the use of more realistic chemical models, quantum chemistry approaches have also proven to accurately predict properties of new materials and efficiently drive experimental research. However, the feasibility of computational simulations decreases with the system size and often a compromise between accuracy and computational cost must be reached, strongly limiting the complexity of the systems and processes that can be investigated.

To understand the physics and chemistry underlying the application of TiO_2 nanostructures in photocatalysis and photovoltaics from a theoretical point of view, TiO_2 nanostructures and extended systems have been extensively studied computationally using a variety of methods [52-67]. Most of these studies focus either on ground state properties of TiO_2 nanosystems or on the calculation of their vertical excited states. For the potential of computational chemistry in modeling photocatalytic applications to be realised, however, one should be able to make relatively accurate predictions of not only the optical absorption spectra, which is routinely done [59,68-71], but also the reduction potentials of the free charge carriers and excitons [72,73] as well as charge transfer processes [57,65,74-83] and the energetics/structural distortion associated with trapped excitons [15,83,84]. Such properties require the calculation of

not only vertical excited state energies but also the energies and geometries of relaxed excited states. The method of choice for calculating such properties is a combination of Density Functional Theory (DFT), for ground state energies and structures, and Time-Dependent DFT (TD-DFT), for their excited state counterparts. Alternative approaches exist in the form of quantum chemical wave function (e.g. Coupled Cluster and Complete Active Space second order Perturbation Theory, CASPT2) [85,86] or Green's function based methods [70,87]. Such alternatives have advantages in terms of reliability and inherent accuracy, but unfortunately currently lack the desired scaling with system size and/or the ease of use of (TD-)DFT. This is especially true when studying the nanostructured materials relevant to applications in photocatalysis and dye-sensitised solar cells, where one has to be able to calculate the properties of systems composed of tens to hundreds of atoms.

To date, no computational studies have focused on the effect of nuclear relaxation (electron/hole self-trapping) in excited state processes for realistic TiO_2 nanoparticles, which as suggested above, would be of fundamental importance in order to gather insights into photocatalytic applications, such as water splitting. Furthermore, all the studies mentioned above, and nearly all work in the literature, employ a combination of (TD)-DFT with conventional semi-local and hybrid exchange and correlation (XC) potentials. As it will be discussed in the next chapters, this approach suffers from a number of potential deficiencies. Due to the lack of accurate experimental results for nanoparticles of intermediate size (< 1 nm), little is know about the accuracy of these approaches in the description of excited state processes of TiO_2 particles. There is therefore an urgent need in the literature for accurate benchmark studies on the performance of these approaches.

1.6 Objectives of this PhD

The long-term goal of this PhD project is to understand if, through the modification of their size/shape and chemical composition (e.g. doping), the properties of TiO_2 nanoparticles can be tuned to favor catalytic reactions that would not be allowed otherwise.

The rest of this thesis will be presented as follows: in the next chapter I briefly introduce the computational methodologies employed during this PhD work. In Chapter 3, I define accurate benchmarks for the description of optical properties in TiO_2 nanoclusters using correlated wave function methods, such as Equation of Motion Coupled Cluster theory (EOM-CC). Following this, in Chapter 4, I then compare EOM-CC results with the predictions of TD-DFT and try to understand which are the shortcomings of the common TD-DFT XC energy functionals in the description of TiO_2 excited states. Moreover, in Chapter 5, using TD-DFT, I try to get some insights into the atomistic and electronic processes associated with excitation and photoluminescence for small TiO_2 nanoclusters. I believe that understanding photoluminescence, and the associated exciton (self) -trapping, is an important step towards getting clear insights of more complicated, but important excited state processes such as photocatalysis and photovoltaics. Chapter 6 consists of the investigation of excited state processes taking place in a realistic TiO_2 nanoparticle (~ 1 nm), with a focus on its photocatalytic ability to split water. In this chapter, standard reduction potentials of the free charge carriers and exciton are calculated for the rutile particle and compared with those of the water splitting half-reactions. In Chapter 7, excited state non-adiabatic dynamic simulations of a small hydrated TiO_2 particle are employed in order to shed light on the mechanistic steps involved in a water splitting reaction. Finally, in Chapter 8, I summarise the results and briefly discuss some of the prospects for future research.

1.7 References

[1] Carp, O.; Huisman, C. L.; Reller, A. *Prog. Solid. State Ch.* **2004**, *32*, 33.
[2] Fujishima, A.; Honda, K. *Nature* **1972**, *238*, 37.
[3] MurdochM; Waterhouse, G. I. N.; Nadeem, M. A.; Metson, J. B.; Keane, M. A.; Howe, R. F.; Llorca, J.; Idriss, H. *Nat. Chem.* **2011**, *3*, 489.
[4] Li, Y.-F.; Liu, Z.-P. *J. Am. Chem. Soc.* **2011**, *133*, 15743.
[5] Green, I. X.; Tang, W.; Neurock, M.; Yates, J. T., Jr. *Science* **2011**, *333*, 736.
[6] Hoffmann, M. R.; Martin, S. T.; Choi, W. Y.; Bahnemann, D. W. *Chem. Rev.* **1995**, *95*, 69.
[7] Gratzel, M. *Nature* **2001**, *414*, 338.
[8] Liu, L.; Chen, X. *Chem. Rev.* **2014**, *114*, 9890.
[9] Hanaor, D. A. H.; Sorrell, C. C. *J. Mater. Sci.* **2011**, *46*, 855.
[10] Di Paola, A.; Bellardita, M.; Palmisano, L. *Catalysts* **2013**, *3*, 36.
[11] Landmann, M.; Rauls, E.; Schmidt, W. G. *J. Phys.: Condens. Matter* **2012**, *24*, 195503.
[12] Navrotsk.A; Jamieson, J. C.; Kleppa, O. J. *Science* **1967**, *158*, 388.
[13] Jamieson, J. C.; Olinger, B.; Dachille, F.; Simons, P. Y.; Roy, R. *Am. Min.* **1969**, *54*, 1477.
[14] Mitsuhashi, T.; Kleppa, O. J. *J. Am. Ceram. Soc* **1979**, *62*, 356.
[15] Kapilashrami, M.; Zhang, Y.; Liu, Y.-S.; Hagfeldt, A.; Guo, J. *Chem. Rev.* **2014**, *114*, 9662.
[16] Chen, X.; Mao, S. S. *Chem. Rev.* **2007**, *107*, 2891.
[17] Luttrell, T.; Halpegamage, S.; Tao, J.; Kramer, A.; Sutter, E.; Batzill, M. *Sci. Rep.* **2014**, *4*.
[18] Maeda, K. *Chem. Commun.* **2013**, *49*, 8404.
[19] Maeda, K. *Catal. Sci. Technol.* **2014**, *4*, 1949.
[20] Maeda, K.; Murakami, N.; Ohno, T. *J. Chem. Phys. C* **2014**, *118*, 9093.
[21] Ravelli, D.; Dondi, D.; Fagnoni, M.; Albini, A. *Chem. Soc. Rev.* **2009**, *38*, 1999.
[22] Kasha, M. *Farad. Discuss.* **1950**, *9*, 14.
[23] Choi, C. L.; Li, H.; Olson, A. C. K.; Jain, P. K.; Sivasankar, S.; Alivisatos, A. P. *Nano Lett.* **2011**, *11*, 2358.
[24] Shevlin, S. A.; Woodley, S. M. *J. Phys. Chem. C* **2010**, *114*, 17333.
[25] Heller, A. *Science* **1984**, *223*, 1141.
[26] Cardona, M.; Harbeke, G. *Phys. Rev.* **1965**, *137*, 1467.
[27] Hosaka, N.; Sekiya, T.; Fujisawa, M.; Kurita, S. *J. Electron Spec. Rel. Phen.* **1996**, *78*, 75.
[28] Hosaka, N.; Sekiya, T.; Kurita, S. *J. Lumin.* **1997**, *72-4*, 874.
[29] Hosaka, N.; Sekiya, T.; Satoko, C.; Kurita, S. *J. Phys. Soc. Jpn.* **1997**, *66*, 877.
[30] Chen, X. *Chinese J. Catal.* **2009**, *30*, 839.
[31] Chiodo, L.; Garcìa-Lastra, J. M.; Mowbray, D. J.; Iacomino, A.; Rubio, A. In *Computational studies of new materials: From nanostructures to bulk energy conversion materials*; George, T. F., Jelski, D., Letfullin, R. R., Zhang, G., Eds.; World Scientific: Singapore, 2011.
[32] van de Krol, R.; Liang, Y.; Schoonman, J. *J. Mater. Chem.* **2008**, *18*, 2311.
[33] In, S.; Orlov, A.; Berg, R.; Garcia, F.; Pedrosa-Jimenez, S.; Tikhov, M. S.; Wright, D. S.; Lambert, R. M. *J. Am. Chem. Soc* **2007**, *129*, 13790.
[34] Khan, S. U. M.; Al-Shahry, M.; Ingler, W. B. *Science* **2002**, *297*, 2243.

[35] Di Valentin, C.; Pacchioni, G.; Selloni, A. *Phys. Rev. B* **2004**, *70*.
[36] Dunnill, C. W.; Parkin, I. P. *Dalton Trans.* **2011**, *40*, 1635.
[37] Umebayashi, T.; Yamaki, T.; Itoh, H.; Asai, K. *Appl. Phys. Lett.* **2002**, *81*, 454.
[38] Calatayud, M.; Minot, C. *J. Phys. Chem. C* **2009**, *113*, 12186.
[39] Dorfman LM; GE, A. *NSRDS-NBS* **1973**, *46*.
[40] Zhang, H. Z.; Banfield, J. F. *J. Phys. Chem. B* **2000**, *104*, 3481.
[41] Trentler, T. J.; Denler, T. E.; Bertone, J. F.; Agrawal, A.; Colvin, V. L. *J. Am. Chem. Soc* **1999**, *121*, 1613.
[42] Lin, J.; Lin, Y.; Liu, P.; Meziani, M. J.; Allard, L. F.; Sun, Y. P. *J. Am. Chem. Soc* **2002**, *124*, 11514.
[43] Kim, C. S.; Moon, B. K.; Park, J. H.; Choi, B. C.; Seo, H. J. *J. Cryst. Growth* **2003**, *257*, 309.
[44] Seifried, S.; Winterer, M.; Hahn, H. *Chem. Vap. Deposition* **2000**, *6*, 239.
[45] Wu, J. J.; Yu, C. C. *J. Phys. Chem. B* **2004**, *108*, 3377.
[46] Yu, J. C.; Yu, J. G.; Ho, W. K.; Zhang, L. Z. *Chem. Comm.* **2001**, 1942.
[47] Zhang, H.; Banfield, J. F. *Chem. Mater.* **2005**, *17*, 3421.
[48] Ichijo, T.; Sato, S.; Fujita, M. *J. Am. Ceram. Soc* **2013**, *135*, 6786.
[49] Cernuto, G.; Masciocchi, N.; Cervellino, A.; Colonna, G. M.; Guagliardi, A. *J. Am. Chem. Soc.* **2011**, *133*, 3114.
[50] Sun, Z. C.; Kim, D. H.; Wolkenhauer, M.; Bumbu, G. G.; Knoll, W.; Gutmann, J. S. *ChemPhysChem* **2006**, *7*, 370.
[51] Zwijnenburg, M. A. *Nanoscale* **2012**, *4*, 3711.
[52] Persson, P.; Bergstrom, R.; Lunell, S. *J. Phys. Chem. B* **2000**, *104*, 10348.
[53] Di Valentin, C.; Pacchioni, G.; Selloni, A. *Phys. Rev. B* **2004**, *70*, 85116.
[54] Qu, Z. W.; Kroes, G. J. *J. Phys. Chem. B* **2006**, *110*, 8998.
[55] Li, S.; Dixon, D. A. *J. Phys. Chem. A* **2008**, *112*, 6646.
[56] Calatayud, M.; Maldonado, L.; Minot, C. *J. Phys. Chem. C* **2008**, *112*, 16087.
[57] De Angelis, F.; Fantacci, S.; Selloni, A. *Nanotechnology* **2008**, *19*, 424002.
[58] Valdés, Á.; Kroes, G. J. *J. Phys. Chem. C* **2010**, *114*, 1701.
[59] Shevlin, S. A.; Woodley, S. M. *J. Phys. Chem. C* **2010**, *114*, 17333.
[60] Wang, T. H.; Fang, Z.; Gist, N. W.; Li, S.; Dixon, D. A.; Gole, J. L. *J. Phys. Chem. C* **2011**, *115*, 9344.
[61] Auvinen, S.; Alatalo, M.; Haario, H.; Jalava, J. P.; Lamminmäki, R. J. *J. Phys. Chem. C* **2011**, *115*, 8484.
[62] Syzgantseva, O. A.; Gonzalez-Navarrete, P.; Calatayud, M.; Bromley, S.; Minot, C. *J. Phys. Chem. C* **2011**, *115*, 15890.
[63] Marom, N.; Moussa, J. E.; Ren, X.; Tkatchenko, A.; Chelikowsky, J. R. *Phys. Rev. B* **2011**, *84*, 245115.
[64] Zhang, J.; Hughes, T. F.; Steigerwald, M.; Brus, L.; Friesner, R. A. *J. Am. Chem. Soc.* **2012**, *134*, 12028.
[65] Li, J.; Wang, H.; Persson, P.; Thoss, M. *J. Chem. Phys.* **2012**, *137*, 22A529.
[66] Scanlon, D. O.; Dunnill, C. W.; Buckeridge, J.; Shevlin, S. A.; Logsdail, A. J.; Woodley, S. M.; Catlow, C. R. A.; Powell, M. J.; Palgrave, R. G.; Parkin, I. P.; Watson, G. W.; Keal, T. W.; Sherwood, P.; Walsh, A.; Sokol, A. A. *Nature Materials* **2013**, *12*, 798.
[67] Chen, M.; Dixon, D. A. *J. Chem. Theory Comput.* **2013**, *9*, 3189.
[68] Blagojevic, V.; Chen, Y. R.; Steigerwald, M.; Brus, L.; Friesner, R. A. *J. Phys. Chem. C* **2009**, *113*, 19806.

[69] Taylor, D. J.; Paterson, M. J. *J. Chem. Phys.* **2010**, *133*, 204302.
[70] Chiodo, L.; Salazar, M.; Romero, A. H.; Laricchia, S.; Della Sala, F.; Rubio, A. *J. Phys. Chem.* **2011**, *135*, 244704.
[71] Galynska, M.; Persson, P. *Int. J. Quant. Chem.* **2013**, *113*, 2611.
[72] Mom, R. V.; Cheng, J.; Koper, M. T. M.; Sprik, M. *J. Phys. Chem. C* **2014**, *118*, 4095.
[73] Stevanovic, V.; Lany, S.; Ginley, D. S.; Tumas, W.; Zunger, A. *Phys. Chem. Chem. Phys.* **2014**, *16*, 3706.
[74] De Angelis, F.; Tilocca, A.; Selloni, A. *J. Am. Chem. Soc.* **2004**, *126*, 15024.
[75] Rocca, D.; Gebauer, R.; De Angelis, F.; Nazeeruddin, M. K.; Baroni, S. *Chem. Phys. Lett.* **2009**, *475*, 49.
[76] Pastore, M.; Fantacci, S.; De Angelis, F. *J. Phys. Chem. C* **2010**, *114*.
[77] De Angelis, F.; Fantacci, S.; Selloni, A.; Nazeeruddin, M. K.; Gratzel, M. *J. Phys. Chem. C* **2010**, *114*, 6054.
[78] De Angelis, F.; Fantacci, S.; Gebauer, R. *J. Phys. Chem. Lett.* **2011**, *2*, 813.
[79] De Angelis, F.; Fantacci, S.; Mosconi, E.; Nazeeruddin, M. K.; Grätzel, M. *J. Phys. Chem. C* **2011**, *115*, 8825.
[80] Nunzi, F.; Mosconi, E.; Storchi, L.; Ronca, E.; Selloni, A.; Grätzel, M.; De Angelis, F. *Energy Environ. Sci.* **2013**, *6*, 1221.
[81] Kandada, A. R.; Fantacci, S.; Guarnera, S.; Polli, D.; Lanzani, G.; De Angelis, F.; Petrozza, A. *ACS applied materials & interfaces* **2013**, *5*, 4334.
[82] Nunzi, F.; Storchi, L.; Manca, M.; Giannuzzi, R.; Gigli, G.; De Angelis, F. *ACS Appl. Mater. Inter.* **2014**, *6*, 2468.
[83] Nunzi, F.; Agrawal, S.; Selloni, A.; De Angelis, F. *J. Chem. Theory Comput.* **2015**.
[84] Zhang, J.; Steigerwald, M.; Brus, L.; Friesner, R. A. *Nano Lett.* **2014**, *14*, 1785.
[85] Andersson, K.; Malmqvist, P. A.; Roos, B. O.; Sadlej, A. J.; Wolinski, K. *J. Phys. Chem.* **1990**, *94*, 5483.
[86] Andersson, K.; Malmqvist, P. A.; Roos, B. O. *J. Phys. Chem.* **1992**, *96*, 1218.
[87] Marom, N.; Kim, M.; Chelikowsky, J. R. *Phys. Rev. Lett.* **2012**, *108*, 106801.

Chapter 2

Theoretical Background

Most of the fundamental aspects of computational chemistry will be revisited in this section, building enough knowledge for the discussion of methodological issues in the later chapters of this thesis. Specifically, this chapter starts with an introduction to some elementary concepts from basic molecular quantum chemistry and then moves on discussing the Hartree-Fock approximation, post-Hartree Fock approaches, Density Functional Theory and Time-Dependent Density Functional Theory. In the last sections other methodologies such as solvation models and excited state molecular dynamics (employed in the later chapters of the thesis) are quickly introduced.

2.1 Foundations of quantum chemistry

In this section some of the fundamental concepts of quantum chemistry will be revisited in order to lay the theoretical foundations for the following discussions of post Hartree-Fock approaches and Density Functional Theory.

2.1.1 Schrödinger equation

The ultimate goal for molecular quantum mechanics is the solution of the time-independent Schrödinger equation

$$\hat{H}\Psi = E\Psi \tag{2–1}$$

Ψ stands for the wave function, which contains all the information that can possibly be known about the quantum system studied. For example, in a system of N electrons and M nuclei, the wave function depends on $3N$ spatial coordinates and N spin coordinates of the electrons and on $3M$ spatial coordinates of the nuclei. $\hat{H}$ corresponds to the Hamiltonian operator, which is a differential operator that when acting on the wave function Ψ represents the total energy E of the quantum system. Due to the complexity of the wave function, the Schrödinger equation is in reality unsolvable without making further approximations for systems containing more than one electron [1].

Taking into account the significant difference between the masses of nuclei and electrons (e.g. the ratio of the mass of one proton to one electron is approximately 1,800), the Schrödinger equation can be simplified further. For example, the *Born-Oppenheimer* (BO) approximation, which is central to quantum chemistry, relies on the idea that nuclei move much slower than electrons, and the motion of nuclei and electrons can be uncoupled. The practical consequence of this approximation is that electrons can be considered as moving in a potential defined by fixed nuclei, and since the nuclei are fixed in space their kinetic energy is zero and the potential energy due to nucleus-nucleus repulsion is a constant term [2]. Thanks to the BO approximation the complete Hamiltonian can be reduced to two components accounting for the electronic and the nuclear-nuclear interactions respectively, so that the Schrödinger equation can be rewritten as

$$\left(\hat{H}_{el} + \hat{V}_{nuc}\right)\Psi = E_{el}\Psi \tag{2–2}$$

$$\hat{H}_{el} = -\frac{1}{2}\sum_{i=1}^{N}\nabla_i^2 - \sum_{i=1}^{N}\sum_{A=1}^{M}\frac{Z_A}{r_{iA}} + \sum_{i=1}^{N}\sum_{j>i}^{N}\frac{1}{r_{ij}} = \hat{T} + \hat{V}_{nuc-e} + \hat{V}_{e-e} \qquad (2\text{–}3)$$

In the expansion of the electronic Hamiltonian (equation 2-3), the indices *i* and *j* run over all the *N* electrons, whereas the label *A* denotes each of the *M* nuclei in the system. The terms in equation 2-3 describe the kinetic energy of the electrons (*T*), the electron – nuclear potential energy ($V_{nuc\text{-}e}$) and the repulsive electron-electron potential ($V_{e\text{-}e}$) energy respectively.

2.1.2 The variational principle

Apart from few trivial exceptions, equation 2–2 cannot be solved analytically. Thus, a specific procedure is needed to systematically approach the wave function of the ground state Ψ_0, i.e. the state, which gives the lowest energy solution E_0 for the system studied. This procedure is the *variational principle*, which states that the energy computed as the expectation value of the Hamilton operator from any guessed trial function Φ will be an upper bound to the energy of the ground state E_0

$$\langle \Phi | \hat{H} | \Phi \rangle = E_\Phi \geq E_0 = \langle \Psi_0 | \hat{H} | \Psi_0 \rangle. \qquad (2\text{–}4)$$

For the *variational principle* to be applicable the trial wave function Φ needs to be normalisable, this entails that Φ must be continuous everywhere and be quadratic integrable [2].

The *variational principle* can be re-written in its compact form

$$E_0 = \min_{\Phi \to N} E[\Phi] = \min_{\Phi \to N} \langle \Phi | \hat{T} + \hat{V}_{nuc-e} + \hat{V}_{e-e} | \Phi \rangle. \qquad (2\text{–}5)$$

Equation 2–5 states that for any allowed *N*-electron wave function, the best approximation to the exact wave function can be reached through a minimisation search among all the possible *N*-electron trial functions. In practical calculations the minimisation search is restricted to a specific sub-set of *N*-electron trial functions, where the size of the sub-set is defined by the quality of the basis set.

2.1.3 Basis sets

Different methods can be used to generate a trial wave function as a starting point for the search of the best approximation to the exact wave function of an *N*-electron system. The basis set used to build the trial wave function should be designed in a way that it

allows for an orderly and systematic extension towards completeness (only reached when the set has an infinite number of functions) and that the functions used should have an analytical form allowing for simple manipulation [3]. In practice, finding a set of functions that combine all these requirements has proved to be a difficult task; therefore, in computational chemistry a finite set of one-electron functions (i.e. atom centered atomic orbitals) is often used for the expansion of the trial wave function:

$$\phi_\mu(r) = \sum_i^N C_{i\mu}\varphi_i(r) \qquad (2\text{–}6)$$

$\phi_\mu(r)$ is the trial function for the specific molecular orbital μ, $\varphi(r)$ is the one-electron analytical function of the basis set used for the description of electron i and $C_{i\mu}$ is the coefficient of the single electron function $\varphi_i(r)$ used in the linear combination of atomic orbitals for the molecular orbital μ. The number of one-electron functions employed in the basis set is determined as a trade off between computational cost and accuracy of the results. Other types of basis sets, e.g. plane waves and orbitals mapped on a set of grid points, can be used to build the trial function, however as in this thesis I employed the atom centered approach, from now on I will concentrate on this specific set of functions.

There are two different types of atom centered basis functions: Slater type orbitals (STOs) and Gaussian type orbitals (GTOs). From a strictly physical point of view, Slater-Type-orbitals (STO) seem to be the natural choice for basis functions, as they exhibit the correct cusp behavior as r approaches to zero with a discontinuous derivative and the correct exponential decay in the tail region as r tends to infinite [2]. Nevertheless, both type of functions can be chosen to form a complete basis, but following the considerations above, a larger number of GTOs is required in order to reach a certain accuracy compared to STOs. Despite this, since analytical techniques for the calculation of the many-center integrals expanded with STO basis sets have only been recently implemented in efficient algorithms for *ab initio* calculations, just a few electronic configuration packages employ the STO approach, i.e. ADF.[4] On the other hand, while GTO have a poorer exponential decay compared to STO and no cusp can be observed near the nucleus, GTOs combine reasonably short expansions with a fast and simple integral evaluation, which results in a overall higher computational efficiency.

GTOs are used almost universally as basis functions in molecular calculations and they are centered at the nuclei of the atoms.

GTOs can be expressed in their Cartesian form

$$\chi_{\zeta,l_x,l_y,l_z}(x,y,z)^{GTO} = Nx^{l_x}y^{l_y}z^{l_z}e^{-\zeta r^2}, \quad (2\text{–}7)$$

where *x,y,z* are the Cartesian coordinates, ζ represents the orbital exponent, which determines how compact (large ζ) or diffuse (small ζ) the resulting function is, and the sum $l_x + l_y + l_z$ in the polynomial pre-factor determines the orbital's angular momentum *l* or in other words, the type of orbital (e.g. $l_x + l_y + l_z = 1$ is a p orbital).

Nowadays, most quantum chemistry codes employ the so called contracted GTO basis set, in which several primitive Gaussian functions are mixed in a fixed linear combination to give one contracted Gaussian function (CGF), such as $\chi_\tau^{CGF} = \sum_a^A d_{a\tau}\chi_a^{GTO}$, where the coefficients $d_{a\tau}$ are chosen in a way that the CGF resembles as much as possible a single STO function [2]. The number of primitive functions used for the expansion of the molecular orbital defines the quality of the CGF basis set (or the accuracy of the results obtained).

The simplest expansion utilises only enough functions to contain all the electrons of the neutral atoms and it is called the *minimal* basis set, e.g. the STO-3G basis set, in which three primitive GTO functions are combined into one CGF. For example, the STO-3G for carbon consists of three CGF obtained from nine primitive GTOs, three each describing the 1s, 2s and 2p atomic orbitals [2]. The next level of accuracy is obtained with the *double-ζ (zeta)* basis sets, where the term ζ refers to the exponent of the primitive GTOs (see equation 2–7) and double means that two contracted functions are employed for each atomic orbital. However, considering that the chemical reactivity is better described by the valence electrons, the expansion to a doublet set of CGF can be limited to the valence orbitals, describing the inert core electrons with the *minimal* set. This defines the *split-valence* basis sets.

The next level of sophistication requires the use of polarisation functions, i.e., functions of higher angular momentum than those occupied in the atom, such as p-functions for hydrogen, which ensure that the orbitals can deform from their initial symmetry to better adapt to the molecular environment and describe the charge polarisation effects [2,5]. Polarised double-zeta or split valence basis sets are employed in many chemical

applications, as they are a balanced compromise between accuracy and efficiency. However, whenever electron correlation is considered, such as in correlated wave function approaches, more polarisation functions with higher angular momentum are required to achieve the same level of convergence. In order to further improve the quality of the basis set used, a series of specific functions can be employed to better describe the outer part of the wave function. Those are the diffuse functions, characterised by small exponents, needed to describe loosely bound electrons inside the quantum system (i.e., anions or excited states).

In this thesis, the class of def2- basis sets (e.g. def2-SVP or def2-TZVP), developed by Ahlrichs *et al.* [6], is routinely used. For specific calculations, especially in Chapter 3, where very accurate results are needed for the definition of benchmarks for the excited states of TiO_2 clusters, higher polarised functions are considered (e.g. def2-TZVPP) or the Dunning correlation consistent triple-ζ aug-cc-pVTZ basis set [7] is employed (this latter basis set is geared toward recovering the correlation energy of the outer electrons). For larger TiO_2 particles (see Chapter 6) as the use of triple-ζ basis-sets is computationally intractable, the double-ζ basis-set (DZP for oxygen and hydrogen atoms and DZDP for titanium atoms) is employed.

2.1.4 The Hartree-Fock Approximation

The Hartree-Fock (HF) approximation consists of a procedure to iteratively obtain the lowest energy of a molecular system, in which the *N*-electron wave function is approximated by a single Slater Determinant Φ_{SD} (equation 2–8), the *antisymmetrised* product of N one-electron wave functions. The antisymmetrisation, which arises from the requirement that $|\Psi^2|$ should be invariant to the exchange of spatial and spin coordinates of any two electrons, introduces exchange effects in the trial wave function [1].

$$\Psi_0 \approx \Phi_{SD} = \frac{1}{\sqrt{N!}} \begin{vmatrix} \varphi_1(x_1) & \dots & \varphi_N(x_1) \\ \vdots & \ddots & \vdots \\ \varphi_1(x_N) & \dots & \varphi_N(x_N) \end{vmatrix} \tag{2–8}$$

The one-electron functions $\varphi_i(x_i)$ shown in equation 2-8 are spin-orbitals and they depend on a spatial orbital function $\chi_i(r)$ and one of the two electron spin coordinates $\alpha(\sigma)$ and $\beta(\sigma)$.

Once the initial guess for the trial wave function is defined, the variational principle is

employed to find the Φ_{SD}, which yields the lowest energy possible within the HF approach (E_{HF}). During the minimisation process the spin-orbitals inside the slater determinant are varied under the constraint that they remain orthonormal and the HF equation is iteratively solved until self-consistency is achieved and the "best" spin-orbitals are obtained. The HF equation is an eigenvalue equation of the form

$$f_i(r_1)\varphi_i(r_1) = \varepsilon_i\varphi_i(r_1) \tag{2–9}$$

Where the $f(r_1)$ is the Fock operator, a one-electron effective operator (equation 2–10), $\varphi(r_1)$ are the eigenfunctions and ε its eigenvalues for the specific *i* spin-orbital.

$$f(r_1) = -\frac{1}{2}\nabla^2 - \sum_{A}^{M}\frac{Z_A}{r_{1A}} + v^{HF}(r_1) \tag{2–10}$$

the Fock operator contains terms for the one-electron kinetic energy, the nucleus-electron interaction and the HF potential (v^{HF}). The HF potential corresponds to the average repulsive potential or field experienced by the electron in the $\varphi_i(r_1)$ orbital due to the presence of the remaining *N-1* electrons. Since each step of the variational principle within the HF approach involves the generation of new spin-orbitals and the calculation of a new HF field, the iterative procedure is defined as the self-consistent-field (SCF) method. The SCF cycle is repeated until the energy no longer changes in the next iteration up to a specific threshold and the spin-orbitals used to generate the Fock operator are assumed to be the same as the eigenfunctions [2].

The HF potential for the $\varphi_i(r_1)$ electron has the form

$$v^{HF}(r_1) = \sum_{j}^{N}(J_j(r_1) - K_j(r_1)). \tag{2–11}$$

Where the *J* corresponds to the Coulomb operator (equation 2–12) and *K* is the exchange contribution (equation 2–13) to the HF potential.

$$J_j(r_1) = \int dr_2 |\varphi_j(r_2)|^2 \frac{1}{r_{12}} \tag{2–12}$$

The Coulomb operator represents the repulsive potential perceived by an electron at position r_1 due to the average charge distribution of a second electron in spin orbital $\varphi_j(r_2)$. The exchange operator *K* has no classical interpretation and can only be defined through its effect when operating on a spin-orbital:

$$K_j(r_2)\varphi_i(r_1) = \int dr_2 \varphi_j^*(r_2)\frac{1}{r_{12}}\varphi_i(r_2)\varphi_j(r_1) \qquad (2\text{–}13)$$

The exchange operator leads to the exchange of the variables of two spin-orbitals. Since spin-orbitals are orthonormal functions, the exchange contributions exist only for electrons with the same spin, whereas for electrons with antiparallel spin the whole integral vanishes. Whenever $i = j$, the Coulomb operator from equation 2–12 will describe the interaction of the charge distribution of one electron with itself. This *self-interaction* is clearly unphysical, however, within the HF approach, when $i = j$ the exchange operator (equation 2–13) is identical to the Coulomb operator and since they enter the HF equation $\langle \Phi_{SD} | \hat{H} | \Phi_{SD} \rangle$ with opposite signs, they exactly cancel each other out [2].

2.1.5 Electron correlation

In the HF approach a single Slater determinant is used as an approximation to a many electron system, allowing for the description of a significant portion of the electron-electron interactions observed in the real wave function. While the HF wave function obtained in the limit of a complete basis set (HF limit, reached with an infinite number of basis functions), is able to account for ~ 99% of the total energy, the remaining 1% has proven to be fundamental for the accurate description of chemical properties of molecules [5]. Following the variational principle, E_{HF} is always larger (i.e., less negative) than the exact ground state energy E_0 (in the non-relativistic case), and the difference between those energies $(E_0 - E_{HF})$ is defined as the *correlation energy* E_{HF}^C [2,8]. As E_0 and $E_{HF} < 0$ and $|E_0| > |E_{HF}|$, E_{HF}^C is always a negative quantity.

The correlation energy is generally separated in two different contributions, which correspond to the *dynamic* and *static correlation*. The first type of correlation originates from the instantaneous repulsion of moving electrons in the real wave function, interaction that is not covered by the mean-field HF potential. This means that in the HF scheme, electrons will be spatially closer to each other then in the real many electron system, resulting in larger electron-electron repulsion overall. The dynamic electron correlation is a short-range effect as it is directly dependent on the $1/r_{12}$ term, which controls the electron-electron repulsion in the Hamiltonian (equation 2-3). Within the dynamic correlation the interaction among electrons with opposite spin, which is the

largest contribution, is generally referred to as *Coulomb correlation*, whereas the same spin interaction is labeled as *Fermi correlation* (already included in the HF energy due to the antisymmetry of a Slater determinant) [2].

The second contribution to the E_{HF}^{C} is the static correlation, which depends on the fact that for specific molecular systems the use of a single Slater determinant is not a good approximation to the exact ground state due to a near degeneracy of single Slater solutions (or electronic configurations). In this case the HF wavefunction is qualitatively wrong and multi-reference approaches, where more than a single Slater determinant is considered, need to be employed for the correct description of the system of interest.

2.2 Post HF methods

The post HF methods are the methods developed to improve the HF solution to the Schrödinger equation [5]. For a given basis set the exact solution to the Schrödinger equation for a particular chemical problem should be obtained with the Full Configuration Interaction method (FCI), where all the possible excited electronic configurations are taken into account, completely recovering the missing correlation energy (both static and dynamic). All the post HF methods, which are systematically improved increasing the number of initial basis functions, should tend to the limit defined by the FCI energy. However, as the FCI limit is very computationally expensive to reach, even for the simplest molecules, approximate post HF methods need to be employed for the description of "real" size systems.

Post HF approaches can be divided in two different categories. Depending on the method used the approximate wave function may consist of either a Configuration State Function (CSF) generated by exciting electrons from a single Slater determinant (e.g. using HF orbitals as reference) or multiple Slater determinants where the molecular orbitals used for the construction of the determinants are made optimum through a SCF procedure [5,9]. When the HF orbitals are used for the generation of the wave function, the final dynamically correlated wave function is called single-reference (SR), such is the case of the Configuration Interaction (CI) and Coupled-Cluster (CC) methods. If more than one type of CSF (each one defined by a different set of orbitals) is taken into account, where non integer orbital occupation is allowed (HF allows only 0 and 2), we refer to the approach as a multi-reference (MR) treatment [9]. An example of the latter approach is the Complete Active Space Self Consistent Field method (CAS-SCF). In the CAS-SCF scheme, the generation of the trial wave function relies on a full CI expansion done on a selected active space, where all the electrons and molecular orbitals of chemical relevance are taken into account. The notation used for CAS-SCF is [*n,m*]-CAS-SCF, where for the generation of the Slater determinants *n* is the number of electrons which are distributed in *m* orbitals in all possible ways.

Along with the definition of the SR and MR approaches, we can also define the electronic character of a specific system. A chemical system is considered to have a Single-Configuration (SC) character if the HF reference represents a "good" zero-order approximation for its description, on the other side whenever multiple Slater

determinants (with optimum molecular orbitals) are required for a reasonable zero-order description, the system is considered to have a Multi-Configuration character (MC). SR methods are a good approximation in order to recover the missing portion of the dynamic correlation of a SC system, while the generally more computationally demanding MR approaches are needed for generating a qualitatively correct wave function (recovering the static correlation) of a MC system [9].

Approaches such as the Complete Active Space 2nd order perturbation theory (CASPT2) perform a second order Moller Plesset [3] perturbation correction on the CAS-SCF wavefunction and therefore recover both static and dynamic correlations. CASPT2 is considered one of the gold standards for excited state calculations, however the treatment of excited state properties of transition metal oxides with this method can be challenging when more than one transition metal atom is considered, as not all the d orbitals can be included in the CAS (in the literature the biggest CAS typically include 16 electrons and 16 orbitals) strongly affecting the results. Furthermore in CAS-SCF all states (including the ground state) are calculated variationally, implying that to guarantee orthogonality between states belonging to the same irreducible representation state-averaging has to be employed, where all such states are optimised together, and the results become slightly dependent on the number of states studied [10].

Despite being a single reference approach, Coupled-Cluster theory is considered as the most promising method for treating MC systems by SR methods. Compared to the standard variational methods (e.g. CI) CC methods are less sensitive to the choice of the orbitals [9]. Furthermore, in a recent work by Yang *et al.* [9] it was shown that CCSDT (a Coupled-Cluster approach which includes Single, Double and Triple excitations) and CCSDTQ (which includes Quadruple excitations as well) successfully describe bond breakings in diatomic molecules even if the restricted HF wave function is a poor reference wave function.

For all the reasons above, since this thesis focuses on the description of the excited states of TiO_2 nanoparticles, and the literature on these systems shows paucity of values obtained experimentally or from post-HF approaches, here, different CC approaches are used to generate accurate benchmarks for Density Functional Theory and Time Dependent Density Functional Theory, methods discussed in the next sub-chapters.

2.2.1 CC and EOM-CC methods

The CC wave function is written as

$$\Psi_{CC} = e^{T}\Phi_0 = (1 + T + \frac{1}{2}T^2 + \frac{1}{6}T^3 + \cdots)\Phi_0 = \sum_{k=0}^{\infty}\frac{1}{k!}T^k\Phi_0. \qquad (2\text{–}14)$$

e^T corresponds to the exponential operator acting on the reference wave function Φ_0, which generally is the HF reference (single slater determinant). Equation 2-14 also shows that the exponential operator can be rewritten as an infinite Taylor expansion of the cluster operator T. The idea of the exact CC approach is to include all corrections of a given type to infinite order [5]. In constructing the CC wave function, the excitations included in the cluster operator are not selected individually, but the operator is partitioned into classes comprising all single (one-electron) excitations, all double (two electrons) excitations, all triple (three electrons) excitations and so on. The cluster operator T is given in terms of operators that generate spin-orbital excitations

$$T = T_1 + T_2 + T_3 + \cdots + T_N \qquad (2\text{–}15)$$

$$T_1\Phi_0 = \sum_{i}^{occ}\sum_{a}^{vir} t_i^a\,\Phi_i^a. \qquad (2\text{–}16)$$

In equation 2-15 the cluster operator has been expanded as a linear combination of all the possible excitation operators for an *N*-electron system, where the T_i operator acting on a HF reference wave function generates all the *i*th excited Slater determinants. Equation 2-16 shows that a single excitation operator, acting on the HF reference space, generates all the possible determinants obtained by exciting one electron from all the occupied orbitals i into all the possible virtual orbitals a. The expansion coefficient t_i^a corresponds to the *amplitude* of the single excitation process. Now, the exponential operator e^T can be rewritten as a function of the T_i operators

$$1 + T_1 + \left(T_2 + \tfrac{1}{2}{T_1}^2\right) + \left(T_3 + T_2T_1 + \tfrac{1}{3!}{T_1}^3\right) + \left(T_4 + T_3T_1 + \tfrac{1}{2}{T_2}^2 + \tfrac{1}{2}T_2{T_1}^2 + \tfrac{1}{4!}{T_1}^4\right) + \cdots. \qquad (2\text{–}17)$$

In equation 2-17, the first parenthesis produces all doubly excited states, which can be divided in two excitation terms: the *connected* (T_2) and *disconnected* (${T_1}^2$). The quadruply excited states (third parenthesis) are generated by five distinct mechanisms,

as for example the disconnected $T_2{}^2$ term corresponds to two non interacting pairs of interacting electrons and the connected T_4 term describes the simultaneous interaction of four electrons [3].

In a given basis set, the exact CC wave function satisfies the time independent non-relativistic Schrödinger equation

$$He^T\Phi_0 = Ee^T\Phi_0. \tag{2–18}$$

For the CC wave function, differently from the Configuration Interaction method, the energy of the system is not extracted through a variational minimisation technique, but the projected Schrödinger equation methods is employed. The CC energy (E_{CC}) can be expressed as

$$E_{CC} = \langle\Phi_0|He^T|\Phi_0\rangle. \tag{2–19}$$

Taking into account the fact that the Hamiltonian operator contains only one- and two-electron operators and expanding the exponential operator from equation 2-17 the CC energy can be rewritten as

$$E_{CC} = E_0 + \sum_{i}^{occ}\sum_{a}^{vir} t_i^a \langle\Phi_0|H|\Phi_i^a\rangle + \sum_{i<j}^{occ}\sum_{a<b}^{vir}(t_{ij}^{ab} + t_i^a t_j^b - t_i^b t_j^a)\langle\Phi_0\big|H\big|\Phi_{ij}^{ab}\rangle. \tag{2–20}$$

As in the CC method the HF orbitals are often used as reference, following the Brillouin's theorem the first matrix elements between the HF reference (Φ_0) and singly excited states (Φ_i^a) are zero [5] and the second matrix elements are just two-electron integrals over MOs. Therefore, only single and double amplitudes (t_i^a and t_{ij}^{ab}) will contribute directly to the CC energy. Although, even if the higher order excitations do not have a direct effect on the CC energy, they contribute indirectly, since all the amplitudes of the excitations are obtained through their projection against the specific excited determinant μ (e.g. Φ_i^a, Φ_{ij}^{ab}, Φ_{ijk}^{abc}, …) and decoupled from the energy E as shown in equation 2-21

$$\langle\mu|e^{-T}He^T|\Phi_0\rangle = 0, \tag{2–21}$$

where the $e^{-T}He^T$ corresponds to the operator commonly defined as the *Similarity Transformed Hamiltonian* $\boldsymbol{H^T}$.

Without truncation of the cluster operator T (equation 2-15), the full CC wave function

contains a larger number of terms than the FCI wave functions, as there is one connected cluster amplitude for each excited determinant. In this case the exponential treatment introduced by the CC approach does not yield any advantage compared to the linear parametrisation of the CI method. The superiority of the CC approach over the CI appears only upon truncation, because even at the truncated level the CC wave function contains contributions from all the determinants in the FCI wave function, with weights obtained from the different excitation processes leading to the determinants [3]. In CC theory the similarity transformed Hamiltonian is not Hermitian and this implies that the method cannot be variational (the CC energy cannot always be the upper bound for the FCI value). However the inclusion of excitation terms (higher order disconnected amplitudes) that are not taken into account in truncated CI, makes the CC method size extensive (unlike truncated CI), which is one of the biggest advantages of this approach.
In CC theory, the most common approximation is the truncation of the cluster operator to the connected doubles, yielding the *coupled cluster singles and doubles* (CCSD) model. In CCSD the T_2 operator describes the important electron-pair interactions and T_1 (by disconnected double contributions ${T_1}^2$) defines the orbital relaxation induced by the field set up by the pair interactions [3]. The CCSD wave function contains contributions from all determinants of the FCI wave function, although the contribution of highly excited determinants, generated by disconnected clusters, are in general less accurately described than those that also contain connected contributions [3]. For example, even if the CCSD model does not include T_4 or T_3T_1 contributions to the quadruples, these determinants are still quite accurately described since the T_2^2 contributions represent the dominant term in the quadruple excitations. However, CCSD does not accurately describe the triple excitations, as the triples are not well represented by disconnected clusters.
For many chemical systems the CCSD model is not accurate enough and the need of accounting for the triple contributions led to the development of a new method, labelled CCSD(T), where the triple excitations are evaluated through perturbation theory and added to the CCSD results. Nevertheless, in order to reach chemical accuracy for some systems the triple contributions have to be included iteratively instead of perturbatively and this leads to the CCSDT approach, which is computationally prohibitive and scales with M^8 (where M corresponds with the number of molecular orbitals of the system).

CCSDT performs very well compared to the MR techniques and successfully describes some of the most complicated chemical systems, such as the single bond dissociation of homolytic molecules [9].

The CC approach is a very powerful tool for the description of ground state systems, but when we are interested in excitation processes we need to use its excited state counterpart: the Equation Of Motion Coupled-Cluster theory (EOM-CC).

In the EOM-CC approach the excited state wave function Ψ_n (n represents the specific excited state) is generated, as shown in equation 2-22, through the action of a linear excitation operator $\mathfrak{R}_n$ (equation 2-23) on the reference state, which is the ground state CC wave function Ψ_{CC}.

$$|\Psi_n\rangle = \mathfrak{R}_n|\Psi_{CC}\rangle \tag{2–22}$$

$$\mathfrak{R}_n = \mathfrak{R}_{n0} + \mathfrak{R}_{n1} + \mathfrak{R}_{n2} + \cdots \tag{2–23}$$

$$\mathfrak{R}_{nx} = \frac{1}{x!^2}\sum_{1}^{N} r_{ijk\ldots}^{abc\ldots\ldots}(n) a_a^\dagger a_i a_b^\dagger a_j a_c^\dagger a_k \ldots \tag{2–24}$$

From the previous formulas, it can be clearly seen that the EOM-CC is MR in the space created by the $\mathfrak{R}_n$ operator. For EOM-CC the extraction of the excited state energies E_n and the relative amplitudes is obtained with a similar procedure used for the ground state CC approach. The truncation in the EOM-CC model is introduced through the linear operator $\mathfrak{R}_n$, which in equation 2-23 can be truncated at the desired level of excitation. The most common truncation in EOM-CC is the inclusion of excitations up to the connected doubles, EOM-CCSD, approach that relies on the CCSD ground state wave function. On the other hand, as Chapter 4 and Chapter 5 of this thesis focus on the definition of accurate EOM-CC benchmarks for the calculation of optical properties of TiO_2 nanoparticles to compare with Density Functional methods, the effect of connected triples on the EOM-CC results is also investigated. For selected TiO_2 particles the excitations were investigated with a number of CC models that combine the CCSD approach with an approximate treatment of triples, such as active space EOM-CCSD(t), as well as with the full EOM-CCSDT approach.

Active space EOM-CCSD(t) constitutes a series of approaches recently developed by *Kowalski et al.* [11], which combine the formal simplicity of the single reference CC

theory with a MR concept of the orbital space, where one selects the leading triply excited clusters via a relatively small set of active orbitals that reflects the nature of the electronic quasidegeneracy of excited state of interest [11].

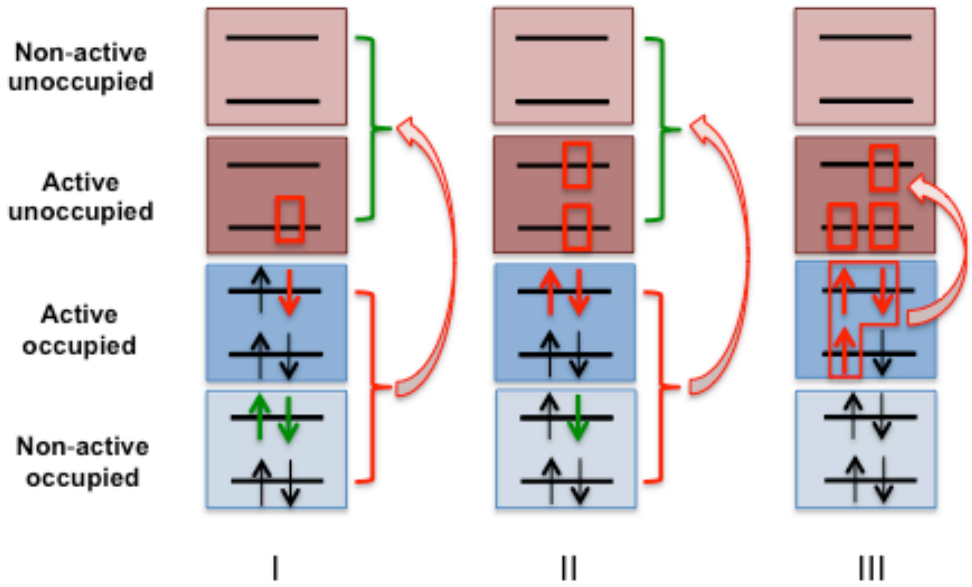

Figure 2.1 Cartoon showing the principle behind the different active space EOM-CCSDt (I/II/III) approaches. The different sections of the orbital space are divided into 4 regions specified on the left (Non-active/Active unoccupied and Active/Non-active occupied). The small arrows represent the electrons (spin-orbitals). The three EOM-CCSDt approaches differ from the number of electrons constrained within the active space for a triple excitation process. Focusing on triple excitation processes only, the red electrons are always excited within the active space (from occupied to unoccupied active orbitals, and their final position is defined by a red box), whereas green electrons can be excited within all the available unoccupied orbitals without any constraints (active and Non-active).

As shown in Figure 2.1, in the EOM-CCSDt(I) model, within the triple excitation at least one occupied spin-orbital index and at least one unoccupied spin-orbital needs to belong to the active space (one red arrow and one red box in Figure 2.1), while in the EOM-CCSDt(II) at least two occupied and two unoccupied spin-orbitals need to belong to the active space. It is easy to understand that the EOM-CCSDt(III) model considers only the triple excitations inside the active space (from occupied to unoccupied spin-orbitals) and the number of determinants generated with this approach will be much smaller than the one produced by the EOM-CCSDt(I) or with the full EOM-CCSDT.

As EOM-CCSDt approaches offer similar results to the very accurate EOM-CCSDT ones, but at a smaller fraction of its computational cost, the performance of these methods was evaluated in this thesis, in order to understand which model allows the

highest accuracy at the lowest cost in the description of excited state properties of transition state metal oxides.

2.3 Density Functional theory

The Density Functional Theory (DFT) relies on the theorems developed in 1964 by Hohenberg and Kohn [12], which show that the ground state electronic energy of a system is completely determined by its electron density, *ρ(r)*. The simplification introduced with the DFT approach is very significant, as for the solution of the time independent Schrödinger equation of a *N*-electron system there is no need to calculate the complicated molecular wave function, which depends on *3N* spatial plus *N* spin variables, but only the molecular electron probability density, *ρ(r)*, that is independent from the number of electrons and defined by just three spatial coordinates [5].

The electron density is a non-negative function, which vanishes at infinity (with an exponential decay) and integrates to the total number of electrons

$$\rho(\mathrm{r} \to \infty) = 0 \tag{2–25}$$

$$\int \rho(r)dr = N. \tag{2–26}$$

Unlike the wave function, *ρ(r)* is a physical observable and can be measured experimentally, e.g. by X-ray diffraction [13]. Another important feature of *ρ(r)* is that at the position of an atom it exhibits a maximum with a finite value due to the attractive force exerted by the positive charge of the nuclei.

Despite the Hohenberg-Kohn theorems supplying a proof of the existence of an exact solution for the Density Functional problem, they do not provide any practical scheme for the calculation of the ground state properties from the electron density. However, in 1965 Kohn and Sham suggested a practical approach, Kohn-Sham (KS) DFT. In the remainder part of this report when talking about DFT I will refer to KS-DFT.

There is a direct analogy between KS-DFT and HF methods, as both define self-consistent equations that must be solved for a set of *independent* electrons in a set of orbitals. The fundamental difference is that in the DFT scheme the effective potential, $v_s(r)$, is defined such that the density, *ρ(r)*, resulting from the summation of the moduli of the squared KS-orbitals, $\varphi_i(r)$, equals the exact ground state density, $\rho_0(r)$, of the real target system of interacting electrons [14]. Using the Kohn-Sham equations the ground state energy of a system can be written as function of the electron density

$$E[\rho(r)] = T_S[\rho] + J[\rho] + E_{nuc-e}[\rho] + E_{XC}[\rho] \quad (2\text{–}27)$$

where $T_S[\rho]$ is the kinetic energy of the non-interacting reference system, $J[\rho]$ is the Hartree or Coulomb energy, $E_{nuc-e}[\rho]$ is the term generated by the attractive interaction between the electrons and the nuclei and $E_{XC}[\rho]$ is the exchange-correlation (XC) energy, which contains everything that is unknown in order to make the above expression exact. In spite of its name, E_{XC} contains not only the classical effect of the electron self-interaction, and the non-classical exchange and correlation, which are contributions to the potential energy of the system, but also a correction to the T_S of the uniform electron gas (used as reference for the real system). In this picture the energy minimisation orbitals, as stated in the KS equations, are

$$\left(-\frac{1}{2}\nabla^2 + v_s(r)\right)\varphi_i(r) = \left(-\frac{1}{2}\nabla^2 + \left[\int \frac{\rho(r')}{|r-r'|}dr' + v_{XC}(r) - \sum_A^M \frac{Z_A}{|r-r_A|}\right]\right)\varphi_i(r) \quad (2\text{–}28)$$
$$= \varepsilon_i\varphi_i(r)$$

where $v_{XC}(r)$ is the XC potential, defined as the functional derivative of $E_{XC}[\rho]$ with respect to $\rho(r)$ *(* $v_{XC}(r) = \delta E_{XC}/\delta\rho(r)$*)*. It is very important to realise that if the exact form of the XC potential were known (which is unfortunately not the case), the closed set of self-consistent equations presented above would yield the exact answer to the electronic structure problem (the correct eigenvalue of the Hamiltonian operator of the Schrödinger equation) [14]. This means that the DFT model is in principle exact and that in every practical DFT calculation the approximation only enters when we have to decide on an explicit form of the unknown functional for the exchange-correlation energy E_{XC} and the corresponding potential v_{XC} [2]. The quality of the density functional approach depends solely on the accuracy of the chosen approximation of E_{XC}, therefore, the central goal of modern DFT, from a theoretical development point of view, is to find better and better approximations to the exchange-correlation contribution.

2.3.1 XC energy functional

The XC energy functional contains all the unknown terms that allow the exact solution of the electronic problem. Little guidance comes from theory on how these functionals should be chosen and over the years many different approximations to the exact XC

energy functional have been proposed. Since the physics underlying the success of current energy functionals is far from being fully understood, we simply do not have any systematic idea on how to arrive at approximations which are closer to the exact functional [2,14]. Unlike wave function based methods (e.g. CC and CAS-SCF), DFT does not allow a systematic improvement of the results solely depending on the choice of the approximate wave function and nowadays the search for better XC energy functionals has a strong 'trial and error' component.

The simplest approximation to the XC energy functional is the local density approximation (LDA), where the density is treated locally as a uniform electron gas. LDA, which was popular in the 70s and 80s, did not produce results of chemical accuracy (bonds in molecules were typically over-estimated by 1eV) and it was soon replaced by the more promising generalised gradient approximation (GGA). With the GGA methods, in order to account for the non-homogeneity of the real electron density (compared to the uniform electron gas), the $\rho(r)$ was not only treated locally, but also supported with information about the gradient of the density, $\nabla\rho(r)$ [2]. While the GGA is generally more accurate than the LDA (getting errors smaller than 5-6 kcal/mol), there is not only one uniquely defined GGA approach and over the years different approximations have been developed (e.g. BLYP, PBE).[15-17]

In the early 90s, Becke suggested replacing a fraction of the GGA exchange with the exact HF-like exchange, and this led to the development of hybrid XC energy functionals, where the exchange correlation term is defined as

$$E_{xc}^{hyb} = E_{xc}^{GGA} + a(E_x - E_x^{GGA}), \tag{2–29}$$

where $E_x(\rho)$ in (2-29) is the exchange energy and is expressed by

$$E_x[\rho] = -\frac{1}{2}\sum_{i,j,\sigma}^{occ} \int dr \int dr' \frac{\varphi_{i\sigma}^*(r)\varphi_{j\sigma}^*(r')\varphi_{i\sigma}(r')\varphi_{j\sigma}(r)}{|r-r'|} \tag{2–30}$$

B3LYP, which belongs to this class of XC energy functionals, is nowadays one of the most popular approximations in use for chemical applications (with an accuracy of 2-3 kcal/mol); it includes 20% of the exact HF-like exchange (HF-like because in DFT the exchange potential is calculated using KS orbitals instead of HF orbitals), and contains a series of parameters determined by fitting to experimental data for atoms and small molecules [14].

In this thesis, in order to probe the effect of the different amounts of HF-like exchange in XC energy functionals on optical properties of TiO_2 particles, DFT calculations employ a variety of XC energy functionals such as PBE, a pure GGA, B3LYP and BHLYP, hybrids and CAM-B3LYP (introduced in subsection 2.4.2 of this Chapter), a Coulomb attenuated XC energy functional.

In the calculation of the total energy of the system**,** the expressions used for the integration of the approximated XC-potentials are fairly complicated mathematical constructs. For these expressions an analytical solution is too computationally demanding and numerical techniques based on a grid to solve these integrals need to be employed [2]. To solve this numerical problem an integration grid that is best suited for the particular situation needs to be used. The behavior of the XC energy functional depends on the features of the electron density, which has cusps at the positions of the nuclei in the molecule. For the calculations in this thesis different numerical integration grids were employed depending on the computational code used. With Turbomole [18] the selected grid consists in a multiple spherical Lebedev grid m3, which proved to be sufficiently accurate for TiO_2 nanoparticles, whereas in the case of Gamess US [19] the Lebedev grid used was defined by 125 radial points in the Euler-MacLaurin quadrature and 302 angular points [20].

2.4 Time Dependent Density Functional Theory

Nowadays DFT is routinely used for the study of ground state properties such as total ground state energies, equilibrium geometries, bond lengths and angles, binding energies, density of states, lattice constants, forces and elastic constants, dipole moments and static polarisabilities. However, if we are interested in the calculation of properties of a quantum chemical system, which is not in its electronic ground state, the time dependent version of DFT needs to be employed. Time dependent density functional theory (TD-DFT) allows to follow the dynamic response of quantum systems that are not at the equilibrium, like for example molecules that have been perturbed by an external field. If during the perturbation the system ends up in one of its electronic excited states, since these are quantum mechanical eigenstates of the Hamiltonian operator, it reaches a stationary state, and TD-DFT can be used to study excited state properties such as energies, geometries, or forces [21]. TD-DFT is closely related to different spectroscopy techniques, which can be distinguished in *linear* and *non-linear* ones. The spectroscopy technique is considered *linear* when the entity of the perturbation is weak enough that the response of the system is proportional to the strength of the perturbation (e.g. UV-Vis spectroscopy). Most applications of TD-DFT nowadays are in this regime, and they are based upon *linear response* theory. Nevertheless, TD-DFT can also be used in the *non-linear* regime, which involves for example atoms and molecules in intense laser fields, where the field is so intense that perturbation theory does not apply. In these applications, the external electric field is comparable or much greater that the static electric field due to the nuclei [22].

All through this thesis *linear response* TD-DFT is employed to investigate optical and photoluminescent properties of TiO_2 nanoparticles and when possible the obtained results are compared to the existing UV-Vis and photoluminescence experimental results.

2.4.1 Formal background of TD-DFT

On formal grounds, TD-DFT is based on the Runge-Gross (RG) theorem established in 1984 [23], which generalises the Hohenberg-Kohn theorem to time dependent external potentials. The RG theorem states that for any fixed initial many-body state there exists a one-to-one correspondence between the evolving densities $\rho(r,t)$ and the time-

dependent potentials $v_{ext}(r,t)$. Also in the case of TD-DFT, a fictitious system of non-interacting electrons moving in a KS potential is defined. Therefore, a system of non-interacting electrons in a Slater determinant of spin-orbital functions with the initial condition $\varphi_i(r,t_0) = \varphi_i^0(r)$ satisfies the following time-dependent Schrödinger equation

$$\left(-\frac{1}{2}\nabla^2 + v_s(\rho)\right)\varphi_i(r,t) = i\frac{\partial}{\partial t}\varphi_i(r,t). \tag{2–31}$$

The electron density of which

$$\rho(r,t) = \sum_{i=1}^{N} |\varphi_i(r,t)|^2, \tag{2–32}$$

exactly that of the interacting system. The XC energy functional is then defined via

$$v_s(r,t) = v_{ext}(r,t) + v_H(r,t) + v_{XC}(r,t), \tag{2–33}$$

where the Hartree potential has the usual form as defined in equation 2-28, but for a time dependent density. The XC energy functional is then a functional of the entire history of the density, the initial interacting wavefunction Ψ_0, and the initial KS reference system Φ_0, $v_{XC}[\rho,\Psi_0,\Phi_0](r,t)$ [22,24]. The TD-DFT potential is a very complex one, much more than for the ground state case, as its knowledge involves the solution of all the time dependent Coulomb-interacting problems [22]. The initial conditions $\varphi_i^0(r)$ assure that only the single-particle orbitals that were initially occupied are time-propagated via the solution of the TD-KS equations, while the evolution of the empty KS orbitals is of no interest for TD-DFT [21].

As the density evolves, the XC energy functional exhibits a *history dependence*, meaning that it is defined not solely by the present density $\rho(r,t)$, but also by its history $\rho(r,t')$ for $0 \leq t' < t$. However, as in the *linear response* regime the perturbing field is weak, the adiabatic approximation is employed, where all the dependence on the past is ignored and only a dependence on the instantaneous density is considered. The adiabatic approximation defines the XC energy functional as local in time (e.g. in the vicinity of the initial state), and it is valid whenever the external time-dependent potential varies very slowly in time. In the linear response regime, the XC energy functional will be continuously modified by small enough perturbations to the density

$$v_{XC}[\rho+\delta\rho](r,t)-v_{XC}[\rho](r,t)=\int dt'\int dr'\,f_{XC}[\rho](r,t,r',t')\delta\rho(r',t'), \qquad (2\text{–}34)$$

where f_{XC} is the XC kernel, which can be rewritten as a functional derivative of the ground state alone:

$$f_{XC}{}^{adia}(r,r',t-t')=\left.\frac{\delta v_{XC}{}^{gs}[\rho_0](r)}{\delta\rho_0(r)}\right|_{\rho_0(r)=\rho(r,t)}\delta(t-t') \qquad (2\text{–}35)$$

The XC kernel plays a central role in the linear response approach, as once this is obtained, the point-wise susceptibility $\chi[\rho_0](r,r',t,t')$, which corresponds to the response of the ground state to a small change in the external potential, can be defined in the frequency domain (after a Fourier transform has been applied) as

$$\chi(r,r',\omega)=\chi_s(r,r',\omega)+f_{HXC}(r_i,r_j,\omega). \qquad (2\text{–}36)$$

When ω matches a true transition of the system, the point-wise susceptibility χ blows up (i.e. it shows a pole as a function of ω) [22]. Analysis of the *linear response* shows that it is generally dominated by the response of the ground state $\chi_s(r,r',\omega)$ KS system and then corrected by TD-DFT via matrix elements of the XC kernel. In the absence of Hartree-exchange-correlation effects $f_{HXC}(r_i,r_j,\omega)$, the allowed transitions are precisely the ones obtained from the KS XC energy functional ($\chi=\chi_s$), however, the presence of the kernel shifts the transition frequencies (energies) away from the KS values to the true values. Intensities of the optical transitions (oscillator strengths) can be extracted in the same calculations, so they are also influenced by the kernel [22].

One of the most popular methods for the extraction of excitation energies in the frequency dependent *linear response* TD-DFT is due to Casida, who showed that finding the poles of χ is equivalent to solving the eigenvalue problem, whose eigenvalues and eigenvector are used to build the absorption spectra [25]

$$\begin{pmatrix}A & B\\ B & A\end{pmatrix}\begin{pmatrix}X\\ Y\end{pmatrix}=\Omega\begin{pmatrix}-1 & 0\\ 0 & 1\end{pmatrix}\begin{pmatrix}X\\ Y\end{pmatrix}, \qquad (2\text{–}37)$$

where *A* and *B* are called the orbital rotation Hessians [26]. The construction of these matrix elements requires the prior diagonalisation of the full ground state DFT problem for the determination of all the (or at least many of them) empty KS states. The Casida equation is then solved through an iterative procedure. Within this approach each

eigenvalue can be solved independently and the final excitation energy of each state is not affected by the number of eigenvalues considered, however only a limited number of the low-lying eigenvalues can be obtained [27]. The eigenvalues Ω_n of equation 2-37 provide the excitation energies of the system, while the eigenvectors (X, Y) yield the spectroscopic oscillator strength and they can be used to assign the symmetry of each transition [27]. This approach is implemented in many computational codes, such as Turbomole [18] and GAMESS US [19], codes employed for most of the calculations shown in this thesis.

Hirata and Head-Gordon [28] proposed a simple approximation to TD-DFT, the Tamm-Dancoff approximation (TDA), obtained by setting $B = 0$ in equation 2-37. TDA corresponds to allowing only excitations between occupied-virtual orbital pairs (represented by the eigenvector X), while neglecting all the virtual-orbital de-excitation transitions (given by the vector Y). This approach has proven extremely successful in recovering the correct singlet state ordering and improving the description of triplet states of problematic systems, which are known to be significantly challenging for TD-DFT [29,30]. The TD-DFT/TDA approach is employed for the non adiabatic excited state dynamic simulations from Chapter 7 of this thesis, as TDA provides better potential energy surfaces especially in regions of strong coupling between the ground state S0 and the lowest excited state S1 [31].

2.4.2 Calculation of forces in TD-DFT

For TD-DFT, different analytical excitation energy gradient approaches have been suggested [32-34]. In this thesis the derivation proposed by Furche and Ahlrichs [34] as implemented in Turbomole [18] and GAMESS US [19] is employed. This approach avoids solving the coupled-perturbed Kohn-Sham equation (CPKS) for each nuclear degree of freedom, by solving the Z-vector equation instead [35]. The methodology developed by Furche and Ahlrichs is based on an efficient atomic orbital basis approach like ground state energy gradient formulas [35]. Within their scheme, once the ground state KS orbitals have been obtained, in a first step the excitation energy Ω and excitation vector $|X, Y\rangle$ (from equation 2-37) are determined, in a second step the Z vector equation is solved and finally in a third step the excited state gradient is evaluated [34]. For the lowest excited states the total computational efforts for steps 1 and 2 are practically comparable to solving the ground state KS equations, whereas for

higher excited states the cost becomes increasingly expensive, since all the lower states have to be calculated as well [34]. The cost of step 3 is virtually identical to that for the analytic computation of ground state gradients. The only terms that are not straightforward to transfer from the ground state to linear response regime are the ones containing third-order functional derivatives and geometric derivatives of the XC energy functional and kernel [34]. However, Furche and Ahlrichs provide a method to reduce them to the same form of XC energy functional and energy, both routinely computed in ground state energy and gradient calculations [34].

2.4.3 Limitations of the TD-DFT approach and possible solutions

Generally the use of TD-DFT yields accurate excited state properties, such as excited state minimum energy bond lengths, vibrational frequencies, forces and dipole moments, and it is well established that conventional GGA and hybrid XC energy functionals are accurate to within a few tenth of an electronvolt (eV) in the description of local excitations [36,37]. However, it is known that standard XC energy functionals are unable to describe the correct physics involved in non local excited state processes, such as charge transfer and Rydberg excitations, which are generally largely underestimated (in the order of few eV) [14]. In CT processes, charge physically moves from one region in the particle or maybe system to a second one, which is spatially separated from the first. These processes can occur in a wide range of chemical systems, such as complexes of two or more molecules, or between different moieties within the same molecule [21]. Therefore, all of the excited state processes that involve two different regions of a system, a donor and an acceptor, can be considered as CT excitations. However, due to the qualitative nature of this problem, is not easy to judge what is the CT character of a certain exciton and to predict how poorly (or accurate) a TD-DFT XC energy functional will perform in the calculation of its excitation energies. For this reason Peach *et al.* [38] suggested a very useful approach, the lambda (Λ) diagnostic test, which allows one to qualitatively estimate the likely degree of error for a TD-DFT calculation of a certain excitation, due to its CT character. The Λ value quantifies the extent of CT character for a specific excitation, evaluating the spatial overlap between the (unperturbed) occupied (orbital i) and virtual (orbital a) orbitals involved in the excitation:

$$\Lambda = \frac{\sum_{i,a} k_{ia}^2 \langle|\varphi_i|\varphi_a|\rangle}{\sum_{i,a} k_{ia}^2} \quad (2\text{–}38)$$

The Λ diagnostic is a dimensionless number and it takes a value between 0 and 1. In equation 2-38 the $\langle|\varphi_i|\varphi_a|\rangle$ is the measure for the spatial overlap between an occupied (φ_i) and a virtual orbital (φ_a), while k_{ia} is the contribution of an occupied-virtual pair (*i*-*a*) to the specific TD-DFT excitation, which can be obtained as $X_{ia} + Y_{ia}$ calculated from Casida's equation (2-37) [38]. A small value of Λ signifies an excitation with a strong CT character, while a large value signifies a short-range or local excitation [38].

The reason for the failure of standard hybrid XC energy functionals in the description of CT excitations is well understood. At long inter-electron separation ($r \longrightarrow \infty$) standard hybrid exchange energy functionals i.e. B3LYP behave as $-0.2r^{-1}$, instead of the exact value of $-r^{-1}$ [39]; where standard hybrid exchange functionals already are an improvement over LDA or pure GGA energy functionals, where there is no r^{-1} dependence in the exchange potential. To overcome the deficiency of standard hybrid exchange potentials Tawada *et al.* [40] developed a long-range corrected exchange energy functional, by employing an Ewald split of the r^{-1} term into:

$$\frac{1}{r} = \frac{1 - erf(\mu r)}{r} + \frac{erf(\mu r)}{r} \quad (2\text{–}39)$$

where the first and second term account for the short-range and long-range behavior respectively. The parameter μ determines the balance between DFT and HF exchange at intermediate r. When $\mu = 0$ the long-range DFT calculation corresponds to the pure DFT approach, while if $\mu = \infty$ it corresponds to the standard HF approach. Following this idea, Yanai *et al.* [39] suggested a new hybrid XC energy functional with improved long-range properties, the Coulomb Attenuated Method (CAM-)B3LYP [39,40], for the accurate description of electronic excitations with a strong CT character. CAM-B3LYP [39,40], which combines the hybrid qualities of B3LYP and the long-range correction presented by Tawada and coworkers, accurately describes excitations to Rydberg states and CT excitations [36], while predicting energetic quantities to the accuracy of B3LYP [39]. CAM-B3LYP comprises of 0.19 HF-like plus 0.81 Becke 1988 (B88) GGA exchange at short-range, and 0.65 HF-like plus 0.35 B88 at long-range, while the intermediate region is smoothly described through the erf with parameter 0.33 r^{-1}[40].

2.5 Einstein equation

As discussed in Chapter 1, when a system in its ground state is perturbed from its equilibrium through the absorption of a photon, once it is on the excited state surface it will relax towards a new excited state minimum and then transition back to the ground state. The kinetics of this processes depend on the probability of spontaneous de-excitation transitions, which could be *radiative* and *non-radiative* in character. Excited state dynamic simulations such as Fewest Switches Surface Hopping, introduced in section 2.7 of this chapter, provide a methodology to predict the probability of *non radiative* or *dark transitions* between two potential energy surfaces (e.g. S1 and S0). However, this methodology cannot provide insights on the probability of de-excitation processes that involve the emission of photons (*bright transitions*). In this thesis, the *Einstein coefficient* A_{21} is employed to predict the probability of spontaneous *radiative* de-excitation processes between state S1 and S0 [41]:

$$A_{21} = \frac{2\pi\omega^2 e^2}{\varepsilon_0 m_e c^3} f_{21} \tag{2–40}$$

Where ω corresponds to the excitation energy of the S0 – S1 transition, f_{21} to its oscillator strength. c the speed of light, e, m_e the charge and mass of the electron respectively and ε_0 the dielectric permittivity of vacuum. The *Einstein coefficient* A_{21} has units 1/s and τ_{21}, the spontaneous de-excitation lifetime is simply calculated as:

$$\tau_{21} = \frac{1}{A_{21}} \tag{2–41}$$

2.6 Solvation methods

The presence of solvent molecules can have strong effects on the electrostatic and geometric properties of nanoparticles. Especially in the case of photochemical reactions, where electron transfer processes take place between the solvated particle and solvent molecules, the inclusion of solvent models becomes pivotal for the correct description of the investigated phenomena.

In order to properly take into account the solvent effects on the properties of the systems of study, different approaches can be employed. The most straightforward method is to run a Molecular Dynamic (MD) simulation on the system of interest treated with an explicit solvent model, where discrete solvent molecules are directly added to the simulation environment. Using MD would allow capturing the temperature dependent dynamic effects and statistical distribution over time of the solvent molecules around the large nanoparticle. However, in order to study excited state processes using this computational approach (discussed in the next section), very long MD runs would be required, making the calculation unfeasible even with the largest supercomputers currently available. Therefore, as a first approximation, when studying excited state processes on large nanoparticles in a solvent, only static effects are considered, neglecting the dynamic contribution from the solvent molecules. Furthermore, it has to be considered that, in order to cover short and long-range solvent effects, a realistic model of a solution should contain hundreds of solvent molecules surrounding the solute, making again the cost of the simulation prohibitively high. To decrease the computational costs of this approach, only the first solvation sphere is often explicitly considered, allowing the fundamental description of short-range solvent effects (e.g. hydrogen bonding for polar solvents). This approximation, however, ignores the long-range effects played by the solvent, such as screening of charges due to solvent polarisation, which could have a large influence on the total energy of the system. Alternatively implicit solvation models can be employed. In these approaches the solvent is approximated as a continuous medium with a dielectric constant instead of individual discrete molecules.

The two most frequently used implicit solvation models, which successfully recover long-range solvation effects with a similar approach, are the *Conductor-like Polarisable Continuum Model* (C-PCM) [42] and the *COnductor-like Screening MOdel* (COSMO) [43].

Both of these approaches employ a cavity defined through interlocking van der Waals surface spheres centred at atomic positions of the solute and the solute molecule forms a cavity within a continuum with a permittivity ε that represents the solvent [5,18]. The generation of screening charges on the cavity surface defines the response of the scaled-conductor medium, which is polarised by the charge distribution in the solute. A C-PCM or COSMO calculation begins with the construction of the cavity surface grid. During each SCF cycle the solute screening charges are calculated and the potential generated by these charges is included in the Hamiltonian. This approach guarantees a variational optimisation of both the molecular orbitals and the screening charges, allowing for the calculation of analytic gradients.

The deviation between both C-PCM and COSMO approximations and the exact solution is rather small and for example in the case of polar solvents it is smaller then 1%. In this thesis both implicit solvation models were employed and they show very similar results. For the simulation of solvent effects on redox properties of large TiO_2 nanoparticles in presence of water (Chapter 6) a hybrid approach was employed. For those systems the first solvation sphere of water molecules was explicitly considered, covering the short-range hydrogen interactions, whereas the inclusion of an implicit model allowed the simulation of the long-range dielectric effect exerted by the bulk.

2.7 Excited state molecular dynamics

In order to investigate both equilibrium thermodynamic and dynamical properties, molecular dynamic approaches (MD), which take into account the effect of time and temperature on the system studied, need to be employed. In MD methods the classical Newtonian equations of motion for a system are solved numerically starting from a pre-specified initial state, providing insights into the microscopic motion of individual atoms [44]. The main virtue of MD is that, thanks to the simple solution of the classical mechanical equations of motion, the method can be employed with systems containing a large number of degrees of freedom. However, since atoms obey the quantum mechanical equations of motion, only considering the solution to the classical equations of motion defines the fundamental limitation of MD approaches. Quantum mechanical effects such as zero-point motion, quantum interferences, and tunneling, which have been shown to be of pivotal importance for the correct prediction of chemical rate processes, are ignored in classical mechanics approaches [45]. Unfortunately, most of the systems of interest considered by chemists nowadays remain too complex to be treated with a fully quantum mechanical MD approach. In order to address the dynamic evolution of such systems, mixed quantum-classical models, with only a subset of nuclear degrees of freedom are needed [46].

Ab initio MD (AIMD) methods are a class of mixed quantum-classical dynamic approaches, where, relying on the BO approximation (see Chapter 2.1.1), nuclear and electronic degrees of freedom are adiabatically separated. In fact, within the AIMD scheme finite temperature Newtonian classical dynamics are combined with nuclear forces obtained from electronic structure calculations (DFT) performed "on the fly" as the simulation proceeds [44]. Since in AIMD the electronic structure of the system is treated explicitly, these approaches are often employed for the study of a wide variety of chemically relevant problems such as the reactivity of molecules in their ground state.

As the focus of this thesis is the investigation of optical and photocatalytic properties of TiO_2 nanoparticles, the MD scheme employed for the study of those systems should also be able to treat adiabatically excited states.

While the BO approximation is generally accurate enough for the study of systems in their electronic ground state, it breaks down whenever two or more PESs are strongly interacting. This means that in order to accurately simulate excited state processes such

as photochemical reactions, radiationless decay and energy and charge transfer, which involve at least two or more strongly coupled BO PESs, non-adiabatic effects need to be taken into account. Currently, the most promising mixed quantum-classical methodology for the description of fast non-adiabatic processes is non-adiabatic molecular dynamics (NAMD) [47]. Unlike nuclear wave-packet propagation methodologies, such as multiconfiguration time dependent Hartree (MCTDH), NAMD does not require previous knowledge of the photochemical/-physical mechanism being investigated and it directly yields observables of experimental relevance, such as quantum yields and fluorescence intensities. [47,48]

Recent advances in the field of computational chemistry led to the development of efficient implementations of NAMD approaches allowing the study of systems that just a few years ago were considered prohibitively expensive. In mixed quantum-classical NAMD there exists two different approaches for computing forces on the nuclei: Ehrenfest dynamics and Tully's Fewest Switches Surface Hopping (FSSH). Ehrenfest dynamics corresponds to the first historically and most straightforward approach, where the nuclei motions evolve classically on a mean-field potential. This mean-field approach, leads to average forces from two or more PESs in regions of weak coupling, and it is not able to describe non-adiabatic transitions between different PESs, behaviour that is undesirable for the simulation of photochemical reactions [47,49]. The second approach, Tully's FSSH, which will be discussed in more detail in the next section, is an efficient classical trajectory algorithm that incorporates the branching of the wave function observed in a fully quantum description, whenever our system enters regions of strong coupling between different PESs.

In this thesis (Chapter 7) a recent implementation of linear TD-DFT NAMD, developed by Tapavicza *et al.* [31,47,50,51], is employed for the study of photochemical reactions of TiO_2 particles in contact with water. The approach developed by *Tapavicza et al.* relies on the previously introduced FSSH scheme. In FSSH NAMD approach, as implemented in Turbomole, excited state energies and non-adiabatic couplings (among two or more PES) are available at low cost and good accuracy from TD-DFT (e.g. thanks to the use of Gaussian basis sets in Turbomole, hybrid XC energy functionals can be readily employed).

Furche and coworkers successfully employed the FSSH/TD-DFT scheme discussed

above for the study of photochemical reactions of cyclohexadiene, vitamin D derivatives, and a cyclobutene derivative, 7,8-dimethylbicyclo[4.2.0]oct-1(6)ene [47,51].

2.7.1 Fewest switches Surface Hopping

In a fully quantum description of physical processes involving non-adiabatic transitions the total wave function splits into branches whenever regions of strong coupling are encountered. Those separated branches initially overlap and interfere, but eventually separate in space and reduce the possibility of further interference, leading to two distinct quantum states [46].

The FSSH scheme, developed by John Tully 1990 [49], consists of an attempt to realistically describe the behaviour of a quantum system whenever a region of strong coupling is encountered. In FSSH each trajectory evolves on a single PES and it is interrupted only, in regions of strong coupling, by sudden switches to another BO state (Figure 2.2).

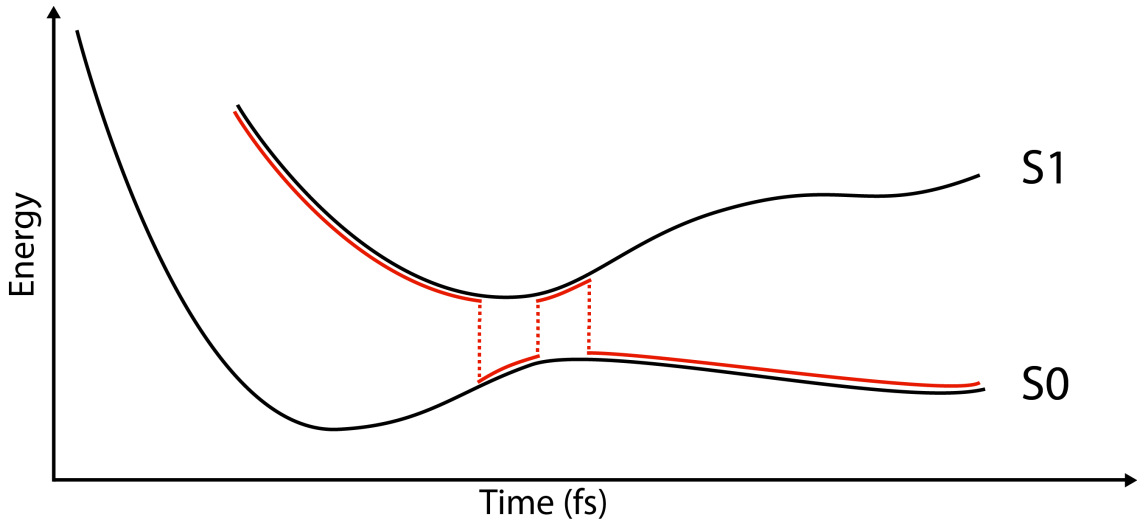

Figure 2.2 Adiabatic molecular dynamics with Fewest Switches Surface Hopping. Solid black lines represent BO PESs (S0 and S1 states), whereas the red line corresponds to the trajectory of the specific MD run. Dashed lines represent the switches between the S1 and S0 states during a FSSH run.

The probability of the switch from one state to the other is calculated at each time step along the trajectory and it depends on the time derivatives of the wave function expansion coefficients (instantaneous change in the state population). Therefore, the instantaneous transition between two states is directly proportional to the strength of their non-adiabatic coupling. Weaker couplings mean slower changes in the wave

function coefficients, thus smaller hopping probability [52]. The transition probability of a switch between state *0* and *1* ($g_{0,1}$) is then compared to a random number, $\zeta \in [0,1]$, and a hop from state *0* to *1* occurs only if:

$$g_{0,1} > \zeta \tag{2–42}$$

If a hop between surfaces is accepted, the momenta of the nuclei are scaled in order to conserve the total energy and the scaling is chosen along the non-adiabatic coupling vector [47]. Between switches, the individual trajectories evolve on single BO states, following Newton's equation of motion.

2.8 Global minimum optimisation

As experimental knowledge on the structure of small inorganic nanoparticles is incomplete, computational approaches need to use specific algorithms in order to build reliable models for the study of the properties of those materials. Numerous computational studies show that as the size of the inorganic nanoparticles increases (> nm), it is reasonable to assume that the structure of the particle will mostly resemble the structure of the most stable polymorph phase for the bulk material. However, it is quite possible for nanoparticles consisting of tens to hundreds formula units (< 1 nm) to have structures other than those deriving from the bulk material.

In order to obtain the best structures for those nanoparticles, through a computational approach, a global minimum search must be employed. These approaches allow the user to efficiently probe the potential energy surface (PES) of each individual nanoparticle structure and to locate the best candidate. In the studies of nanoparticles the PES represents the potential energy of a given system as a function of all the relevant atomic or molecular coordinates. Any displacement over the PES corresponds to changes in atomic coordinates and a minimum is a point from which a small displacement in any direction increases the potential energy [53]. As shown in Figure 2.3, the potential energy surface of even an apparently simple system may support a very large number of local minima, where the most stable minimum (lowest in energy) is known as the global minimum (GM). Locating the global minimum on a PES is a very complex task, as the size of the particle increases, the search space and the difficulty of finding the target configuration increase rapidly and so does the uncertainty of whether the most stable structure found is the GM [53].

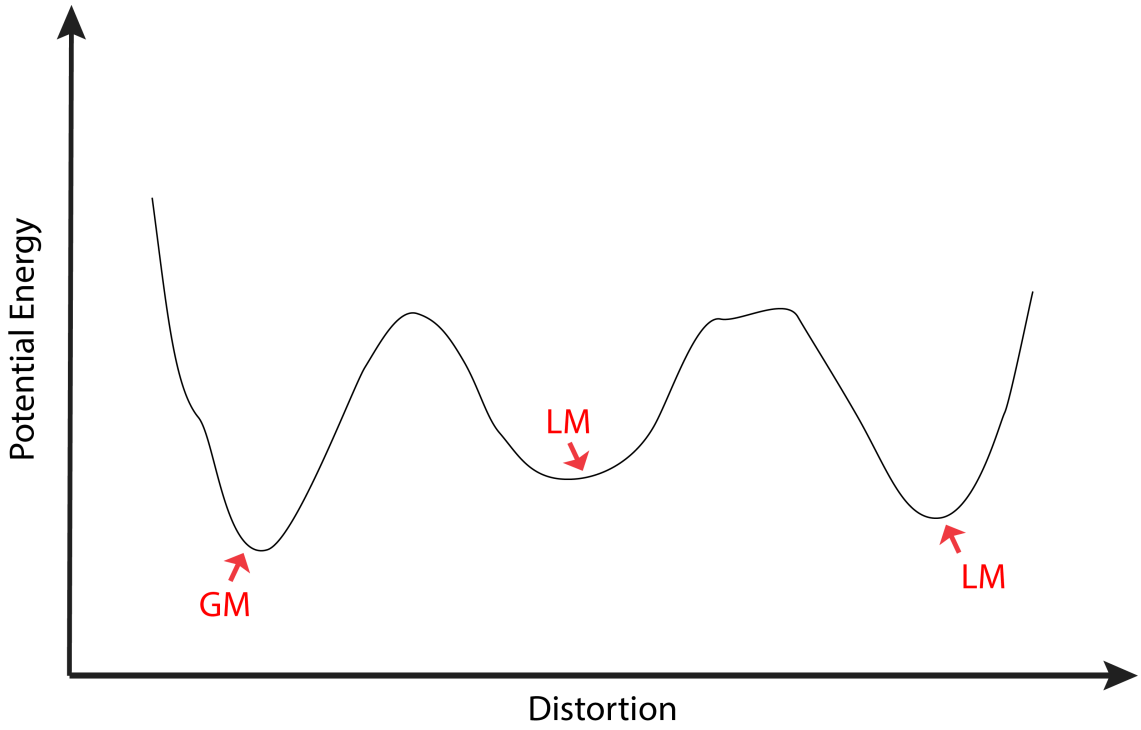

Figure 2.3 Schematic representation of a one-dimensional PES and its relevant points GM (Global minimum) and LM (Local Minimum).

The search of GM structures for TiO_2 nanoparticles is not the focus of this thesis, however most of the structures used in Chapters 3, 4 and 5 correspond to tentative GM particles obtained from previous works. Nowadays a combination of methods such as simulated annealing, Monte Carlo Basin Hopping or genetic algorithms are used to explore the energy landscape and tackle the GM problem. Generally in all these algorithms, during the search for the GM the energy of formation per cluster is defined using interatomic potentials [54], after which accurate *ab initio* (DFT) calculations for the more plausible configurations found are employed.

2.9 References

[1] Szabo, A.; Ostlund, N. S. *Modern quantum chemistry, introduction to advanced electronic structure theory*; McGraw-Hill, Inc.: New York, 1989; Vol. 1982.

[2] Wolfram Koch; Holthausen, M. C. *A chemist's guide to density functional theory*; Second Edition ed.; Wiley-VCH Verlag GmbH: Weinheim, New York, Chichester, Brisbane, Singapore, Toronto, 2001.

[3] Helgaker, T.; Jorgensen, P.; Olsen, J. *Molecular electronic-structure theory*; Wiley, 2000.

[4] te Velde, G.; Bickelhaupt, F. M.; Baerends, E. J.; Guerra, C. F.; Van Gisbergen, S. J. A.; Snijders, J. G.; Ziegler, T. *J. Comput. Chem.* **2001**, *22*, 931.

[5] Jensen, F. *Introduction to computational chemistry* New York, 2001.

[6] Weigend, F.; Ahlrichs, R. *Phys. Chem. Chem. Phys.* **2005**, *7*, 3297.

[7] Balabanov, N. B.; Peterson, K. A. *J. Chem. Phys.* **2005**, *123*.

[8] Lowdin, P. O. *Adv. Chem. Phys.* **1959**, *2*, 207.

[9] Yang, K. R.; Jalan, A.; Green, W. H.; Truhlar, D. G. *J. Chem. Theory Comput.* **2012**, *9*, 418.

[10] Berardo, E.; Hu, H.; Kowalski, K.; Zwijnenburg, A. M. *J. Chem. Phys.* **2013**, *139*.

[11] Kowalski, K.; Hirata, S.; Wloch, M.; Piecuch, P.; Windus, T. L. *J. Chem. Phys.* **2005**, *123*.

[12] Hohenberg, P.; Kohn, W. *Phys. Rev. B* **1964**, *136*, B864.

[13] Koch, H.; Jorgensen, P. *J. Chem. Phys.* **1990**, *93*, 3333.

[14] Burke, K. *J. Chem. Phys.* **2012**, *136*.

[15] Becke, A. D. *Phys. Rev. A* **1988**, *38*, 3098.

[16] Lee, C. T.; Yang, W. T.; Parr, R. G. *Phys. Rev. B* **1988**, *37*, 785.

[17] Perdew, J. P.; Burke, K.; Ernzerhof, M. *Phys. Rev. Lett.* **1996**, *77*, 3865.

[18] Furche, F.; Ahlrichs, R.; Haettig, C.; Klopper, W.; Sierka, M.; Weigend, F. *WIREs Comput. Mol. Sci.* **2014**, *4*, 91.

[19] Schmidt, M. W.; Baldridge, K. K.; Boatz, J. A.; Elbert, S. T.; Gordon, M. S.; Jensen, J. H.; Koseki, S.; Matsunaga, N.; Nguyen, K. A.; Su, S. J.; Windus, T. L.; Dupuis, M.; Montgomery, J. A. *J. Comput. Chem.* **1993**, *14*, 1347.

[20] Ahlrichs, R.; Bar, M.; Haser, M.; Horn, H.; Kolmel, C. *Chem. Phys. Lett.* **1989**, *162*, 165.

[21] Ullrich, C. *Time-dependent density-functional theory: Concepts and applications* Oxford, 2012.

[22] Burke, K.; Department of Chemistry, U. o. C. I., Ed. 2007.

[23] Runge, E.; Gross, E. K. U. *Phys. Rev. Lett.* **1984**, *52*, 997.

[24] Burke, K.; Wagner, L. O. *Int. J. Quantum Chem.* **2013**, *113*, 96.

[25] Marches, M. A. L.; Ullrich, C.; Nogueira, F.; Rubio, A.; Burke, K.; Gross, E. K. U. *Time-dependent density functional theory*; Springer, 2006.

[26] Furche, F.; Ahlrichs, R. *J. Chem. Phys.* **2004**, *121*, 12772.

[27] Rocca, D., SISSA, 2007.

[28] Hirata, S.; Head-Gordon, M. *Chem. Phys. Lett.* **1999**, *314*, 291.

[29] Peach, M. J. G.; Williamson, M. J.; Tozer, D. J. *J. Chem. Theory Comput.* **2011**, *7*, 3578.

[30] Peach, M. J. G.; Warner, N.; Tozer, D. J. *Mol. Phys.* **2013**, *111*, 1271.

[31] Tapavicza, E.; Tavernelli, I.; Rothlisberger, U. *Phys. Rev. Lett.* **2007**, *98*.

[32] Van Caillie, C.; Amos, R. D. *Chem. Phys. Lett.* **1999**, *308*, 249.
[33] Van Caillie, C.; Amos, R. D. *Chem. Phys. Lett.* **2000**, *328*, 446.
[34] Furche, F.; Ahlrichs, R. *J. Chem. Phys.* **2002**, *117*, 7433.
[35] Chiba, M.; Tsuneda, T.; Hirao, K. *J. Chem. Phys.* **2006**, *124*, 144106.
[36] Peach, M. J. G.; Benfield, P.; Helgaker, T.; Tozer, D. J. *J. Chem. Phys.* **2008**, *128*, 44118.
[37] Elliott, P.; Furche, F.; Burke, K. *Excited states from time-dependent density functional theory* Reviews in computational chemistry, 2009.
[38] Peach, M. J. G.; Benfield, P.; Helgaker, T.; Tozer, D. J. *J. Chem. Phys.* **2008**, *128*.
[39] Yanai, T.; Tew, D. P.; Handy, N. C. *Chem. Phys. Lett.* **2004**, *393*, 51.
[40] Tawada, Y.; Tsuneda, T.; Yanagisawa, S.; Yanai, T.; Hirao, K. *J. Chem. Phys.* **2004**, *120*, 8425.
[41] Hilborn, R. C. *Am. J. Phys.* **1982**, *50*, 982.
[42] Mennucci, B.; Tomasi, J. *Journal of Chemical Physics* **1997**, *106*, 5151.
[43] Klamt, A.; Schuurmann, G. *J. Chem. Soc., Perkin Trans. 2* **1993**, 799.
[44] Tuckerman, M. E. *J. Phys.: Condens. Matter* **2002**, *14*, 1297.
[45] Hammes-Schiffer, S.; Tully, J. C. *J. Chem. Phys.* **1994**, *101*, 4657.
[46] Prezhdo, O. V.; Rossky, P. J. *J. Chem. Phys.* **1997**, *107*, 825.
[47] Tapavicza, E.; Bellchambers, G. D.; Vincent, J. C.; Furche, F. *Phys. Chem. Chem. Phys.* **2013**, *15*, 18336.
[48] Curchod, B. F. E.; Rothlisberger, U.; Tavernelli, I. *Chimia* **2012**, *66*, 174.
[49] Tully, J. C. *J. Chem. Phys.* **1990**, *93*, 1061.
[50] Tapavicza, E.; Tavernelli, I.; Rothlisberger, U.; Filippi, C.; Casida, M. E. *J. Chem. Phys.* **2008**, *129*.
[51] Tapavicza, E.; Meyer, A. M.; Furche, F. *Phys. Chem. Chem. Phys.* **2011**, *13*, 20986.
[52] Duncan, W. R.; Stier, W. M.; Prezhdo, O. V. *J. Am. Chem. Soc.* **2004**, *127*.
[53] Wales, D. J. *Energy landscapes with applications to clusters, biomolecules and glasses*; Cambridge: Cambridge, 2003.
[54] M. Matsui; Akaogi, M. *Mol. Simulation* **1991**, *6*, 239.

Chapter 3

Equation of Motion Coupled Cluster calculations on TiO_2 nanoclusters

In this chapter, different flavours of Equation of Motion Coupled Cluster theory are employed to define accurate benchmarks for the calculation of vertical excitation energies of small TiO_2 clusters. Specifically, in this section, the effects of the inclusion of triple excitations in the Coupled Cluster expansion are investigated for the calculation of the energies of the four lowest excited states of the TiO_2 monomer, Ti_2O_4 dimer and Ti_3O_6 trimer global minimum geometries.

The content of this chapter has been taken from the following published work:
Berardo, E.; Hu, H. S.; Kowalski, K.; Zwijnenburg, M. A. Coupled cluster calculations on TiO_2 nanoclusters. *J. Chem. Phys.* **2013**, *139*, 64313.

Regarding the results included in the following chapter, I have conducted all the EOM-CCSD calculations on Hector HPC and on local UCL computational resources. Dr. Karol Kowalski and Dr. Han-Shi Hu have performed the most computationally expensive EOM-CCSDT calculations (for the dimer and trimer) on local facilities at the Pacific Northwest National Laboratory.

3.1 Introduction

Understanding the excited state properties of Titania nanostructures (i.e. nanocluster, nanoparticles, nanotubes) is extremely topical for their importance for emerging technological applications. Transition metal oxides, however, are potentially challenging materials for standard computational methods used to study the excited state properties of nanosized systems (e.g. TD-DFT and GW/BSE). There is, therefore, a clear need for accurate correlated quantum chemistry benchmark calculations to compare the performance of the standard computational methods with. Because of the computational scaling of accurate quantum chemistry methods such benchmark calculations by definition will focus on small gas phase clusters containing only one to three transition metal atoms and will predominantly focus on their vertical excitation energies (in this chapter, adiabatic excitation energies, defined in Chapter 1, are just investigated for the smallest particle, the TiO_2 monomer).

Ideally, the quantum chemistry method used for the benchmark calculations should yield results as close as possible to the exact solution of the electronic time-independent non-relativistic Schrödinger equation (or in practice a Full Configuration Interaction (FCI) calculation for the same basis-set). This means, as already discussed in Chapter 2, a method that describes all contributions to the electron correlation beyond the *Fermi correlation* (or exchange, already included in the HF theory). In other words, a method that ideally describes both *dynamic* (Coulomb) and *static* correlation equally well. Furthermore, the ideal method treats the electronic ground state and excited state on the same well-balanced footing and is unambiguously defined.

In practice such an ideal method does not exist. FCI is prohibitively expensive for everything but atoms and very small molecules and all the other methods are effectively primarily geared towards describing either *dynamic* (e.g., truncated Configuration Interaction, CI, or Coupled Cluster, CC, methods) or *static* (e.g., Complete Active Space Self Consistent Field, CASSCF, and other multireference-SCF based methods) electron correlation. Although, taking the above into account, CASSCF with a well-defined and well-balanced Complete Active Space (CAS, the active space of orbitals for which essentially a full CI is performed, typically consisting of 6-16 orbitals and containing 6-16 electrons) followed by a second-order perturbation step (combined in

CASPT2, Complete Active Space 2nd order Perturbation Theory) is likely to recover at least a large part of the *dynamic* correlation. Equally CCSDT has been shown to recover, at least, part of the *dynamic* correlation and to perform well for classic ground state *static* correlation problems such as the breaking of bonds [1]. Finally, within the CC framework the ground state energy is calculated using a total energy approach while the excitation energy are obtained using an Equation-Of-Motion formalism, while within, for example, CASSCF all states (including the ground state) are calculated variationally. The latter means that to guarantee orthogonality between states belonging to the same irreducible representation *state-averaging* has to be employed, where all such states are optimised together, and the results might become slightly dependent on the number of states studied. Both CASSCF/CASPT2 [2] and CC theory (EOM-CCSD) [2,3] have previously been used to study excitations for the TiO_2 monomer and found to yield very similar results. Use of more approximate methods (CIS, CIS(D), CC2) have also been reported in the literature, but were found to give very unreliable results when compared with CASPT2 and EOM-CCSD [3]. As for transition metal clusters it is not clear-cut which orbitals and electrons to include in the active space and a strategy of simply including all valence electrons and orbitals is only tractable for the TiO_2 monomer (in part because of the 5 d-orbitals per titanium atom), CC will be the focus of this study. EOM-CCSD, EOM-CCSDT and a number of CC models that combine CCSD models with some approximate treatment of the triples are employed here, and used to predict spectra for the global minimum (GM) energy geometries of not only the TiO_2 monomer but also the Ti_2O_4 dimer and the Ti_3O_6 trimer (see Figure 3.1) [4-9]. In this section of my thesis, I will specifically investigate the effect of including triple excitations into the CC expansion (i.e., EOM-CCSDT) and the required balance between treating the triples contribution iteratively and/or approximating part of the triples contribution perturbatively.

In the remainder of this chapter, first CC theory with the different possible CC models, already discussed in Chapter 2, will be quickly revisited together with the technical details of the practical calculations (section 3.2), which will then be followed by a discussion of the results for the different clusters (section 3.3 – 3.4) and finally by the conclusions (section 3.5).

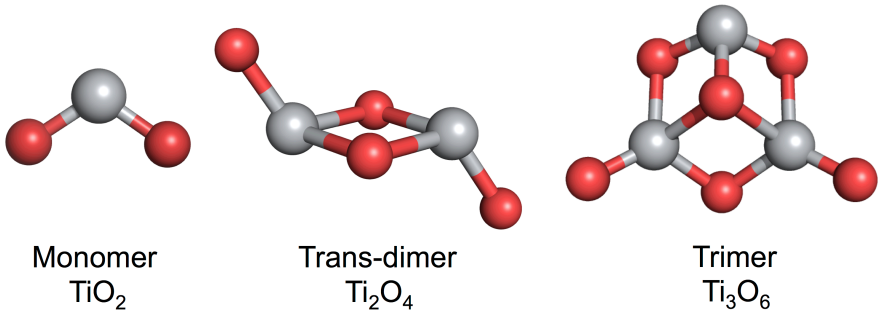

Figure 3.1 Structures of the three $(TiO_2)_n$ global minima for n = 1 – 3. Grey and red spheres represent titanium and oxygen atoms respectively.

3.2 Methodology

3.2.1 Equation of Motion Coupled Cluster Theory

Recalling Chapter 2, the Equation-of-motion Coupled Cluster theory (EOM-CC) [10-12] can be viewed as an excited state extension of the single reference CC formalism, where the wavefunction of K-th $|\Psi_K\rangle$ state is obtained by acting with the state-specific excitation operator R_K onto an already correlated CC ground state wavefunction (Equation 2-22).

In this study of TiO_2 clusters several EOM-CC methods were used, including EOM-CCSD [13,14], EOM-CCSDT (EOMCC with single, double, and triple excitations) [15-17], and several variants of the active-space EOM-CCSDT approach (EOM-CCSDt) [18], where the selection of the most important triple excitations is made using an active space. More specifically, the EOM-CCSDt(III)/ EOM-CCSDt(II)/ EOM-CCSDt(I) family of active space EOM-CC methods was employed [19], and as already discussed in Chapter 2, this set of methodologies includes an increasing subset of triple excitations. For example, in the most rudimentary EOM-CCSDt(III) approach only the triple excitations inside the active space (from occupied to unoccupied spin-orbitals) are considered. The EOM-CCSDt(I) and EOM-CCSDt(II) approaches use larger domain of triple excitations, where at least one or two electrons respectively need to belong to the active space (occupied and unoccupied active spin-orbitals). In addition to the iterative EOM-CC methods various non-iterative completely renormalised EOM-CCSD(T) approaches (CR-EOM-CCSD(T)) [20] and its reduced variant (r-CR-EOMCCSD(T)

method of Ref. [21]) were also utilised, where in this case the effect of triply excited configurations is accounted for in a perturbative manner. Although the EOM-CCSDT approach is capable of providing very accurate estimates of excitation energies for a wide class of excited states its applicability is limited by its steep numerical scaling proportional to N^8, where N defines the number of electrons in the system of study. For this reason the EOM-CCSDT can be used in calculations for relatively small molecular systems.

3.2.2 Computational Details

The geometry of all the structures used in this work were optimised at the DFT level with the hybrid B3LYP [22] XC energy functional in conjunction with the triple-ζ def2-TZVP basis set [23]. The harmonic frequencies at these optimised geometries were calculated employing the same DFT setup to verify that the optimised structures correspond to minima on the ground state potential energy surface. Use of the B3LYP optimised ground state structure instead of a CCSD/CCSDT optimised structure was found to introduce differences in the calculated excitation energies of less than 0.05 eV in case of the monomer, and is the only realistic alternative for larger clusters.

The electronic ground state of all the clusters studied in this work is a closed-shell singlet. The optimised structure for the monomer (TiO_2) has a C_{2v} geometry with Ti-O bond length (1.641 Å) and O-Ti-O bond angle (111.8°) in good agreement with the accurate multireference-CI (MRCI) [24] results obtained by Grein *et al.* [25], who found a bond length of 1.640 Å and O-Ti-O bond angle of 112.0° respectively. The optimised structure for the lowest energy dimer (Ti_2O_4) has a C_{2h} geometry with O-Ti (terminal bonds) bond lengths of 1.627 Å and Ti-O bond lengths of 1.847 Å, which compares well with the minimum energy geometry found by Li and Dixon using CCSD(T) [7] with bond lengths of 1.648 Å and 1.863 Å respectively. A large set of other dimer structures is known, where two of them lie relatively close in energy to the global minimum [4,7,26]. These two structures, with C_{2v} and C_s symmetry respectively, lie 0.25 and 0.73 eV higher in energy than the lowest energy dimer (B3LYP), and are not considered in this chapter but discussed later in Chapter 4. The optimised trimer structure (Ti_3O_6) with two terminal and one 3-fold coordinated oxygen atom (Figure 3.1), has C_s symmetry and it is in agreement with the GM obtained in previous studies

at B3LYP level [5-9,26-29]. Previous studies found a multitude of higher lying isomers on the trimer energy landscape, with a series of different coordination environments for the titanium and oxygen atoms. Among this set, the lowest energy alternative trimer structure (also with C_s symmetry) has two terminal oxygen atoms, a three-fold coordinated titanium atom and lies 0.36 eV higher in energy (B3LYP) [26]. Again, the excitations of this cluster are not studied in this chapter, but discussed in Chapter 4.

The singlet vertical excitation energies of the four lowest-lying excited states for the DFT ground state geometries have been calculated with various approximations of CC theory discussed above, in section 3.2.1. The most computationally expensive EOM-CCSDT calculations for the trimer molecule have been performed using 2000 cores on the Olympus cluster (Atipa Cluster, Opteron 6272 16C 2.100GHz, Infiniband QDR) at the Pacific Northwest National Laboratory. To calculate adiabatic excitation energies in the case of the monomer, relevant excited states were relaxed using EOM-CCSD, while keeping the point group symmetry fixed, followed in the case of EOM-CCSDT by a EOM-CCSDT single-point vertical excited state calculation on the EOM-CCSD optimised geometry of the lowest excited state.

The performance of the EOM-CC methods has been tested for a series of different basis sets. The selected basis sets are the small split-valence def2-SV(P) basis-set [30] and the larger triple-ζ def2-TZVPP basis set [23], which from now on will be defined as SV and TZ respectively. Moreover, for selected systems also the triple-ζ aug-cc-pVTZ [31] basis set was used to compare with literature results (further referred to as ATZ). The majority of the CC calculations, for reasons of computational tractability, employed the frozen core approximation, where only the valence electrons are correlated (i.e, the 1s orbitals of the oxygen atoms and the 1s to 3p orbitals of the titanium atoms are frozen in the CC calculations). However, for the smallest structure in this work (TiO_2) it has been possible to obtain the vertical excitation at the EOM-CCSD level of theory, employing the def2-TZVPP and the aug-cc-pVTZ all electron approach, which from now on will be referred to as aeTZ and aeATZ respectively. The electronic character of the excitations found by CC methods is interpreted in terms of the single and double electron orbital excitations with the largest EOM-CC amplitudes (t_1 and t_2), where amplitudes were considered as significant when $t_n > 0.1$ and as leading contributions for $t_n > 0.25$. The largest EOM-CC amplitudes are reported in specific R-vector

normalisation employed by the EOM-CC eigensolver.

The DFT ground state calculations, finally, were performed with the Turbomole 6.4 code [32], while all the coupled cluster calculations employed the Tensor Contraction Engine (TCE) module [33] of the NWChem 6.1 package [34].

3.3 Results

In this section, I will discuss the trends in the lowest excitation energies of the three TiO_2 clusters calculated with the different method combinations, then investigate the role of including triples excitations in the CC approximation and the practical balance between including triples and the quality of basis-sets one can employ.

3.3.1 Monomer

Figure 3.2 shows the four lowest excitation energies of the TiO_2 monomer cluster. As can be seen all method combinations (except for the all-electron SV EOM-CCSD calculation) find the same ordering of excited states energies and relative gaps (i.e., a large gap between S_1 and S_2, 1^1B_2 and 1^1A_2, and smaller gaps between S_2 and S_3 and S_3 and S_4). Increasing the basis-set quality from the split-valence SV basis-set to the larger triple-ζ zeta TZ basis-set is found to result in a consistent upward shift in the calculated excitation energies of ~ 0.2 eV. On the opposite, going from the frozen core approximation to an all electron calculation, where feasible, results in a consistent downward shift in the calculated excitation energies of ~ 0.1 eV. Including triples iteratively using EOM-CCSDt(I) and EOM-CCSDT leads to a consistent down-ward shift of up to ~ 0.25 eV, when compared to EOM-CCSD excitations both for SV and TZ basis sets. EOM-CCSDt(II) yields excitations very close in energy to those calculated with EOM-CCSD, while EOM-CCSDt(I) predicts values that are slightly lower than those obtained with EOM-CCSDT. For EOM-CCSDt(III), the active space methods with the smaller subset of triple excitations employed, for which the values are not shown in Figure 3.2 and that yield values higher in energy than those obtained with EOM-CCSD. The non-iterative pertubative triples CR-EOM-CCSD(T) method, finally, yields results that lie generally ~ 0.1 eV above the values obtained with plain EOM-CCSD.

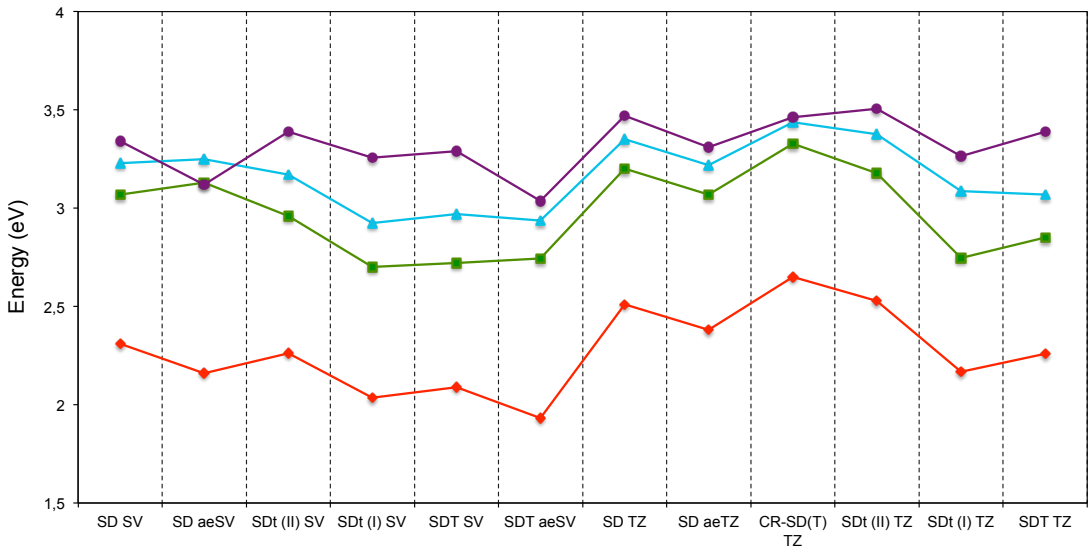

Figure 3.2 Trend in the four lowest excitation energies of the TiO_2 monomer as calculated with different method combinations (1^1B_2 red-line, 1^1A_2 green-line, 2^1B_2 blue-line, and 2^1A_1 purple-line; B_2 and B_1 labels interchanged to yield labels consistent with previous theoretical studies).

The EOM-CCSD aeTZ data from Figure 3.2 agree very well with EOM-CCSD, CASPT2 and MRCI results from the literature. The difference with the literature EOM-CCSD data is consistently smaller than 0.06 eV and with the published CASPT2 data is smaller than 0.1 eV for the lowest two excitations and less than 0.2 eV for the next two, while the difference with the literature MRCI data is smaller than 0.05 eV for all but the $2A_1$ excitation. While it was not possible to run EOM-CCSDT aeTZ calculations for all irreducible representations due to the computational cost involved with such calculations, aeTZ EOM-CCSDT results for the lowest $^1B_2$ excitation (2.12 eV) show a 0.14 eV further downward shift when going from the frozen-core approximation to including all-electrons, in-line with what is observed for EOM-CCSD/aeTZ, EOM-CCSD/aeATZ, and EOM-CCSDT/aeSV. The EOM-CCSDT aeTZ for the 1^1B_2 state (and the other states by extrapolation) thus lies ~ 0.3 eV lower than the corresponding states found with CASPT2 and MRCI.

Comparison with experimental spectral data for the TiO_2 molecule is complicated as typically adiabatic rather than vertical excitation energies are reported [35-37]. The most recent experimental study on molecular beams of TiO_2 molecules reports an adiabatic excitation energy of 2.18 eV [37] for a state identified, partly based also on previous computational work, as the 1^1B_2 state. Previous experimental work on TiO_2 in

a neon solid matrix [35] also yielded another adiabatic excitation energy at 1.97 eV (together with what was identified as the 1^1B_2 vertical excitation at 2.37 eV, slightly higher than in the molecular beam experiment). This 1.97 eV adiabatic excitation was assumed to originate from a linear TiO_2 isomer instead of the global minimum bent C_{2v} isomer studied here, in practice because none of the computational studies performed till that date had predicted any excitation energy lower than 2.4 eV. Finally, the authors of the more recent molecular beam experiments [37] report not seeing the 1.97 eV adiabatic excitation (but do not show the relevant spectral range in the paper), which they argue is due to the fact that the linear isomer is a higher energy isomer that might not be created in the laser ablation process used to prepare the TiO_2 clusters for their molecular beam.

To compare the results of this chapter with experiments the lowest two (i.e. 1^1B_2 and 1^1A_2) excited states were optimised using EOM-CCSD, followed by single-point EOM-CCSDT calculations, where possible, and the adiabatic excitation energies (difference between the excited state energy of the excited state relaxed geometry and the ground state energy of the initial GM structure) were then finally calculated. Just as in previous work [2], it is observed here that for the 1^1B_2 state the optimisation results in a decrease of the O-Ti-O angle to ~ 101°, while the optimised 1^1A_2 geometry becomes effectively linear (O-Ti-O angle to ~ 180°), where the exact angle depends on the specific basis-set used. Table 3.1 gives the obtained adiabatic excitation energies.

Table 3.1 Adiabatic excitation energies for the first (1^1B_2) and second (1^1A_2) lowest excited states of the monomer as calculated with EOM-CCSD and EOM-CCSDT (single points on EOM-CCSD optimised geometries, only where tractable) with the SV, TZ and ATZ basis-sets (all electron results, where tractable, are given between parentheses).

State	Method	SV	TZ	ATZ
$\mathbf{1^1B_2}$	EOM-CCSD	2.21 (2.11)	2.42 (2.32)	2.45 (2.35)
	EOM-CCSDT	1.80 (1.73)	2.01 (1.92)	---
$\mathbf{1^1A_2}$	EOM-CCSD	2.43	2.64 (2.48)	2.64 (2.47)
	EOM-CCSDT	2.05	2.32	---

Focusing on the larger basis-set results (i.e. TZ and ATZ) it is clear that EOM-CCSD yields a 1^1B_2 adiabatic excitation energy that lies relatively close (< 0.2 eV) to the value measured in the molecular beam experiment, especially when including the core-electrons in the EOM-CCSD calculations (i.e. using aeTZ and aeATZ basis-sets). This fits with the previous computational work of Lin *et al.* [2] who made a similar observation for their EOM-CCSD calculations. The EOM-CCSDT calculations yield values that lie further away from experiment (below instead of above). Specifically, an all electron EOM-CCSDT calculation with the aeTZ basis-set yields a 1^1B_2 adiabatic excitation energy of 1.92 eV (2.01 eV with the frozen-core approximation). However, it is tantalizing to note that this 1.92 eV value lies very close to the 1.97 eV value measured in the neon matrix [35]. One could suppose that the 2.18 eV peak (molecular beam experiment) then finds its origin in an adiabatic excitation into a higher excited state of the monomer (e.g. 2^1B_2 and 2^1A_1). While it is found in this study that the 1^1A_2 state lies in the correct range it would make an unlikely candidate for the 2.18 eV adiabatic excitation in this scenario, as an $^1A_2$ excitation is symmetry forbidden (at least in the case of vertical excitations at both the ground state and relaxed excited state geometries) and hence would have low intensity. Most importantly, these calculations suggest that the original identification of the 1.97 eV adiabatic excitation as originating from a linear isomer might need to be revisited.

In the case of the vertical excitation, the leading single electron HF excitation contributions to the lowest 1^1B_2 state for both EOM-CCSD and EOM-CCSDT, shown in Figure 3.3, is HOMO -> LUMO and HOMO -> LUMO+2 ($t_1 > 0.25$). In all cases the relevant occupied orbital involve p-orbitals on the terminal oxygen atoms, while the unoccupied virtual orbitals are d-like orbitals located on the central titanium atom. There are no significant double electron HF excitation contributions ($t_2 > 0.1$).

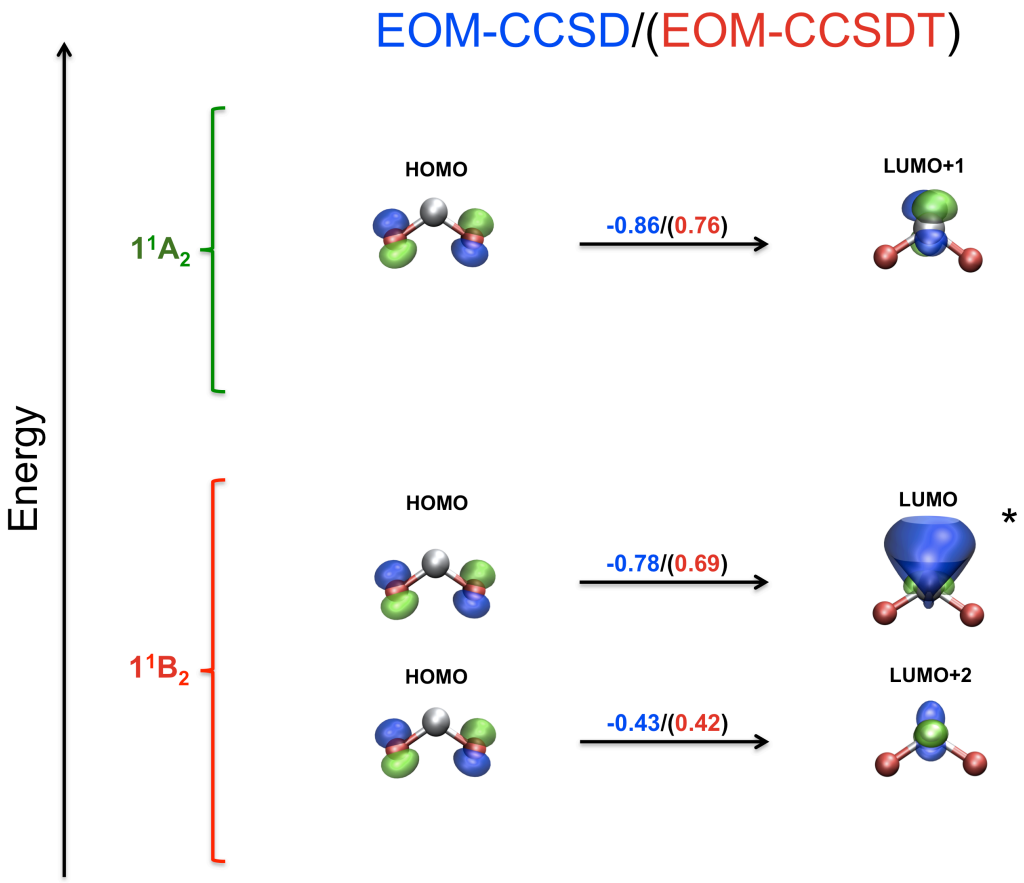

Figure 3.3 Leading single electron HF excitation contributions to the two lowest energy excitations for the monomer (1^1B_2 and 2^1A_1) calculated with EOM-CCSD and EOM-CCSDT. For each contribution the EOM-CCSD amplitude is specified in blue, while the EOM-CCSDT one is expressed in red in brackets. The isodensity plots for the HF orbitals are calculated at a value of 0.1 a.u. (0.05 a.u. for the orbitals that are labelled with a star), where the green lobes represent the positive portion of the wavefunction and the blue orbitals correspond to the negative one.

3.3.2 Dimer

Figure 3.4 shows the four lowest excitation energies for the trans Ti_2O_4 dimer cluster. Just as for the monomer, all method combinations find the same ordering of excited states and relative gaps. Also in this case the effect of increasing the basis-set from SV to the triple-ζ zeta TZ is an upward shift of ~0.2 eV, while the iterative inclusion of triples causes a downward shift of ~0.3 eV when moving from EOM-CCSD to EOM-CCSDT. In this case the inclusion of perturbative triples within CR-EOM-CCSD(T) has a better effect than for the monomer, but still does not seem to improve beyond EOM-CCSD (which are shifted upwards by ~0.05 eV). Finally, all methods predict the

excitation energies for the dimer to consistently lie higher in energy than their monomer counterparts (by ~1.4 eV for the lowest excitation and ~0.8 eV for all the others).

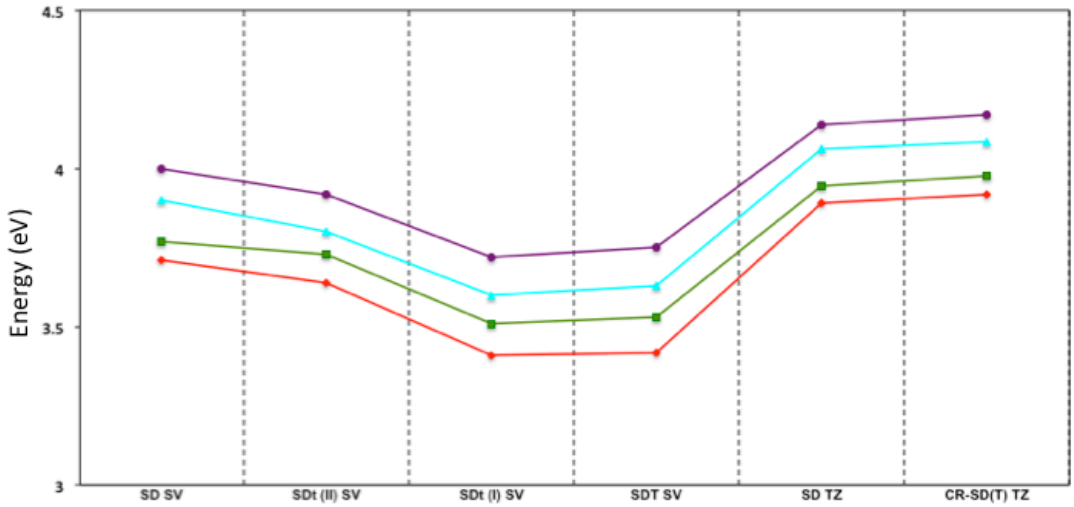

Figure 3.4 Trend in the four lowest excitation energies of the Ti_2O_4 trans dimer as calculated with different method combinations (1^1B_g red-line, 1^1A_u green-line, 1^1B_u blue-line, and 2^1A_g purple-line).

The leading single electron HF excitation contributions to the lowest energy ^1B_g excitation for both EOM-CCSD and EOM-CCSDT, as shown in Figure 3.5, are HOMO → LUMO, HOMO → LUMO+3, HOMO-1 → LUMO+1. In all cases, the relevant occupied orbitals involve p-orbitals on both the terminal and two-fold coordinated oxygen atoms, while the virtual orbitals are predominantly localised on the two titanium atoms. Just as for the monomer, there are no significant double electron HF excitation contributions ($t_2 > 0.1$).

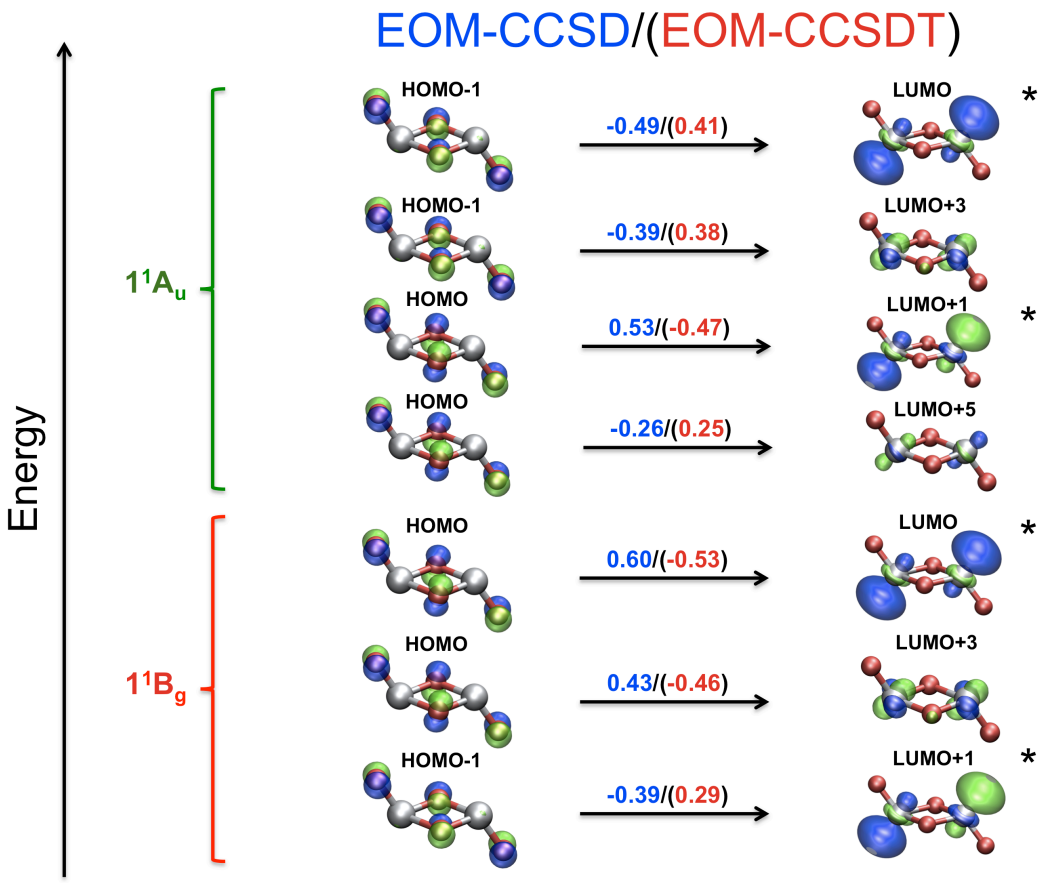

Figure 3.5 Leading single electron HF excitation contributions to the two lowest energy excitations for the dimer (1^1B_g and 1^1A_u) calculated with EOM-CCSD and EOM-CCSDT. For each contribution the EOM-CCSD amplitude is specified in blue, while the EOM-CCSDT one is expressed in red in brackets. The isodensity plots for the HF orbitals are calculated at a value of 0.1 a.u. (0.05 a.u. for the orbitals that are labelled with a star), where the green lobes represent the positive portion of the wavefunction and the blue orbitals correspond to the negative one.

3.3.3 Trimer

Figure 3.6 shows the four lowest (two lowest for EOM-CCSDT, where fully converging two excitations per irreducible representation was found to be numerically intractable on the computational resources available) excitation energies calculated for the Ti_3O_6 trimer cluster. Here, in contrast to the monomer and dimer, a clear effect of including triples is observed beyond a simple downward shift in energy. The lowest two excitations change ordering upon including a certain amount of pertubative triples. For EOM-CCSD, CR-EOM-CCSD(T) and EOM-CCSDt(III) the lowest singlet excitation has A" symmetry, while for EOM-CCSDt(II), EOM-CCSDt(I) and EOM-CCSDT the lowest singlet root has A' symmetry. A similar switch can also be observed for the second pair of excitations. The fact that a switch is seen in EOM-CCSDt(II), EOM-

CCSDt(I) and EOM-CCSDT, where it was possible to converge multiple excitations for the former methods, confirms that the observed switch is real and not an artifact resulting from the iterative solver missing the lowest lying excitation.

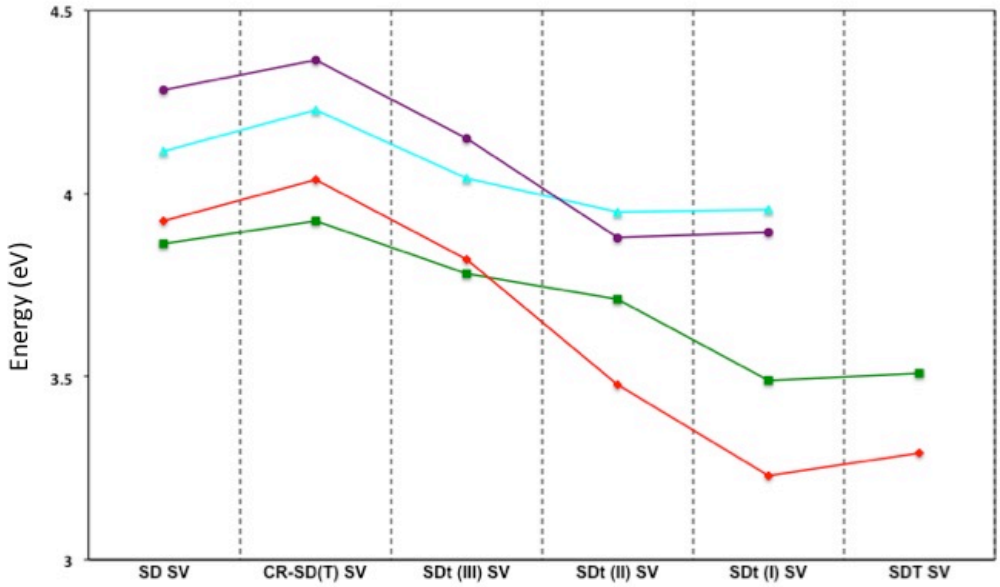

Figure 3.6 Trend in the four lowest excitation energies of the Ti_3O_6 trimer as calculated with different method combinations ($2^1A'$ green-line, $1^1A''$ red-line, $2^1A''$ blue-line, and $3^1A'$ purple-line).

The energy of the trimer excitations relative to those of the monomer are less sensitive to the inclusion or not of pertubative triples. All methods consistently predict that the lowest trimer excitation lies ~1.4 eV higher in energy than its monomer counterpart and is similar in energy to the lowest excitation of the dimer (slightly higher for EOM-CCSD and slightly lower for EOM-CCSDT).

The leading single electron HF excitation contributions to the lowest energy A' excitation for EOM-CCSD and EOM-CCSDT are HOMO -> LUMO, HOMO -> LUMO+2 and HOMO -> LUMO+8. As can be seen in Figure 3.7 the occupied orbitals in these excitations are typically localised on the terminal oxygen atoms, while the virtual orbitals are predominantly localised on the triply coordinated titanium atom. The main contributions to the lowest energy $^1A''$ orbital are both in the case of EOM-CCSD and EOM-CCSDT HOMO-7 -> LUMO and HOMO-7 -> LUMO+2. The virtual orbitals are again localised on the three-fold coordinated titanium atom but the occupied orbitals

are predominantly localised on the three oxygen atoms located around the three-fold coordinated titanium atom instead of the terminal oxygen atoms. The 1^1A" excitation thus appears more localised while the 2^1A' excitation has more long-distance charge-transfer character. Just as for the monomer and dimer, finally, there are no significant double electron HF excitation contributions for either the lowest 2^1A' and 1^1A" excitations.

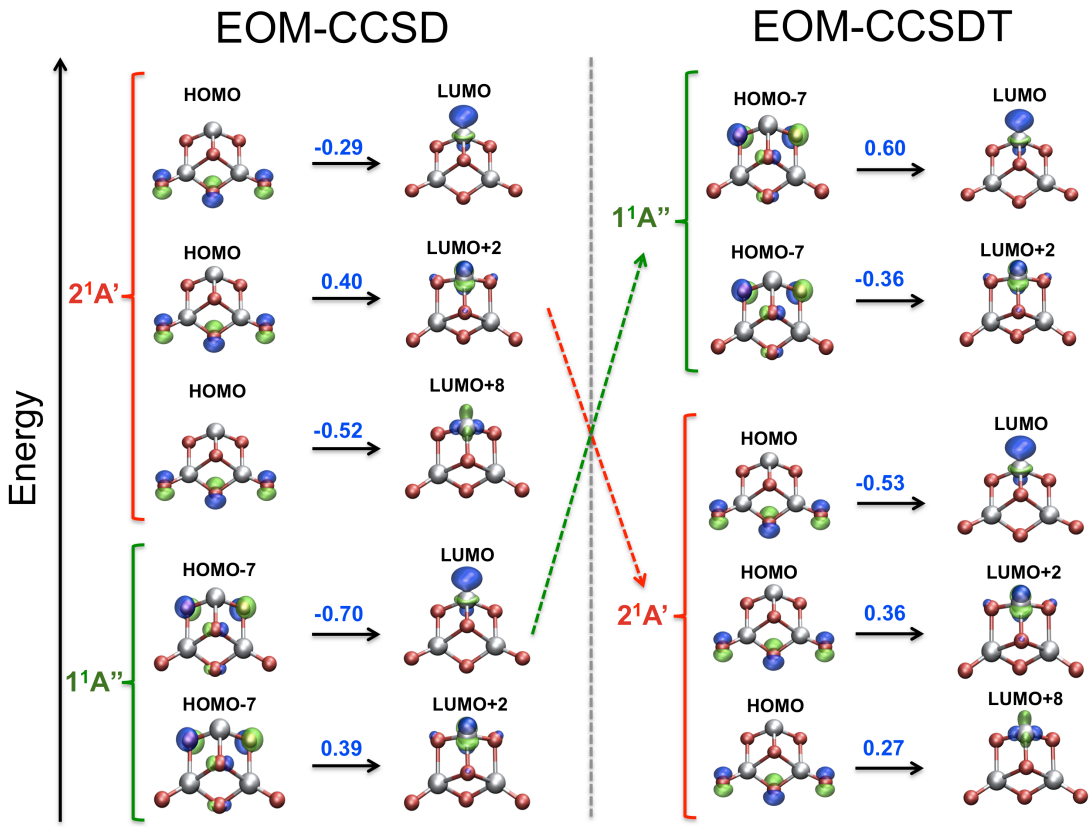

Figure 3.7 Leading single electron HF excitation contributions (t_1 > 0.25) to the two lowest energy singlet A' and A" excitations for the trimer, calculated with EOM-CCSD and EOM-CCSDT. For each contribution the amplitude value is specified in blue. The isodensity plots for the HF orbitals are calculated at a value of 0.1 a.u., where the green lobes represent the positive portion of the wavefunction and the blue orbitals correspond to the negative one.

3.4 Discussion

When considering the effect of including triples in coupled cluster calculations, two different but interrelated effects have to be distinguished: (i) a (rigid) shift in excitation energies and (ii) a crossing of excited states. All three clusters studied here show a non-negligible type (i) effect, where the EOM-CCSDT excitation energies are invariably

located 0.3–0.4 eV below the EOM-CCSD excitation energies. For the trimer also a type (ii) effect was observed, where the $1^1A''$ and $2^1A'$ states cross when going from EOM-CCSD to EOM-CCSDT. The lowest excited states for all clusters are dominated by single-electron excitations (see above) so it is unlikely that effect (i) and (ii) are related to excitations having double excitation character, and hence their origin must lie in an improved description of *static* (and *dynamic*) correlation. The rigid shift (i) might be ironically related to an improved description of the ground state in the CCSDT calculation that precedes the EOM-CCSDT excited state calculation. This might also explain why methods based on non-iterative triples (e.g., CR-EOM-CCSD(T)) do not yield improved results relative to EOM-CCSD. Such methods add triples corrections to the excited state but describe the ground state with standard CCSD. The exact origin of the crossing of states for the trimer is also unknown but it might be related to the fact that, as outlined above, the $2^1A'$ and $1^1A''$ excitations have a fundamentally different chemical character, while for the monomer and dimer all lowest excited states have a similar character. Another contributing fact might be that, as can be seen in Figure 3.8, the spectrum of Hartree-Fock orbitals that enter the EOM-CC calculation becomes denser with increasing cluster size and unoccupied orbitals end up lying increasingly close in energy. It is also of note that the lowest singlet $2^1A'$ excitation for the trimer is an extreme case in terms of the number of the significant amplitudes ($t_1 > 0.1$) changing when going from EOM-CCSD to EOM-CCSDT. For the lowest $2^1A'$ excitation of the trimer, the number of significant amplitudes changes from 10 to 3 (i.e., seven amplitudes decrease to a $t_1 < 0.1$), while the number of significant amplitudes for the $1^1A''$ excitation stays constant and the observed difference for the lowest excitations of the other clusters is at most a reduction of two. The 0.1 cut-off is to a certain extent arbitrary, but the large change for the $2^1A'$ excitation and lack of change for the $1^1A''$ excitation respectively, suggests that the origin of the state crossing is a different description of the $2^1A'$ state in EOM-CCSD and EOM-CCSDT. This is, finally, corroborated by the fact that for the $2^1A'$ trimer excitation, the largest amplitude involves different HF orbitals when going from EOM-CCSD to EOM-CCSDT (from HOMO → LUMO+8 to HOMO → LUMO, see Figure 3.7), again something not observed for the other clusters or the lowest $1^1A''$ excited state of the trimer.

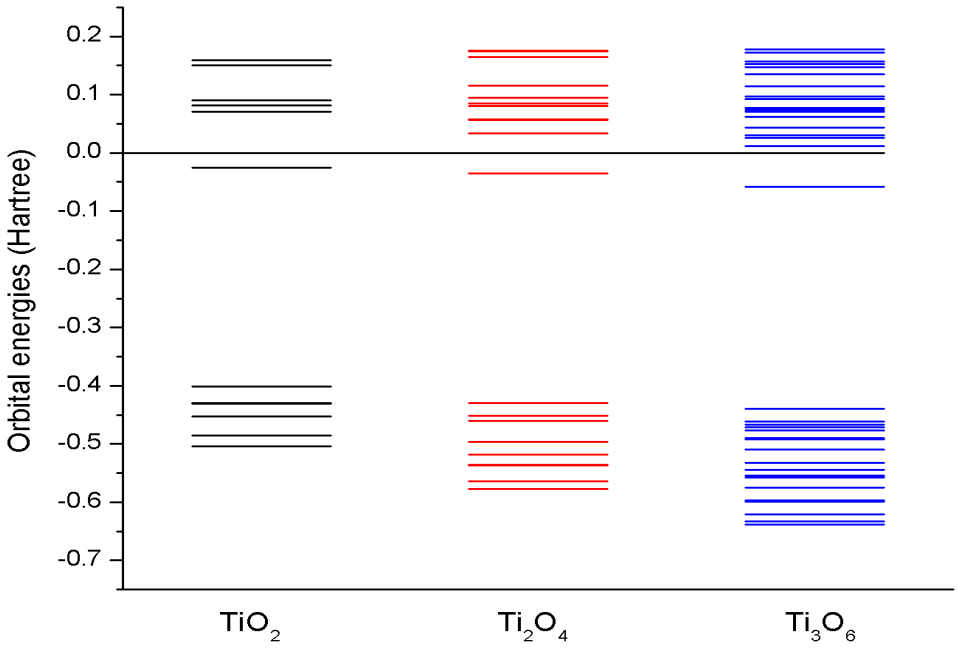

Figure 3.8 Energy ordering of the HF orbitals (occupied and virtuals) for the TiO_2 monomer (black lines), Ti_2O_4 dimer (red lines), and Ti_3O_6 trimer (blue lines). All the energies are in Hartrees.

The computational cost of EOM-CCSDT relative to EOM-CCSD (N^8 vs. N^6 scaling) is found to be a practical constraint on the size of systems that can be studied and/or the size of basis-sets that can be employed. Specifically, in the case of the monomer EOM-CCSDT calculations with the triple-ζ TZ and aeTZ basis sets were found to be feasible on contemporary parallel machines while for the larger clusters only EOM-CCSDT calculations with the smaller SV basis-set were found to be tractable. There is thus, currently at least, for the dimer and trimer a tradeoff between improving the method (i.e., including triples) and maintaining the quality of the basis-set (i.e., the need to reduce the basis-set from TZ to SV). The EOM-CCSDt(I) active-space method was found to yield results that are very close to full EOM- CCSDT at a lower computational cost. However, while use of EOM-CCSDt(I) generally allowed more roots to be studied than where feasible with EOM-CCSDT, the computational savings were typically not sufficient to allow the usage of a larger basis-set. EOM-CCSDT and EOM-CCSDt(I) calculations for clusters larger than the trimer were found to be currently numerically intractable. Coupled cluster approaches where triples are treated perturbatively (e.g., CR-EOM-CCSD(T)), while displaying advantageous scaling compared to EOM-CCSDT and EOM-CCSDt(I), were found to offer no advantage over EOM-CCSD and sometimes

even found to produce worse result. EOM-CCSD is thus the only feasible coupled cluster approach for systems that are too large to treat with either EOM-CCSDT or EOM-CCSDt(I). These results suggest that when type (i) effects dominate an approximate idea of the possible EOM-CCSDT spectrum might be obtained by pragmatically shifting the EOM-CCSD spectrum by a rigid amount.

Finally, focusing on the chemistry rather than methodology, the results shown in this chapter suggests that, independently of the exact method used, there is a distinct upward shift in excitation energies when going from the monomer to the dimer and trimer. The lowest energy excitations of the dimer and trimer are predicted to lie more than 1 eV higher in energy than that of the monomer. A tentative explanation for this difference in lowest excitation energy might lie in the oxygen coordination of the titanium atoms in the different clusters (two-fold in the monomer, three-fold in the dimer, and three/four-fold for the trimer) and hence the electrostatic field experienced by the excited electrons localised on the titanium atoms.

3.5 Conclusions

In this chapter, coupled cluster methods were used to study the optical excitations of TiO_2 clusters containing one to three titanium atoms. The specific focus has been on EOM-CC methods that included contributions of triples such as the full EOM-CCSDT, the approximate iterative active-space EOM-CCSDt(I) method, and approaches that treat triples perturbatively, e.g., CR-EOM-CCSD(T). These calculations show that there is a non-negligible effect of adding triples, mostly in the form of a downward shift in excitation energies relative to those obtained by EOM-CCSD, and that the approximate iterative active-space EOM-CCSDt(I) method yields results that are in good agreement with full EOM-CCSDT. Methods that treat triples perturbatively, in contrast, are found to yield results that are not better or even worse than those obtained by EOM-CCSD. Finally, for the larger clusters, there is a tradeoff between method and basis-set, where calculations using methods that include iterative triples are currently only feasible with moderately sized basis-sets.

3.6 References

[1] Yang, K. R.; Jalan, A.; Green, W. H.; Truhlar, D. G. *J. Chem. Theory Comput.* **2012**, *9*, 418.
[2] Lin, C.-K.; Li, J.; Tu, Z.; Li, X.; Hayashi, M.; Lin, S. H. *R. Soc. Chem. Adv.* **2011**, *1*, 1228.
[3] Taylor, D. J.; Paterson, M. J. *J. Chem. Phys.* **2010**, *133*, 204302.
[4] Hamad, S.; Catlow, C. R. A.; Woodley, S. M.; Lago, S.; Mejias, J. A. *J. Phys. Chem. B* **2005**, *109*, 15741.
[5] Qu, Z. W.; Kroes, G. J. *J. Phys. Chem. B* **2006**, *110*, 8998.
[6] Calatayud, M.; Maldonado, L.; Minot, C. *J. Phys. Chem. C* **2008**, *112*, 16087.
[7] Li, S.; Dixon, D. A. *J. Phys. Chem. A* **2008**, *112*, 6646.
[8] Shevlin, S. A.; Woodley, S. M. *J. Phys. Chem. C* **2010**, *114*, 17333.
[9] Syzgantseva, O. A.; Gonzalez-Navarrete, P.; Calatayud, M.; Bromley, S.; Minot, C. *J. Phys. Chem. C* **2011**, *115*, 15890.
[10] Comeau, D. C.; Bartlett, R. J. *Chem. Phys. Lett.* **1993**, *207*, 414.
[11] Geertsen, J.; Rittby, M.; Bartlett, R. J. *Chem. Phys. Lett.* **1989**, *164*, 57.
[12] Stanton, J. F.; Bartlett, R. J. *J. Chem. Phys.* **1993**, *98*, 7029.
[13] Monkhorst, H. J. *Int. J. Quantum Chem.* **1977**, 421.
[14] Koch, H.; Jorgensen, P. *J. Chem. Phys.* **1990**, *93*, 3333.
[15] Nakatsuji, H.; Hirao, K. *Chem. Phys. Lett.* **1977**, *47*, 569.
[16] Nakatsuji, H.; Hirao, K. *J. Chem. Phys.* **1978**, *68*, 2053.
[17] Nakatsuji, H.; Hirao, K. *J. Chem. Phys.* **1978**, *68*, 4279.
[18] Kowalski, K.; Piecuch, P. *J. Chem. Phys.* **2001**, *115*, 2966.
[19] Kowalski, K.; Hirata, S.; Wloch, M.; Piecuch, P.; Windus, T. L. *J. Chem. Phys.* **2005**, *123*.
[20] Kowalski, K.; Piecuch, P. *J. Chem. Phys.* **2004**, *120*, 1715.
[21] Kowalski, K.; Valiev, M. *Int. J. Quantum Chem.* **2008**, *108*, 2178.
[22] Becke, A. D. *J. Chem. Phys.* **1993**, *98*, 5648.
[23] Weigend, F.; Ahlrichs, R. *Phys. Chem. Chem. Phys.* **2005**, *7*, 3297.
[24] Grimme, S.; Waletzke, M. *J. Chem. Phys.* **1999**, *111*, 5645.
[25] Grein, F. *J. Chem. Phys.* **2007**, *126*.
[26] Chen, M.; Dixon, D. A. *J. Chem. Theory Comput.* **2013**, *9*, 3189.
[27] Liu, Y.; Yuan, Y.; Wang, Z.; Deng, K.; Xiao, C.; Li, Q. *J. Chem. Phys.* **2009**, *130*, 174308.
[28] Marom, N.; Kim, M.; Chelikowsky, J. R. *Phys. Rev. Lett.* **2012**, *108*, 106801.
[29] Taylor, D. J.; Paterson, M. J. *Chem. Phys.* **2012**, *408*, 1.
[30] Schafer, A.; Horn, H.; Ahlrichs, R. *J. Chem. Phys.* **1992**, *97*, 2571.
[31] Balabanov, N. B.; Peterson, K. A. *J. Chem. Phys.* **2005**, *123*.
[32] Ahlrichs, R.; Bar, M.; Haser, M.; Horn, H.; Kolmel, C. *Chem. Phys. Lett.* **1989**, *162*, 165.
[33] Lai, P.-W.; Zhang, H.; Rajbhandari, S.; Valeev, E.; Kowalski, K.; Sadayappan, P. In *Proceedings of the international conference on computational science, iccs 2012*; Ali, H., Shi, Y., Khazanchi, D., Lees, M., VanAlbada, G. D., Dongarra, J., Sloot, P. M. A., Eds. 2012; Vol. 9, p 412.
[34] Valiev, M.; Bylaska, E. J.; Govind, N.; Kowalski, K.; Straatsma, T. P.; Van Dam, H. J. J.; Wang, D.; Nieplocha, J.; Apra, E.; Windus, T. L.; de Jong, W. A. *Comp. Phys. Commun.* **2010**, *181*, 1477.

[35] Garkusha, I.; Nagy, A.; Guennoun, Z.; Maier, J. P. *Chem. Phys.* **2008**, *353*, 115.
[36] Wang, H.; Steimle, T. C.; Apetrei, C.; Maier, J. P. *Phys. Chem. Chem. Phys.* **2009**, *11*, 2649.
[37] Zhuang, X. J.; Le, A.; Steimle, T. C.; Nagarajan, R.; Gupta, V.; Maier, J. P. *Phys. Chem. Chem. Phys.* **2010**, *12*, 15018.

Chapter 4

Modelling vertical excited states in TiO_2 nanoparticles with a TD-DFT based description

In this chapter, some of the EOM-CC benchmarks defined in Chapter 3 are employed to evaluate the accuracy of different TD-DFT XC energy functionals for the description of vertical low-energy excitations in naked and hydrated TiO_2 nanoparticles. Specifically, in this chapter, I will investigate the cases for which EOM-CC and TD-DFT give a qualitatively different interpretation and focus on the origin of the discrepancy (CT excitations).

The content of this chapter has been taken from the following published work:
Berardo, E.; Hu, H. S.; Shevlin, S. A.; Woodley, S. M.; Kowalski, K.; Zwijnenburg, M. A. Modeling Excited States in TiO_2 Nanoparticles: On the Accuracy of a TD-DFT Based Description. *Journal of Chemical Theory and Computation* **2014**, *10*, 1189-1199.

Regarding the results included in the following chapter, I have performed all the DFT/TD-DFT calculations, whereas Dr. Karol Kowalski and Dr. Han-Shi Hu performed the EOM-CCSD/T calculations on specific TiO_2 nanoparticles.

4.1 Introduction

In Chapter 3, it was shown how correlated wavefunction methods such as EOM-CCSD/CCSDT can be employed to define accurate benchmarks for the calculation of optical properties of TiO_2 gas phase clusters. However, the poor scaling of such methods with the number of electrons in the cluster means that these approaches can only be used for very small systems containing merely a few transition metal atoms. For example, the majority of the work in the literature, in which correlated wavefunction methods are employed, focuses on the description of the excited states of the TiO_2 monomer [1-3]. The largest system studied to date with a correlated wavefunction method for TiO_2 particles is the $(TiO_2)_3$ trimer, already discussed in the previous chapter of this thesis.

There is therefore a clear need for a computational approach that would allow to investigate excited state properties and processes in nanosystems of experimental relevance (~20/30 TiO_2 units, ~1 nm in size). To understand the physics and chemistry underlying the application of TiO_2 nanostructures in photocatalysis and photovoltaics from a theoretical point of view, TiO_2 nanostructures and extended systems have been computationally extensively studied using a variety of methods [4-19]. Most of these studies employ either ground state DFT or its excited state variant TD-DFT. As introduced in Chapter 2, TD-DFT is a genuine excited state method that can be used for any number of excitations of any multiplicity. However, just like DFT in the case of the ground state, TD-DFT suffers from the fact that the results are to a smaller or larger degree dependent on the XC energy functional used. This might be especially true for TiO_2 and other transition metal containing systems.

In this chapter, the performance of TD-DFT will be compared with correlated wavefunction benchmarks for a number of relevant nanoparticle structures; sampling a range of titanium environments such as threefold, fourfold and fivefold coordination. Here, the EOM-CC results discussed in the previous chapter are compared with the TD-DFT results obtained with the PBE, B3LYP, CAM-B3LYP and BHLYP XC energy functionals. The analysis of the performance of these methods is limited, in this chapter, to the calculation of the vertical singlet excitation spectra of the nanoparticles, the equivalent of the experimental UV-VIS absorption spectra. In this study, attention is specifically paid to the lowest singlet excitation (S1), as this excitation, following

Kasha's principle [20], is the likely source of fluorescence (luminescence) and the state relevant to applications such as photocatalysis and photovoltaics. An accurate description of this state at the ground state geometry is, therefore, a crucial starting point for future computational work on TiO_2 nanoparticles that will focus on modelling phenomena that involve excited state relaxation, following the ideas developed by my research group [21-26] and others [27-30].

Differently from the previous chapter, where the structures were simple TiO_2 gas phase clusters of little interest for any photocatalytic and photovoltaic experiment, here larger and surface hydrated particles are investigated. To stress my intent of describing systems of experimental relevance, from this chapter on, whenever referring to a TiO_2 structure, I will use the term "nanoparticle", even if the system only contains few TiO_2 units. The structures investigated in this chapter consist in a series of TiO_2 naked and hydrated nanoparticles, which span from the smallest one of only 3 atoms (monomer) to the largest system of 39 atoms.

4.2 Methodology

The geometry of each TiO_2 nanoparticle used in this work was optimised at the DFT level with the hybrid B3LYP XC energy functional in conjunction with the triple-ζ def2-TZVP basis set. The electronic ground state of all the nanoparticles studied in this work is assumed to be a closed-shell singlet.

For the naked $(TiO_2)_n$ nanoparticles, where $n = 1 – 13$, the GM geometries reported by a number of other groups [10,31-36] were employed. To investigate a larger range of titanium and oxygen coordination environments, a number of metastable isomers (i.e. local minima for a given cluster-size that lie higher in energy than the GM) were also examined. For the $(TiO_2)_2$ dimer this included two metastable nanoparticles that were labelled "*cis*" and "*club*", with C_{2v} and C_s symmetry respectively [32,34], while for the trimer $(TiO_2)_3$ one higher metastable isomer with C_1 symmetry was included and labelled as "*alt*" [32,34,37]. The geometries of the stable and metastable nanoparticles for the $n = 1 – 13$ sub-set are shown in Figure 4.1.

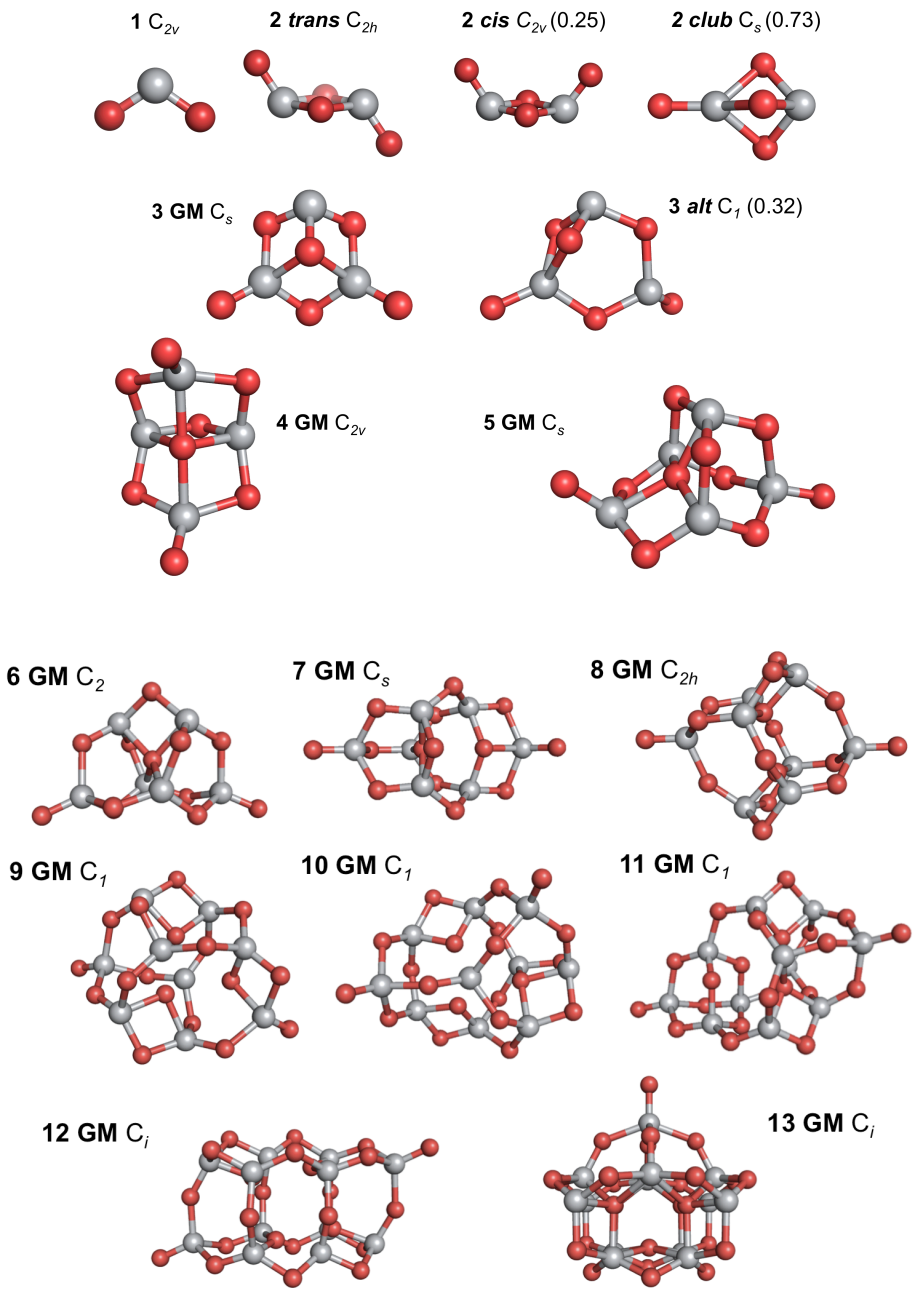

Figure 4.1 Global minimum (GM) molecular comformations for $(TiO_2)_n$ nanoparticles with n = 1 – 13. For the dimers $(TiO_2)_2$ and trimers $(TiO_2)_3$, metastable particles are also shown. Labels include point group symmetry and for the non-GM structures, the energy difference in eV relative to the GM energy calculated at the B3LYP/def2-TZVP level. Red spheres denote oxygen ions, whereas grey spheres denote titanium ions.

The hydrated systems, $(TiO_2)_n(H_2O)_m$ where n and m range from 1 – 3, were obtained through the saturation of all the under-coordinated titanium and oxygen atoms present in the naked nanoparticles with hydroxyl groups and protons respectively. For the generation of the hydrated particles, I assumed that titanium atoms are normally

coordinated by at least four oxygen atoms and oxygen atoms form at least two bonds. All the hydrated nanoparticles are shown in Figure 4.2. The DFT optimised structures include $Ti(OH)_4$, with S_4 symmetry, $(TiO_2)_2(H_2O)_2$, with C_{2v} symmetry, $(TiO_2)_2(H_2O)$, $(TiO_2)_3(H_2O)_2$ and $(TiO_2)_3(H_2O)_3$ all with C_1 symmetry.

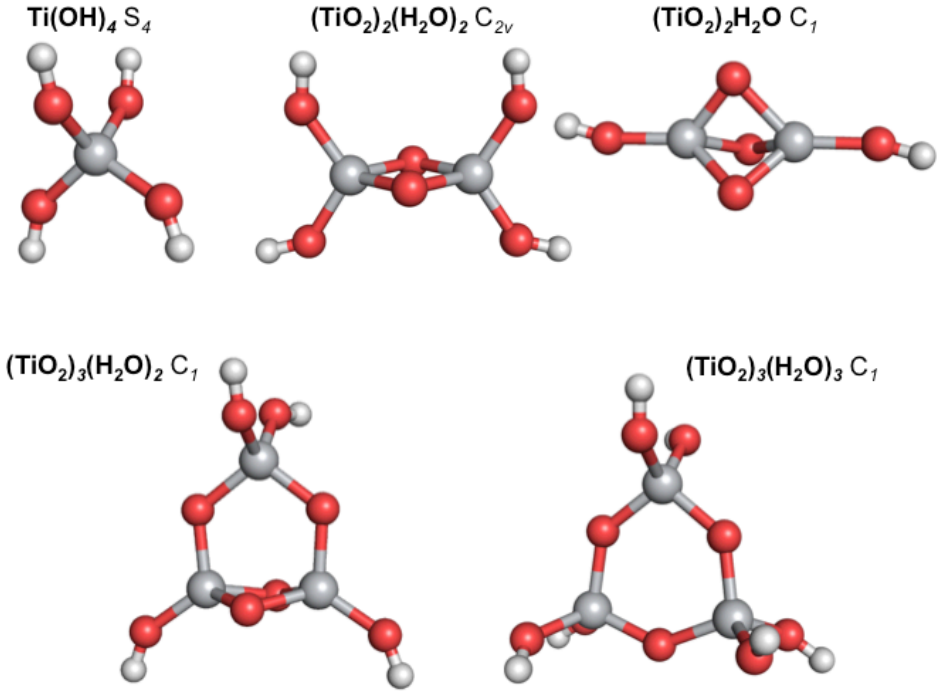

Figure 4.2 $(TiO_2)_n(H_2O)_m$ hydrated nanoparticles, with n and m ranging between 1 and 3. In order to saturate relevant defects, one water molecule is added per singly coordinated oxygen atom in the originally naked particles [with as only exception the $(TiO_2)_3(H_2O)_3$ structure, where one additional water molecule was added to generate the same coordination environment for all the titanium atoms]. For each structure the symmetry of the B3LYP/def2-TZVP minimum is given.

For all the B3LYP optimised geometries the energies of the lowest singlet excited states were obtained at the TD-DFT/def2-TZVP level with different XC energy functionals; the pure GGA PBE [38], the hybrids B3LYP and BHLYP [39] and the range-separated hybrid XC energy functional CAM-B3LYP [40]. For selected B3LYP optimised geometries the four lowest energy excited states were also calculated with the two different CC approaches; EOM-CCSD and EOM-CCSDT.

Due to the high computational cost required, the structures of B3LYP nanoparticles larger than the monomer were not re-optimised with the CC approaches. However, in order to test the approximation made by employing the B3LYP optimised geometries, the complete set of naked nanoparticles investigated in this work was also re-optimised with the PBE, CAM-B3LYP and BHLYP XC energy functionals, and used to calculate

the respective vertical excitations. The use of B3LYP optimised structures, when compared to their fully optimised ground state counterparts for each different XC energy functional, was found to introduce an average difference of ~0.1 eV in the calculated vertical excitation energies for the $(TiO_2)_n$ particles.

While for all TD-DFT calculations the def2-TZVP basis set was employed, in the case of the EOM-CC methods two different basis sets were used; the split-valence def2-SV(P) basis-set [41] and the larger triple-ζ def2-TZVPP basis set [42]. Like in Chapter 3, these two basis sets will be referred to as SV and TZ, respectively. All the CC calculations, for reasons of computational tractability, employed the frozen core approximation where only the valence electrons are correlated.

The DFT/TD-DFT calculations employing the PBE, B3LYP and BHLYP XC energy functional were performed with the Turbomole 6.4 code [43], while the TD-DFT results obtained for the CAM-B3LYP XC energy functional and the Λ diagnostic (introduced in Chapter 2) were calculated with the GAMESS US code (version 26 October 2012) [44]. The EOM-CC calculations employed the Tensor Contraction Engine (TCE) module [45] of the NWChem 6.1 package [46]. The Pymol Molecular Graphics System [47] was used for the graphic representations of the TiO_2 nanoparticles, while VMD [48] for the visualisation of the differences between the ground state and excited state densities.

4.3 Results & Discussion

In this section, I will first compare the lowest vertical excitation energies of the $(TiO_2)_n$ GM nanoparticles obtained with the four different TD-DFT XC energy functionals; PBE, B3LYP, BHLYP and CAM-B3LYP. I will then discuss how the choice of the XC energy functional affects the shape of the TD-DFT optical spectrum, and in particular, focus on the $(TiO_2)_n$ particles for which different trends in their excitations energies are observed. Next, to further understand what is the origin of the differences between excitation energies calculated with various XC energy functionals, I discuss the excitation energies of a selection of small nanoparticles (n = 1 - 5) with relevant defects using EOM-CC and compare the TD-DFT results (TD-B3LYP and TD-CAMB3LYP) with the EOM-CC benchmark values. Moreover, through the calculation of the Λ diagnostic I try to analyse the origin of the trends shown by the different XC energy functionals, confirming the usefulness of this diagnostic test for the detection of potential CT problems in TD-DFT calculations. Finally, I define some EOM-CC benchmarks for hydrated structures and try to understand if after hydration the differences between the values predicted with the various XC energy functionals still persist.

4.3.1 TD-DFT vertical excitations for $(TiO_2)_n$

As shown in Figure 4.3 the four different XC energy functionals considered exhibit a similar trend in the description of the lowest excitation energy (S1, the absorption on-set) for the $(TiO_2)_n$ GM nanoparticles. There appears to be a constant energy shift that is dependent upon the amount of exact HF-like exchange (HFLE) included in each of the XC energy functionals employed. For example, PBE with 0% HFLE gives the lowest excitation energies, while BHLYP with 50% of HFLE yields the highest values. Excitation energies obtained using B3LYP that has 20% HFLE and CAM-B3LYP, with 19% at short range and 65% at long range, lie in between the PBE and BHLYP values. However, aside from the similarities observed among the four data series, it is easy to see that the trend for TD-PBE and TD-B3LYP has two clear dips of ~0.5 eV, at $(TiO_2)_3$ and $(TiO_2)_{10}$, which are absent in the CAM-B3LYP and BHLYP results. In addition, the PBE XC energy functional results show a similar but smaller dip for the $(TiO_2)_6$ structure, while TD-B3LYP places this excitation in between the energies obtained for

$(TiO_2)_5$ and $(TiO_2)_7$, and whereas TD-CAM-B3LYP and TD-BHLYP predict a local maximum in the trend for this geometry. Both of the lowest excitations for the $(TiO_2)_3$ and $(TiO_2)_{10}$ nanoparticles correspond to states with weak absorption intensity (i.e. low oscillator strength). However, it is important to stress that they are not dark states (excitations with zero absorption intensity); with TD-B3LYP the oscillator strengths are 9×10^{-5} (although two orders of magnitude weaker than the most intense excitation among the hundred lowest excitations) and 3.6×10^{-4} (one order of magnitude weaker), respectively.

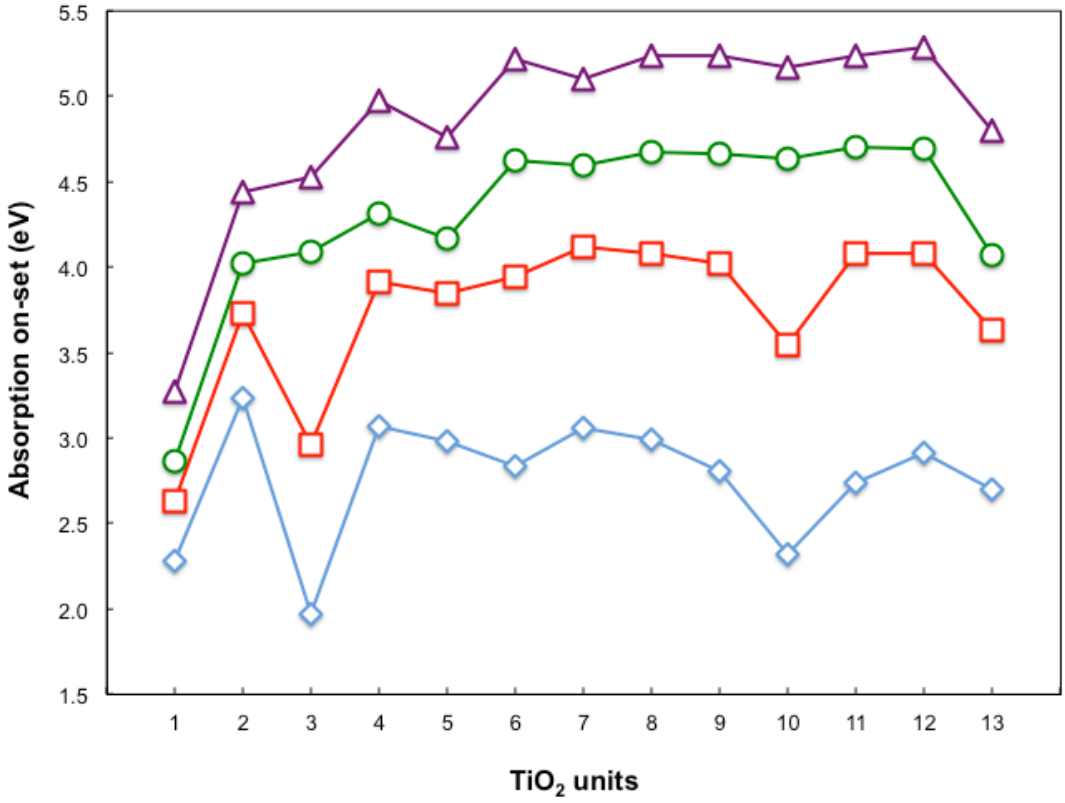

Figure 4.3 Lowest singlet excitation energies calculated with different TD-DFT XC energy functionals for the B3LYP/def2-TZVP optimised ground state $(TiO_2)_n$ GM structures. PBE values are represented by blue diamond markers, B3LYP red squares, CAMB3LYP green circles and BHLYP excitations are defined as purple triangles.

Inline with the observations above, if the predictions of XC energy functionals with none or low HFLE (PBE and B3LYP provide similar trends) are plotted against the energies calculated with CAM-B3LYP and BHLYP a clear difference can be observed. Figure 4.4 shows that there is a good linear fit between the TD-CAM-B3LYP and TD-BHLYP predicted absorption on-set values of the GM nanoparticles (R^2 of 0.99, with R^2 being the coefficient of determination of the fit, which ranges between 0 and 1; as R^2

approaches to 1, the quality of the fit improves), while the correlation between TD-CAM-B3LYP and TD-B3LYP absorption on-sets is much weaker (R^2 of 0.80). Not surprisingly the clearest outliers in the latter case are the absorption on-set values for $(TiO_2)_3$ and $(TiO_2)_{10}$ GM nanoparticles.

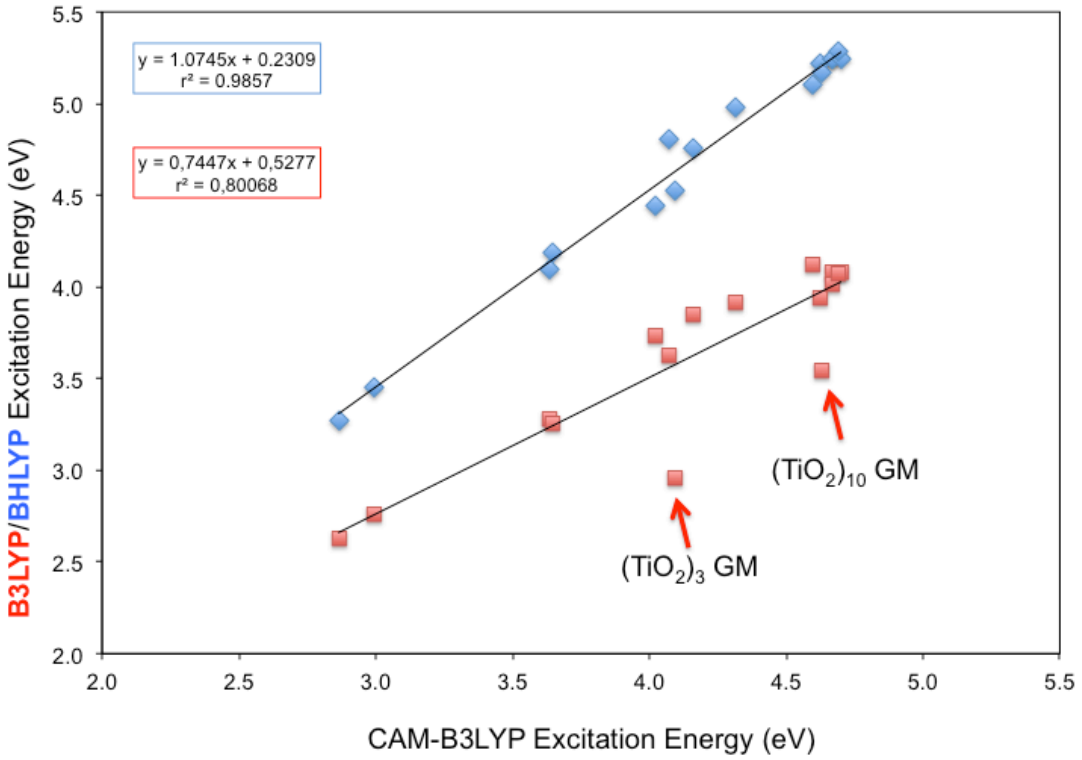

Figure 4.4 The TD-B3LYP and TD-BHLYP lowest excitation energies plotted against the TD-CAM-B3LYP values for all the $(TiO_2)_n$ naked nanoparticles investigated in this work. The BHLYP/CAM-B3LYP comparison is shown as blue diamonds, while the B3LYP/CAM-B3LYP comparison is shown as red squares. For both comparisons the trend line (black thin line), the expression and the r^2 correlation coefficient are shown on the graph. For the B3LYP/CAM-B3LYP comparison the two values that lie furthest from the trend line are highlighted.

As shown in Figure 4.5 also the trends for the next two excited states (the 2nd and 3rd lowest singlet excitations, S2 and S3) for the same set of nanoparticles were calculated. The trends found for these higher excited states are very similar to the ones observed for the lowest excited state shown in Figure 4.3. The two dips for the $(TiO_2)_3$ and $(TiO_2)_{10}$ structures are still there for the S2 and S3 states calculated with TD-PBE and TD-B3LYP. The S2 and S3 states for $(TiO_2)_3$ exhibit absorption intensities (as calculated with TD-B3LYP) one order of magnitude more intense than the lowest excitation, while for $(TiO_2)_{10}$ the S2 and S3 states have a weaker intensity than the S1 state.

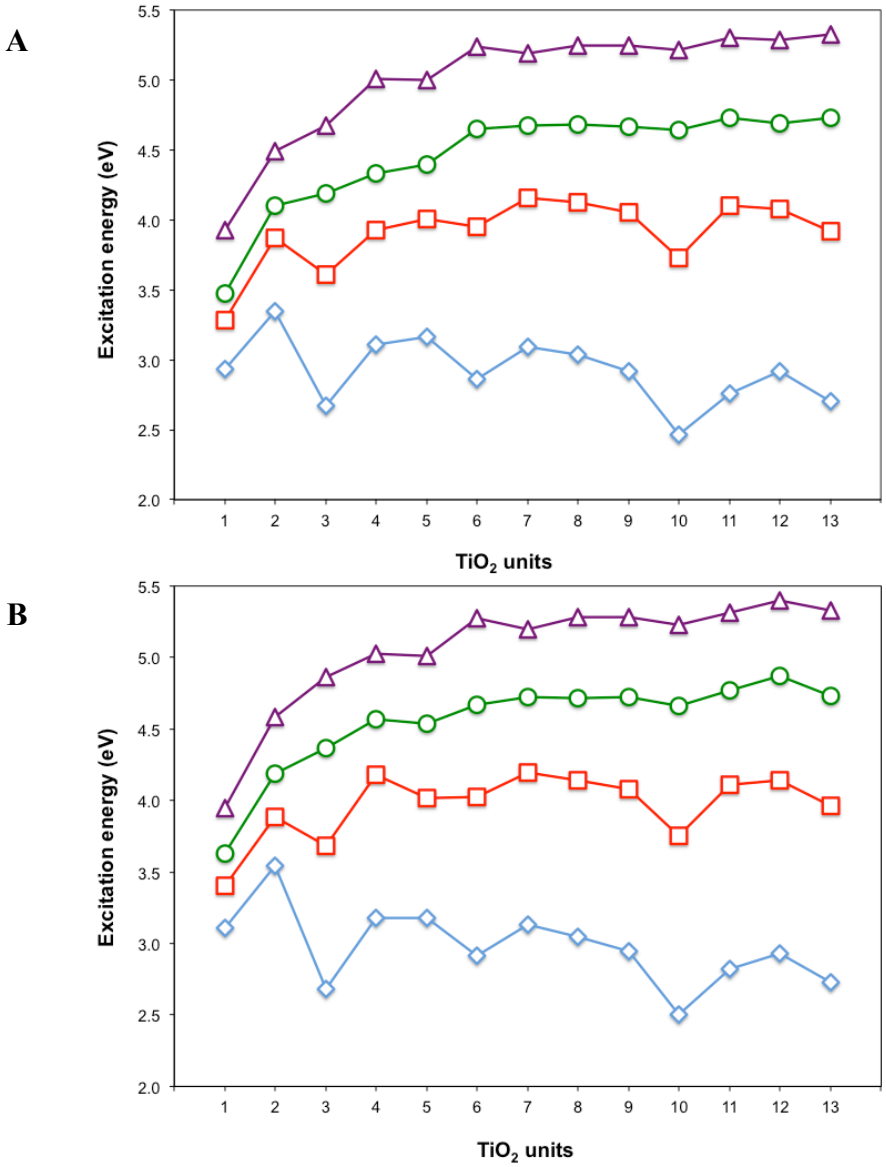

Figure 4.5 Trends for the 2nd (top, **A**) and 3rd (bottom, **B**) lowest excited state for the GM nanoparticles calculated with TD-DFT and different XC energy functionals. Cyan line and diamonds TD-PBE, red line and squares TD-B3LYP, green line and circles TD-CAM-B3LYP, purple line and triangles TD-BHLYP.

The underestimation of the excitation energies observed when using pure GGA XC energy functionals or hybrid XC energy functionals with a small HFLE contribution (e.g. B3LYP) is thus not limited to the lowest excited state, but it has an influence on higher energy states as well and therefore on the overall shape of the optical spectrum. In order to understand the size of this underestimation on the whole spectrum, the shape of the optical spectra calculated with different XC energy functionals for the anomalous $(TiO_2)_3$, $(TiO_2)_{10}$ and $(TiO_2)_6$ nanoparticles was also compared as shown in Figure 4.6 A-C (for all of the XC energy functionals employed only the 2-6 eV excitation range is shown).

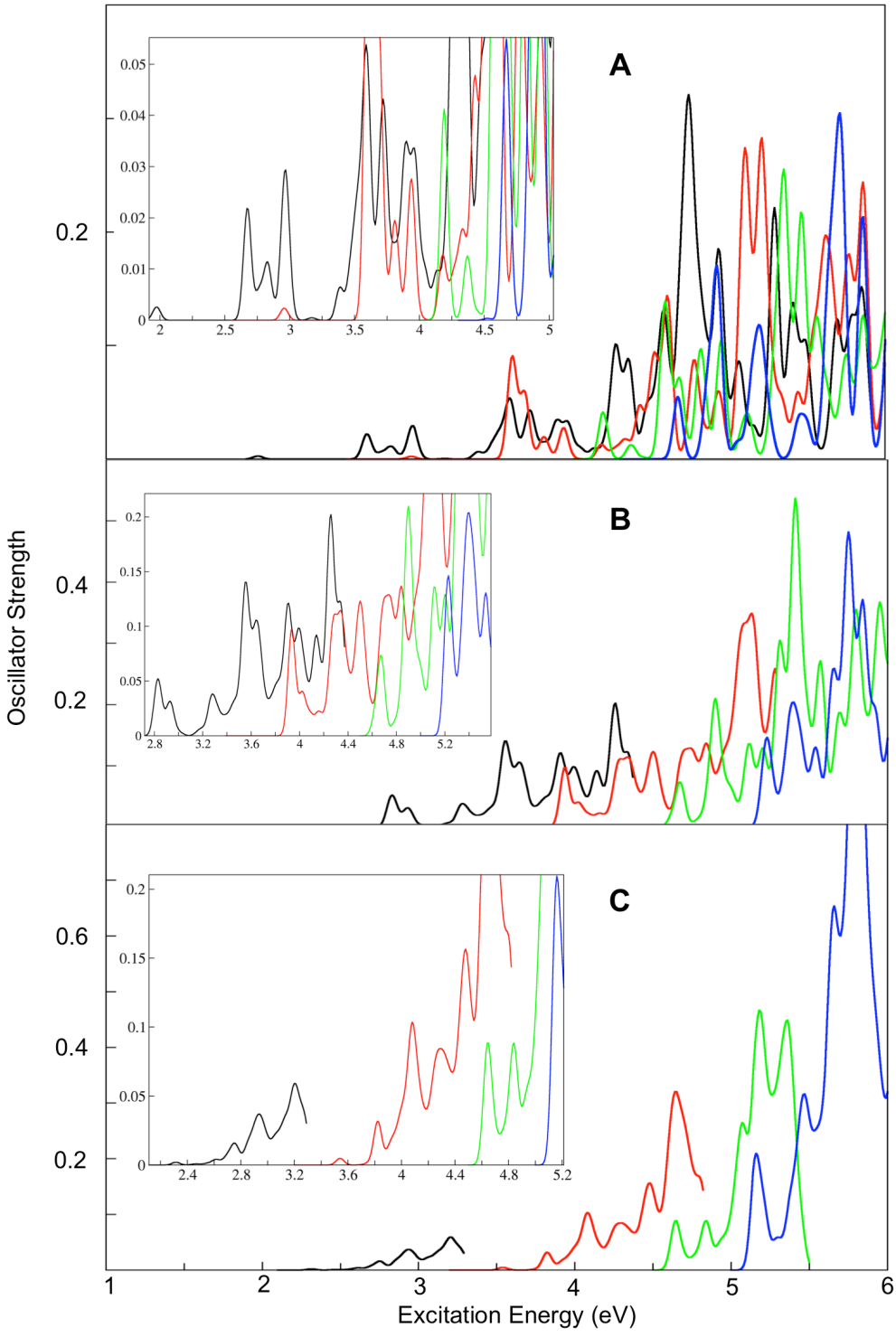

Figure 4.6 TD-DFT calculated optical spectra (100 lowest excitations, or 50 lowest in the case of TD-CAM-B3LYP for reasons of computational tractability) of (A) $(TiO_2)_3$ GM (B) $(TiO_2)_6$ GM and (C) $(TiO_2)_{10}$ GM optimised structures at the B3LYP/def2-TZVP level. In the left corner of each spectrum an insert is shown, where the low energy peaks are highlighted. The black line represents the TD-PBE results, the red line TD-B3LYP, the green line TD-CAM-B3LYP, while the blue line corresponds to the TD-BHLYP spectra. All excitations plotted are represented as Gaussians with a standard deviation of 0.03 eV.

The different shapes of the spectra for $(TiO_2)_3$ emphasise the influence of the chosen XC energy functional. TD-PBE and TD-B3LYP XC energy functionals predict a weak shoulder at low energies (1.97 and 2.96 eV, respectively), followed by an approximate 0.7 eV gap to the next peak. In the case of TD-CAM-B3LYP and TD-BHLYP no such large gap is observed and the most intense peaks, for both of these XC energy functionals, seem to roughly agree after being rigidly shifted by ~0.5 eV. When the TD-B3LYP spectrum is shifted upwards by ~1 eV and compared to the TD-CAM-B3LYP spectrum, it can be clearly seen that the two XC energy functionals show a poor agreement in the lower energy range of the spectrum, with B3LYP underestimating the first excitation energy and completely missing the lower energy features predicted by TD-CAM-B3LYP. The two XC energy functionals show a much better agreement at higher energies, and although the intensities do not match perfectly, all the peaks fall within the same range of energies. The TD-B3LYP, TD-CAM-B3LYP and TD-BHLYP calculated spectra for the n = 6 GM nanoparticle, after a rigid shift is applied, show a very good agreement on the position of the excitation peaks. A suitable shift could not be found in order to match the spectrum generated using the PBE XC energy functional. Finally, for the spectrum of the $(TiO_2)_{10}$ structure shown in Figure 4.6 C, as expected, a similar behaviour to the $(TiO_2)_3$ structure is observed. For example, the TD-PBE and TD-B3LYP calculated spectra show a very weak shoulder at lower energies, which, even after a rigid shift in energy, cannot be made to coincide with any of the peaks predicted by TD-CAM-B3LYP or TD-BHLYP.

4.3.2 TD-DFT vs EOM-CC for naked nanoparticles

As observed in the previous section, the lowest energy excitation for the $(TiO_2)_3$ and $(TiO_2)_{10}$ structures is described differently depending on the XC energy functional employed in the TD-DFT calculation. To define the accuracy of these TD-DFT results EOM-CC calculations were performed (some of the EOM-CC results are taken from Chapter 3). For reasons of computational tractability, this investigation is confined to particles of a similar size to the $(TiO_2)_3$ structure, introduced in the previous chapter. Because the GM $(TiO_2)_3$ nanoparticle exhibits a three-coordinated titanium atom and a three-coordinated oxygen atom, structural elements not present in the other GM for n = 1 – 5, metastable structures of two and three TiO_2 units reported in the literature, which have similar coordination environments for titanium and/or oxygen atoms to the $(TiO_2)_3$

nanoparticle, were also considered. One of these structures is the so-called *club* isomer, a $(TiO_2)_2$ isomer that is 0.73 eV (B3LYP/def2-TZVP) higher in energy than the $n = 2$ GM and a $n = 3$ isomer that lies 0.32 eV higher in energy than the $n = 3$ GM. The latter particle has a three-coordinated titanium atom, and in contrast with the trimer GM, no three-coordinated oxygen atoms. For completeness, TD-DFT and EOM-CC excitations for another $(TiO_2)_2$ isomer, which is the *cis* version of the *trans* GM and lies 0.25 eV higher in energy (B3LYP/def2-TZVP), were also compared. All of these structures are shown in Figure 4.1.

In Figure 4.7 and Figure 4.8 the four lowest excitation energies of the $(TiO_2)_2$ and $(TiO_2)_3$ global minima respectively, are plotted as a function of the chosen energy method combination; TD-DFT (B3LYP and CAM-B3LYP) and different flavours of EOM-CC; EOM-CCSD/TZ, EOM-CCSD/SV and EOM-CCSDT/SV. As discussed in Chapter 3, care should be taken when comparing absolute excitation energies, as the convergence with respect to basis-sets (TZ or better) and CC excitation level (EOM-CCSDT or better) are currently only numerically tractable for the smallest system studied (TiO_2 monomer), and even then supercomputing facilities are required. For this reason, in this chapter, I focus primarily on the relative ordering of the different excitations, exploiting the fact that these small nanoparticles are highly symmetric and the excited states thus span a number of different irreducible representations.

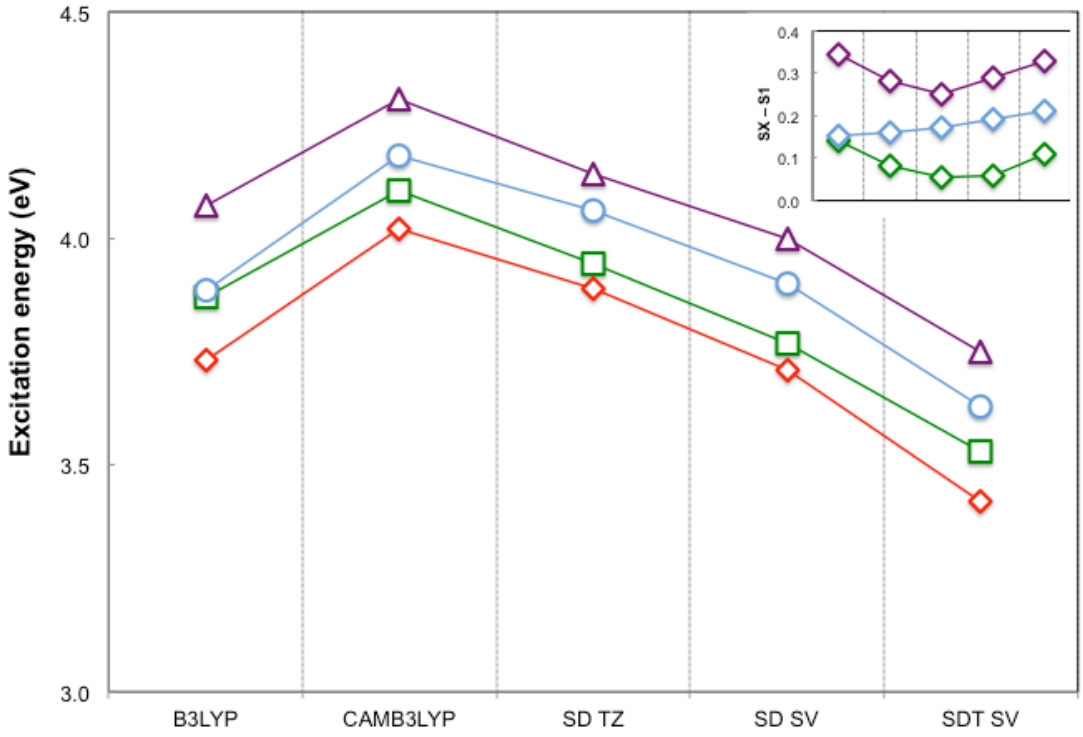

Figure 4.7 Trend in the four lowest excitation energies of the $(TiO_2)_2$ GM dimer as calculated with different method combinations (1^1B_g red diamonds, 1^1A_u green squares, 1^1B_u blue circles, and 2^1A_g purple triangles). SD and SDT stand for EOM-CCSD/T, while SV and TZ correspond to the def2-SVP and def2-TZVPP basis sets. All the TD-DFT calculations (B3LYP and CAM-B3LYP) employed the def2-TZVP basis set. All the EOM-CC data shown were taken from the results of Chapter 3. The insert shows, for all the methods employed, the difference between the higher excited states (e.g. S4, S3 and S2) compared to the lowest excited energy S1.

The $(TiO_2)_2$ GM case in Figure 4.7 is representative for most small particles. The same energetic ordering of the lowest excited states is observed for TD-DFT and the different EOM-CC flavours, with roughly similar spacing between the different excited states (except that the gap between the S2 and S3 excited states is much reduced for TD-B3LYP; this is clearly shown in the insert of Figure 4.7, where for each method the energy of the SX state was plotted against the energy of the lowest excited state S1). The $(TiO_2)_3$ data in Figure 4.8 paints, however, a different picture as there are a number of crossovers between the lowest excited states. For this case, I compare first the TD-B3LYP and TD-CAM-B3LYP results, which are, in line with the discussion above, very different. Not only is the energy difference between the S1 and S2 states reduced from 0.6 eV for TD-B3LYP to only 0.1 eV for TD-CAM-B3LYP, but the next couple of excited states also lie much closer in energy for TD-B3LYP than for TD-CAM-

B3LYP. Some of the higher lying excited states effectively become degenerate in the case of TD-B3LYP, and show a different ordering than found with TD-CAM-B3LYP. The TD-CAM-B3LYP and all EOM-CC results, in contrast, are very similar (with the exception of an interchange between the close-lying S1/S2 states for both sets of EOM-CCSD results).

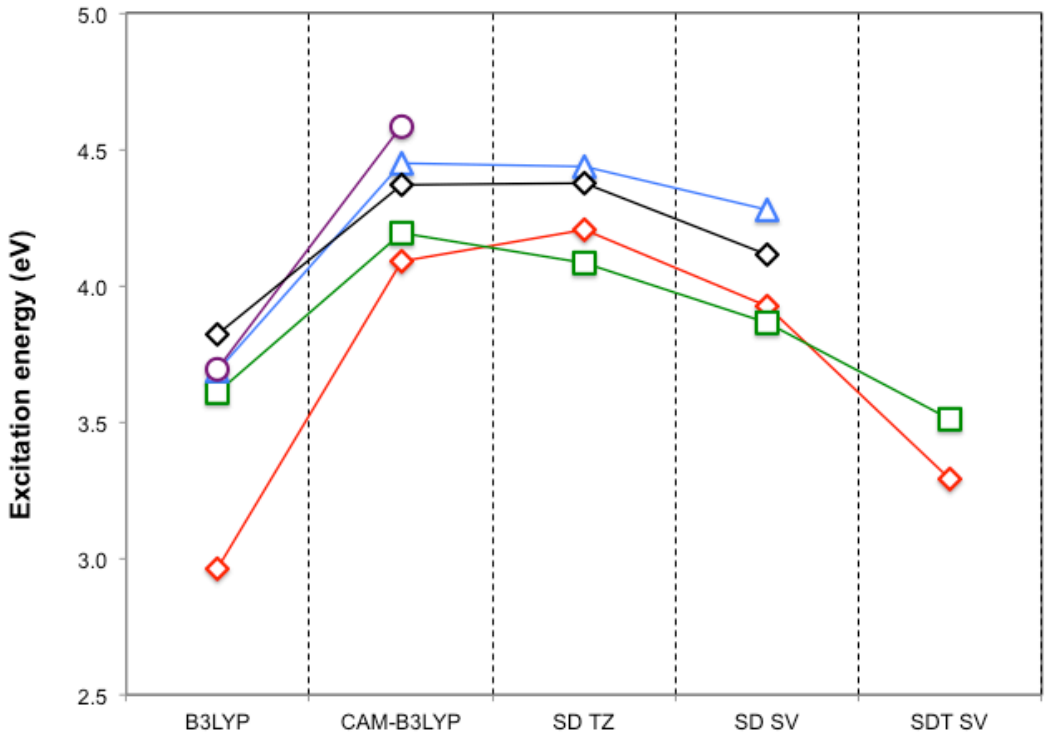

Figure 4.8 Trend in the five lowest excitation energies of the $(TiO_2)_3$ GM trimer as calculated with different method combinations (2^1A' red diamond, 1^1A" green square, 3^1A' blue triangle, 4^1A' purple circle and 2^1A" black diamond). SD and SDT stand for EOM-CCSD/T, while SV and TZ correspond to the def2-SVP and def2-TZVPP basis sets. All the TD-DFT calculations (B3LYP and CAM-B3LYP) employed the def2-TZVP basis set. All the EOM-CC data bar the EOM-CCSD TZ (SD TZ) excitation energies where taken from the results of Chapter 3.

Having compared the energies of different excited states of individual particles, I now compare, the excitation energies between the ground and lowest excited states for sets of nanoparticles. Again, calculations were performed with both TD-DFT (TD-B3LYP and TD-CAM-B3LYP) and EOM-CC methods (EOM-CCSDT/SV up to $(TiO_2)_3$, EOM-CCSD/TZ up to $(TiO_2)_4$, and EOM-CCSD/SV up to $(TiO_2)_5$). Figure 4.9 A shows the TD-DFT results and Figure 4.9 B and C the EOM-CCSD/T TZ and EOM-CCSD/T SV data respectively. Overall, TD-DFT and EOM-CC predict similar magnitudes of excitation energies as well as a similar ordering of the lowest excited states of the

different nanoparticles. For example, all methods employed here predict the same ordering of the lowest energy excitations of the dimer and monomer (*trans* > *cis* > *club* > monomer). TD-DFT and EOM-CCSD/SV also agree on where the lowest excitation energies of $(TiO_2)_4$ and $(TiO_2)_5$ global minima (diamonds in Figure 4.9) lie relative to that of the dimer. However, for the $(TiO_2)_3$ GM nanoparticle (diamond) the different methods give widely different results. TD-CAM-B3LYP predicts that the lowest excitation energy of the $(TiO_2)_3$ GM to be slightly higher than that for the $(TiO_2)_2$ GM (diamond). In contrast, TD-B3LYP places the $(TiO_2)_3$ GM lowest excitation in a similar energy range as the lowest excitation of the $(TiO_2)_2$ *club* isomer (triangle) and below the *alt* trimer (circle). EOM-CCSD/TZ and EOM-CCSD/SV in Figure 4.9 B and C respectively, predict that the lowest excitation energy of the $(TiO_2)_3$ GM lies slightly higher than that of the $(TiO_2)_2$ GM, while EOM-CCSDT/SV puts the lowest excitation energy of the $(TiO_2)_3$ GM slightly below that of the $(TiO_2)_2$ GM.

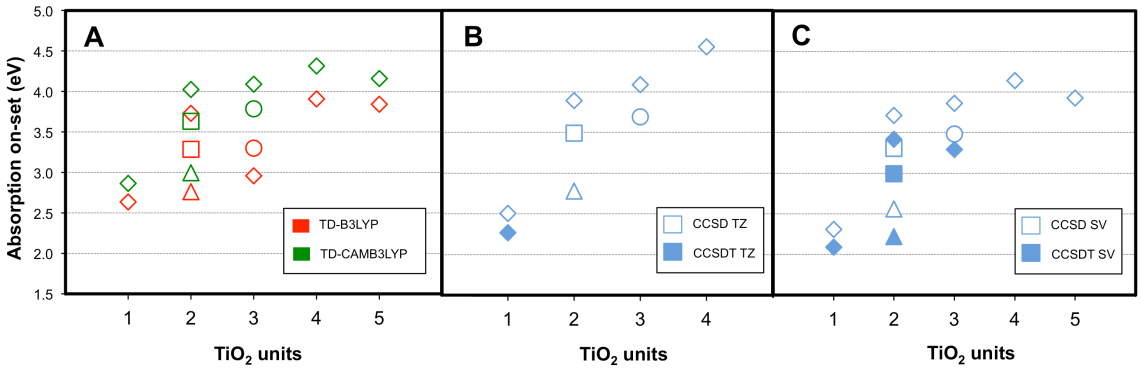

Figure 4.9 Comparison of TD-DFT excitation energies with EOM-CC results for a series of selected $(TiO_2)_n$ nanoparticles, with n = 1 - 5. The global minima (GM) are represented by diamond markers, the metastable *cis* and *club* dimers by squares and triangles, respectively, and the metastable trimer (*alt*) by circles. (A) Comparison of TD-CAMB3LYP (green markers) and TD-B3LYP (red) excitations. (B) Comparison between EOM-CCSD and EOM-CCSDT results with the high quality TZ basis set. (C) Comparison between EOM-CCSD and EOM-CCSDT results with the small SV basis set.

Overall, both in terms of the relative energies of different excitations of the nanoparticles and between different structures, EOM-CC calculations suggest that TD-DFT does a reasonable job in describing electronic excitations of TiO_2 nanoparticles. Although, XC energy functionals with no or low percentages of HFLE, such as PBE and B3LYP, struggle for specific structures. TD-CAM-B3LYP (and TD-BHLYP), in contrast, yield lowest excitation energies qualitatively consistent with EOM-CC for all structures studied. Finally, when considering absolute excitation energies, taking into account the caveats discussed above, those obtained with TD-CAM-B3LYP lie

generally quantitatively closest to the EOM-CC data. I, therefore, would recommend using this XC energy functional, where possible, to model excited state processes in TiO_2 nanoparticles.

4.3.3 The charge transfer character of the TD-DFT excitations

As already discussed in Chapter 2, it is well known that the use of standard XC energy functionals with no HFLE (i.e. GGA) or a low percentage of HFLE (i.e. B3LYP) in TD-DFT can result in the underestimation of charge transfer (CT) excitations, where the origin and final destination of the excited electron are separated spatially. It is tantalizing to suppose that this erroneous energetic stabilisation of CT states might be the origin of the discrepancy between TD-PBE and TD-B3LYP on one hand and TD-CAM-B3LYP, TD-BHLYP and EOM-CC on the other hand. Hence, it is important to try to characterise the CT character of the excitations for the different nanoparticles, as calculated with TD-DFT. In this section, the Λ diagnostic suggested by *Peach et al*. [49] is employed for this purpose. As already discussed in Chapter 2, this Λ diagnostic quantifies the spatial overlap between the occupied and virtual orbitals involved in the TD-DFT excitation, and hence is an estimate of the CT character of a specific excitation. The Λ value corresponds to a dimensionless number, which varies from 0 (no overlap between the occupied and virtual orbitals responsible for a TD-DFT excitation) to 1 (complete overlap between the occupied and virtual orbitals).

In the original paper by *Peach et al*. [49], it is suggested that a TD-DFT excitation with small Λ may be associated with large CT errors, while in contrast small CT errors are associated with large Λ. In this fashion, the authors suggest that, for example, TD-PBE excitations with $\Lambda < 0.4$ or TD-B3LYP excitations with $\Lambda < 0.3$ are likely to contain a significant error, while for TD-CAM-B3LYP essentially no correlation is observed between errors and spatial overlap, as measured by Λ [49]. These limits, however, have been obtained for a set of organic molecules, and to my knowledge no one has to date published similar thresholds for inorganic systems, e.g. metal oxides.

Figure 4.10 shows Λ values calculated with TD-B3LYP for the three lowest excitations obtained for the n = 1 - 13 GM $(TiO_2)_n$ nanoparticles. The Λ values were calculated also for the PBE, CAM-B3LYP and BHLYP XC energy functionals for all the GMs and the metastable isomers, those values not contained in Figure 4.10, will be commented in the text where necessary. For the lowest excited state (S1, blue diamonds in Figure

4.10), all of the TD-B3LYP Λ values lie below the threshold (0.30) defined by *Peach et al.* for hybrid XC energy functionals. However, among the TD-B3LYP calculated Λ values for the S1 state, perhaps not surprisingly, both the $(TiO_2)_3$ and $(TiO_2)_{10}$ GM nanostructures are clearly the lowest, with some other particles $(TiO_2)_7$, $(TiO_2)_{11}$, $(TiO_2)_9$ showing moderately low values as well. For the non-GM structures, the *alt* trimer has the lowest Λ value (0.14). Λ values for the higher excited states (S2 and S3), as shown in Figure 4.10, can be, depending on the particular structure, both larger and smaller than that of S1. Examples of nanoparticles with Λ values for higher excited states that lie below their S1 counterparts include $(TiO_2)_5$ (S2), $(TiO_2)_9$ (S2) and $(TiO_2)_{13}$ (S3).

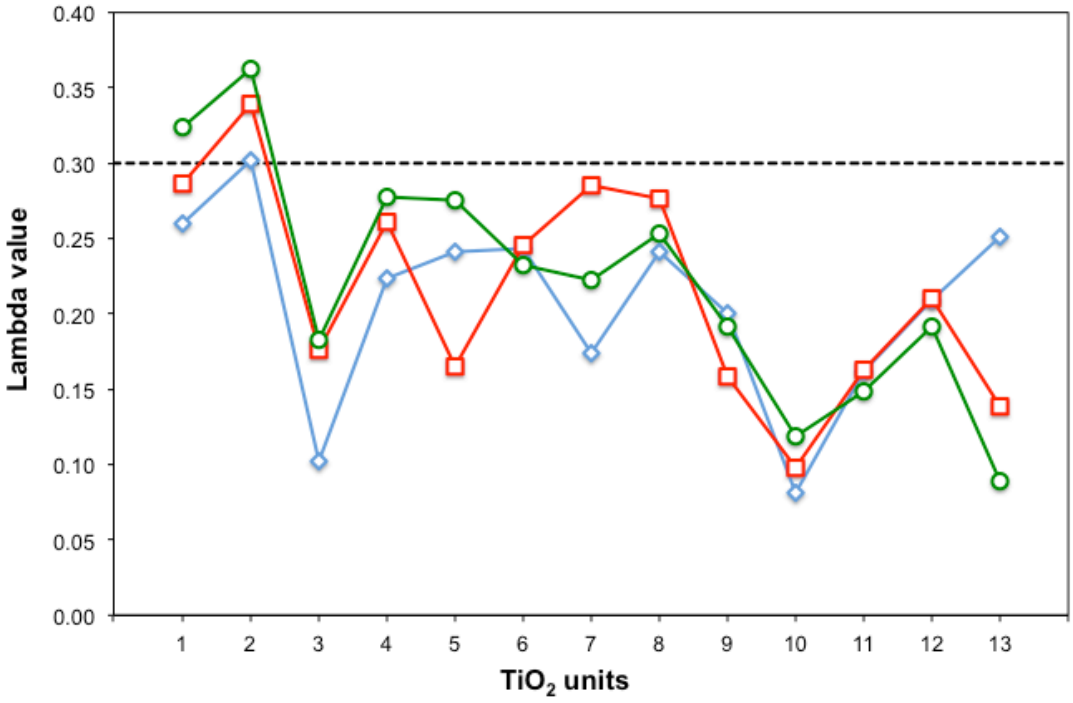

Figure 4.10 Λ values for the three lowest excited states (lowest state shown by blue diamonds, second lowest state by red squares and third lowest state by green circles) of $(TiO_2)_n$ nanoparticles, with n = 1 – 13, calculated with B3LYP XC energy functional. The dashed black line shows the Λ threshold defined by *Peach et al*. for organic systems.[49]

The Λ data for the titania nanoparticles yield a number of interesting observations. Firstly, all the Λ values for the TiO_2 structures are smaller than typical Λ values for organic systems, i.e. the TiO_2 nanoparticles consistently have a smaller overlap of the orbitals involved in the excitation. I believe that this arises from the fact that excitations in inorganic systems, such as TiO_2, typically involve the displacement of an electron from one sub-lattice (using the term lattice loosely) to another sub-lattice, here from

orbitals based on oxygen atoms to those based on titanium atoms. In such a scenario, even local excitations (i.e. excitations where both centres involved are spatially close) might have low Λ values, especially if the material is rather ionic and there is thus only limited overlap between orbitals on either sub-lattice. The good qualitative fit between the TD-DFT and EOM-CC results for excitations with Λ values between 0.15 and 0.3, strongly suggests that these are not excitations which are badly described by XC energy functionals due to CT related problems. A more interesting observation is that the excitations of which the description is problematic with TD-PBE and TD-B3LYP, both relative to that in TD-CAM-B3LYP and TD-BHLYP and to that by EOM-CC, are the same excitations that have very low Λ. This observation suggests that the reason why the description of these specific excitations is problematic within TD-PBE and TD-B3LYP is that they have an especially strong CT character and hence the states involved are erroneously stabilised, i.e. lie lower in energy relative to the S0 ground state than they should be.

This erroneous stabilisation is not limited to the lowest excitation. For example, as outlined above, the second excitation (S2) of the $(TiO_2)_5$ structure has a rather low Λ value, substantially lower than that of S1 and S3, and it is interesting to compare in this context the predictions of TD-B3LYP with those obtained with other methods. The S2 excited state in TD-B3LYP belongs to the A" irreducible representation (just as S0 and S1, and hence it can be labelled as the 3^1A" state), while in EOM-CC (and in TD-CAM-B3LYP and TD-BHLYP) S2 belongs to the A' irreducible representation (the 1^1A' state) and S3 in contrast is the 3^1A" state. This swap in the energetic ordering of the lowest two states is probably a direct result of the erroneous CT related stabilisation of the 3^1A" state in TD-B3LYP, which shifts it below the 1^1A' state.

4.3.4 The microscopic picture

A close inspection of the atomic structures of the nanoparticles studied, the orbitals involved in the excitations and the ground state/excited state density differences, suggests that the problematic CT excitations typically involve one or more singly coordinated oxygen atoms as the origin of the excited electron and hence the location of the formed hole. The structural fragment on which the excited electron localises varies and can be, for instance, a titanium atom with nominally only three oxygen atoms in its first coordination sphere (as found for the $(TiO_2)_3$ GM and $(TiO_2)_2$ *club* structures, see

Figure 4.11) or a fragment constituted of three four-coordinated titanium atoms surrounding a common three-coordinated oxygen atom (as found for the $(TiO_2)_{10}$ GM structure, see Figure 4.12 A. The specific case of $(TiO_2)_{10}$ example represents a potentially misleading case, where even if the Λ value is extremely low, 0.081, the excited state density difference shown in Figure 4.12 A exhibits an overlap between the hole, blue density and the electron, green density. However, a careful analysis of the leading orbital contributions to the TD-B3LYP excitation, shown in Figure 4.12 B, suggests that the overlap between electron-hole is completely fictitious as the hole, HOMO-2 and HOMO, clearly localise on different regions of the molecule when compared to the electron, LUMO). The presence of these structural fragments, however, is no guarantee that the lowest excitations will have CT character. This is illustrated, for example, by the case of the $(TiO_2)_2$ *club* isomer (see Figure 4.11). This structure has both a singly coordinated oxygen atom and a triply coordinated titanium atom, but its lowest three excitations all have reasonable TD-B3LYP Λ values (0.23, 0.24 and 0.24 for S1, S2 and S3, respectively) and their TD-B3LYP excitation energies qualitatively agree with EOM-CC results.

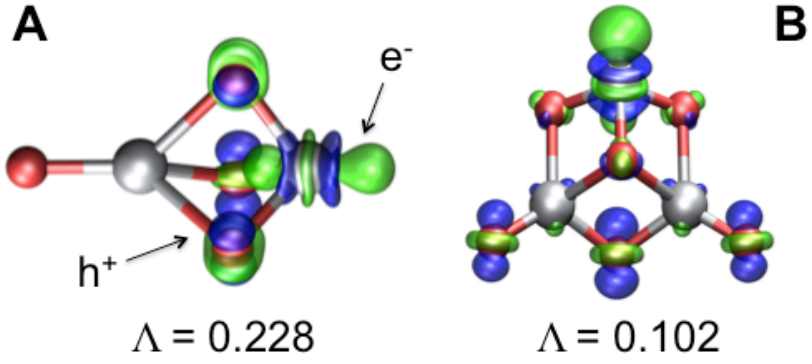

Figure 4.11 TD-B3LYP lowest singlet excited state density difference and Λ value obtained for (A) the *club* dimer and (B) the GM trimer. In both pictures the green lobes represent regions of excess electron density (where the excited electron component of the excited state is located, e^-), whereas the blue lobes, represent regions deficient in electron density (where the hole component is found, h^+).

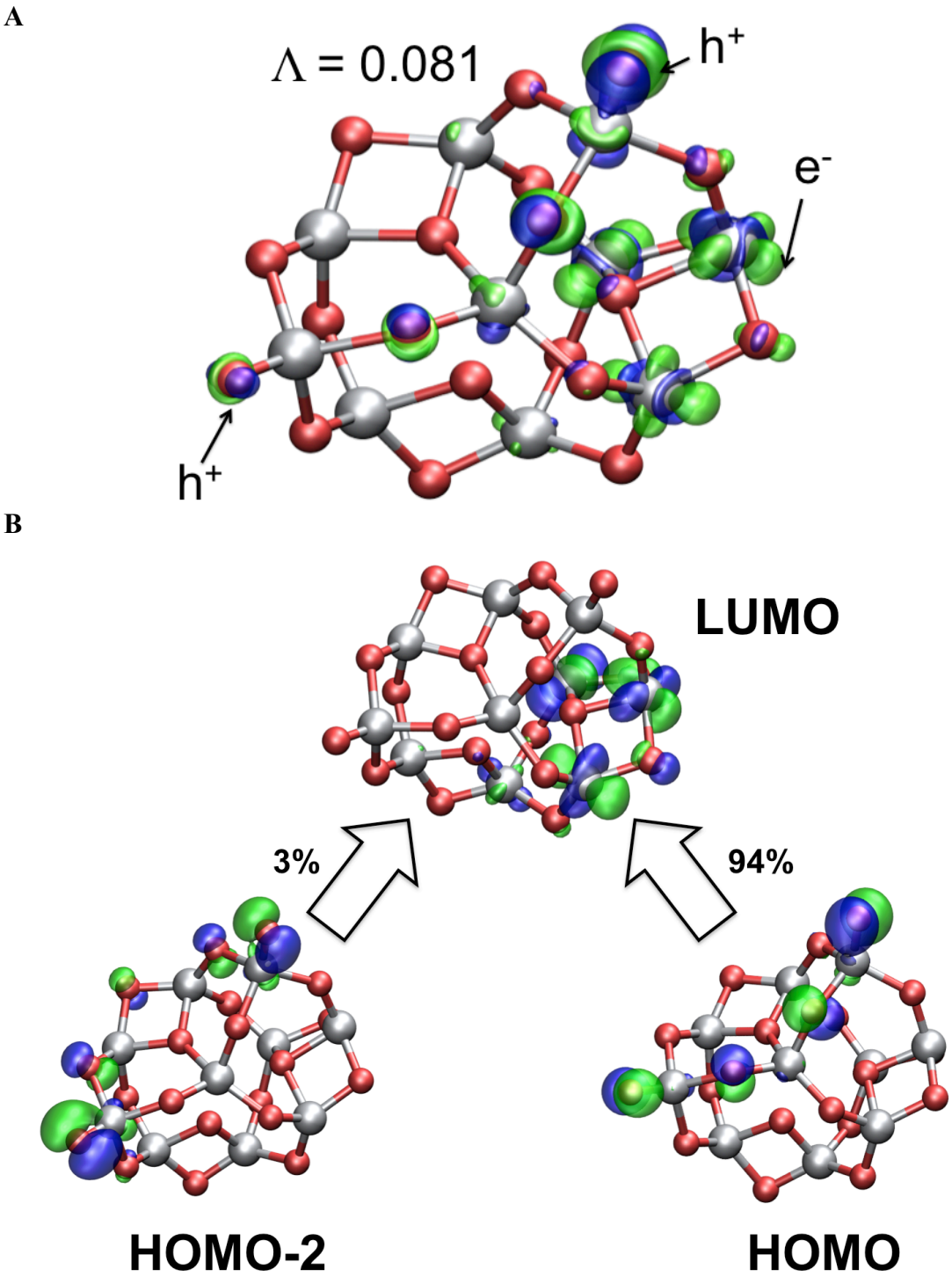

Figure 4.12 (A) TD-B3LYP lowest singlet excited state density difference and Λ value obtained for the $(TiO_2)_{10}$ structure. The green lobes represent excess regions of electron density (where the excited electron component of the excited state is located, e^-) whereas the blue lobes represent regions deficient in electron density (where the hole is found, h^+). **(B)** Leading B3LYP orbital contribution to the lowest TD-B3LYP singlet excited state excitation. The isodensity plots for the orbitals are calculated at a value of 0.05 a.u., where the green and blue lobes represent the sign of the wavefunction. The probability of each transition is defined in %.

When rationalising the above observations, a choice has to be made between a semi-ionic or a semi-covalent reference frame. In the latter reference, one can think of low-energy excitations as the transfer of an electron between two well-defined centres that deviate electronically and structurally from the bonding pattern in the remainder of the particle. In contrast, in the semi-ionic reference the "centres" involved in low-energy excitations are much less well-defined and importantly much less obvious upon inspections. The hole and electron component of an excitation could be smeared out over a number of ions, with the precise ions involved (i.e. localisation sites) governed by a subtle interplay between the on-site electrostatic potential (the energetic cost of adding or removing an electron from a specific ion) and the electrostatic interaction between the excited electron and the remaining hole (i.e. the exciton binding energy). Intuitively, the latter picture seems closer to what it is observed for $(TiO_2)_n$ nanoparticles. The wide range of first coordination Ti-O distances in the particles, and the fact that the Ti-O distances for the singly coordinated oxygen atoms is always virtually the same (1.6 Å), independent of the coordination number of the nearest titanium atom, also suggests that the semi-ionic reference frame is the most apt description of TiO_2 nanoparticles. While in this picture it is relatively difficult to link structure to excitations, there is one important thing that can be noted. While singly coordinated oxygen atoms have generally the lowest on-site electrostatic (or Madelung) potential and are the centres from which an electron gets removed if one does a single-point calculation for the cation, this does not mean, however, that it will be involved in the lowest energy excitation (or more generally in low energy excitations). For example, for $(TiO_2)_4$ the first two lowest excitations do not involve the singly coordinated oxygen atoms, while for $(TiO_2)_5$ only the second excitation (with TD-B3LYP, see discussion in section 4.3 and Figure 4.13) involves the singly coordinated oxygen atom. The lowest excitation of the $(TiO_2)_2$ *club* dimer, also, does not involve the singly coordinated atom (see Figure 4.11). The hole and excited electron in this case are localised in close proximity, maximising excited electron-hole overlap (Λ) and minimizing the charge-transfer character of the excitation. Clearly there is thus a subtle balance between the on-site electrostatic potential and the electrostatic interaction between electron and hole, where the latter in practice is sufficiently strong to change which parts of the nanoparticles are involved in low energy excitations.

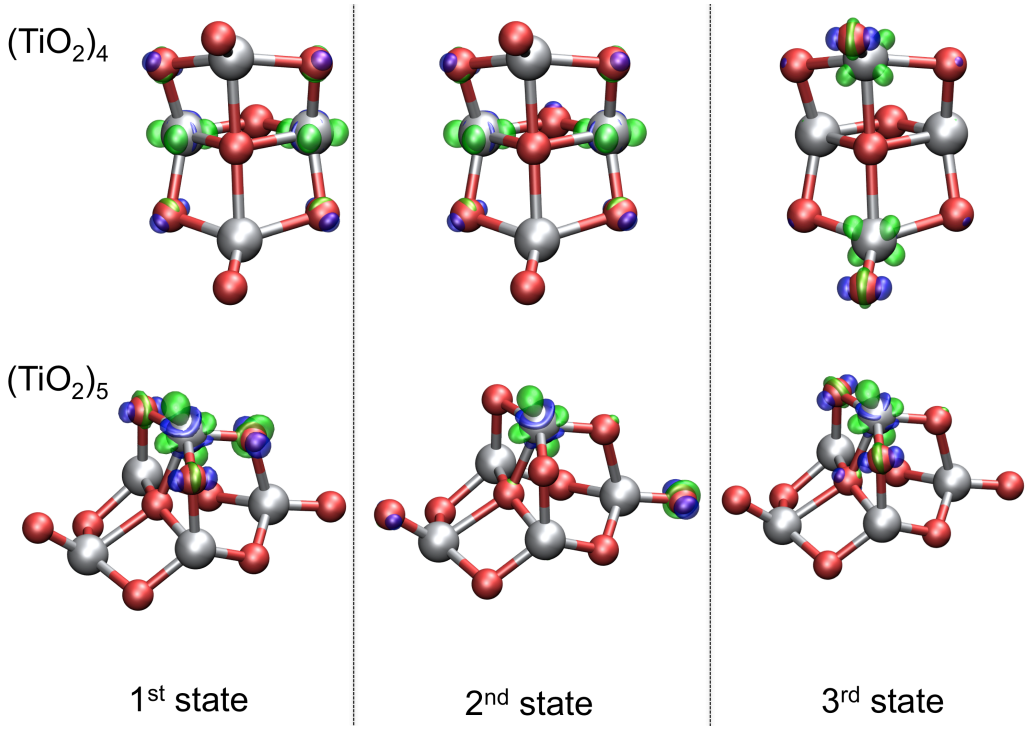

Figure 4.13 TD-B3LYP calculated excited state density difference for the 1st, 2nd and 3rd lowest singlet states for the $(TiO_2)_4$ and $(TiO_2)_5$ GM nanoparticles. In all the structures the green lobes represent the excess of electron density (e^-), whereas the blue regions picture the deficiency of electron density (h^+ or hole). The isodensity plots for the excited state density difference are calculated at a value of 0.02 a.u.

Taking into account the discussion above, it is likely that the location of excited electron and hole will change during excited state processes that involve nuclear displacement (e.g. relaxation see Chapter 5). As a result the electronic character of an excitation, its Λ value, and the ability of TD-DFT to correctly describe the excitation might also change.

4.3.5 Hydrated nanoparticles; TD-DFT vs. EOM-CC

Upon hydration, all the centres discussed above (i.e. singly coordinated oxygen atoms and under-coordinated titanium atoms) are saturated by the addition of hydroxyl groups ($–OH^-$) and protons (H^+). Hydration is strongly exothermic (e.g. -250 kJ/mol for H_2O) in the case of $(TiO_2)_2$, in line with previous estimates from the literature [50]. As structural and electronic features of the naked systems are modified, so are the orbitals involved in the optical excitation. In Figure 4.14 the comparison between the TD-B3LYP, TD-CAM-B3LYP and EOM-CCSD def2-SVP absorption on-set for a series of hydrated $(TiO_2)_n(H_2O)_m$ systems, is presented, where n and m range from 1 – 3. The addition of water to the naked nanoparticles results in a blue shift of their optical spectra. Figure 4.14 also shows, in line with the discussion above, how the CAM-B3LYP

excitations always lie at higher energies than their B3LYP counterparts, with a mean difference of 0.29 eV. It is important to notice that, unlike with what is observed for specific naked structures (e.g. $(TiO_2)_3$ and $(TiO_2)_{10}$), there is generally good agreement between B3LYP and CAM-B3LYP excitations for all hydrated nanoparticles. In this case, the Λ values computed for the B3LYP excitations for the hydrated nanoparticles are generally higher than those calculated for the naked structures (excitation energies and calculated lambda diagnostics are shown in appendix A). Moreover, the TD-DFT results with both XC energy functionals show a generally good agreement with those obtained using EOM-CCSD/SV, with an average absolute difference of 0.27 eV for B3LYP and 0.20 eV for CAM-B3LYP. Hydration thus seems to effectively remove the centres responsible for the problematic CT excitations, and more importantly, suggests that TD-B3LYP in general will give good results for hydrated systems.

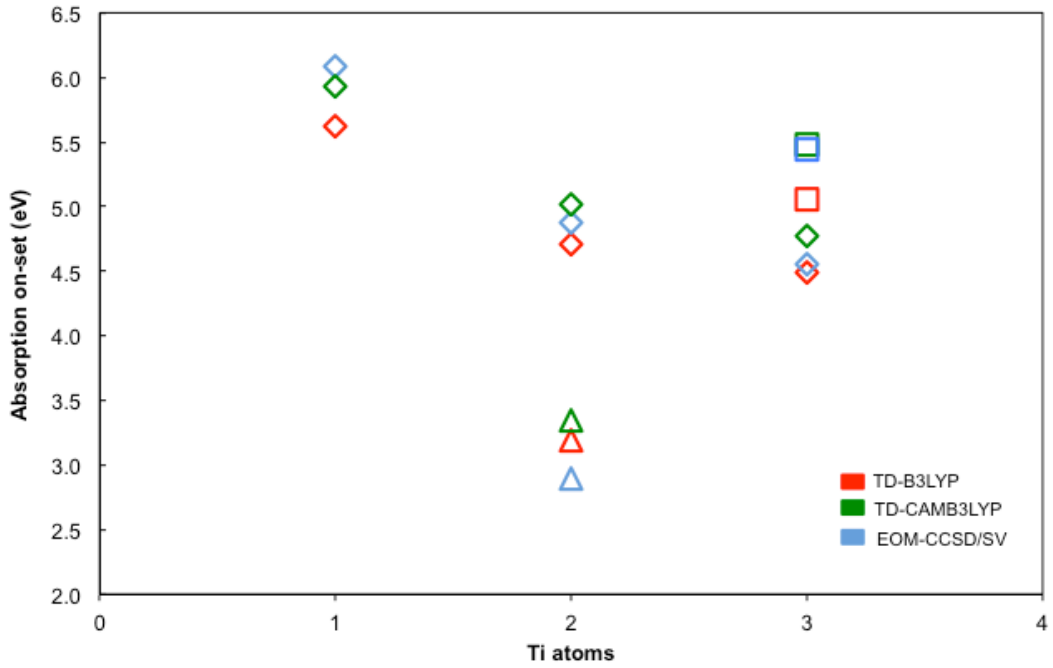

Figure 4.14 Comparison between TD-DFT (B3LYP, red markers and CAM-B3LYP, green markers) lowest singlet excitations and EOM-CCSD def2-SV(P) (blue markers) for hydrated $(TiO_2)_n(H_2O)_m$ particles, where n and m range between 1 and 3. The diamond markers represent the $Ti(OH)_4$, $(TiO_2)_2(H_2O)_2$ and $(TiO_2)_3(H_2O)_2$ structures respectively, the triangle marker the $(TiO_2)_2H_2O$ particle, and the square the $(TiO_2)_3(H_2O)_3$ nanostructure.

4.4 Conclusions

In this chapter, the suitability of TD-DFT to describe low-energy excitations in TiO_2 nanoparticles was investigated through a comparison with the results of EOM-CC quantum chemistry calculations. TD-DFT generally gives a good qualitative and also, in the case of TD-B3LYP and TD-CAM-B3LYP, a quantitative fit to excitation energies predicted by the more accurate, but computationally much more expensive EOM-CC method. However, for selected particles, e.g. $(TiO_2)_3$ GM structure, large deviations from EOM-CC results were observed when using the TD-PBE and TD-B3LYP XC energy functionals. Calculation of Λ diagnostic, which provides a measure of the orbital overlap between the orbitals involved in the excitation, and visual inspection of the excited state density differences in these cases, suggests that problems arise for these systems when computing charge-transfer excitations, the energy of which relative to local excitations is underestimated by TD-PBE and TD-B3LYP. Such problems are completely absent for TD-CAM-B3LYP and TD-BHLYP. Based on this and the overall good quantitative fit of TD-CAM-B3LYP and EOM-CC results, the use of this XC energy functional is suggested when studying excitations in TiO_2 nanoparticles, where possible. Finally, hydration of these particles removes the structural centres responsible for the problematic charge-transfer excitations and all XC energy functionals studied here yield a good qualitative fit to EOM-CC results for hydrated particles.

4.5 References

[1] Taylor, D. J.; Paterson, M. J. *J. Chem. Phys.* **2010**, *133*, 204302.
[2] Lin, C.-K.; Li, J.; Tu, Z.; Li, X.; Hayashi, M.; Lin, S. H. *R. Soc. Chem. Adv.* **2011**, *1*, 1228.
[3] Taylor, D. J.; Paterson, M. J. *Chem. Phys.* **2012**, *408*, 1.
[4] Persson, P.; Bergstrom, R.; Lunell, S. *J. Phys. Chem. B* **2000**, *104*, 10348.
[5] Di Valentin, C.; Pacchioni, G.; Selloni, A. *Phys. Rev. B* **2004**, *70*, 85116.
[6] Li, S.; Dixon, D. A. *J. Phys. Chem. A* **2008**, *112*, 6646.
[7] De Angelis, F.; Fantacci, S.; Selloni, A. *Nanotechnology* **2008**, *19*, 424002.
[8] Rocca, D.; Gebauer, R.; De Angelis, F.; Nazeeruddin, M. K.; Baroni, S. *Chem. Phys. Lett.* **2009**, *475*, 49.
[9] Blagojevic, V.; Chen, Y. R.; Steigerwald, M.; Brus, L.; Friesner, R. A. *J. Phys. Chem. C* **2009**, *113*, 19806.
[10] Shevlin, S. A.; Woodley, S. M. *J. Phys. Chem. C* **2010**, *114*, 17333.
[11] Chiodo, L.; Maria Garcia-Lastra, J.; Iacomino, A.; Ossicini, S.; Zhao, J.; Petek, H.; Rubio, A. *Phys. Rev. B* **2010**, *82*, 45207.
[12] Wang, T. H.; Fang, Z.; Gist, N. W.; Li, S.; Dixon, D. A.; Gole, J. L. *J. Phys. Chem. C* **2011**, *115*, 9344.
[13] Auvinen, S.; Alatalo, M.; Haario, H.; Jalava, J. P.; Lamminmäki, R. J. *J. Phys. Chem. C* **2011**, *115*, 8484.
[14] Marom, N.; Moussa, J. E.; Ren, X.; Tkatchenko, A.; Chelikowsky, J. R. *Phys. Rev. B* **2011**, *84*, 245115.
[15] Zhang, J.; Hughes, T. F.; Steigerwald, M.; Brus, L.; Friesner, R. A. *J. Am. Chem. Soc.* **2012**, *134*, 12028.
[16] Li, J.; Wang, H.; Persson, P.; Thoss, M. *J. Chem. Phys.* **2012**, *137*, 22A529.
[17] Nunzi, F.; Mosconi, E.; Storchi, L.; Ronca, E.; Selloni, A.; Grätzel, M.; De Angelis, F. *Energy Environ. Sci.* **2013**, *6*, 1221.
[18] Scanlon, D. O.; Dunnill, C. W.; Buckeridge, J.; Shevlin, S. A.; Logsdail, A. J.; Woodley, S. M.; Catlow, C. R. A.; Powell, M. J.; Palgrave, R. G.; Parkin, I. P.; Watson, G. W.; Keal, T. W.; Sherwood, P.; Walsh, A.; Sokol, A. A. *Nature Materials* **2013**, *12*, 798.
[19] Galynska, M.; Persson, P. *Int. J. Quantum Chem.* **2013**, *113*, 2611.
[20] Kasha, M. *Farad. Discuss.* **1950**, *9*, 14.
[21] Zwijnenburg, M. A. *Nanoscale* **2011**, *3*, 3780.
[22] Zwijnenburg, M. A.; Illas, F.; Bromley, S. T. *Phys. Chem. Chem. Phys.* **2011**, *13*, 9311.
[23] Zwijnenburg, M. A.; Sousa, C.; Illas, F.; Bromley, S. T. *J. Chem. Phys.* **2011**, *134*, 64511.
[24] Zwijnenburg, M. A. *Nanoscale* **2012**, *4*, 3711.
[25] Zwijnenburg, M. A. *Phys. Chem. Chem. Phys.* **2013**, *15*, 11119.
[26] Zwijnenburg, M. A.; Sokol, A. A.; Sousa, C.; Bromley, S. T. *J. Chem. Phys.* **2009**, *131*, 34705.
[27] Zhang, R.-Q.; De Sarkar, A.; Niehaus, T. A.; Frauenheim, T. *Phys. Status Solidi. B* **2012**, *249*, 401.
[28] Wang, Y.; Zhang, R.; Frauenheim, T.; Niehaus, T. A. *J. Phys. Chem. C* **2009**, *113*, 12935.
[29] Wang, X.; Zhang, R. Q.; Lee, S. T.; Frauenheim, T.; Niehaus, T. A. *Appl. Phys.*

Lett. **2008**, *93*, 243120.
[30] Sundholm, D. *Phys. Chem. Chem. Phys.* **2004**, *6*, 2044.
[31] Hamad, S.; Catlow, C. R. A.; Woodley, S. M.; Lago, S.; Mejias, J. A. *J. Phys. Chem. B* **2005**, *109*, 15741.
[32] Qu, Z. W.; Kroes, G. J. *J. Phys. Chem. B* **2006**, *110*, 8998.
[33] Calatayud, M.; Maldonado, L.; Minot, C. *J. Phys. Chem. C* **2008**, *112*, 16087.
[34] Marom, N.; Kim, M.; Chelikowsky, J. R. *Phys. Rev. Lett.* **2012**, *108*, 106801.
[35] Syzgantseva, O. A.; Gonzalez-Navarrete, P.; Calatayud, M.; Bromley, S.; Minot, C. *J. Phys. Chem. C* **2011**, *115*, 15890.
[36] Chen, M.; Dixon, D. A. *J. Chem. Theory Comput.* **2013**, *9*, 3189.
[37] Chiodo, L.; Salazar, M.; Romero, A. H.; Laricchia, S.; Della Sala, F.; Rubio, A. *J. Phys. Chem.* **2011**, *135*, 244704.
[38] Perdew, J. P.; Burke, K.; Ernzerhof, M. *Phys. rev. Lett.* **1996**, *77*, 3865.
[39] Becke, A. D. *J. Chem. Phys.* **1993**, *98*, 5648.
[40] Yanai, T.; Tew, D. P.; Handy, N. C. *Chem. Phys. Lett.* **2004**, *393*, 51.
[41] Schafer, A.; Horn, H.; Ahlrichs, R. *J. Chem. Phys.* **1992**, *97*, 2571.
[42] Weigend, F.; Ahlrichs, R. *Phys. Chem. Chem. Phys.* **2005**, *7*, 3297.
[43] Ahlrichs, R.; Bar, M.; Haser, M.; Horn, H.; Kolmel, C. *Chem. Phys. Lett.* **1989**, *162*, 165.
[44] Schmidt, M. W.; Baldridge, K. K.; Boatz, J. A.; Elbert, S. T.; Gordon, M. S.; Jensen, J. H.; Koseki, S.; Matsunaga, N.; Nguyen, K. A.; Su, S. J.; Windus, T. L.; Dupuis, M.; Montgomery, J. A. *J. Comput. Chem.* **1993**, *14*, 1347.
[45] Lai, P.-W.; Zhang, H.; Rajbhandari, S.; Valeev, E.; Kowalski, K.; Sadayappan, P. In *Proceedings of the international conference on computational science, iccs 2012*; Ali, H., Shi, Y., Khazanchi, D., Lees, M., VanAlbada, G. D., Dongarra, J., Sloot, P. M. A., Eds. 2012; Vol. 9, p 412.
[46] Valiev, M.; Bylaska, E. J.; Govind, N.; Kowalski, K.; Straatsma, T. P.; Van Dam, H. J. J.; Wang, D.; Nieplocha, J.; Apra, E.; Windus, T. L.; de Jong, W. A. *Comp. Phys. Commun.* **2010**, *181*, 1477.
[47] Schrödinger The pymol molecular graphics system, version 1.4.1, schrödinger, llc; 2010
[48] Humphrey, W.; Dalke, A.; Schulten, K. *J. Mol. Graphics Modell.* **1996**, *14*, 33.
[49] Peach, M. J. G.; Benfield, P.; Helgaker, T.; Tozer, D. J. *J. Chem. Phys.* **2008**, *128*, 44118.
[50] Pandey, L. B.; Aikens, C. M. *J. Phys. Chem. A* **2012**, *116*, 526.

Chapter 5

Describing excited state relaxation and localisation processes in TiO_2 nanoparticles with TD-DFT

In this chapter, the description of excited state relaxation in naked and hydrated TiO_2 nanoparticles is investigated using EOM-CCSD and TD-DFT with three XC energy functionals; B3LYP, CAM-B3LYP and BHLYP. The differences in the predictions of TD-B3LYP, TD-CAM-B3LYP and TD-BHLYP are studied through investigation of structural changes and photoluminescence energy obtained from each XC energy functional.

The content of this chapter has been taken from the following published work:
Berardo, E.; Hu, H.-S.; van Dam, H. J. J.; Shevlin, S. A.; Woodley, S. M.; Kowalski, K.; Zwijnenburg, M. A. Describing Excited State Relaxation and Localisation in TiO_2 Nanoparticles Using TD-DFT. *J. Chem. Theory Comput.* **2014**, *10*, 5538-5548.
Regarding the results included in the following chapter, I have performed all the DFT/TD-DFT calculations and the EOM-CCSD calculations on the $(TiO_2)_2$ nanoparticle.

5.1 Introduction

TiO_2 is the archetypal water splitting photocatalyst and semiconductor material for dye-sensitised solar cells. As already mentioned in Chapter 1, in its use as a photocatalyst, absorption of light excites electrons from the valence band of the material to the conduction band, which leaves holes in the former and results in the creation of excited electron – hole pairs. These excitons can then, either directly or after having been ionised into "free" electrons and holes, reduce protons to hydrogen and oxidise water to oxygen. The excitons can, however, also annihilate or become trapped. Similar processes take place in dye-sensitised solar cells, where electrons are excited from the highest occupied molecular orbital to the lowest unoccupied molecular orbital of the dye and subsequently transferred to the semiconductor (i.e. titania), while the formed holes react with a redox mediator in solution.

In order to engineer and optimise photovoltaic applications of specific TiO_2 nanoparticles, it is crucial to properly understand the behaviour of both excitons and free charge carriers (free electrons, holes) in those systems. Therefore, for the potential of computational chemistry to be realised, one should be able to make relatively accurate predictions of not only the optical absorption spectra, as already discussed in Chapter 4, but also of the reduction potentials of the free charge carriers and excitons, as well as the energetics and the structural distortion associated with trapped excitons. Such properties require the calculation of not only vertical excited state energies but also the energies and geometries of relaxed excited states.

In this chapter, the work from Chapter 4 on vertical excitations is extended by exploring the effect of the choice of XC energy functional on the excited state relaxation processes and the nature of the lowest singlet excited state (S1) minima. Here, the S1 potential energy surface is explored in the downhill direction, as determined from the TD-DFT analytical gradients, in order to find the S1 minima in the so-called Frank-Condon region and, subsequently, characterise these minima in terms of their photoluminescence (PL) energy and Stokes' shift (Figure 5.1 A). In some cases also what appears to be conical intersections (CXs) are encountered, where the ground and excited state potential energy surfaces touch and the PL energy goes to zero (Figure 5.1 B).

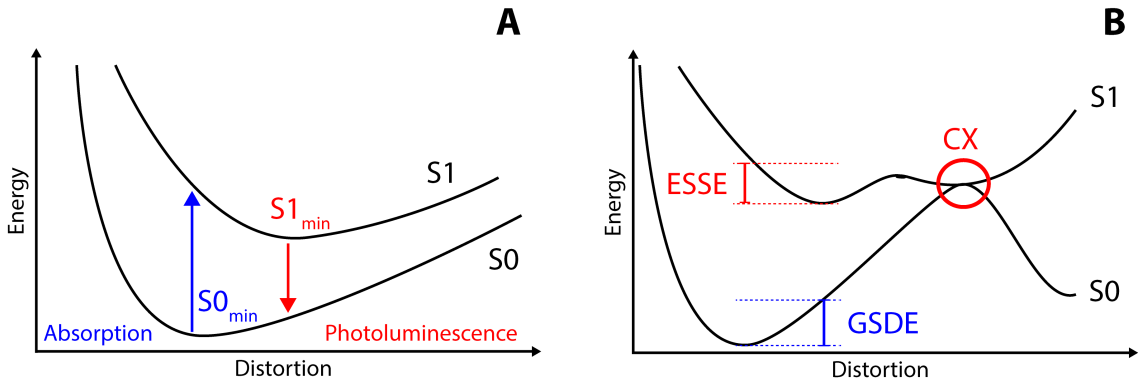

Figure 5.1 Cartoon of the ground (S0) and lowest excited state (S1) energy surfaces and special points there on for the case of absorption followed by photoluminescence (**A**) and a conical intersection (CX) where the two surfaces touch (**B**). Figure **B** also shows the Excited State Stabilisation Energy (ESSE) and the Ground state Destabilisation Energy (GSDE). Please note that in the case of the CXs found with TD-B3LYP, differently from what drawn in Figure **B**, there is no barrier separating the CX from the ground state geometry.

The TD-DFT calculations will be limited to TD-B3LYP, TD-BHLYP and TD-CAM-B3LYP; omitting TD-PBE, as the TD-PBE vertical excitations, (as already shown in Chapter 4), are by far the furthest away from the CC benchmarks. For the smaller $(TiO_2)_2$ particle, the predictions of TD-DFT will also be compared with EOM-CCSD [1,2]. Using this approach, it will be show that TD-CAM-B3LYP and TD-BHLYP make very similar predictions regarding the geometries and properties of the S1 minima of TiO_2 nanoparticles. Which, moreover, in the case of $(TiO_2)_2$ agree with results obtained using EOM-CCSD, whereas employing TD-B3LYP yields drastically different results. While the particles used in this study, $(TiO_2)_n$ with n = 1 – 10, are by necessity smaller than those studied experimentally, I believe that the methodological issue discussed here are independent of size-range.

5.2 Methodology

Following on from the previous chapter, the excited state properties of TiO_2 nanoparticles were studied using a combination of DFT and TD-DFT. The geometry of the lowest singlet excited state (S1) of each TiO_2 particle has also been relaxed using TD-DFT to obtain the S1 minimum energy geometry. Like in Chapter 4, also here I will be focusing on the lowest singlet excitation, as this state is the likely source of luminescence emitted by the nanoparticle as well as the state relevant to photocatalysis (in accordance with Kasha's rule, discussed in Chapter 1).

All the DFT/TD-DFT calculations are performed using the GAMESS US code (version 1st May 2013) and employ the def2-TZVP [3] basis set and a range of different XC energy functionals: the hybrid B3LYP and BHLYP XC energy functionals and the range-separated CAM-B3LYP XC energy functional. Differently from Chapter 4, where B3LYP optimised structures were employed for the calculation of the TD-DFT vertical excitations with the different XC energy functional, here, the same XC energy functional was used for geometry optimisation and the calculation of vertical excitations. For all the ground and excited state energy minimisations the convergence criteria for the maximum Cartesian component of the gradient is chosen to be equal to 1 x 10^{-4} Hartree $Bohr^{-1}$. For a sub-set of particles, the TD-DFT calculations were repeated using the Turbomole 6.5 code [4-7] in order to obtain the TD-B3LYP and TD-BHLYP excited state/ground state density difference plots. Such calculations gave the same geometries and (excitation) energies as obtained using GAMESS US.

For the specific case of the $(TiO_2)_2$ GM nanoparticle, both the S0 and S1 geometries were also relaxed with the EOM-CCSD. The EOM-CCSD calculations employed, for reasons of numerical tractability, the def2-SV(P) basis-set [8]. All EOM-CCSD were performed using the Tensor Contraction Engine (TCE) module of the NWChem 6.3 code [9].

The naked structures considered here consist in a subset (n = 1 – 10) of the tentative GM structures of $(TiO_2)_n$ particles already discussed in Chapter 4 and shown in Figure 4.1 A and B. A small number of hydrated particles is also considered here, see Figure 5.2, some of these structures were previously introduced in Chapter 4. For the graphic

representations of the $(TiO_2)_n$ nanoparticles and excited state/ground state density differences the VMD visualisation software was employed [10].

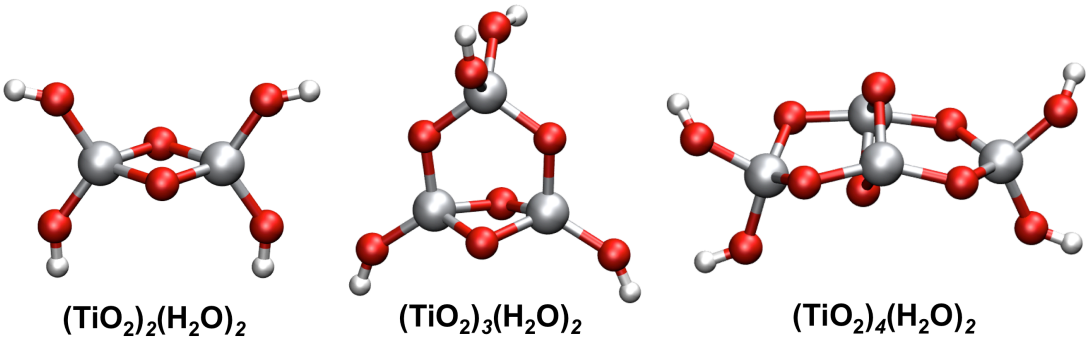

Figure 5.2 S0 minimum energy geometries for the $(TiO_2)_n(H_2O)_2$ hydrated structures obtained from the addition of a water molecule per singly coordinated oxygen atom in the originally naked particles. Red spheres denote oxygen atoms, whereas gray and white represent titanium and hydrogen atoms respectively.

5.3 Results

In this section the properties and character of the S1 minima obtained with the different XC energy functionals are compared, including differences in the predicted photoluminescence signature. For selected TiO_2 nanoparticles, I will focus in detail on the effect of the use of different XC energy functionals on the structural and electronic changes associated with the excited state relaxation responsible for the red shift between absorption and photoluminescence.

5.3.1 Photoluminescence and excited state relaxation

For each nanoparticle the geometry of the lowest singlet excited state (S1) was relaxed along a downhill path in order to find the S1 excited state minimum energy geometry. Subsequently, for each of the S1 minimum energy geometries, the harmonic frequencies were calculated in order to verify that the found stationary points indeed correspond to minima on the respective S1 potential energy surfaces. Figure 5.3 shows the trends in the PL energy with particle size for the different XC energy functionals and Figure 5.4 shows the trends in the Stokes' shift, the difference between the S1 vertical excitation (Figure 4.3, Chapter 4) and PL energy. Table 5.1, finally, contains the two contributions to the Stokes' shift; the excited state stabilisation energy (ESSE) and the ground state destabilisation energy (GSDE).

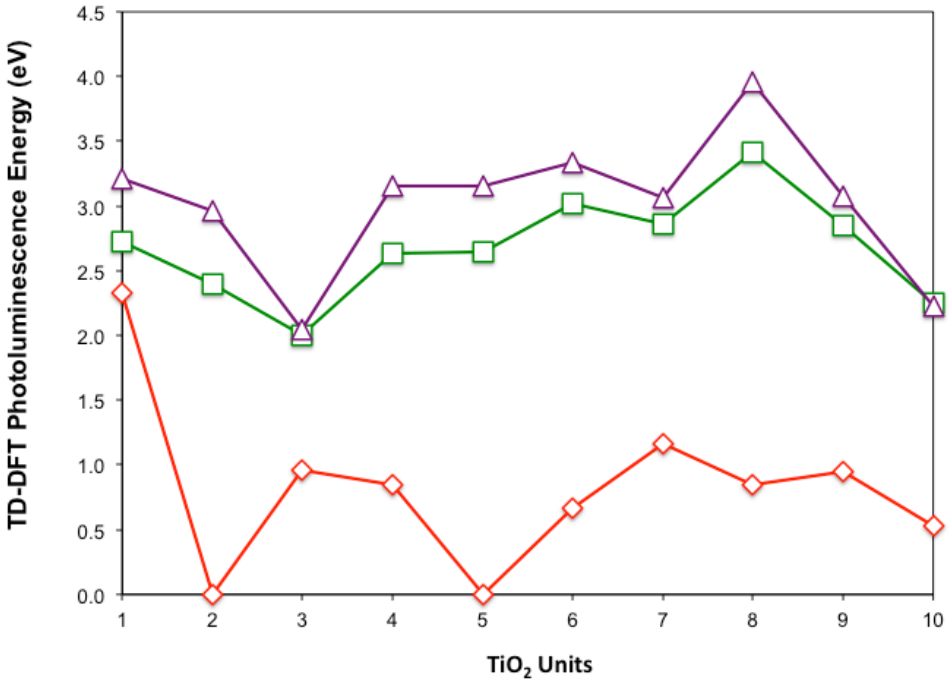

Figure 5.3 TD-DFT calculated photoluminescence energies for the naked $(TiO_2)_n$ particles; TD-B3LYP (red diamonds), TD-CAM-B3LYP (green squares) and TD-BHLYP (purple triangles). All values are in eV.

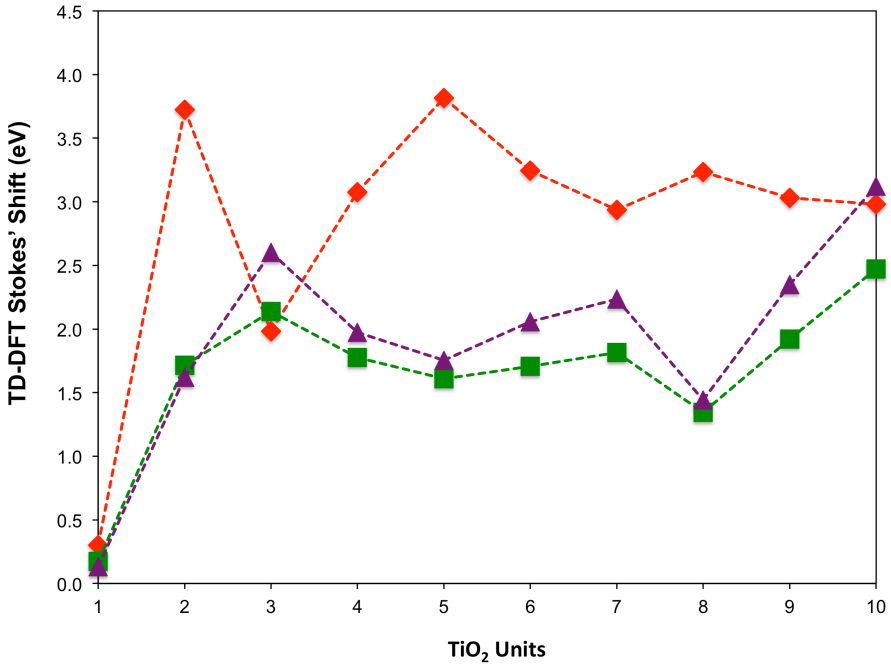

Figure 5.4 TD-DFT calculated Stokes' shift for the naked $(TiO_2)_n$ particles; TD-B3LYP (red diamonds), TD-CAM-B3LYP (green squares) and TD-BHLYP (purple triangles). All values are in eV.

From Figure 5.4 and Table 5.1 it is clear that all XC energy functionals predict that for all nanoparticles, with the exception of $(TiO_2)_1$ the relaxation on the S1 surface is associated by a significant Stokes' shift. This Stokes' shift is the result of both an energetic stabilisation of the excited state and a destabilisation of the ground state when going from the ground state geometry to the excited state minimum energy geometry. The ESSE and GDSE, shown in the cartoon in Figure 5.1 B, are as a rule of similar magnitude, where the latter in the case of TD-CAM-B3LYP and TD-BHLYP at least is generally slightly larger than the former.

Table 5.1 Lowest vertical excitation energy (EE), photoluminescence energy (PLE), excited state stabilisation energy (ESSE) and ground state destabilisation energy (GSDE) values as calculated with different XC energy functionals for the $(TiO_2)_n$ particles.[a]

TiO_2	TD-B3LYP				TD-CAMB3LYP				TD-BHLYP			
	EE	**PLE**	**ESSE**	**GSDE**	**EE**	**PLE**	**ESSE**	**GSDE**	**EE**	**PLE**	**ESSE**	**GSDE**
1	2.64	2.33	0.22	0.09	2.90	2.73	0.06	0.11	3.34	3.21	0.05	0.09
2	3.72	**0.00**	**0.35**	**3.37**	4.11	2.39	0.71	1.00	4.58	2.96	0.75	0.87
3	2.94	0.96	0.93	1.05	4.14	2.00	0.81	1.33	4.65	2.04	1.09	1.51
4	3.92	0.85	1.46	1.62	4.42	2.64	0.71	1.07	5.13	3.16	0.82	1.15
5	3.82	**0.00**	**0.44**	**3.38**	4.25	2.64	0.64	0.97	4.91	3.15	0.69	1.06
6	3.91	0.67	0.74	2.50	4.72	3.02	0.64	1.07	5.39	3.34	0.82	1.24
7	4.10	1.16	1.49	1.45	4.67	2.86	0.77	1.05	5.30	3.06	1.07	1.17
8	4.08	0.85	1.54	1.69	4.76	3.41	0.51	0.83	5.40	3.57	0.56	0.88
9	3.98	0.95	1.50	1.54	4.77	2.84	0.74	1.18	5.42	3.07	1.01	1.35
10	3.51	0.53	2.80	0.18	4.72	2.24	0.87	1.60	5.35	2.23	1.27	1.85

[a] *The TD-B3LYP results for both $(TiO_2)_2$ and $(TiO_2)_5$ structures shown in bold correspond to the energies calculated at the conical intersection between S1 and S0. All values are shown in eV.*

Comparing the predictions of TD-DFT calculations using the different XC energy functionals, it appears that the results obtained with TD-CAM-B3LYP and TD-BHLYP are very similar (average difference between predicted PL energies of 10%), whereas those from TD-B3LYP are substantially different (average difference of 70%). Just as the case for the vertical excitation energies in Chapter 4, the TD-BHLYP PL energies are generally shifted to higher values than their TD-CAM-B3LYP counterparts. The exception are two nanoparticles; $(TiO_2)_3$ and $(TiO_2)_{10}$, for which the TD-BHLYP and TD-CAM-B3LYP PL energies essentially coincide. Figure 5.4 demonstrates that the latter observation is related to the fact that while the TD-BHLYP and TD-CAM-B3LYP Stokes' shifts are overall very similar, the difference between the two XC energy functionals is the largest for $(TiO_2)_3$ and $(TiO_2)_{10}$. More generally, there appears to be

an inverse relationship between the difference in predicted Stokes' shift and the difference in predicted PL energy.

TD-B3LYP predicts, in contrast to TD-CAM-B3LYP and TD-BHLYP, not only much lower PL energies, as could naively have been expected on basis of what is observed for the vertical excitation energies (Figure 4.3, Chapter 4), but overall also much larger Stokes' shifts. The extent of TD-B3LYP relaxation thus appears to be much larger than that for the other XC energy functionals, suggesting that the effect of switching XC energy functional here goes beyond a simple rigid shift and that instead the TD-B3LYP S1 excited state minima are different in structure and/or chemical character than their TD-CAM-B3LYP and TD-BHLYP counterparts. As shown in Figure 5.3, when employing TD-B3LYP it is also predicted for two structures, $(TiO_2)_2$ and $(TiO_2)_5$, what appear to be conical intersections, not observed for TD-CAM-B3LYP and TD-BHLYP. EOM-CCSD/def2-SVP S1 relaxation for $(TiO_2)_2$, intractable for larger nanoparticles, yields an excited state minimum energy geometry that is similar in structure and properties to that found for TD-CAM-B3LYP and TD-BHLYP and distinctly different from that obtained with TD-B3LYP (see below). Finally, for two structures; $(TiO_2)_3$ and $(TiO_2)_{10}$, the Stokes' shift predicted by TD-B3LYP is nearly identical to that obtained using TD-CAM-B3LYP and TD-BHLYP. I believe this fit to be completely fortuitous. Moreover, as TD-B3LYP substantially underestimates the vertical excitation energies for these particles and predicts significantly lower PL values than TD-CAM-B3LYP and TD-BHLYP (differences in both cases > 1 eV), the successful prediction of Stokes' shift for these two particles is of little or no practical use.

5.3.2 Charge-transfer character

In Chapter 4 it was shown that TD-B3LYP struggles to describe vertical excitations of selected nanoparticles due to a spurious stabilisation of charge transfer states. In that case, the Λ diagnostic of Peach and co-workers [11] was employed to probe for such potentially problematic CT states. In Chapter 4 it was also found that vertical excitations of TiO_2 particles with a Λ diagnostic of 0.15 or less were severely underestimated [12].

In order to test if the extended excited state relaxation observed for TD-B3LYP is related to (changes in) the CT character of the lowest excited state, the S1 Λ diagnostic

was calculated for the S1 minimum energy structures (S1/S1). Table 5.2 compares the S1/S1 Λ diagnostic values with those calculated at the ground state minimum energy geometries (S1/S0). While Λ diagnostic values of all three of the XC energy functionals are given, we focus on those for TD-B3LYP as previous work [11,13] showed that only for TD-B3LYP (and GGA XC energy functionals) there appears to be a link between the value of the Λ diagnostic and the likeliness that the description of a particular excitation is problematic due to its CT character.

Table 5.2 Λ diagnostic values as calculated with TD-B3LYP, TD-CAM-B3LYP and TD-BHLYP both for $S1/S0_{min}$ (vertical excitations) and $S1/S1_{min}$ (photoluminescence energy, PLE) minimum energy structures. For all the nanoparticles studied only the lowest energy excited state minimum is shown in this table.[a]

TiO_2	$S1/S0_{min}$			$S1/S1_{min}$		
	B3LYP	**CAM-B3LYP**	**BHLYP**	**B3LYP**	**CAM-B3LYP**	**BHLYP**
1	0.26	0.26	0.25	0.24	0.26	0.25
2	0.30	0.29	0.28	(0.10)	0.20	0.22
3	0.10	0.18	0.10	0.15	0.13	0.12
4	0.22	0.27	0.27	0.17	0.24	0.26
5	0.24	0.24	0.23	(0.11)	0.23	0.22
6	0.25	0.31	0.30	0.13	0.29	0.27
7	0.19	0.32	0.29	0.15	0.27	0.24
8	0.24	0.33	0.33	0.14	0.29	0.36
9	0.19	0.29	0.28	0.13	0.32	0.31
10	0.08	0.27	0.22	0.10	0.16	0.16

[a]*The two values shown in brackets correspond to the structures for which a CX between S1 and S0 was observed. The Λ diagnostic values are dimensionless numbers.*

Table 5.2 shows that the TD-B3LYP Λ diagnostic decreases to values of 0.17 or lower when going from the ground state to the excited state minimum energy geometry. The exception are the two nanoparticles for which S1 already has a strong CT character at the ground state minimum energy geometry, $(TiO_2)_3$ and $(TiO_2)_{10}$, in which cases the Λ diagnostic values are found to slightly increase, and the monomer, for which the Λ diagnostic values stays approximately constant. For most particles, the CT character of the S1 states thus appears to increase during excited state relaxation. Moreover, after relaxation, the S1 Λ diagnostic value is now in almost all cases suggestive of potential problems in describing this state with TD-B3LYP due to its CT character ($\Lambda \leq 0.15$).

These low Λ diagnostic values are probably part of the origin of the large discrepancy between the predictions of TD-B3LYP and those obtained with TD-CAM-B3LYP and

TD-BHLYP observed above. Another, more perverse, related reason might be that CT states are spuriously stabilised by TD-B3LYP and that there is thus a fictitious energetic driving force during energy minimisation for a state, where possible, to increase its CT character. While it is hard to unequivocally demonstrate that this is happening for any of the TiO_2 nanoparticles, it is inline with the observation that for almost all particles the S1 Λ diagnostic value decreases in the case of TD-B3LYP during excited state relaxation. S1 Λ diagnostic values for other XC energy functionals than TD-B3LYP indeed show a small increase (e.g. $(TiO_2)_9$) or only a very minor decrease upon excited state relaxation for selected particles. Moreover, something very similar was observed in the case of an organic system (4-dimethylamino)benzonitrile) [14], where problems with describing CT excitations, in the case of low-HFLE XC energy functionals, also appear to drive the structure towards a spurious excited state minimum with a low Λ diagnostic value, which is furthermore structurally dramatically different from that found with TD-CAM-B3LYP and approximate CC theory (CC2).

5.3.3 (Electronic) structure of the predicted S1 minima

Having discussed overall trends in PL energy, Stokes' shift and CT character, I will now focus on the (TD-)DFT predictions for three specific nanoparticles; $(TiO_2)_2$, $(TiO_2)_3$ and $(TiO_2)_6$. These structures were specifically chosen as they represent interesting cases where the use of the different XC energy functionals results in different predictions for the properties of the vertical and/or relaxed excited states.

$(TiO_2)_2$ As discussed above, TD-B3LYP predicts what appears to be a conical intersection between S0 and S1 for $(TiO_2)_2$, while in the case of TD-CAM-B3LYP and TD-BHLYP S1 minima were obtained with photoluminescence energies of 2.39 and 2.96 eV respectively. Figure 5.5 compares the S0 and S1 minimum energy structures obtained with the different XC energy functionals and EOM-CCSD. All method combinations predict very similar C_{2h} S0 minima but make rather different predictions for the S1 minimum energy structures (even if the final symmetry is C_s in all cases).

In the case of TD-CAM-B3LYP, TD-BHLYP and EOM-CCSD the symmetry lowering to C_s is associated with an elongation of one of the two terminal Ti-O bonds and a flattening of the angle between the terminal oxygen atom in this Ti-O bond and the main Ti_2O_2 plane of the particle (i.e. the O-Ti-Ti angle). Figure 5.6, which displays the

density difference between S0 and S1 for the S0 and S1 minimum energy geometries for (TD-)B3LYP and (TD-)BHLYP, shows that in the case of TD-BHLYP this structural distortion is associated with a localisation of the hole and excited electron component of the excited state on the same side of the particle. The structure of the rest of the particle stays relatively unchanged compared to the structure of the ground state minimum energy geometry.

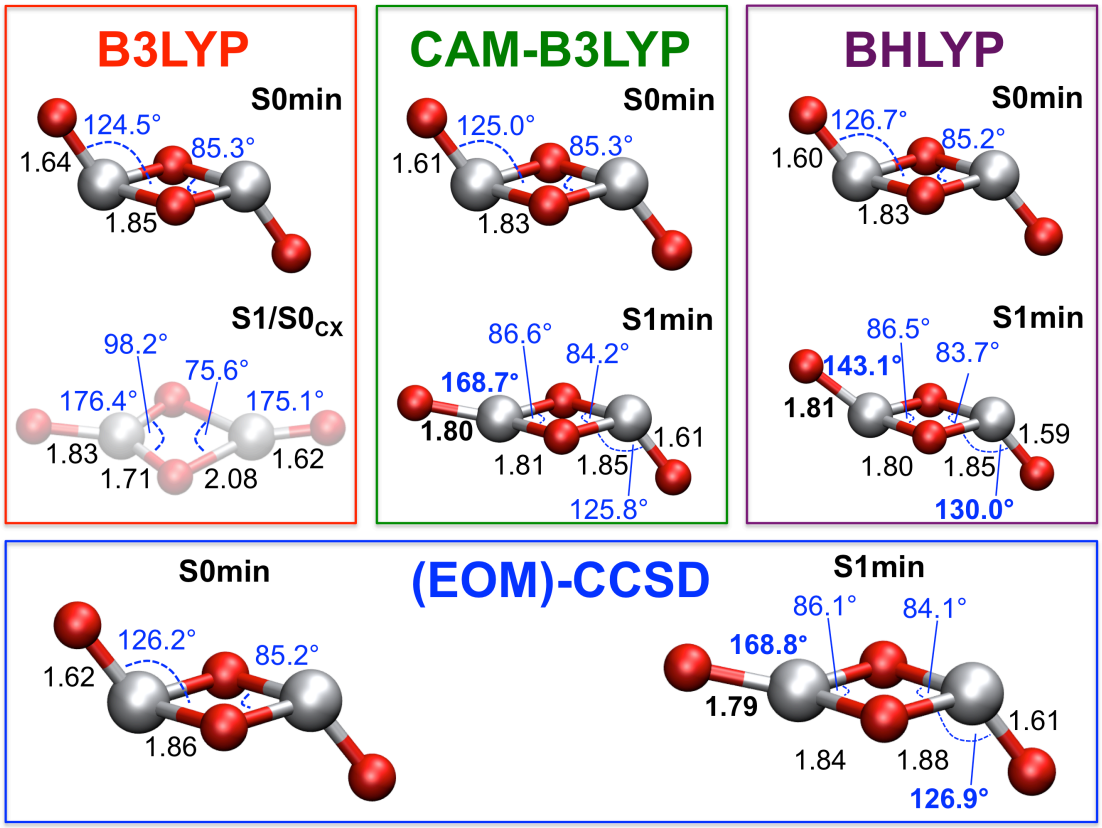

Figure 5.5 Comparison of the geometries of the ground (S0) and lowest excited state (S1) minimum energy structures for the tentative $(TiO_2)_2$ GM structure obtained with the different method combinations. TD-B3LYP S1/S0 CX structure is shown semi-transparent.

The structure of the TD-B3LYP S0/S1 conical intersection is very different from the S1 minimum energy geometries found by the other method combinations. After S1 excited state relaxation the structure of the whole particle is flattened. One of the terminal Ti-O bonds elongates to 1.83 Å and its O-Ti-Ti angle reaches approximately 176°. The length of the other terminal Ti-O bond stays roughly unchanged, while its O-Ti-Ti angle also increases from 124.5° in the ground state to approximately 175°. In line with this rather different S1 structure, Figure 5.6 shows that in the TD-B3LYP S0/S1 CX-structure the electron and hole components are localised on opposite sides of the nanoparticle instead

of on the same side, as seen for TD-BHLYP. It also explains the much larger CT character and rather low S1 TD-B3LYP Λ diagnostic value. Finally, the stronger elongation of the terminal Ti-O bond in the case of TD-B3LYP, relative to that seen by the other method combinations, is probably due to the fact that in the TD-B3LYP case the δ^+ (hole component of the excited state) charge does not sit on the titanium atom of the elongated terminal Ti-O bond.

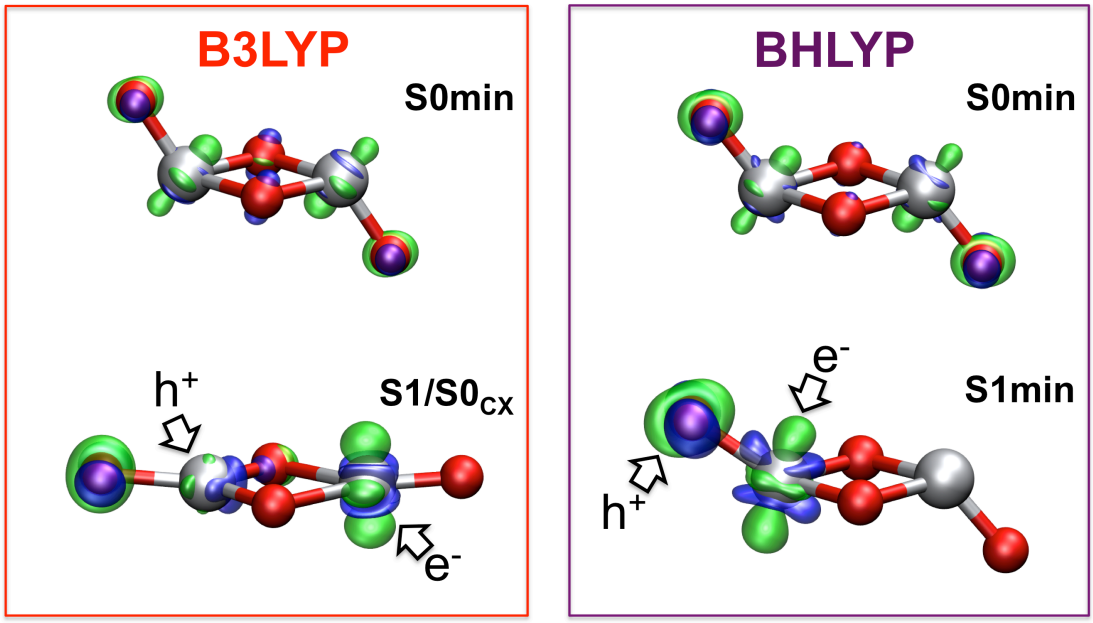

Figure 5.6 TD-B3LYP and TD-BHLYP excited state density difference plots obtained for the vertical (S_0/S_{0min}) and PL (S_1/S_{1min}) excitations of the $(TiO_2)_2$ GM structure. The isodensity plots for the excited state density are calculated at a value of 0.02 au, where the green lobes represent regions of excess electron density (where the excited electron component of the excited state is located, e^-), whereas the blue lobes represent regions deficient in electron density (where the hole component is found, h^+).

A similar analysis can be performed for the $(TiO_2)_5$ nanoparticle, which corresponds to the other case where TD-B3LYP predicts a CX between the S0 and S1 surfaces, whereas TD-CAM-B3LYP and TD-BHLYP find a stable S1 minimum.

$(TiO_2)_3$ In our previous work we found that the vertical S1 excitation at the ground state geometry of $(TiO_2)_3$ had strong CT character for all XC energy functionals considered. After excited state relaxation, we find here, as discussed above, for all XC energy functionals stable S1 minima with similar Stokes' shifts of ~2 eV. In line with these observations, Figure 5.7 shows that the S0/S1 density difference for the ground state minimum energy geometry is very similar for both TD-B3LYP and TD-BHLYP and

that the same holds for the S1 excited state minimum energy geometry. Both for the ground and excited state geometries, the density difference clearly shows that the S1 state is a CT state, involving both the 3-coordinated titanium atom (excited electron component of the excited state) and the two terminal oxygen atoms (hole component of the excited state). The excited state relaxation is associated with a localisation of the hole component of the excited state on one of the two terminal oxygen atoms. Figure 5.7 shows that this localisation is associated with an asymmetric distortion of the particle structure, including an elongation of 0.2 Å of the Ti-O bond involving the terminal oxygen atom on which the hole becomes localised.

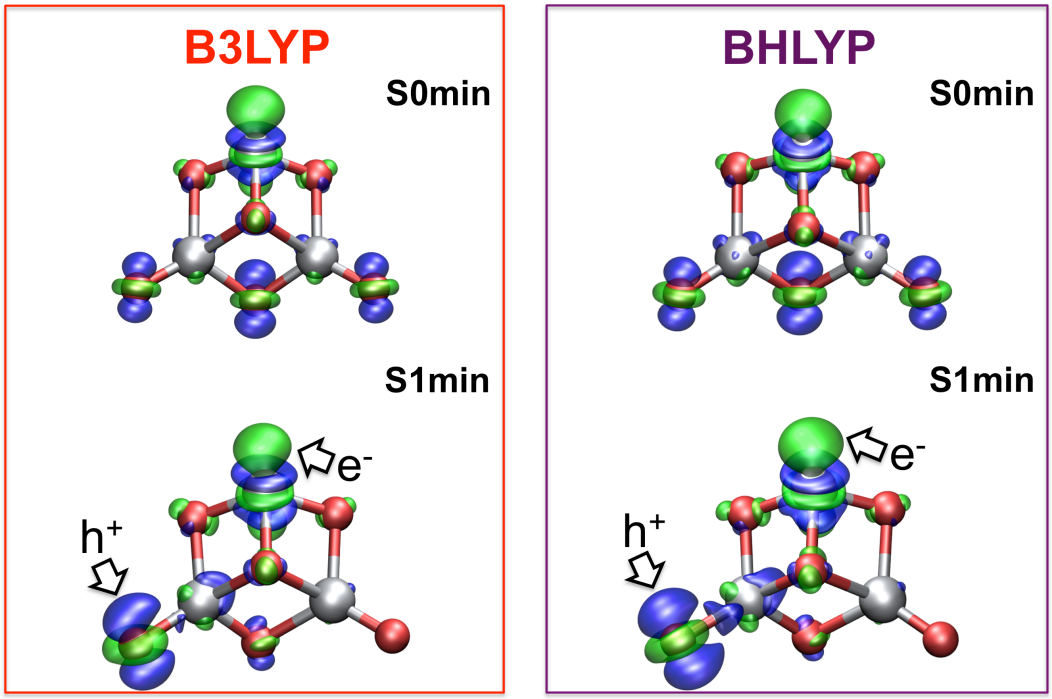

Figure 5.7 TD-B3LYP and TD-BHLYP excited state density difference plots obtained for the vertical (S_0/S_{0min}) and PL (S_1/S_{1min}) excitations of the $(TiO_2)_3$ GM structure. The isodensity plots for the excited state density are calculated at a value of 0.02 au, where the green lobes represent regions of excess electron density (where the excited electron component of the excited state is located, e^-), whereas the blue lobes represent regions deficient in electron density (where the hole component is found, h^+).

$(TiO_2)_6$ If the two structures for which we found the CXs are ignored, $(TiO_2)_6$ is the nanoparticle with the largest difference between the PL energy predicted by TD-B3LYP and that obtained with TD-CAM-B3LYP and TD-BHLYP. For TD-B3LYP, the S1 Λ diagnostic value also decreases strongly moving from the S1/S0 to the S1/S1 geometry, but shows only a slight reduction for TD-CAM-B3LYP and TD-BHLYP. It is,

therefore, not surprising that Figure 5.8 shows that S0/S1 density differences for both the ground and excited state minimum energy structures are completely different for TD-B3LYP and TD-BHLYP. For example, the hole component of the TD-B3LYP excited state involves one of the two terminal oxygen atoms, whereas for TD-BHLYP both the hole and excited electron components of the excited state are localised on the center of the nanoparticle. The relaxed structures shown in Figure 5.8 are, as a result, also substantially different.

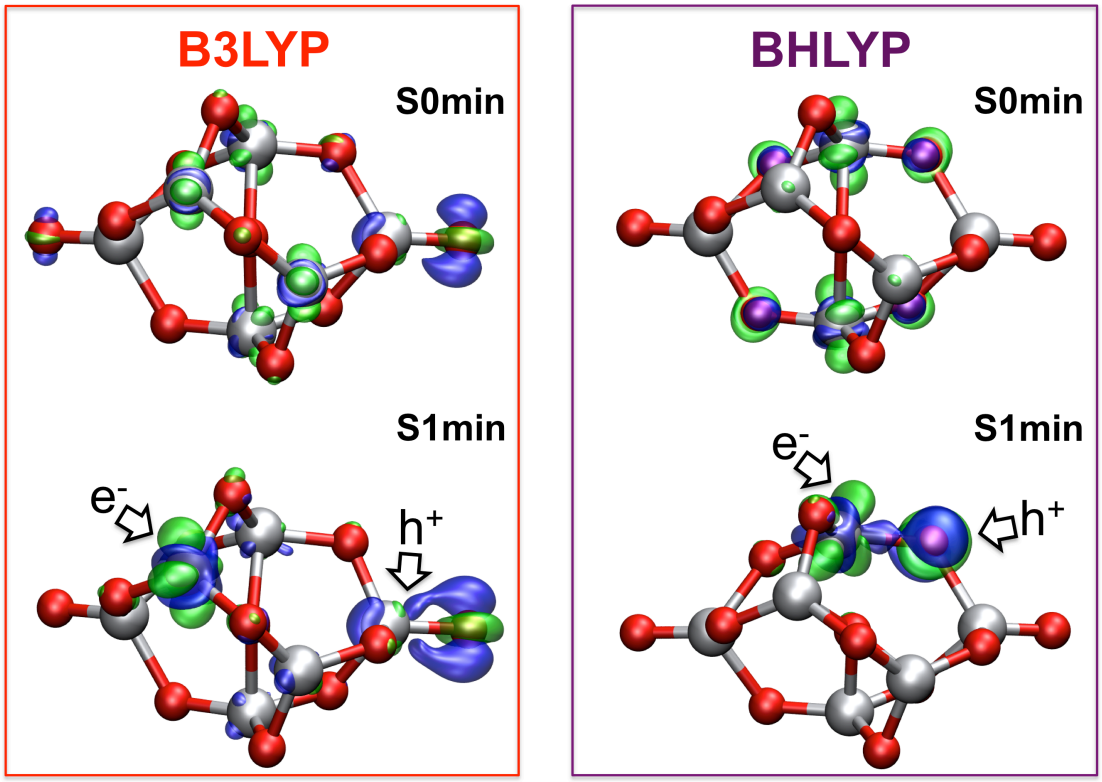

Figure 5.8 TD-B3LYP and TD-BHLYP excited state density difference plots obtained for the vertical (S_0/S_{0min}) and PL (S_1/S_{1min}) excitations of the $(TiO_2)_6$ GM structure. The isodensity plots for the excited state density are calculated at a value of 0.02 au, where the green lobes represent regions of excess electron density (where the excited electron component of the excited state is located, e^-), whereas the blue lobes represent regions deficient in electron density (where the hole component is found, h^+).

5.3.4 Hydrated particles

Finally, excited state relaxation is also considered for the case of hydrated structures. In Chapter 4 was found that TD-B3LYP in general appears to predict reasonable vertical excitation energies for hydrated systems. I believe this is due to the fact that hydration saturates the coordination of the under-coordinated atoms, e.g. terminal oxygen atoms,

that otherwise give rise to CT states, see Figure 5.9.

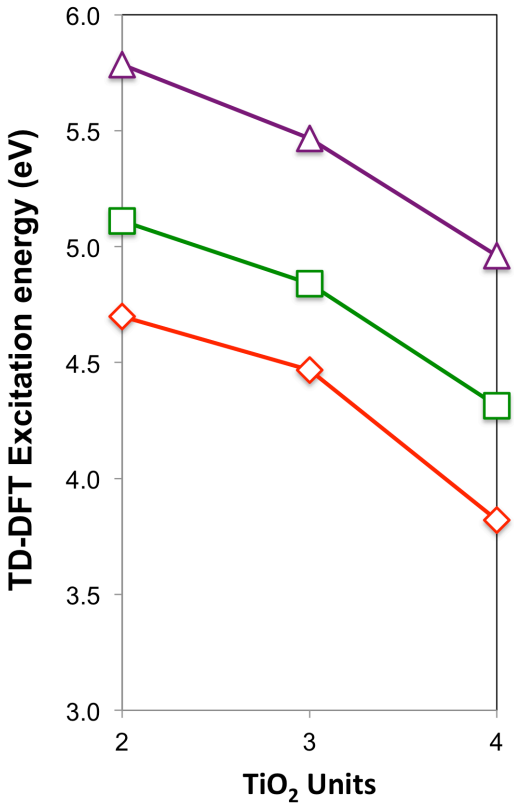

Figure 5.9 TD-DFT lowest vertical excitation energies for the hydrated particles obtained with the different XC energy functionals: TD-B3LYP (red diamonds), TD-CAM-B3LYP (green squares) and TD-BHLYP (purple triangles). All values are in eV.

While the description of vertical excitations is non-problematic with TD-B3LYP, the same does not appear to be necessarily true in the case of excited state relaxation.

In particular, as shown in Figure 5.10 and Figure 5.11, for the $n = 2$ unit the PL energy is far lower when calculated with TD-B3LYP than when TD-CAM-B3LYP and TD-BHLYP are employed. This is not the case for the other two hydrated particles, where TD-DFT calculations with all XC energy functionals make similar predictions. For the latter particle, TD-B3LYP predicts a much lower photoluminescence energy than TD-CAM-B3LYP and TD-BHLYP. Similarly, the TD-B3LYP S1 Λ diagnostic values for $(TiO_2)_3(H_2O)_2$ and $(TiO_2)_4(H_2O)_2$ do not change much between the S0 and S1 minimum energy geometries, whereas the $(TiO_2)_2(H_2O)_2$ TD-B3LYP S1 Λ diagnostic value plummets (see Table 5.3). Using TD-B3LYP it is predicted that during excited state relaxation the character of the S1 state of $(TiO_2)_2(H_2O)_2$ changes from a non-CT state to a CT state. The S1 character of the same particle with the other XC energy functionals,

as well as that for the other hydrated particles, in contrast, appears to not substantially change.

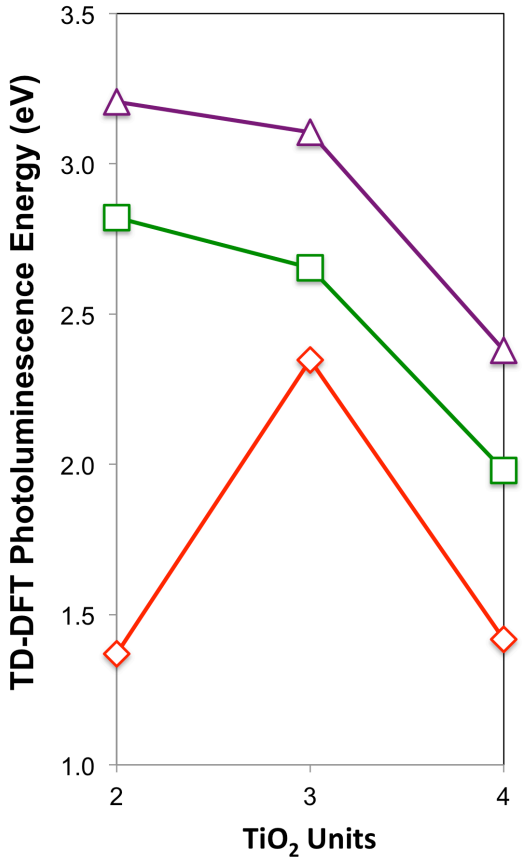

Figure 5.10 TD-DFT calculated photoluminescence energies for the hydrated particles: TD-B3LYP (red diamonds), TD-CAM-B3LYP (green squares) and TD-BHLYP (purple triangles). All values are in eV.

The density difference plots for the $(TiO_2)_2(H_2O)_2$, $(TiO_2)_3(H_2O)_2$ and $(TiO_2)_4(H_2O)_2$ particles shown in Figure 5.12, Figure 5.13 and Figure 5.14, respectively, support the observations above. Specifically, for the $(TiO_2)_2(H_2O)_2$ particle, the use of TD-B3LYP and TD-BHLYP yields similar density differences for the ground state geometry but rather different density differences in the case of the S1 minimum energy structures. TD-B3LYP predicts an excited state minimum structure where the hole-component of the excited state is localised on the oxygen of one of the hydroxyl groups and the excited electron component on the titanium atom furthest away from this hydroxyl. In line with the discussion above, this is a clear CT state. TD-BHLYP, in contrast, finds an excited state minimum where, just as in the ground state geometry, both the hole and excited electron component of the excited state are localised on the centre of the nanoparticle and in which the hydroxyl groups do not partake.

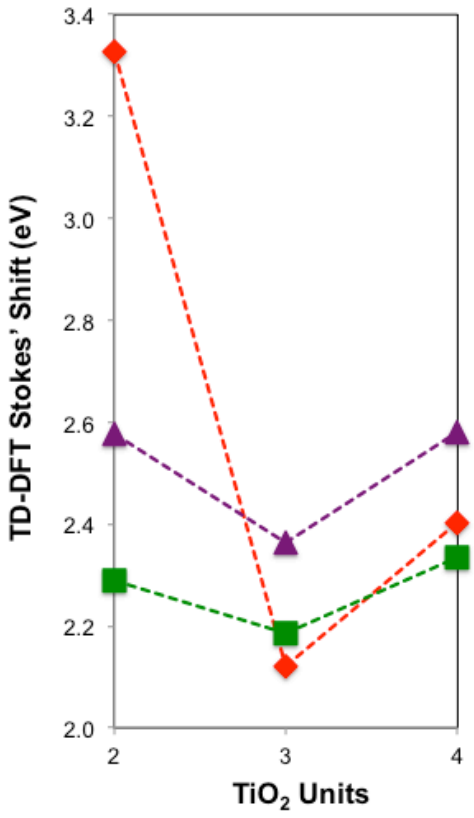

Figure 5.11 TD-DFT calculated Stokes' shift for the hydrated particles: TD-B3LYP (red diamonds), TD-CAM-B3LYP (green squares) and TD-BHLYP (purple triangles). All values are in eV.

The example of the $(TiO_2)_2(H_2O)_2$ particle suggests that even if the use of TD-B3LYP for vertical nanoparticles is non-problematic, one can not guarantee that the same would also be the case when describing excited state relaxation. Moreover, the apparent change of a non-CT into a CT state suggest that this might perhaps be another example of the spurious stabilisation of CT states driving a state to increase its CT character. Concentrating on the TD-CAM-B3LYP and TD-BHLYP results, it can be seen that, just as was the case of the naked particles, excited state relaxation for the hydrated particles is associated with rather large Stokes' shift of 2-3 eV. Also, just as for the naked particles, the contribution of ground state distortion and excited state stabilisation to the Stokes' shift are both significant.

Table 5.3 Vertical excitation energies (EE), photoluminescence (PLE) and corresponding Λ diagnostic values as calculated with TD-B3LYP, TD-CAM-B3LYP and TD-BHLYP for the hydrated particles.[a]

$(TiO_2)_n$	TD-B3LYP				TD-CAMB3LYP				TD-BHLYP			
$(H_2O)_2$	EE	Λ	PLE	PLE Λ	EE	Λ	PLE	PLE Λ	EE	Λ	PLE	PLE Λ
2	4.70	0.30	1.37	0.10	5.11	0.31	2.82	0.37	5.78	0.31	3.21	0.37
3	4.47	0.31	2.35	0.37	4.84	0.31	2.65	0.37	5.47	0.31	3.10	0.35
4	3.82	0.32	1.42	0.32	4.31	0.32	1.98	0.36	4.96	0.30	2.38	0.38

[a]*For all the nanoparticles studied only the lowest energy excited state minimum is shown in this table. EE and PLE values are shown in eV, whereas the Λ diagnostic values are dimensionless numbers.*

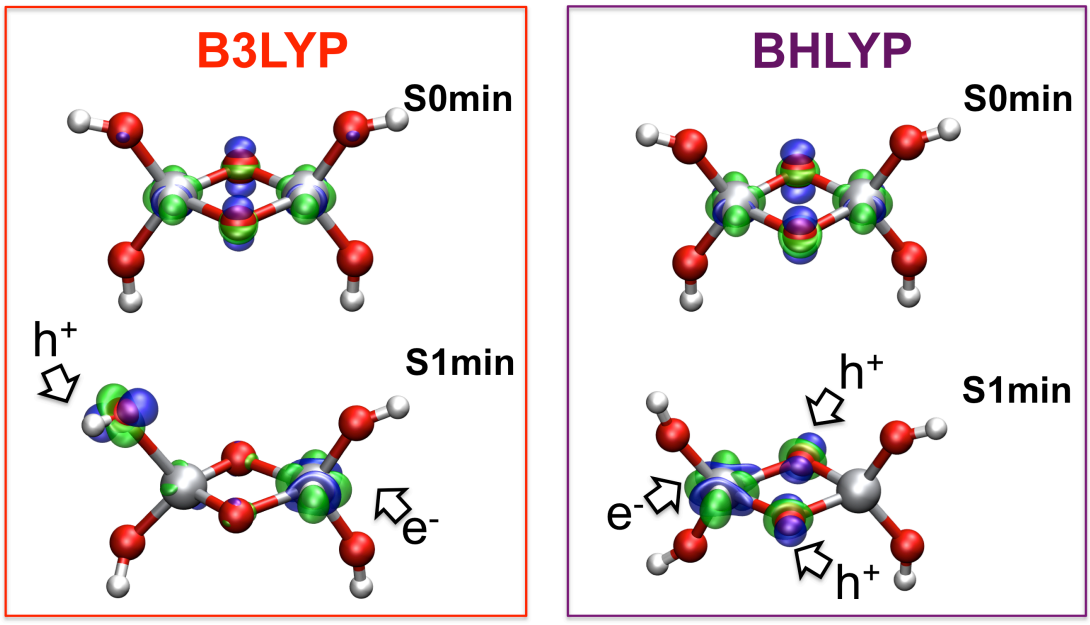

Figure 5.12 TD-B3LYP and TD-BHLYP excited state density difference plots obtained for the vertical (S_0/S_{0min}) and PL (S_1/S_{1min}) excitations of the $(TiO_2)_2(H_2O)_2$ particle. The isodensity plots for the excited state density are calculated at a value of 0.01 au, where the green lobes represent regions of excess electron density (where the excited electron component of the excited state is located, e^-), whereas the blue lobes represent regions deficient in electron density (where the hole component is found, h^+).

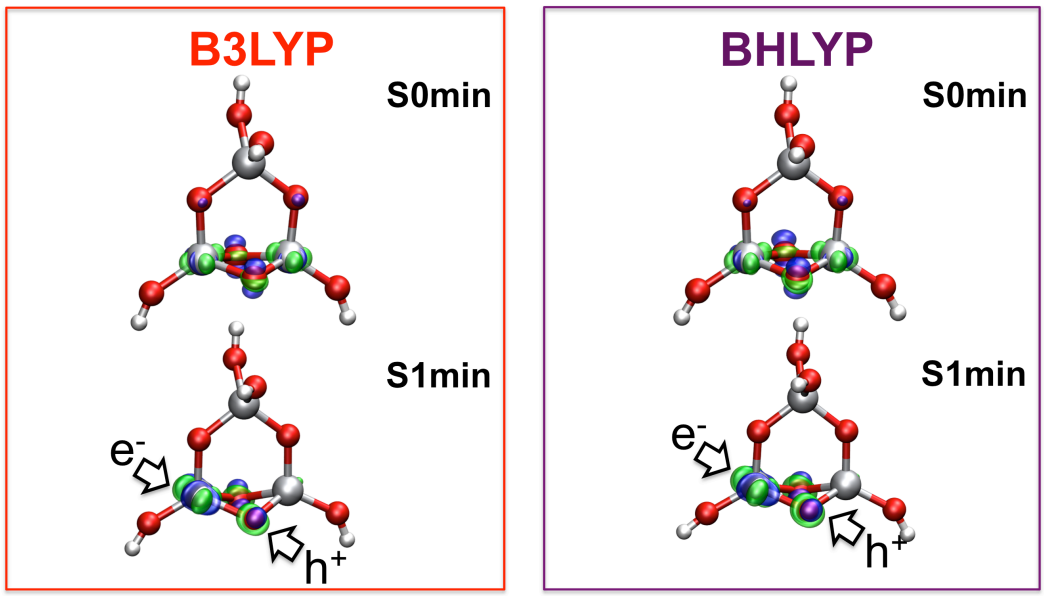

Figure 5.13 TD-B3LYP and TD-BHLYP excited state density difference plots obtained for the vertical (S_0/S_{0min}) and PL (S_1/S_{1min}) excitations of the $(TiO_2)_3(H_2O)_2$ particle. The isodensity plots for the excited state density are calculated at a value of 0.01 au, where the green lobes represent regions of excess electron density (where the excited electron component of the excited state is located, e^-), whereas the blue lobes represent regions deficient in electron density (where the hole component is found, h^+).

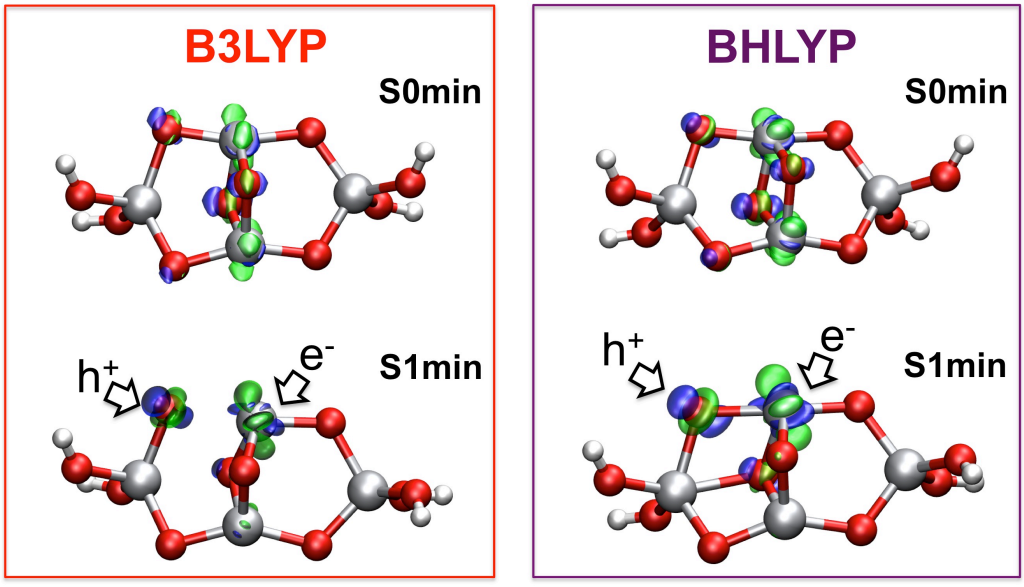

Figure 5.14 TD-B3LYP and TD-BHLYP excited state density difference plots obtained for the vertical (S_0/S_{0min}) and PL (S_1/S_{1min}) excitations of the $(TiO_2)_4(H_2O)_2$ particle. The isodensity plots for the excited state density are calculated at a value of 0.01 au, where the green lobes represent regions of excess electron density (where the excited electron component of the excited state is located, e^-), whereas the blue lobes represent regions deficient in electron density (where the hole component is found, h^+).

5.4 Discussion

From the results discussed above, it is clear that TD-B3LYP predicts considerably different PL energies, Stokes' shifts, chemical character and geometries for the S1 minima of $(TiO_2)_n$ nanoparticles than TD-CAM-B3LYP and TD-BHLYP. Due to the high cost of calculations involving CC excited state relaxation, it has only been possible to compare TD-DFT results directly with CC theory for $(TiO_2)_2$. For this nanoparticle, TD-CAM-B3LYP and TD-BHLYP find a stable minimum with PL energies and Stokes' shifts that quantitatively fit with those obtained with EOM-CCSD, whereas TD-B3LYP predicts instead an apparent S0/S1 conical intersection. Moreover, the fact that use of TD-B3LYP results in almost all cases in Λ diagnostic values of 0.15 or less for the S1 minima/conical intersection structures obtained, strongly suggests that the problem lies with TD-B3LYP. Where TD-B3LYP gives reasonable results for vertical excitations at ground state geometries for most nanoparticles and fails dramatically only in selected cases, the problem with excited state relaxation appears much more widespread, and TD-B3LYP results are likely to be severely wrong for any naked TiO_2 particle. Moreover, analogous problems are likely to occur when using GGA XC energy functionals or hybrid XC energy functionals with a similar or smaller amount of HFLE as B3LYP (e.g. PBE0, appendix B shows the behaviour of PBE0 XC energy functional in comparison to B3LYP, CAM-B3LYP and BHLYP for the calculation of the vertical excitation energy and of the photoluminescence for the lowest excited state of a small set of TiO_2 nanoparticles).

Description of excited states for hydrated particles, non-problematic and unambiguous in the case of vertical excitations as all XC energy functionals give similar results, appears also to become problematic when going beyond the ground state geometry. As discussed above, for selected particles, TD-B3LYP finds a S1 minimum with clear CT character, whereas use of any of the other XC energy functionals yields non-CT S1 minima. Due to the high computational cost, for the hydrated particles, it has not been possible to define CC benchmark data. However, as the origin of the discrepancy between TD-B3LYP and TD-CAM-B3LYP/TD-BHLYP is similar as in the case of the naked particles, I believe that it is likely that the problem again results from using TD-B3LYP. Again, I expect that similar problems are likely to occur when using GGA XC

energy functionals or hybrid XC energy functionals with a low percentage of HFLE to describe excited state relaxation in hydrated titania particles.

For many particles, the character of S1 changes from a local excitation to a CT state after excited state relaxation when using TD-B3LYP, whereas the character of the excited state does not change when using TD-CAM-B3LYP and TD-BHLYP. Concluding, it can be said that the spurious energetic stabilisation of CT states in TD-B3LYP in effect may result in a fictitious driving force towards minima with a strong CT character.

Based on the qualitative fit with EOM-CCSD, both in terms of PL energy for $(TiO_2)_2$ and vertical excitations for $(TiO_2)_2$ to $(TiO_2)_6$ and selected hydrated particles, TD-CAM-B3LYP should be preferred over TD-BHLYP for excited state properties. Furthermore, CAM-B3LYP is known to well reproduce other non-excited state properties [15]. However, in the absence of CAM-B3LYP or range-separated XC energy functionals in general, BHLYP appears to be a good alternative, possibly in combination with a posterior rigid red-shift of the predicted excitation energies.

Focussing on the TD-CAM-B3LYP and TD-BHLYP results, there is a clear variation from particle to particle in the predicted Stokes' shift and photoluminescence energy. This variation probably finds its origin in the different sites that the excited electron and hole components of the excited state localise upon in the different structures. As previously hypothesised in Chapter 4 for the case of vertical excitations, the latter is probably the result of a subtle interplay between the on-site electrostatic potential and the electrostatic interaction between electron and hole. However, in the case of excited state relaxation, there is probably an additional contributing factor; differences in ionic polarisability between different sites in the (different) particle(s). The degree to which different sites allow stabilisation of the excited electron and hole components of the excited state by structural distortion, e.g. the elongation of the titanium – terminal oxygen bond upon localisation of the hole component on the terminal oxygen atom. Finally, a similar subtle interplay is probably responsible why one encounters CT problems for some hydrated particles and not for other very similar hydrated particles.

5.5 Conclusions

In this chapter the description of excited state relaxation in TiO_2 nanoparticles has been investigated by (TD-)DFT. Three common XC energy functionals TD-B3LYP, TD-CAM-B3LYP and TD-BHLYP have been employed for the investigation of excited state properties in particles ranging in size from $(TiO_2)_2$ to $(TiO_2)_{10}$. It was found that use of TD-CAM-B3LYP and TD-BHLYP yields qualitatively similar results for all structures, that are furthermore consistent with predictions of EOM-CCSD for $(TiO_2)_2$. TD-B3LYP, in contrast, is found to make rather different predictions, including an apparent conical intersection for $(TiO_2)_2$ that is not observed for correlated wavefunction calculations. In line with what was observed in Chapter 4, the issue with TD-B3LYP appears to be its inherent tendency to spuriously stabilise the energy of CT states. Even for hydrated particles, for which vertical excitations are generally well described with all XC energy functionals, use of TD-B3LYP appears to result in charge-transfer problems for some specific particles. This spurious stabilisation drives TD-B3LYP excited state optimisations to different structures than those obtained using TD-CAM-B3LYP or TD-BHLYP. On basis of these observations, I recommend the use of CAM-B3LYP, BHLYP or similar XC energy functionals when describing processes taking place on the excited state potential energy surfaces of TiO_2 nanostructures. Finally, focusing on the TD-CAM-B3LYP and TD-BHLYP results, excited state relaxation in naked and hydrated TiO_2 nanoparticles is predicted to be associated with a large Stokes' shift. The exact magnitude of the Stokes' shift and PL energy depends on the sites on which the excited electron and hole components of the excited state localise upon.

5.6 References

[1] Comeau, D. C.; Bartlett, R. J. *Chem. Phys. Lett.* **1993**, *207*, 414.
[2] Stanton, J. F.; Bartlett, R. J. *J. Chem. Phys.* **1993**, *99*, 5178.
[3] Weigend, F.; Ahlrichs, R. *Phys. Chem. Chem. Phys.* **2005**, *7*, 3297.
[4] Ahlrichs, R.; Bar, M.; Haser, M.; Horn, H.; Kolmel, C. *Chem. Phys. Lett.* **1989**, *162*, 165.
[5] Furche, F.; Ahlrichs, R. *J. Chem. Phys.* **2002**, *117*, 7433.
[6] van Wuellen, C. *J. Comput. Chem.* **2011**, *32*, 1195.
[7] Furche, F.; Ahlrichs, R.; Haettig, C.; Klopper, W.; Sierka, M.; Weigend, F. *WIREs Comput. Mol. Sci.* **2014**, *4*, 91.
[8] Schafer, A.; Horn, H.; Ahlrichs, R. *J. Chem. Phys.* **1992**, *97*, 2571.
[9] Valiev, M.; Bylaska, E. J.; Govind, N.; Kowalski, K.; Straatsma, T. P.; Van Dam, H. J. J.; Wang, D.; Nieplocha, J.; Apra, E.; Windus, T. L.; de Jong, W. A. *Comp. Phys. Commun.* **2010**, *181*, 1477.
[10] Humphrey, W.; Dalke, A.; Schulten, K. *J. Mol. Graphics Modell.* **1996**, *14*, 33.
[11] Peach, M. J. G.; Benfield, P.; Helgaker, T.; Tozer, D. J. *J. Chem. Phys.* **2008**, *128*, 44118.
[12] Berardo, E.; Hu, H. S.; Shevlin, S. A.; Woodley, S. M.; Kowalski, K.; Zwijnenburg, M. A. *J. Chem. Theory Comput.* **2014**, *10*, 1189.
[13] Berardo, E.; Hu, H.-S.; Shevlin, S. A.; Woodley, S. M.; Kowalski, K.; Zwijnenburg, M. A. *J. Chem. Theory Comput.* **2014**, *10*, 1189.
[14] Wiggins, P.; Williams, J. A. G.; Tozer, D. J. *J. Chem. Phys.* **2009**, *131*, 091101.
[15] Yanai, T.; Tew, D. P.; Handy, N. C. *Chem. Phys. Lett.* **2004**, *393*, 51.

Chapter 6

Modelling the photocatalytic properties of a realistic rutile TiO_2 nanoparticle

In this chapter, a range of optical and excited state properties for a realistic TiO_2 rutile nanoparticle are investigated, including the optical gap, the predicted photoluminescence signal, the sites where the exciton self-traps, and the structural distortion associated with the localisation. Standard reduction potentials of the free charge carriers and exciton are also calculated for the rutile particle and compared with those of the water splitting half-reactions to examine the thermodynamic ability of this particle to drive the photocatalytic splitting of water.

The content of this chapter has been taken from the following work:

Berardo, E.; Zwijnenburg, M. A. Modelling the water splitting activity of a TiO_2 rutile nanoparticle. *J. Phys. Chem. C,* 2015, **199**, 13384 - 13393

6.1 Introduction

TiO_2 nanoparticles are the quintessential photocatalyst. Loaded with a noble metal co-catalyst (Pd, Pt, Rh) both rutile [1-4] and anatase [5-7] nanoparticles catalyse the overall splitting of water into molecular hydrogen and oxygen when illuminated with ultraviolet light, while without noble metals they act as photocatalysts for the degradation of organic molecules [8-11] and drive the individual water splitting half-reactions in the presence of a suitable electron or hole donor [12-14]. Some of these reactions are endothermic and part of the photon energy becomes incorporated in the reaction products (e.g. overall water splitting), a situation sometimes also referred to as artificial photosynthesis [15]. In other cases, these reactions are exothermic, e.g. organic pollutant degradation, and the illuminated photocatalyst acts as a catalyst in the classical sense and improves the reaction rate.

As already introduced in Chapter 1, there is an on-going discussion about the relative position of the (reduction potentials associated with the) conduction band in anatase and rutile [16-20], as well as the defect chemistry of TiO_2 and how this can be used to reduce the optical gap from the ultraviolet to the visible part of the spectrum [19]. Finally, there is dependence of the photocalytic activity on particle size and morphology, about which there are very contrasting reports in the literature. For example, work on the reduction of protons, as part of overall water splitting or in the presence of a sacrificial electron donor, suggest a decrease in photocatalytic activity with decreasing particle size [7,21,22], while other studies that focus on the degradation of organic molecules report an increase in activity instead [13,23,24].

Following from the previous chapters of this thesis it can be seen how computational approaches can be used to accurately describe specific properties of TiO_2 nanoparticles. However, in order to investigate photocatalytic processes, a more detailed computational methodology has to be defined.

As mentioned previously in Chapter 1, during use as a photocatalyst the particle can exist in a number of different electronic states; the electronic ground state (P), an electronically excited excitonic state (P^*) or an anionic (P^-) or cationic (P^+) state. Starting from the ground state, absorption of light with energy higher than the optical gap results in the excitation of the particle and the formation of an exciton. This exciton subsequently can ionise into a free electron and free hole, where free signifies that the

excited electron and hole are sufficiently spatially separated that their effective interaction is negligible, for example on two different particles (or on a very large nanoparticle). This free electron and hole can take part in interesting chemistry but also recombine to reform an exciton in a process referred to as electron-hole recombination. Excitons, finally, can decay at any stage back to the ground state under the emission of light, luminescence, or via a non-radiative route, internal conversion, where the excess energy is dissipated in the form of phonons (vibrations).

Both the exciton and the free charge carriers can in principle localise on a fragment of the particle (self-trap, e.g. a self-trapped exciton) or become trapped on a structural defect (e.g. a free electron trapped by an oxygen vacancy) [25-29]. Especially self-trapped exciton formation appears to be very structure sensitive; bulk rutile only has free non-trapped excitons while in bulk anatase excitons appear to self-trap [30-33]. Experimentally, self-trapping is observable by the different spectroscopic signatures of free and trapped states. For example, in the case of excitons, a red shift between the optical gap and the photoluminescence maxima is a signature of a self-trapped exciton.

Modelling such complex processes is a challenging task, especially deciding what to include and what not. However, I believe that a certain number of essential features should be considered in order to have a realistic model. Both the free charge carriers and the exciton can in principle drive the water splitting half-reactions by providing electrons and holes with the necessary chemical potential [34]. Any attempt at modelling a photocatalyst should therefore, in my opinion, consider both free charge carriers and excitons. This is especially true when considering nanoparticles. For many bulk solids the difference between the energy required for creating a pair of free charge carriers and that needed to make an exciton (i.e. the optical gap) is very small (for example 4 meV for bulk rutile [35]) and the potentials associated with excitons and free charge carriers are thus approximately degenerate. The same is not necessarily true in the case of nanoparticles. Furthermore, because of the known potential for (self)-trapping in TiO_2, see above, one ideally should also consider the effect of structural relaxation when studying photocatalysts. Finally, taking into account the need to understand the explicit effect of particle size and the fact that at least in the case of overall water splitting the photocatalyst will operate immersed in water, it appears sensible to study hydroxylated nanoparticles, the surface of which is covered by a

further monolayer of adsorbed water molecules. The latter explicit description of surface water possibly used in conjunction with a dielectric continuum solvation model to reproduce the effect of bulk water. Relevant previous work on TiO_2 generally did not consider excitons and focused instead on studies of free charge carriers in either periodic 2D-slabs [26,28,36] or in nanoparticles [19,37-40]. While the selected papers [41-56] that do consider excitons, mostly in the case of nanoparticles, generally do not consider exciton self-trapping and often focus on unhydroxylated naked particles in vacuum.

Following the logic set out above, I report here the first DFT/TD-DFT calculations on a hydroxylated rutile nanoparticle, where the effect of solvation and trapping is explicitly included. The particle's optical properties, photoluminescence signal, self-trapping energies and geometries involved with the relaxation are calculated, along with the standard reduction potentials for the exciton and free charge carriers. Finally, all these data are employed to discuss how the photocatalytic ability of nanoparticles might differ from their larger counterparts, the role of surface flexibility therein and why studies on water splitting and organic molecule degradation give fundamentally different results.

6.2 Theoretical approach

In the following section, the methodology employed for calculating the thermodynamic ability of photocatalysts to drive half-reactions, such as those underlying water splitting, is discussed. First, I will, however, review the potentials of the water splitting half-reactions and what thermodynamic constraints these put on the required photocatalyst free charge carrier and exciton (standard) reduction potentials.

6.2.1 Water Splitting

The overall water splitting reaction is a combination of two half-reactions (both written in line with convention as reductions):

$$2H^+ + 2e^- \rightleftarrows H_2 \tag{6–a}$$

$$O_2 + 4H^+ + 4e^- \rightleftarrows 2H_2O \tag{6–b}$$

During water splitting, the reduction of protons to molecular hydrogen or Hydrogen Evolution Reaction, (HER, reaction (6–a)) will run in the forward direction, and the oxidation of water to molecular oxygen and protons or Oxygen Evolution Reaction (OER, reaction (6–b)) in the direction opposite to written.

In order for both of these half-reactions to take place and overall water splitting to occur, a photocatalyst will have to provide electrons for the HER, and accept electrons, or in other words donate holes, to drive the half-reaction OER. The (standard) reduction potential of the free charge-carriers and/or excitons of a photocatalyst should thus straddle those of HER and OER (see Figure 6.1). Moreover, as experimentally half-reaction HER has a standard reduction potential of 0 V relative to the Standard Hydrogen Electrode (SHE) at pH 0 and half reaction OER a standard reduction potential of 1.23 V, a successful photocatalyst needs to provide at least this amount of potential to split water. In practice, generally, a larger potential (e.g. 1.9 V) is required to overcome energetic losses and kinetic barriers, the difference between the effective and equilibrium potentials being the over-potential. For reactions other than water splitting, e.g. reduction of protons in the presence of a sacrificial electron donor or degradation of organic pollutants, finally, a very similar analysis must be performed.

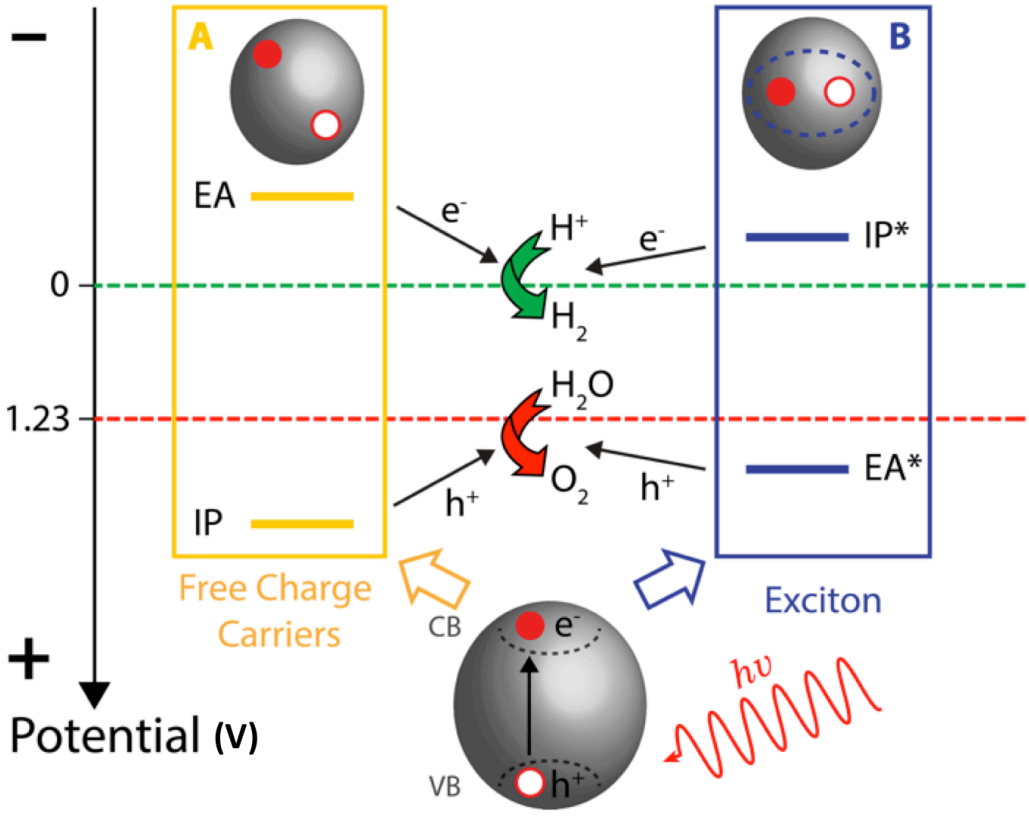

Figure 6.1 Scheme showing how the (standard) reduction potentials (IP, EA and EA* and IP*) of the ideal photocatalyst (nanoparticle) straddle the proton reduction and water oxidation potentials (HER as green and OER as red broken lines, respectively). *hv* defines the energy of the photon absorbed by the nanoparticle, $\mathbf{e}^-$ and $\mathbf{h}^+$ stand for electron and hole respectively, while VB and CB are the Valence and Conduction Bands of the particle. **A** Represents the Free Charge Carriers scenario, where electron and hole are spatially separated within the particle and do not feel reciprocal Coulombic interactions. **B** Represents the Exciton scenario, where electron and hole are strongly inter-correlated and can be described as the electron-hole pair, or exciton.

6.2.2 Modelling the photocatalyst

When evaluating the ability of a photocatalyst to drive either or both of the water splitting half-reactions, the thermodynamic driving force for each of the possible electronic states that the photocatalyst can be in must be considered (P, P^*, P^+ and P^-, see above), as well as how likely it is for the photocatalyst to be in any of those states. Focussing first on the first issue, the relevant half-reactions for the different photocatalysts states, written in line with convention as reductions, are:

$$P^+ + e^- \rightleftarrows P^* \quad (6\text{–c})$$

$$P^* + e^- \rightleftarrows P^- \quad (6\text{–d})$$

$$P + e^- \rightleftarrows P^- \quad (6\text{–e})$$

$$P^+ + e^- \rightleftarrows P \quad (6\text{–f})$$

In half-reactions (6–c) and (6–e) the exciton and the free electron serve as reductants; the TiO_2 nanoparticle donates electrons and the half-reactions will run in the opposite direction to that written above. In the other two half-reactions (6–d) and (6–f), the nanoparticle accepts electrons (donates holes) and the exciton and the free hole act as oxidants. The potentials of these half-reactions, as well as those of water splitting and other solution phase reactions, can be easily calculated from the negative of the free energies of the respective half-reactions via:

$$E^0 = -\frac{\Delta G(x)}{nF} \quad (6\text{–1})$$

Where n is the number of electrons involved in the half-reaction and F the Faraday constant.

The reduction potential of half-reaction (6–f) is equal to the ionisation potential, the free energy required to remove an electron from the top of the photocatalyst valence band, and is hence further labelled as IP. Similarly, the reduction potential of reaction (6–e) equals the electron affinity, the free energy released upon adding one electron to the bottom of the photocatalyst conduction band, and labelled as EA. Similarly, the potentials of half-reactions (6–c) and (6–d) can be thought of as the excited state ionisation potential IP*, the free energy required to remove the excited electron from the exciton, and the excited state electron affinity EA*, the free energy released upon adding an electron to the exciton and annihilate the exciton hole component in the process, respectively.

In line with above, for proton reduction to occur in the presence of the photocatalyst the potentials of half-reaction (6–c) and/or (6–e) (IP* and EA respectively) should be more negative than that of half-reaction (6–a). Similarly for water oxidation the potential of half-reaction (6–d) and/or (6–f) (EA* and IP respectively) should be more positive than that of half-reaction (6–b) (see Figure 6.1). Moreover, there should be a sufficient

overpotential, of the order of a couple of tenths of V, in all cases, to guarantee measurable kinetics.

The second issue, how likely it is for the photocatalyst to be in a certain electronic state, can, at least on thermodynamic grounds, be analysed in terms of the free energy of the following reaction:

$$P^* + P \rightleftarrows P^+ + P^- \qquad (6\text{–}g)$$

The (free) energy of this reaction is commonly referred to as the exciton binding energy (EBE); the difference between the free energy required for forming a pair of free charge carriers and that needed to form an exciton. Positive values of the exciton binding energy signify that an exciton is more stable than the free charge carriers and that additional energy needs to be invested to ionise the exciton. Alternatively, free electrons or holes can be generated as side-product of the exciton donating an electron or hole (half-reactions (6–c) and (6–d)).

6.2.3 Redox potentials

The Gibbs free energies for each relevant species discussed above can be obtained as the sum of three different contributions:

$$G(x) = U(x) + G_{vib}(x) + G_{sol}(x) \qquad (6\text{–}2)$$

Where U is the electronic energy, G_{vib} the sum of the vibrational, rotational and translational contributions to the free energy and G_{sol} the solvation free energy. In this work, the photocatalyst's G_{vib} is neglected for numerical tractability reasons, as calculating the (excited state) frequencies of particles with more than 150 atoms is computationally very expensive. Previous studies done by the Zwjinenburg group suggest that the effect of this approximation on the photocatalyst's potentials is generally very small [34,57]. In the case of the water splitting potentials, however, all the terms from equation (6–2) are taken into account.

Another possible approximation consists in the calculation of the IP, EA, IP* and EA* potentials, employing only the ground-state geometry of the neutral photocatalyst, ignoring nuclear relaxation and trapping. This corresponds to the vertical

approximation, briefly touched upon in the introduction, which can be contrasted with the adiabatic approximation, where the minimum energy geometry of each species (P, P^*, P^+ and P^-) is used when calculating the potentials. The nanoparticle's properties involving free (vertical) and self-trapped (adiabatic) species are generally different. Which of these extremes is most relevant depends on the inherent timescale of the phenomena we are interested in relative to that of nuclear relaxation; much shorter – vertical- and much longer -adiabatic.

Finally, since both of the water splitting half-reactions involve protons, for which the calculation of the free energy is a challenging task [58,59], the experimentally determined absolute value of the standard hydrogen electrode (4.44 V) was used instead [60,61] for the potential of half-reaction HER. The proton free-energy ($G(H^+)$), required for the calculation of the potential of half-reaction OER, is then determined via:

$$G(H^+) = \frac{1}{2}G(H_2) - \Delta G(SHE) \tag{6–3}$$

6.2.4 Computational details

Here a combination of DFT and TD-DFT is employed to calculate the properties of the photocatalyst nanoparticles in their different (redox) states and the potentials associated with them. DFT is used to describe the properties of the P, P^+ and P^- states, and linear response TD-DFT for those of P^*.

Within this computational scheme, the geometry of the nanoparticle is firstly optimised in the P, P^+ and P^- states using DFT. Second, the vertical excitation spectrum is calculated at the ground state geometry and subsequently the geometry of the nanoparticle is relaxed in its excited P* state (modelled as the lowest singlet, S1, excitation) using TD-DFT. Third, the vertical triplet excitation energies on the P and P* geometries is calculated, as well as at an approximate T1 minimum energy geometry obtained by optimising the particle in its triplet state using DFT. For the water potentials, finally, all the relevant species (H_2O, O_2, H_2) are optimised using DFT and subsequently frequency calculations are performed on the obtained minimum energy structures to calculate the vibrational contribution to the free energy $G_{vib}(x)$ (see equation (6–2)). Finally, in all calculations, except when explicitly stated, the effect of bulk water is incorporated through use of a dielectric continuum solvent model, where

the properties of the environment are characterised by its relative dielectric permittivity (ε). This approach allows to determine the $G_{sol}(x)$ contribution to the free energy of each species (see equation (6–2)).

The primary nanoparticle structural model considered in this work corresponds to a solvated and hydroxylated cut of the bulk rutile structure, a 3x3x3 rutile nanoparticle previously discussed by Friesner and coworkers [37,39,40], defined by four (110) and two (001) planes respectively and with a ~ 1 nm core (Figure 6.2 A). This is perhaps the smallest rutile particle that still preserves essential features of the bulk structure. The central titanium atom in the particle has a bulk-like 6-fold coordination environment, while all the other titanium atoms have at least four oxygen atoms in their first coordination sphere, of which at most two are part of a surface hydroxyl. The coordination environments of the titanium atoms at the surface of the particle have been further saturated through the adsorption of a monolayer of molecular water. To probe methodological issues calculations on the rutile nanoparticle were complemented with calculations on a smaller hydrated particle; $(TiO_2)_4(OH)_4(H_2O)_6$ (Figure 6.2 B).

Following Chapter 5, this work focuses on DFT and TD-DFT calculations using the CAM-B3LYP XC energy functional [62]. However, also in this case, CAM-B3LYP calculations are complemented with selected B3LYP [63] calculations. All the DFT/TD-DFT calculations employ the all-electron double-ς DZDP basis set (DZP for Oxygen and Hydrogen atoms) [64]. In the CAM-B3LYP calculations, the solvent effects are approximated with the Conductor-like Polarisable Continuum method (C-PCM) [65] dielectric solvent model, whereas for the B3LYP and BHLYP calculations the COSMO [66] dielectric screening model are employed. As already stated in Chapter 2, the two different approaches lead to similar results, as in both cases the ε is chosen equal to 78 resembling solvation in water and the solvation cavity for the solute is generated using van der Waals radii of 2.293, 1.72 and 1.3 Å for Ti, O and H atoms, respectively. In all the calculations full geometry optimisations in the presence of solvent effects are considered, except in the case of TD-DFT excitations involving the COSMO model, as no COSMO excited state gradients are currently available in the code employed for the calculations. For those calculations (B3LYP and BHLYP) the TD-DFT excited state are optimised in vacuum and then the effect of COSMO is

considered as single point calculations on the gas phase excited state minimum geometries. Finally, for all the ground and excited state optimisations the convergence criteria for the maximum Cartesian component of the gradient is chosen to be equal to 1 x 10^{-3} Hartree $Bohr^{-1}$.

All the CAM-B3LYP results are obtained using the GAMESS US code [67], while Turbomole [68-70] is employed for the calculation using the B3LYP XC energy functional. Finally, for plotting the relevant orbitals of the nanoparticles the WXMacMolPlt visualisation software [71] is used.

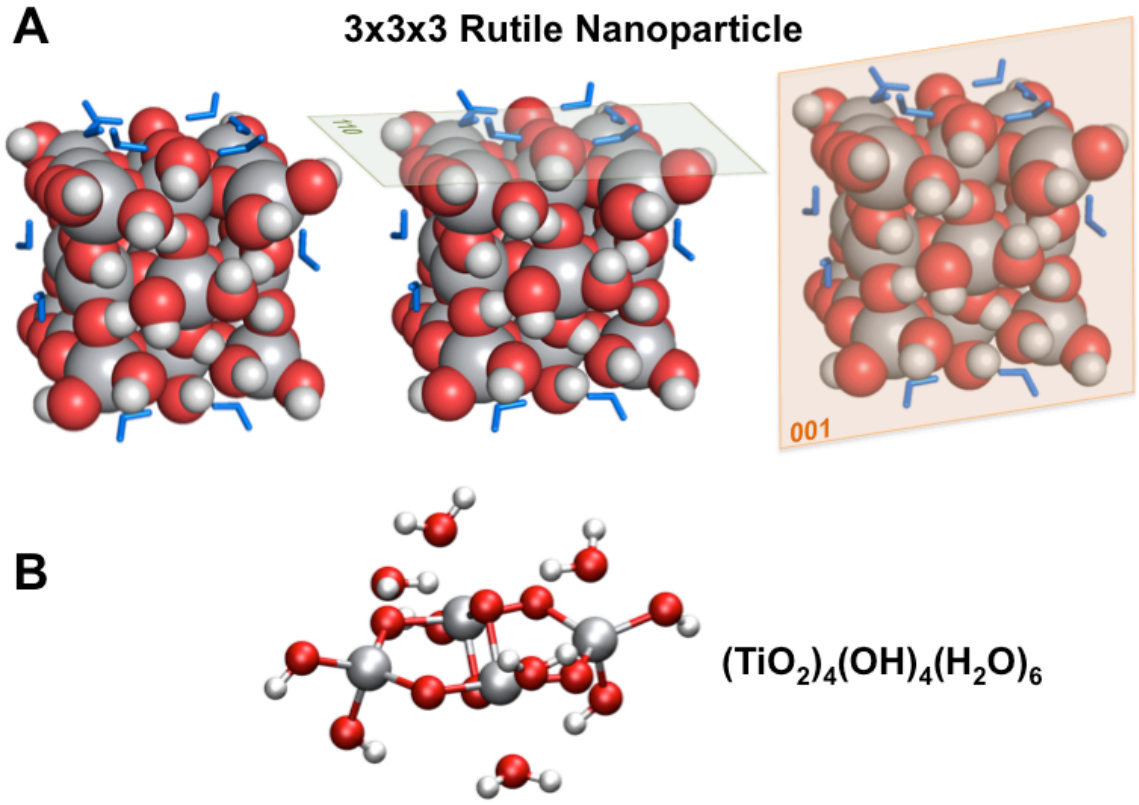

Figure 6.2 A TiO_2 rutile nanoparticle, defined by 23 TiO_2 units and 34 water molecules, 18 reacted on the particle's surface and 16 in its molecular state (pictured as blue lines), which amount to a total of 171 atoms. The crystal planes that define the particle are also shown; four 110 (light green, top middle figure) and two 001 planes (light orange, top right figure). **B** $(TiO_2)_4(OH)_4(H_2O)_6$ particle, which corresponds to the fully hydrated version of the particle already discussed in Chapters 4 and 5.

6.3 Results and discussion

In this section the predicted optical, electronic and photocatalytic properties of the hydrated rutile nanoparticle will be discussed and compared with those of the smaller nanoparticle, as well as, bulk TiO_2.

6.3.1 Free exciton

The TD-CAM-B3LYP predicted optical gap of the hydrated rutile nanoparticle, the energy required to make the free S1 exciton ($S1/S0_{min}$), is 4 eV. The rutile nanoparticle is thus clearly predicted to absorb only ultraviolet or higher-energy/shorter-wavelength light, even if TD-CAM-B3LYP probably slightly overestimates the absorption onset [54,55]. The optical gap of the rutile nanoparticle is red-shifted relative to that of the smaller hydroxylated nanoparticle ($(TiO_2)_4(OH)_4(H_2O)_6$, 4.3 eV) and blue-shifted relative to that of bulk rutile (3.0 eV) [30].

The excitation responsible for the S1 exciton is predicted to have essentially HOMO (VB) → LUMO (CB) character (49%, see Figure 6.3). The HOMO (hole component of the exciton) is delocalised over all the oxygen atoms in the core of the nanoparticle and the LUMO (excited electron component of the exciton) delocalised over the titanium atoms in the middle plane of the particle (see Figure 6.3). This assignment is supported by the difference between the Löwdin charges of the atoms in the ground and S1 excited state. These Löwdin S1-S0 charge differences display clear evidence of excess negative charge on the titanium atoms in the middle plane (excited electron component) and excess positive charge (hole component) on the oxygen atoms in the core of the particle.

The predicted oscillator strength of the free S1 exciton, finally, is rather low (see Table 6.1). While not dark, the absorption on-set is likely to be low in intensity compared to excitonic excitations at higher energy/shorter wavelength. Based on this oscillator strength, the lifetime of the free S1 exciton, or at least the lifetime neglecting radiationless de-excitation through internal conversion, can be estimated using the Einstein equation (introduced in Chapter 2) to be approximately 0.2 ms, rather long in line with the low oscillator strength.

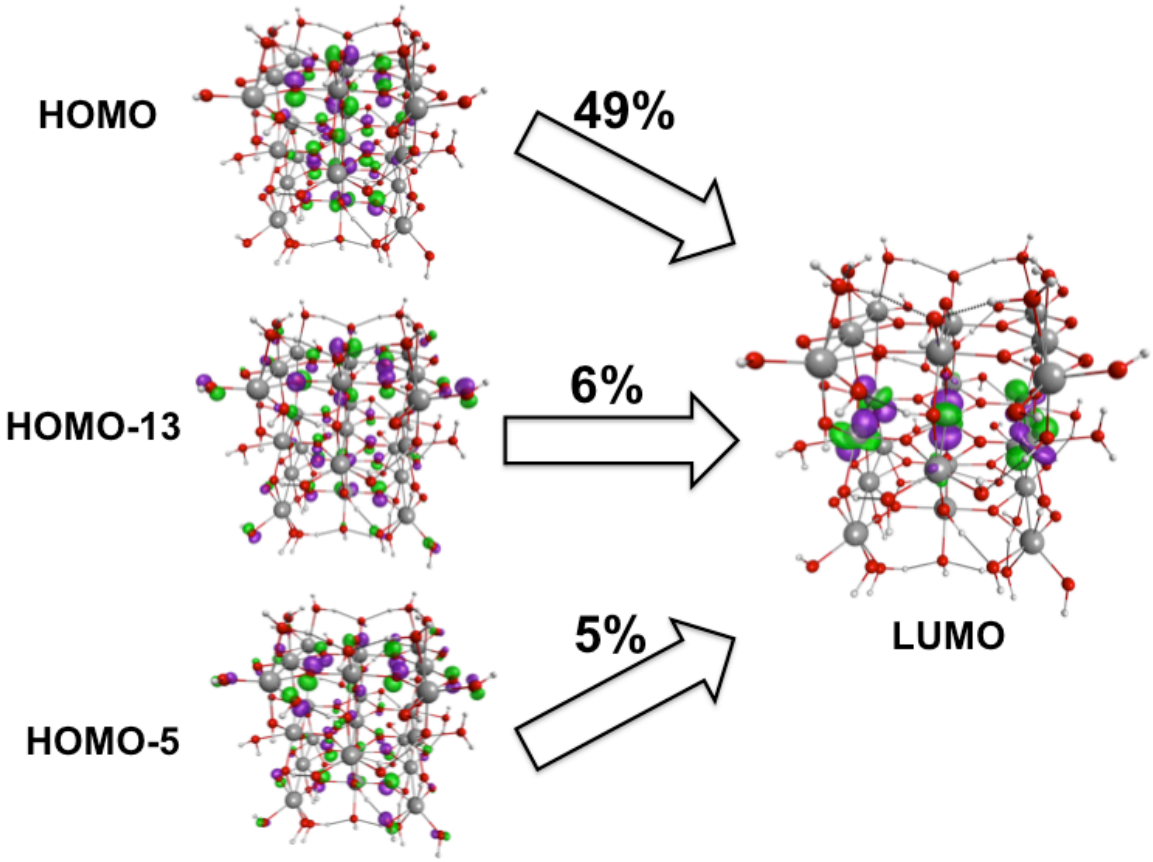

Figure 6.3 Leading CAM-B3LYP orbital contributions to the lowest TD-CAM-B3LYP S1 excitation for the TiO_2 rutile nanoparticle (only the ones larger than 5% are shown). The isodensity plots for the orbitals are calculated at a value of 0.1 a.u., where the green and purple lobes represent the sign of the wavefunction.

Table 6.1 Vertical excitation ($S1/S0_{min}$) and luminescence ($S1/S1_{min}$) energies (EE) of the lowest S1 state for the TiO_2 rutile nanoparticle, as calculated with TD-CAM-B3LYP and TD-B3LYP. For each EE also the Λ value and its oscillator strength (*f*) is shown. As already discussed in Chapter 5, the Stokes' shift is calculated as the difference of the $S1/S0_{min}$ and $S1/S1_{min}$ energies. All the energies are shown in eV.

	TD-CAM-B3LYP			**TD-B3LYP**		
	S1/S0	**S1/S1**	**Stokes**	**S1/S0**	**S1/S1**	**Stokes**
EE	4.0	3.0	1.0	3.2	1.1	2.1
Λ	0.241	0.245	---	0.244	0.054	---
f	7E-06	1E-06	---	2E-05	4E-06	---

6.3.2 Exciton self-trapping

After excited state relaxation on the S1 potential energy surface, an excited state minimum ($S1_{min}$) at which the trapped S1 exciton ($S1/S1_{min}$) is 0.7 eV more stable than at the ground state geometry ($S1/S0_{min}$) was found. The vertical singlet luminescence (fluorescence) signature of this self-trapped exciton is predicted to be 3.0 eV, red-shifted by 1.0 eV compared with the absorption on-set (values in Table 6.1).

The considerable excited state relaxation and Stokes' shift, though smaller than that of the smaller hydrated nanoparticles (~ 1.5 – 2.0 eV) previously discussed in Chapter 5 [55], is clearly linked to the significant localisation induced by self-trapping. Analysis of S1-S0 Löwdin charge differences for the self-trapped exciton geometry shows that both components of the exciton have become localised on atoms on the top (110) face of the particle. The majority of the hole component on a 2-coordinated oxygen atom and the majority of the excited electron component on two 4+1b+1t coordinated titanium atoms adjacent to this oxygen atom (see Figure 6.4, where 4+1b+1t signifies that these titanium atoms are coordinated by 4 oxygen atoms, 1 bridging hydroxyl and 1 terminal hydroxyl). The largest structural distortion associated with the exciton localisation is the elongation of the bond distances between the 2-coordinated oxygen atom (pictured in blue in Figure 6.4) and the two adjacent titanium atoms (green atoms in Figure 6.4) by ~10%.

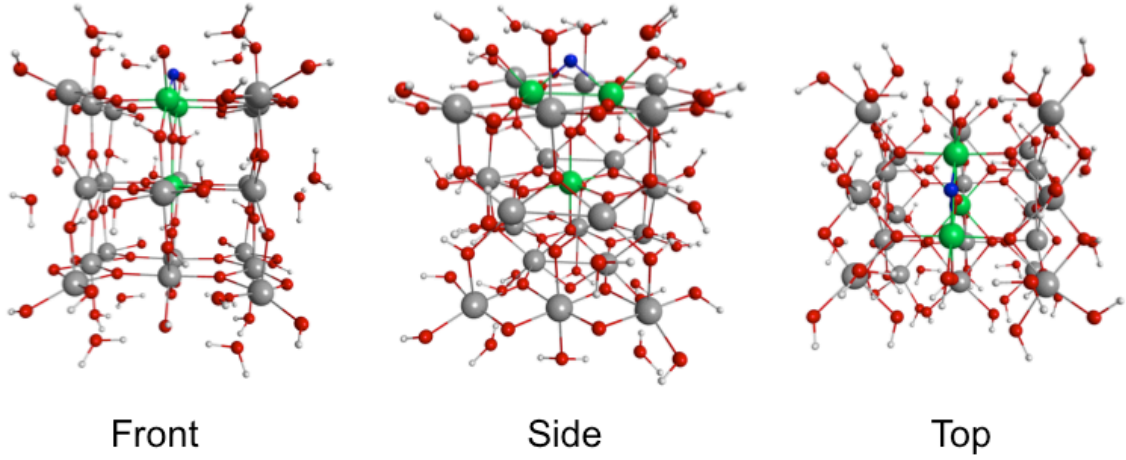

Figure 6.4 Geometry of the TD-CAM-B3LYP relaxed S1 excited state minimum ($S1/S1_{min}$) for the TiO_2 rutile nanoparticle. Red spheres denote oxygen atoms, whereas gray and white represent titanium and hydrogen atoms respectively. The green (Ti atoms) and blue (O atoms) spheres represent the atoms that are mostly involved with the exciton (hole and electron) self-trapping.

The oscillator strength of the S1 self-trapped exciton is slightly reduced compared to that of its free counterpart at the ground state geometry (Table 6.1). This, together with the resulting relatively long lifetime of the self-trapped exciton (~ 3 ms), again calculated using the Einstein equation might make this fluorescence hard to be observed experimentally. Dark de-excitations, possibly coupled with phosphorescence from the lowest triplet state (T1 exciton) populated through intersystem crossing modulated by spin-orbit coupling, are likely to be the more prominent route for the system to relax back to the ground state.

The predicted bright S1 exciton lifetimes, for both the free and the self-trapped versions, are roughly three orders of magnitudes longer than the overall exciton lifetime determined experimentally for rutile single crystals through transient adsorption spectroscopy (< 1 ns) [72]. There is no practical and easy way to calculate the dark internal conversion contribution to the exciton de-excitation rate for such large particles. In fact, such a calculation would require surface-hopping excited-state molecular dynamic calculations, which are currently tractable for systems containing ~ 5 heavy atoms only. However, as the direct gap of bulk rutile goes together with a short exciton lifetime in rutile single crystals and vice versa the non-direct gap in bulk anatase with a long(er) exciton lifetime in anatase single crystals (> 10 ns) [72], it is likely that the bulk exciton lifetime is dominated by bright de-excitation. In which case, it appears that going from the bulk to nanoparticles at least significantly reduces the bright exciton de-excitiation rate.

Excited state relaxation, finally, is also a good illustration for the need to employ the range-separated CAM-B3LYP functional when studying larger TiO_2 nanoparticles. As can be seen in Table 6.1, TD-B3LYP predicts a much red-shifted fluorescence signal (1.1 eV) and a much larger energy difference between the free and self-trapped exciton ($S1/S0_{min}$ and $S1/S1_{min}$), i.e. a greater degree of excited state relaxation.

Calculations of the Λ diagnostic developed by *Peach et al.* [73], suggest that, in line with what previously observed in Chapters 4 and 5 on smaller nanoparticles, these large differences relative to what TD-CAM-B3LYP predicts arise from the fact that the lowest singlet exciton obtains a strong CT character while relaxing.

6.3.3 Free electron and hole

As shown in Table 6.2, the rutile nanoparticle is predicted using CAM-B3LYP to have a vertical ionisation energy of 7.9 eV and a vertical electron affinity of 3.4 eV. The energy required to make a pair of free charge carriers, the quasiparticle or band gap, therefore is calculated to be 4.5 eV. As a result these calculations suggest that thus 0.5 eV is required to ionise the S1 exciton into a free electron on one particle and a free hole on another particle (free charge carriers scenario shown in Figure 6.1 A, where however the rutile nanoparticle is too small for an excited electron and hole to be separated sufficiently far for them to not interact and two particles need to be considered).

Just as the S1 exciton, both the excess electron and hole are predicted to strongly and barrierlessly self-trap as small polarons (electron or hole localised on a specific lattice site surrounded by a deformed lattice) on fragments of the rutile nanoparticle with self-trapping energies of 1.1 and 2.1 eV respectively. The adiabatic ionisation energy 5.8 eV is significantly reduced relative to its vertical counterpart, while the adiabatic electron affinity is moderately larger than the vertical electron affinity at 4.5 eV. More importantly perhaps, ionisation of the (self-trapped) exciton (discussed in section 6.3.2) into a self-trapped electron on one particle and self-trapped hole on another particle is strongly favoured energetically (by 1.7 eV). Calculations using the B3LYP XC energy functional shown in Table 6.2, predict similar trends.

Based on the analysis of the Löwdin spin population, the free electron self-trapping is associated with a complete localisation of the excess electron on the central 6-coordinated titanium atom, forming in essence a Ti^{3+} centre. While the hole is predicted to self-trap nearly completely on a 2-coordinated oxygen atom on the top (110) face of particle, forming a O^- centre. The latter 2-coordinated oxygen atom is the same atom where the excited electron component of the exciton is predicted to localise on in the case of the self-trapped exciton (shown in Figure 6.4). In both cases the trapping is associated with elongation of the bonds around the atom on which the charge becomes trapped (by 3 – 5% in the case of the trapped electron and 13.5 – 14.5% for the trapped hole).

Table 6.2 Vertical and Adiabatic energies for the EA, IP, EA* and IP* introduced in section 6.2.2. The Quasiparticle gap (QP, e.g. difference between IP and EA) and the Exciton Binding Energy (EBE, e.g. difference between TD-DFT optical gap and QP) are also shown. All the values are shown in eV.

	TD-CAM-B3LYP		**TD-B3LYP**	
	Vertical	**Adiabatic**	**Vertical**	**Adiabatic**
EA	3.4	4.5	3.4	4.0
IP	7.9	5.8	7.2	5.8
EA*	7.4	7.9	6.6	6.0
IP*	3.9	2.4	4.0	3.8
QP	4.5	1.2	3.9	1.7
EBE	0.5	-2.1	0.7	0.6

The calculated electron self-trapping energy obtained in this thesis for the 3x3x3 rutile nanoparticle (1.1 eV) is slightly larger than predicted by Friesner and co-workers for the larger 5x5x5 counterpart (0.5 eV) [39]. Similar electron and hole self-trapping energies of 1.5 and 1.3 eV respectively are observed for the smaller $(TiO_2)_4$ hydrated nanoparticle.

The free charge-carrier trapping energies predicted for the rutile nanoparticle are also considerably larger than those previously reported for bulk rutile and (non-hydrated) rutile surfaces [27-29], irrespective of the XC energy functional used (see Table 6.2), even if similar small polaron Ti^{3+}/O^- centres are formed in both the bulk and the nanoparticle. This is especially true for the case of the free hole, where the trapping energy found for the rutile nanoparticle (2.2 eV) is an order of magnitude larger than the one calculated for bulk rutile (0.1 eV) [27] and more than two times as large as that predicted for different unhydrated rutile surfaces (0.01 – 0.10 eV) [28]. The predicted vertical potentials for the free charge-carriers, finally, are similar in magnitude as those calculated for the low-energy (non-hydrated) bulk rutile surfaces using GW/DFT [36]. This is especially true in the case of the IP potential (GW/DFT IP_{110} 7.51 eV), while the EA potential of the nanoparticle is less negative than its predicted bulk analogue (EA_{110} 4.67 eV).

In Table 6.2 an interesting trend is observed for the EBE, which in the adiabatic case for TD-CAM-B3LYP becomes exergonic. This effect has also been noticed for the smaller hydrated particle in the presence of the implicit solvent (e.g. PCM/COSMO), whereas all the EBEs show positive values when calculations are done in the gas phase. Physically EBE describes how strongly the electron and the hole are interacting in the

exciton. When EBE approaches to zero, the electron and hole are weakly interacting to a point that they can be considered as free charge carriers (the TD-DFT Optical gap is equal to the QP gap). This could suggest that whenever the EBE is negative, for the electron and hole, confined on a specific nanoparticle or on two different particles after the self-trapping has taken place, the interaction with the solvent is thermodynamically favored compared to their reciprocal interaction. The implicit solvent (described as a dielectric continuum, in this case $\varepsilon = 78$), strongly stabilises the electron and hole and pulls the two charges apart, therefore leading to a larger degree of self-trapping of the charges on the surface of the particle (especially in the case of the hole). To my knowledge, no previous studies investigated this interesting phenomenon, which I think could be worth focusing on in future works.

6.3.4 Triplet exciton

A triplet exciton (T1) can be formed from the S1 exciton through intersystem crossing, mediated by spin-orbit coupling. At the ground state geometry the free T1 exciton is effectively degenerate with the free S1 exciton. It has not been possible to perform a TD-DFT energy minimisation for the T1 exciton as the code employed for the TD-CAM-B3LYP calculations (GAMESS US) lacks analytical TD-DFT gradients for triplet excited-states. However, as the T1 and S1 excitons are also effectively degenerate at the S1 self-trapped exciton geometry, this singlet/triplet near degeneracy appears to be a global feature of the rutile nanoparticle S1/T1 excited-state potential energy surfaces.

6.3.5 Redox potentials

Using the information discussed above one can calculate the reduction potentials associated with the two different scenarios introduced in this chapter: the free charge-carriers and the excitons. Figure 6.5 shows the (TD-)CAM-B3LYP predicted vertical and adiabatic potentials relative to the standard hydrogen electrode (4.44 V). Figure 6.5 also includes the potentials for the reduction of protons and the oxidation of water, as calculated with CAM-B3LYP (green and red lines respectively). While CAM-B3LYP improves the description of excited states in TiO_2 relative to B3LYP, it gives a slightly worse description of the water potentials, overestimating the potential difference associated with the overall water splitting reaction (B3LYP 1.05 V, CAM-B3LYP 1.55

V vs. 1.23 V experimentally). The potentials for the water half-reaction, finally, are given both for the case of pH 0 (dashed lines) and pH 7 (dotted lines). As observed in Figure 6.5, moving from pH 0 to pH 7 corresponds to a rigid shift of 0.57 eV to the energy levels of the water redox potentials. However, the latter case is probably most relevant, not only because pH 7 is the pH of fresh water, but also because pH 7 is closest to the point of zero charge of rutile TiO_2 (~ pH 5), inline with the studied rutile nanoparticle neither being protonated nor deprotonated.

The vertical and adiabatic potentials predicted by TD-CAM-B3LYP, in Figure 6.5, are rather different. Focussing first on the vertical potentials, there is a clear driving force for water oxidation by both free holes (IP) and the free exciton (EA^*). There is also a small driving force for proton reduction by both the free electron (EA) and free exciton (IP*). The adiabatic potentials, however, suggest that after self-trapping both proton reduction and water oxidation by self-trapped charge-carriers is endergonic, while both are strongly exergonic in the case of the self-trapped exciton. This latter is of limited practical use, however, as reduction (IP*) or oxidation (EA*) driven by the self-trapped exciton inherently generates self-trapped free charge carriers (half-reactions (6–c) and (6–d), Ti^{3+}/O^- centres) that are chemically inert with respect to water.

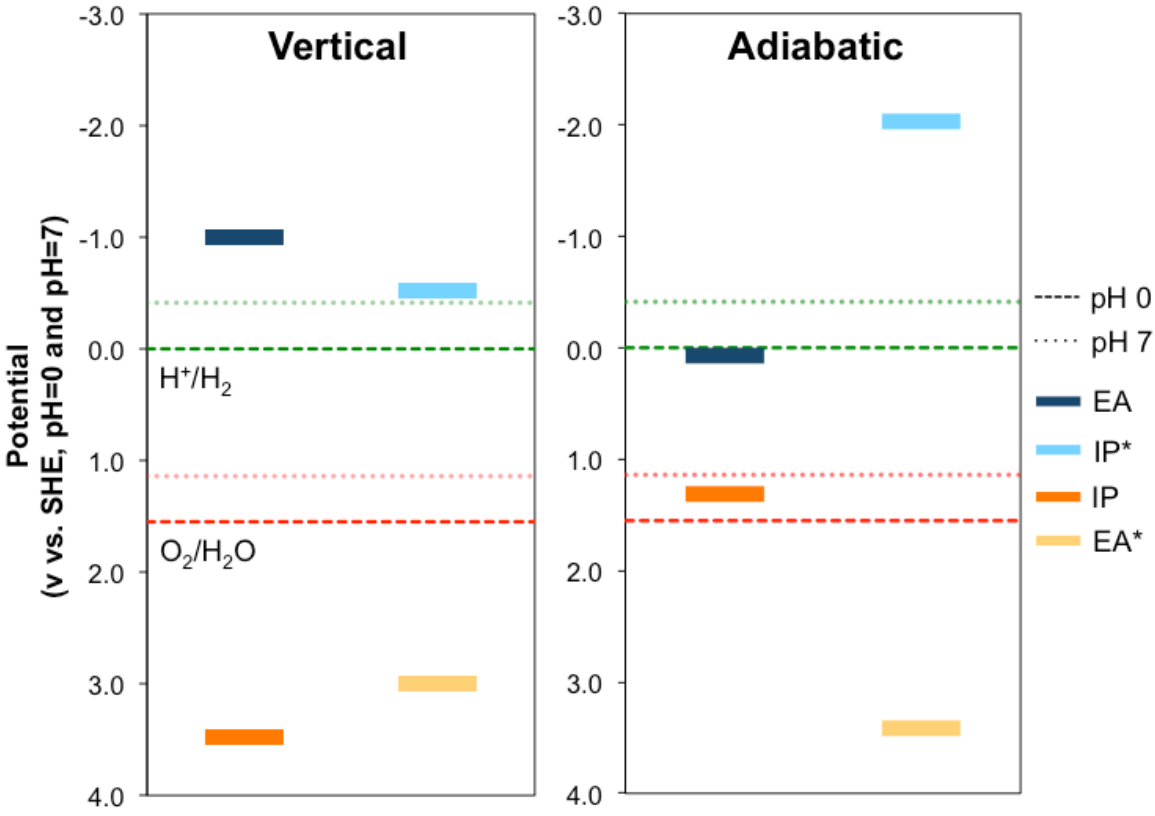

Figure 6.5 (TD-)CAM-B3LYP predicted EA, IP, EA* and IP* vertical and adiabatic potentials of the TiO_2 rutile nanoparticle in water, compared to the water-splitting reduction (green line) and oxidation (red line) potentials at pH = 0 (broken lines) and pH = 7 (dotted lines).

Potentials for the triplet exciton are not shown in Figure 6.5, but because of the apparent near degeneracy between the T1 and S1 exciton, see above, they most likely will lie very close if not on top of their S1 equivalents.

What is observed for (TD-)CAM-B3LYP is in line with the potentials calculated with (TD-)B3LYP, which describe a very similar behaviour. Also with (TD-)B3LYP the IP and EA adiabatic potentials do not catalyse spontaneously neither the reduction or the oxidation half reactions for the overall water splitting reaction.

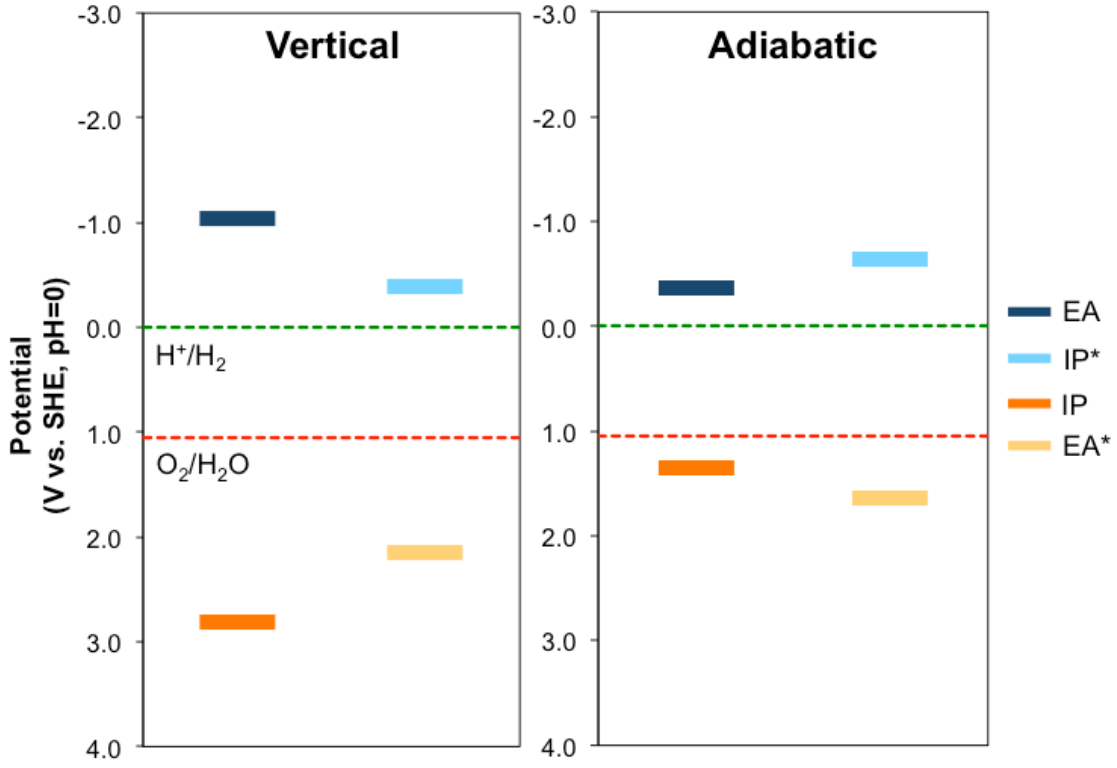

Figure 6.6 (TD-)B3LYP predicted EA, IP, EA* and IP* vertical and adiabatic potentials of the TiO_2 rutile nanoparticle in water, compared to the water-splitting reduction (green line) and oxidation (red line) potentials at pH = 0.

6.4 Water splitting and the effect of particle size

The rutile nanoparticle potentials discussed above, present an interesting situation, where the material's thermodynamic ability to drive the water splitting half reactions is significantly different for free and self-trapped electronic states. To a certain extent, the sets of vertical and adiabatic potentials represent two different physical limits. Vertical potentials describe the situation where the rate of the elementary half-reactions driven by the photocatalyst, or the rate of hole and/or electron transport to a co-catalyst, is significantly faster than the nuclear relaxation associated with self-trapping, while adiabatic potentials represent the exact opposite limit. In the absence of the ability to perform ab-initio excited state molecular dynamic calculations on such particles (introduced in Chapter 2 and employed in Chapter 7 on a small TiO_2 nanoparticle), it is difficult to be sure which situation is more realistic for a working rutile nanoparticulate photocatalyst. However, as without self-trapping, dissociation of an exciton into free charge carriers is predicted to be substantially endergonic, see above, and as the rate of any chemical surface reaction is likely to be at best comparable to the rate of nuclear relaxation in the particle, the adiabatic case is probably the most relevant in practice. This would mean that small rutile nanoparticles, like that studied here, are thermodynamically unable to drive the splitting of water. A possible exception to this conclusion would be in the case that addition of a (noble metal) co-catalyst leads to the formation of a heterojunction and a field that field-ionises excitons and sweeps the free electrons or holes out of the rutile nanoparticle.

Building forward on this analysis, one can speculate that the fact that the vertical and adiabatic potentials are significantly different might be one of the reasons behind the experimentally observed change in water splitting activity with particle size. To investigate this hypothesis, we would ideally compare the vertical and adiabatic potentials calculated for the rutile nanoparticles and the rutile bulk. While, as discussed above, calculated vertical potentials for rutile slabs with different surfaces have been reported in the literature, we are not aware of any calculated adiabatic potentials for bulk rutile (surfaces). However, as the difference between the vertical and adiabatic potentials in the case of the free charge carriers (half-reactions (6–e) and (6–f), EA and IP) is essentially their respective self-trapping energies, the self-trapping energies predicted for the nanoparticle and the bulk can be used to estimate how the difference

between the two sets of potentials might change with particle size.

As discussed above, irrespective of the XC energy functional used, the free charge-carrier trapping energies predicted for the small nanoparticle and the rutile nanoparticle (3x3x3) are considerably larger than those previously reported for bulk rutile and rutile surfaces, as well as those calculated for a larger rutile nanoparticle (5x5x5). It thus stands to reason that the magnitude of the difference between the adiabatic and vertical potentials will decrease with increasing particle size and will be at its largest for small nanoparticles. Assuming that the vertical potentials do not change much with particle size, in line with the observed similarities between our calculated nanoparticle vertical potentials and those reported for bulk slabs, this would suggest that the driving forces for reduction and oxidation by self-trapped free charge carriers (IP and EA) is smallest for rutile nanoparticles and increase with increasing particle size. Following the same logic, and while we lack information on the self-trapping of excitons for bulk rutile (surfaces), it is likely that the difference between the vertical and adiabatic potentials involving the exciton (IP* and EA*) should also decrease with increasing particle size. Assuming again roughly constant vertical potentials, the driving forces for reduction and oxidation by the self-trapped exciton would then be largest for rutile nanoparticles and decrease with increasing particle size. This approximate analysis thus suggests that on thermodynamic grounds the activity of rutile nanoparticles should decrease when reducing the particle size and that the limiting factor is the decline in the driving forces for oxidation and reduction by the free charge carriers.

The origin of these large differences between the vertical and adiabatic potentials for the nanoparticle, as well as the large underlying self-trapping energies, is most likely the fact that the nanoparticle structure is much less constrained, more polarisable, compared to that of bulk rutile TiO_2. The atoms in the nanoparticle are hence freer to move when attempting to minimise the strain associated with the localisation of a free charge-carrier or exciton on them.

6.5 Conclusions

In conclusion, small rutile TiO_2 nanoparticles are predicted to be thermodynamically unable to drive photocatalytic water splitting because of the strong self-trapping of free electrons and holes in such nanoparticles. A comparison with the self-trapping energy values calculated for free charge carriers in bulk rutile (surfaces), which are much smaller, further suggests that the experimentally observed reduction in water splitting activity with particle size might be the direct result of the increased stabilisation of self-trapped free charge carriers relative to their non-trapped counterparts in nanoparticles. The origin of the strong self-trapping of free charge carriers in small nanoparticles, finally, is probably related to the fact that the atoms on the surfaces of these nanoparticles are structurally less constrained, even relative to atoms on bulk surfaces.

6.6 References

[1] Maeda, K. *Chem. Commun.* **2013**, *49*, 8404.
[2] Maeda, K. *Catal. Sci. Technol.* **2014**, *4*, 1949.
[3] Maeda, K.; Murakami, N.; Ohno, T. *J. Chem. Phys. C* **2014**, *118*, 9093.
[4] Amano, F.; Nakata, M.; Ishinaga, E. *Chem. Lett.* **2014**, *advpub*.
[5] Sato, S.; White, J. M. *Chem. Phys. Lett.* **1980**, *72*, 83.
[6] Tang, J.; Durrant, J. R.; Klug, D. R. *J. Am. Chem. Soc.* **2008**, *130*, 13885.
[7] Banno, H.; Kariya, B.; Isu, N.; Ogawa, M.; Miwa, S.; Sawada, K.; Tsuge, J.; Imaizumi, S.; Kato, H.; Tokutake, K.; Deguchi, S. *Green and Sustainable Chemistry* **2014**, *4*, 87.
[8] Ohno, T.; Sarukawa, K.; Matsumura, M. *J. Phys. Chem. B* **2001**, *105*, 2417.
[9] Shkrob, I. A.; Sauer, M. C. *J. Phys. Chem. B* **2004**, *108*, 12497.
[10] Testino, A.; Bellobono, I. R.; Buscaglia, V.; Canevali, C.; D'Arienzo, M.; Polizzi, S.; Scotti, R.; Morazzoni, F. *J. Am. Chem. Soc.* **2007**, *129*, 3564.
[11] Kim, W.; Tachikawa, T.; Moon, G.-h.; Majima, T.; Choi, W. *Angew. Chem. Int. Ed.* **2014**, *53*, 14036.
[12] Ni, M.; Leung, M. K. H.; Leung, D. Y. C.; Sumathy, K. *Renew. Sust. Energ. Rev.* **2007**, *11*, 401.
[13] Prieto-Mahaney, O.-O.; Murakami, N.; Abe, R.; Ohtani, B. *Chem. Lett.* **2009**, *38*, 238.
[14] Abe, R. *Bull. Chem. Soc. Jpn.* **2011**, *84*, 1000.
[15] Ravelli, D.; Dondi, D.; Fagnoni, M.; Albini, A. *Chem. Soc. Rev.* **2009**, *38*, 1999.
[16] Li, G.; Gray, K. A. *Chem. Phys.* **2007**, *339*, 173.
[17] Kumar, S. G.; Devi, L. G. *J. Phys. Chem. A* **2011**, *115*, 13211.
[18] Scanlon, D. O.; Dunnill, C. W.; Buckeridge, J.; Shevlin, S. A.; Logsdail, A. J.; Woodley, S. M.; Catlow, C. R. A.; Powell, M. J.; Palgrave, R. G.; Parkin, I. P.; Watson, G. W.; Keal, T. W.; Sherwood, P.; Walsh, A.; Sokol, A. A. *Nature Materials* **2013**, *12*, 798.
[19] Kapilashrami, M.; Zhang, Y.; Liu, Y.-S.; Hagfeldt, A.; Guo, J. *Chem. Rev.* **2014**, *114*, 9662.
[20] Quesada-Cabrera, R.; Sotelo-Vazquez, C.; Bear, J. C.; Darr, J. A.; Parkin, I. P. *Adv. Mater. Interfaces* **2014**, *1*, n/a.
[21] Ohtani, B.; Ogawa, Y.; Nishimoto, S. *J. Chem. Phys. B* **1997**, *101*, 3746.
[22] Kočí, K.; Obalová, L.; Matějová, L.; Plachá, D.; Lacný, Z.; Jirkovský, J.; Šolcová, O. *Appl. Catal. B* **2009**, *89*, 494.
[23] Anpo, M.; Shima, T.; Kodama, S.; Kubokawa, Y. *J. Phys. Chem.* **1987**, *91*, 4305.
[24] Xu, N. P.; Shi, Z. F.; Fan, Y. Q.; Dong, J. H.; Shi, J.; Hu, M. Z. C. *Ind. Eng. Chem. Res.* **1999**, *38*, 373.
[25] Mattioli, G.; Alippi, P.; Filippone, F.; Caminiti, R.; Amore Bonapasta, A. *J. Phys. Chem. C* **2010**, *114*, 21694.
[26] Di Valentin, C.; Selloni, A. *J. Phys. Chem. Lett.* **2011**, *2*, 2223.
[27] Varley, J. B.; Janotti, A.; Franchini, C.; Van de Walle, C. G. *Phys. Rev. B* **2012**, *85*.
[28] Zawadzki, P.; Laursen, A. B.; Jacobsen, K. W.; Dahl, S.; Rossmeisl, J. *Energy Environ. Sci.* **2012**, *5*, 9866.
[29] Spreafico, C.; VandeVondele, J. *Phys. Chem. Chem. Phys.* **2014**, *16*, 26144.
[30] Dehaart, L. G. J.; Blasse, G. *J. Sol. State Chem.* **1986**, *61*, 135.

[31] Sildos, I.; Suisalu, A.; Aarik, J.; Sekiya, T.; Kurita, S. *J. Lumin.* **2000**, *87–89*, 290.
[32] Watanabe, M.; Hayashi, T. *J. Lumin.* **2005**, *112*, 88.
[33] Kernazhitsky, L.; Shymanovska, V.; Gavrilko, T.; Naumov, V.; Fedorenko, L.; Kshnyakin, V.; Baran, J. *J. Lumin.* **2014**, *146*, 199.
[34] Guiglion, P.; Butchosa, C.; Zwijnenburg, M. A. *J. Mater. Chem. A* **2014**, *2*, 11996.
[35] Pascual, J.; Camassel, J.; Mathieu, H. *Phys. Rev. B* **1978**, *18*, 5606.
[36] Stevanovic, V.; Lany, S.; Ginley, D. S.; Tumas, W.; Zunger, A. *Phys. Chem. Chem. Phys.* **2014**, *16*, 3706.
[37] Blagojevic, V.; Chen, Y.-R.; Steigerwald, M.; Brus, L.; Friesner, R. A. *J. Phys. Chem. C* **2009**, *113*, 19806.
[38] Li, Y.-F.; Liu, Z.-P. *J. Am. Chem. Soc.* **2011**, *133*, 15743.
[39] Zhang, J.; Hughes, T. F.; Steigerwald, M.; Brus, L.; Friesner, R. A. *J. Am. Chem. Soc.* **2012**, *134*, 12028.
[40] Zhang, J.; Steigerwald, M.; Brus, L.; Friesner, R. A. *Nano Lett.* **2014**, *14*, 1785.
[41] Rocca, D.; Gebauer, R.; De Angelis, F.; Nazeeruddin, M. K.; Baroni, S. *Chem. Phys. Lett.* **2009**, *475*, 49.
[42] Shevlin, S. A.; Woodley, S. M. *J. Phys. Chem. C* **2010**, *114*, 17333.
[43] Taylor, D. J.; Paterson, M. J. *J. Chem. Phys.* **2010**, *133*, 204302.
[44] Sanchez-de-Armas, R.; Oviedo, J.; San-Miguel, M. A.; Sanz, J. F. *J. Chem. Theory Comput.* **2010**, *6*, 2856.
[45] De Angelis, F.; Fantacci, S.; Gebauer, R. *J. Phys. Chem. Lett.* **2011**, *2*, 813.
[46] Chiodo, L.; Salazar, M.; Romero, A. H.; Laricchia, S.; Della Sala, F.; Rubio, A. *J. Phys. Chem.* **2011**, *135*, 244704.
[47] Auvinen, S.; Alatalo, M.; Haario, H.; Jalava, J. P.; Lamminmäki, R. J. *J. Phys. Chem. C* **2011**, *115*, 8484.
[48] Taylor, D. J.; Paterson, M. J. *Chem. Phys.* **2012**, *408*, 1.
[49] Berardo, E.; Hu, H.; Kowalski, K.; Zwijnenburg, A. M. *J. Chem. Phys.* **2013**, *139*.
[50] Galynska, M.; Persson, P. *Int. J. Quant. Chem.* **2013**, *113*, 2611.
[51] Kandada, A. R.; Fantacci, S.; Guarnera, S.; Polli, D.; Lanzani, G.; De Angelis, F.; Petrozza, A. *ACS Appl. Mater. Inter.* **2013**, *5*, 4334.
[52] Mattioli, G.; Amore Bonapasta, A.; Bovi, D.; Giannozzi, P. *J. Phys. Chem. C* **2014**.
[53] Hung, L.; Baishya, K.; Öğüt, S. *Phys. Rev. B* **2014**, *90*, 165424.
[54] Berardo, E.; Hu, H.-S.; Shevlin, S. A.; Woodley, S. M.; Kowalski, K.; Zwijnenburg, M. A. *J. Chem. Theory Comput.* **2014**, *10*, 1189.
[55] Berardo, E.; Hu, H.-S.; van Dam, H. J. J.; Shevlin, S. A.; Woodley, S. M.; Kowalski, K.; Zwijnenburg, M. A. *J. Chem. Theory Comput.* **2014**, *10*, 5538.
[56] Nunzi, F.; Agrawal, S.; Selloni, A.; De Angelis, F. *J. Chem. Theory Comput.* **2015**.
[57] Butchosa, C.; Guiglion, P.; Zwijnenburg, M. A. *J. Phys. Chem. C* **2014**, *118*, 24833.
[58] Zhan, C.-G.; Dixon, D. A. *J. Phys. Chem. A* **2001**, *105*, 11534.
[59] Bryantsev, V. S.; Diallo, M. S.; Goddard Iii, W. A. *J. Phys. Chem. B* **2008**, *112*, 9709.
[60] Trasatti, S. *J Electroanal. Chem. Interfacial Electrochem* **1974**, *52*, 313.

[61] *The absolute electrode potential: An explanatory note (recommendations 1986)* **1986**, *209*, 417.
[62] Yanai, T.; Tew, D. P.; Handy, N. C. *Chem. Phys. Lett.* **2004**, *393*, 51.
[63] Becke, A. D. *J. Chem. Phys.* **1993**, *98*, 5648.
[64] Godbout, N.; Salahub, D. R.; Andzelm, J.; Wimmer, E. *Can. J. Chem* **1992**, *70*, 560.
[65] Tomasi, J.; Mennucci, B.; Cammi, R. *Chem. Rev.* **2005**, *105*, 2999.
[66] Klamt, A.; Schuurmann, G. *J. Chem. Soc., Perkin Trans. 2* **1993**, 799.
[67] Schmidt, M. W.; Baldridge, K. K.; Boatz, J. A.; Elbert, S. T.; Gordon, M. S.; Jensen, J. H.; Koseki, S.; Matsunaga, N.; Nguyen, K. A.; Su, S. J.; Windus, T. L.; Dupuis, M.; Montgomery, J. A. *J. Comput. Chem.* **1993**, *14*, 1347.
[68] van Wuellen, C. *J. Comput. Chem.* **2011**, *32*, 1195.
[69] Furche, F.; Ahlrichs, R.; Haettig, C.; Klopper, W.; Sierka, M.; Weigend, F. *WIREs Comput. Mol. Sci.* **2014**, *4*, 91.
[70] Furche, F.; Ahlrichs, R. *J. Chem. Phys.* **2004**, *121*, 12772.
[71] Bode, B. M.; Gordon, M. S. *J. Mol. Graphics Mod.* **1998**, *16*, 133.
[72] Xu, M.; Gao, Y.; Moreno, E.; Kunst, M.; Muhler, M.; Wang, Y.; Idriss, H.; Wöll, C. *Phys. Rev. Lett.* **2011**, *106*, 138302.
[73] Peach, M. J. G.; Benfield, P.; Helgaker, T.; Tozer, D. J. *J. Chem. Phys.* **2008**, *128*, 44118.

Chapter 7

Excited State Dynamics of a Small TiO_2 Nanoparticle in Contact with Water Molecules

This study attempts to elucidate the dynamics of the excited state processes involved in the photochemical water splitting reaction observed experimentally on TiO_2 nanoparticles. Specifically, in this chapter the photo-dynamics of a small hydrated TiO_2 nanoparticle are investigated by employing the linear response TD-DFT Fewest Switches Surface Hopping method (TD-DFT/FSSH).

The work in this chapter has been done during my summer visit to the group of Prof. Filipp Furche at the University of California Irvine.

7.1 Introduction

As already discussed in Chapters 1 and 6, the discovery of photocatalytic water splitting on TiO_2 based materials has triggered world-wide efforts in order to understand its reaction mechanism and improve the material's properties. However, due to the lack of direct experimental evidence, different models of the mechanism lead to contradicting conclusions and the individual steps of the water splitting reaction are still under debate. Originally, the water splitting reaction on rutile TiO_2 surfaces was believed to be initiated via an acid-base type of mechanism [1,2], by a nucleophilic attack of a water molecule to a Ti-O-Ti bridge oxygen, accompanied by the transfer of a surface trapped hole [3]. Only recently, Tan *et al.* [4] demonstrated in a scanning tunneling microscope study of photo-induced water dissociation on a rutile TiO_2 (110) surface that the initial step of the water splitting mechanism should correspond to a photo-oxidation, as shown in reaction (7–1):

$$H_2O + h^+ \rightarrow \cdot OH + H^+ \qquad (7\text{–}1)$$

where h^+ corresponds to a hole in TiO_2 generated after the absorption of light. Nonetheless, it needs to be kept in mind that the specific water splitting mechanism could depend on many different factors, such as sample's size, structure (e.g. surface, nanoparticle or nanotube) and environment, making the experimental identification of universal structure−property relationships for TiO_2 based materials even more challenging.

Atomistic modelling of TiO_2/water interfaces can provide insightful details into the microscopic physical and chemical processes involved during the water splitting reaction [5]. Previous theoretical studies on photocatalytic applications of rutile and anatase TiO_2 surfaces employed ground state calculations (e.g. DFT) to investigate the effect of excited electronic states on reaction energetics [3,6-13], while completely neglecting charge transfer processes, which can strongly affect the overall water splitting reaction rate [14]. There is therefore a clear need for a computational method that allows the efficient treatment of excited state electron-hole dynamics in TiO_2 based materials [14]. With this intent in mind, Prezhdo *et al*. [15-17] have successfully employed non-adiabatic excited state dynamics to describe photo-induced charge separation in dye sensitised semiconductor solar cells (e.g. TiO_2 based technology).

Tritsaris *et al*. [14], focusing on the photocatalytic applications of TiO_2, have recently used the Ehrenfest approximation (Chapter 2) within the framework of the real-time TD-DFT propagation to investigate the dynamics of the photogenerated hole at the rutile TiO_2/water interface.

In this chapter, I will focus on dynamic processes taking place on the excited state PES of a small TiO_2 nanoparticle in direct contact with water molecules. Specifically, I will investigate the particle's excited state lifetimes, analyse the effects of time and temperature on its emission spectrum and define, where possible, the first steps of the water splitting mechanism. The methodology employed in this chapter consists of the linear response TD-DFT Fewest Switches Surface Hopping (TD-DFT/FSSH). This methodology was recently implemented by Tapavicza *et al.* [18,19] in Turbomole and enabled non-adiabatic molecular dynamic simulations for molecular systems of the size of vitamin D (i.e. small nanoparticles, ~ 25 atoms) with 0.2-0.4 ns total simulation times. In addition, this particular TD-DFT/FSSH implementation in Turbomole uses atom-centered basis sets, which allow the efficient use of hybrid XC energy functionals. As discussed in Chapters 4, 5 and 6, hybrid XC energy functionals are of fundamental importance for the accurate description of excited state processes in TiO_2 nanoparticles.

7.2 Methodology

The TiO_2 structure used in this study is the small hydroxilated $(TiO_2)_4$ nanoparticle, already discussed in Chapters 4 and 5, with two additional molecules of water adsorbed (Figure 7.1). As CAM-B3LYP is not currently implemented in Turbomole 6.6, the computational package used for this study, all the DFT and TD-DFT calculations employed either the B3LYP and BHLYP XC energy functionals. In order to keep the calculations tractable on the available computational resources, the small def2-SV(P) basis set was used in all the MD simulations (Table 7.1 and section 7.3.2 show a comparison of def2-SV(P) and def2-TZVP results). A total of two excited states were considered at each time step, but only coupling between the ground and first excited states (namely, S0 and S1) was considered in the surface-hopping algorithm.

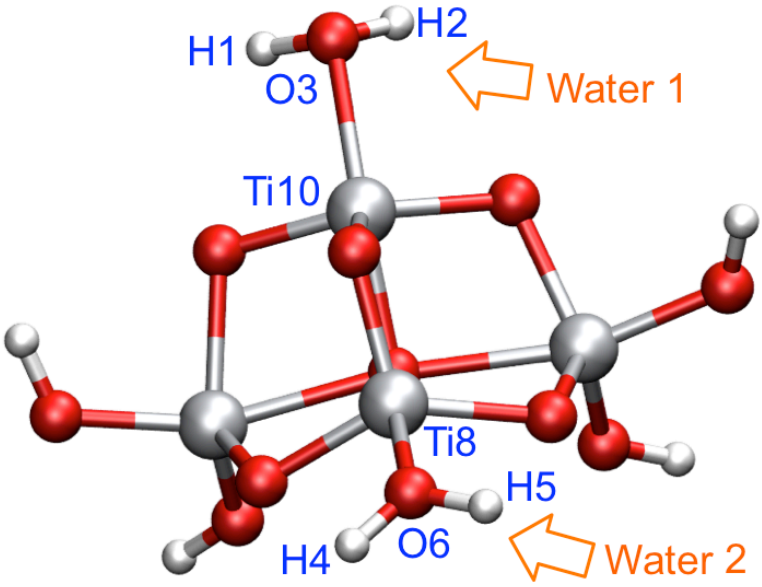

Figure 7.1 $(TiO_2)(OH)_4(H_2O)_2$ particle, where the two molecularly absorbed waters and the relevant atoms discussed later in the text are labeled explicitly. Red spheres denote oxygen atoms, whereas gray and white represent titanium and hydrogen atoms respectively.

The initial structures for the TD-DFT/FSSH trajectories were taken from a ground state BO molecular dynamics run (BOMD, trajectory at 300 K), where the total energy of the system was kept constant (NVE-ensemble). The BOMD simulations employed a time step of 40 a.u. (~ 1 fs) for the propagation of the nuclear positions and were propagated for around 3 ps. For each XC energy functional, 30 initial structures and velocities were chosen randomly from the ground state BOMD trajectories as starting points for the TD-DFT/FSSH simulations. For each trajectory the nanoparticles were excited in their

first excited state (S1) and the nuclear positions were propagated conserving the total energy of the system (NVE). The TD-DFT/FSSH simulations employed a time step of 40 a.u. and the trajectories were propagated for 2 ps.

Previous works [19,20] found that, despite the general accuracy of TD-DFT for the calculation of excitation energies and forces, it predicts the intersection space between two PESs with wrong dimensionality. In adiabatic TD-DFT there is only one degree of freedom that splits the degeneracy in the close vicinity of the CX; instead of a touching point, there is a touching seam if the PES is plotted along the branching coordinates [19]. Nevertheless, this qualitative failure of TD-DFT is only found in the proximity of the CX and recent works by Tapavictza [21] and Huix-Rolland [22] showed that in adiabatic TD-DFT the point of contact is described as a small intersection circle that exhibits an area of singlet instabilities. In all the excited state calculations shown in this chapter the Tamm-Dancoff Approximation (TDA) to TD-DFT, already introduced in Chapter 2 of this thesis, was employed. TDA is employed to contain convergence difficulties that arise in regions of strong coupling between the ground state S0 and the lowest excited state S1 surfaces during a TD-DFT/FSSH trajectory. As shown in previous studies, TD-DFT/TDA exhibits smaller instability regions on the PESs and whenever a trajectory reaches a single instability (i.e. imaginary excitation energy in TD-DFT/TDA) a switch to the ground state is enforced [18,21,23,24]. This approximation has been shown to provide an accurate prediction of the excited state dynamics comparable to CASSCF [18,19,24].

7.3 Results & Discussion

In this section, I will first discuss the results of the ground state dynamics in preparation for the FSSH/TD-DFT simulations. Then, after comparing the vertical excitation energies calculated for the two XC energy functionals (B3LYP and BHLYP) and commenting on the effect of basis set size on the final energy differences, I will present the overall results of the TD-DFT/FSSH MD. Finally, I will analyse some selected FSSH/TD-DFT trajectories in detail and discuss the mechanism of the initial steps of the water splitting reaction.

7.3.1 Ground state BOMD

Changes in the particle's bond distances during the BOMD trajectories for both B3LYP and BHLYP suggest that thermal effects randomly influence the movement of the nuclei, but no clear chemical reaction involving the molecularly absorbed waters (where bonds are broken and new ones formed) is observed during the propagation of both trajectories. Figure 7.2 shows how the bond lengths of the atoms labeled in Figure 7.1 vary during the B3LYP and BHLYP trajectories. It can be seen that during the MD the bond lengths oscillate around their equilibrium distance. The selected bond lengths (H1-H2, H4-H5 and O3-Ti10, O6-Ti8) oscillate around 1.6 and 2.1 Å, for the H-H and O-Ti distances respectively. Figure 7.2 demonstrates how during the whole length of the ground state MD trajectories the two molecularly absorbed waters do not split (i.e. no O-H bond break is observed and the waters' H-H distance is kept constant) and remain in close proximity of the TiO_2 particle. A similar analysis can be performed in the case of trajectories propagated at higher temperatures. For example, in Figure 7.3 a B3LYP trajectory at 500 K does not show any clear difference, apart from larger oscillations caused by higher thermal motion, when compared with the room temperature runs (300 K).

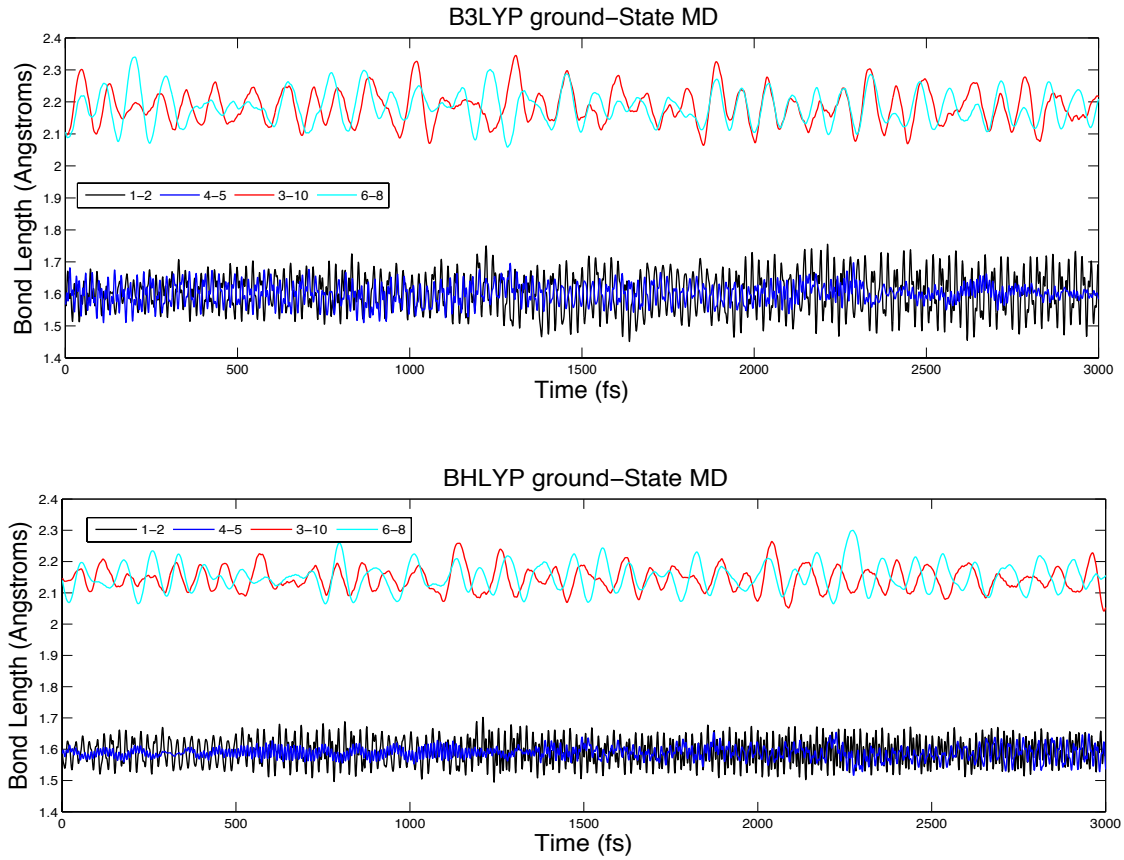

Figure 7.2 B3LYP (top) and BHLYP (bottom) bond distances (Å) vs time (fs) in a ground state BOMD trajectory at 300 K. The atom numbers shown in the legend refer to the labels in Figure 7.1.

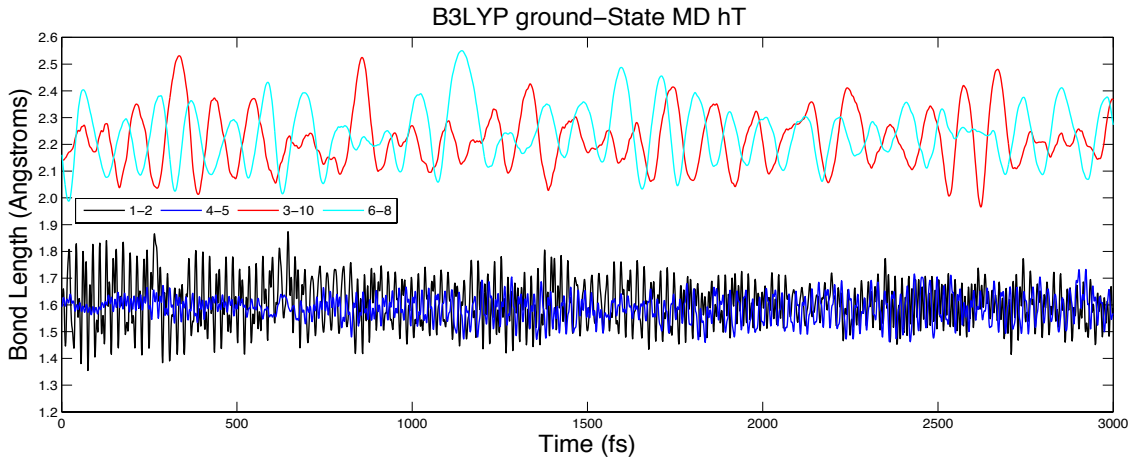

Figure 7.3 Bond distances (Å) vs time (fs) for a high temperature (500 K) B3LYP ground state BOMD trajectory.

7.3.2 Vertical Excitation Energies

The lowest two vertical singlet excitation energies for the $(TiO_2)(OH)_4(H_2O)_2$ particle have been computed with TD-B3LYP and TD-BHLYP and the two different def2-SV(P) and def2-TZVP basis sets (Table 7.1). In agreement with the results from the previous chapters, the use of TD-BHLYP over TD-B3LYP generally results in a rigid upward shift of the excitation energies by approximately 1 eV. However, it needs to be kept in mind that this comparison at the ground state geometries might hide issues with describing the excited PES for geometries far away from the ground state equilibrium one, as already discussed in Chapter 5. TD-DFT/def2-TZVP calculations suggest that for the case of both XC energy functionals the S2-S1 energy gap is equal to 0.2 eV. Furthermore, for the case of both XC energy functionals, the use of the smaller basis set results in a downward shift of the excitation energies of approximately 0.2 eV and a final S2-S1 energy difference of 0.1 eV. All the excited states calculated in Table 7.1 are predicted to be non-dark in character, but they all are predicted to show very weak absorption intensities (i.e. $f \sim 10^{-3}/10^{-4}$), where the specific value is both XC energy functional and basis set dependent. As the use of the smaller basis set leads to a redshift of the two lowest excitation energies of approximately 0.2 eV, which is within the accuracy of the DFT approach, but at a much smaller computational cost relative to def2-TZVP, def2-SV(P) was employed throughout this work.

Table 7.1 Excitations energies (ΔE) are in eV.

State		TD-B3LYP		TD-BHLYP	
		def2-SV(P)	**def2-TZVP**	**def2-SV(P)**	**def2-TZVP**
S1	**ΔE**	4.0	4.1	5.0	5.2
	f	3.0E-04	7.0E-04	1.0E-03	2.1E-03
S2	**ΔE**	4.1	4.3	5.1	5.4
	f	3.7E-04	1.0E-03	6.0E-04	4.5E-04

7.3.3 TD-DFT/FSSH Excited state dynamics

In order to understand how the temperature might affect the excited state properties of TiO_2 nanosystems, for both B3LYP and BHLYP 30 different TD-DFT/FSSH trajectories were propagated using initial geometries chosen randomly from the ground state BOMD trajectories of the small TiO_2 particle (discussed in Section 7.3.1). The

small differences in the initial TiO_2 particle's geometries and velocities lead to different independent SH trajectories. As shown in Figure 7.4 the distribution in the initial conditions of the 30 different trajectories and the high thermal disorder at 300 K lead to a spread in the ground and excited state energies during the propagation. From Figure 7.4 no clear conclusions can be drawn about any specific excited state trajectory, as different initial conditions strictly influence the time ranges of excited state processes, however B3LYP and BHLYP simulations show an inherent difference. In the case of both XC energy functionals, all the FSSH MD trajectories are initially on the lowest excited state (S1 green dots are located on the red line), but for B3LYP a prominent de-excitation process (transition from S1 to S0) is observed in the initial stages of the trajectories specifically. For B3LYP most surface hops take place before 1 ps, with all the trajectories in the final stages of the simulation being propagated on the ground state surface (S0). For BHLYP, as already discussed earlier, the S1-S0 gap is higher in energy and therefore the overall de-excitation processes, which depend from the non-adiabatic couplings between S0 and S1, are less probable if compared to the B3LYP case. For BHLYP even after 2 ps some of the initial trajectories are still being propagated on the lowest excited state S1.

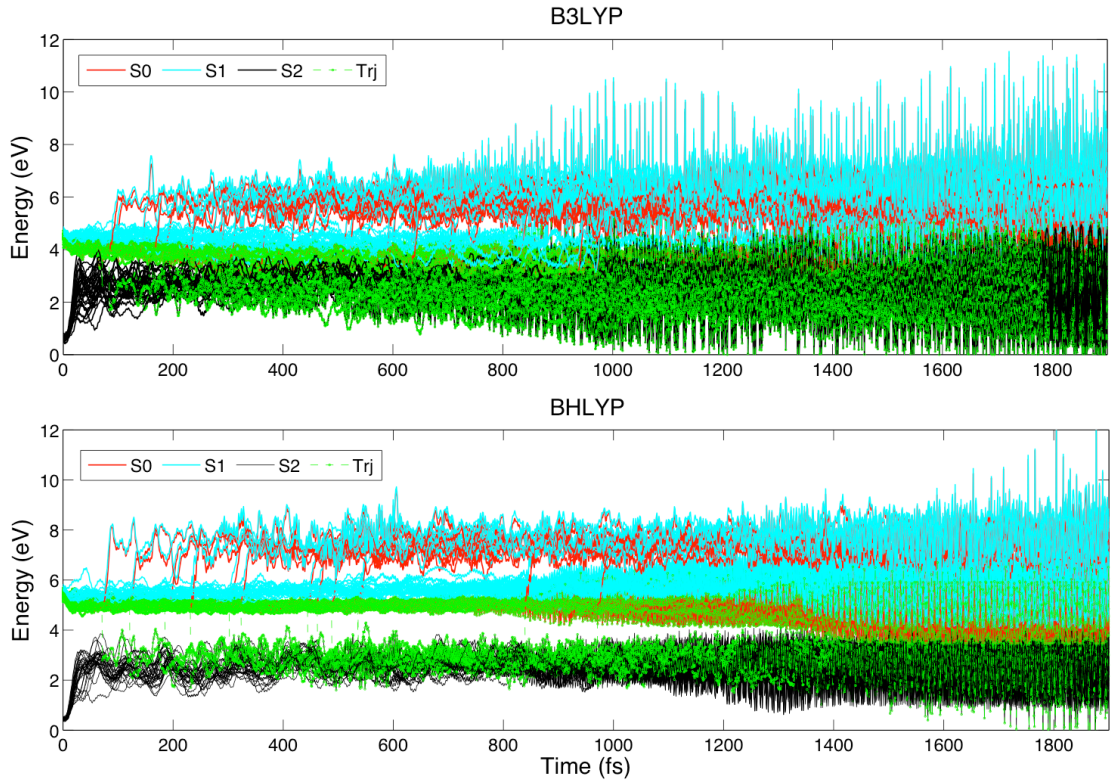

Figure 7.4 Set of 30 FSSH MD trajectories for the TiO_2 particle as calculated with B3LYP (top) and BHLYP (bottom). The energy at each step of the trajectory is compared with the GM ground state energy (eV) and plotted against time (fs). Black lines represent the ground state (S0), red the lowest excited state (S1), cyan the second lowest excited state (S2), and green dots indicate the current state for which nuclear forces are calculated. Green dashed lines indicate the trajectories for which a surface hop between S1 and S0 was observed.

7.3.4 Excited state relaxation lifetime

Experimentally, the decay of the excited state population of nanoparticles can only be measured indirectly, for example by techniques such as pump and probe spectroscopy, which probe the absorption and emission of the excited state. Theoretically the nanoparticle's bright lifetimes can be investigated through the use of the Einstein equation (already employed in Chapter 6 for the rutile particle), whereas excited state populations and non-radiative de-excitation processes are directly available from TD-DFT/FSSH simulations. When the Einstein equation is used to calculate the bright lifetimes for the TiO_2 particle, the absolute relaxation times obtained for the vertical excitation from the ground state geometry correspond to 2 and 0.4 μs for B3LYP and BHLYP, respectively. However, as already discussed in Chapter 2, the Einstein equation only takes into account the S0-S1 energy gap and the oscillator strength of the electronic transition, while completely neglecting the dynamic effects on the non-

radiative relaxation processes. For this reason the results obtained with the Einstein equation can only be used as a qualitative measure for the overall lifetime of TiO_2 nanoparticles. On the other side, the analysis of the S1 average populations versus simulation time shown in Figure 7.5 for the FSSH MD trajectories clearly suggests that non-radiative de-excitation processes have shorter relaxation times compared to bright de-excitation phenomena. Furthermore, a clear difference in prediction is observed for the two XC energy functionals employed. The smaller S1-S0 energy gap, as calculated with B3LYP/FSSH MD, results in faster relaxation times when compared with BHLYP. B3LYP predicts a non-radiative de-excitation half-life of around 600 fs, where at approximately 1700 fs all the B3LYP trajectories are on the S0 surface and no more re-crossing S0-S1 surface-hops are observed until the end of the simulation.

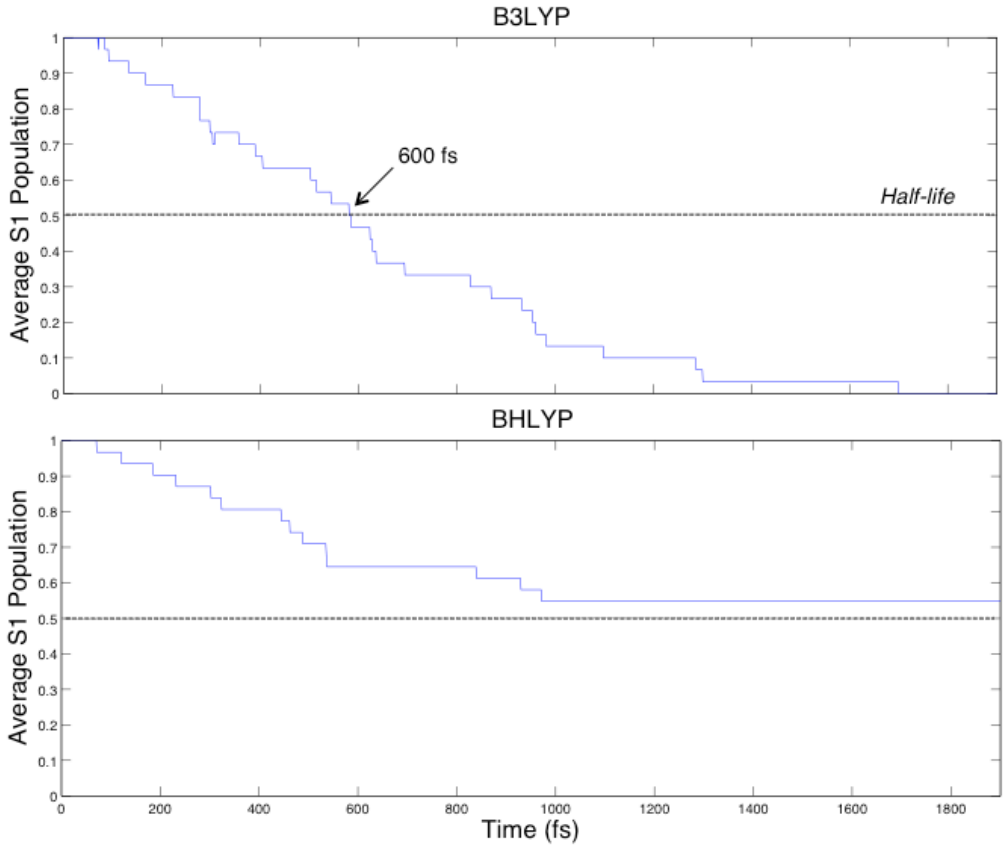

Figure 7.5 Average S1 population (blue line) vs time (fs) of 30 trajectories for the excited state dynamics of the TiO_2 particle as calculated with B3LYP (top) and BHLYP (bottom). For each trajectory, the S1 population is calculated as the square of the TD-DFT Surface Hopping coefficients of the state S1 at each step of the propagation. The black dashed line highlights half-life time, namely the time at which the S1 excited state population corresponds to 0.5.

BHLYP predicts the opposite, longer de-excitation dynamics, and at the end of the simulation only half (0.55) of the total trajectories relaxed to the S0 ground state, while

the remaining half is still propagated on the S1 state. Unluckily, due to the high computational costs required for the TD-DFT/FSSH calculations (for a 2 ps run each one of the 30 trajectories took approximately 1 month running on 8 Xenon processors), the BHLYP trajectories could not be propagated for simulation times longer than 2 ps. However, from these results it is evident how B3LYP predicts relaxation times that are approximately three times shorter (or more) than those obtained from BHLYP. As already mentioned earlier, this difference in relaxation times can be correlated to the larger S0-S1 energy gap as predicted with BHLYP, where weaker non-adiabatic couplings between the two surfaces lead to a lower surface-hopping transition probability. The difference in relaxation times predicted by the two XC energy functionals could also be dependent from the inability of TD-B3LYP to successfully describe CT processes. As discussed in Chapters 4 and 5, hybrid XC energy functionals with low percentage of HF-like exchange generally underestimate excitation energies for TiO_2 nanoparticles when CT processes are being investigated. Moreover, it was also shown that differently from other XC energy functionals, B3LYP erroneously predicted the presence of conical intersections (CX) when the excited state of specific TiO_2 particles were optimised along the S1 state. The results from the B3LYP/FSSH MD suggest, in fact, that most of the trajectories relax from S1 to S0 in the direct vicinity of a CX, regions that correspond to a problematic feature of a PES when described by adiabatic TD-DFT. Levine *et al.* [20] have demonstrated that the higher dimension of the intersection space described by TD-DFT might increase the probability of hitting the intersection seam and cause a faster relaxation to S0 whenever in the proximity of a CX [19].

7.3.5 Excitation-fluorescence spectrum

From the TD-DFT/FSSH simulation it is possible to reproduce the excitation-fluorescence spectrum, which can be obtained by plotting the time average of the oscillator strengths as a function of the absorption and emission energies. Figure 7.6 shows the results obtained for the B3LYP and BHLYP trajectories. For both spectra in Figure 7.6 it can be observed that the emission spectrum is red-shifted compared to the absorption spectrum. The absorption spectra for both XC energy functionals are in good agreement with the vertical excitations shown in Table 7.1. B3LYP emission spectrum is characterised by two main features falling at 1.5 and 0.5 eV, respectively, with the

latter being the most intense one. BHLYP emission spectrum shows a large peaks falling in the energy range from 1.5 to 3.5 eV. In line with the findings from Chapter 5 and with what already discussed above, it looks like B3LYP predicts a larger difference between absorption and emission energies, leading to a larger Stokes' shift (~ 3.5 eV).

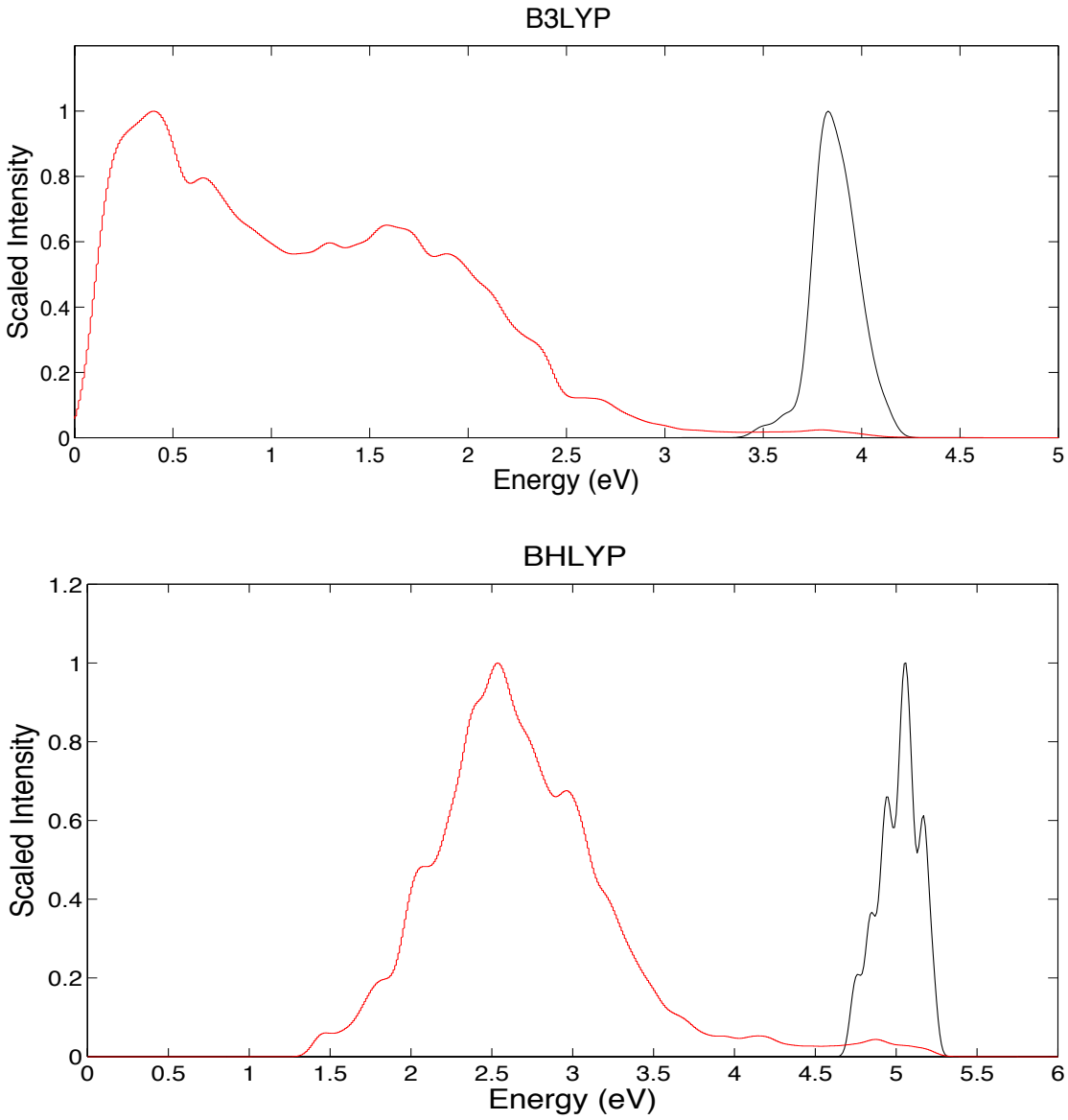

Figure 7.6 B3LYP and BHLYP absorption (black) and emission (red) spectra calculated from 30 TD-DFT/FSSH trajectories of the TiO_2 particle. For every individual spectrum a Gaussian broadening with a standard deviation of 0.05 eV was applied and the intensity of each spectrum has been normalised against the most intense peak. The absorption spectrum was obtained by averaging all the spectra of the first step of the TD-DFT/FSSH simulations. The emission spectrum was averaged over all the S1 excited states calculated prior the observed surface hop during the FSSH simulation.

7.3.6 Analysis of specific interesting TD-DFT/FSSH trajectories

In this section, I will analyse in detail two specific interesting trajectories produced

during the TD-DFT/FSSH simulations for B3LYP and BHLYP, for which a water splitting reaction was observed.

B3LYP In this example (Figure 7.7), the S1-S0 surface-hop takes place at approximately 400 fs in the proximity of a conical intersection between the two PESs. This case is representative for most of the B3LYP trajectories, since the surface-hop is generally observed in the vicinity of a CX, and after the S1-S0 transition has taken place, the two states diverge energetically from each other, with the final trajectory evolving on the ground state surface. The analysis of the time propagation of the system's bond distances shows that in this case both water molecules react with the TiO_2 particle during the simulation.

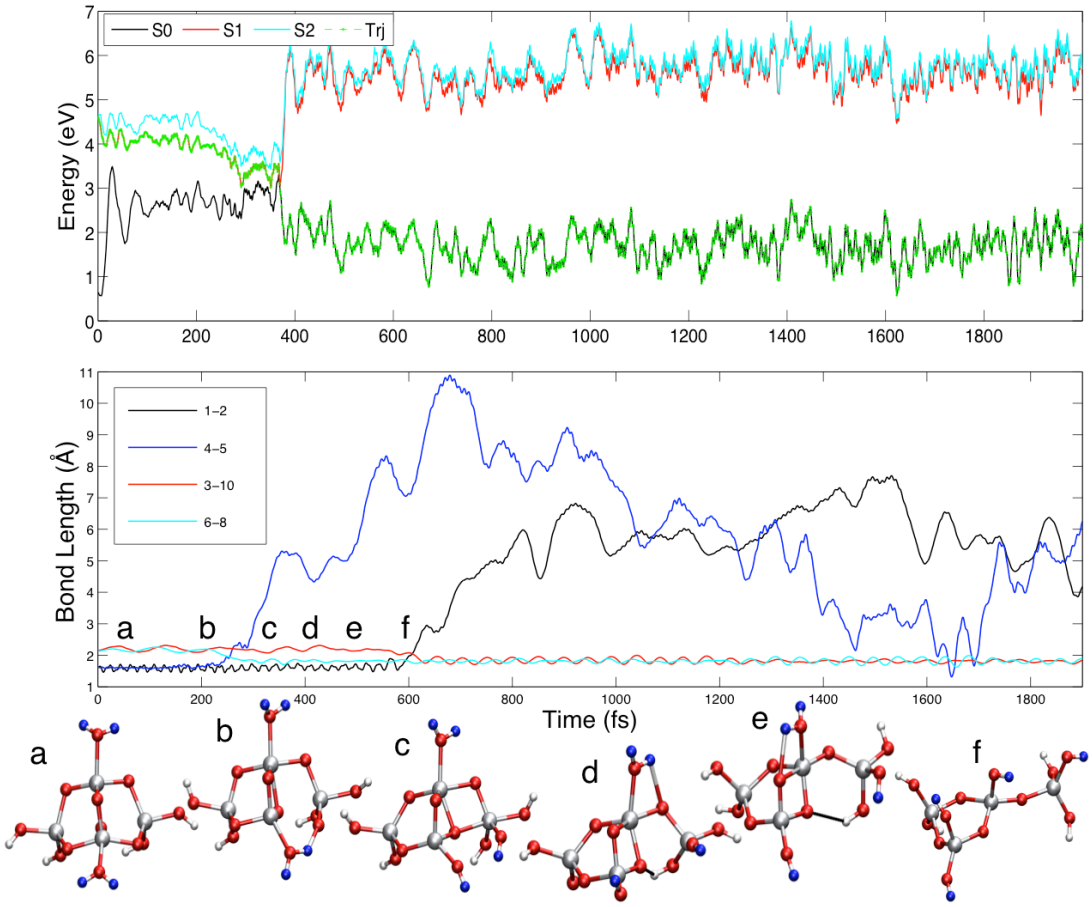

Figure 7.7 (Top) Example of B3LYP trajectory of excited state dynamics in which a –OH rupture is observed in both the molecularly absorbed waters. Black lines represent the ground state (S0), red the lowest excited state (S1), cyan the second lowest excited state (S2), and green dots indicate the current state for which nuclear forces are calculated. Green dashed lines indicate the trajectories for which a surface hop between S1 and S0 was observed. (Bottom) Changes in bond lengths (Å) vs time (fs) along the specific B3LYP trajectory and the molecular structures of the significant points (labeled a-f) of the trajectory. The atom numbers shown in the legend refer to the labels in Figure 7.1 and the hydrogen atoms (H1, H2, H4 and H5) from the molecularly absorbed waters are shown in blue in the molecular structures below the graph.

The bottom part of Figure 7.7 illustrates that both H4-H5 and H1-H2 distances increase drastically in the time range from 200 to 800 fs after the initial excitation. Precisely, at approximately 200 fs, when the trajectory is still propagated on the S1 excited state, the proton H5 from the bottom water molecule is exchanged between the water and the TiO_2 particle (the H bonds to a particle's oxygen atom, detail c in bottom Figure 7.7). During the first OH bond breaking process, while the trajectory is still on the S1 state, the system's temperature slightly increases from 400 to 620 K, leading to a higher thermal movement. The trajectory then hops to the ground state and at around 600 fs the second water molecule starts splitting (details e-f in bottom Figure 7.7), donating the H1 proton to one of the particle's oxygen atoms. The S1-S0 surface hop coincides with a

steep increase in the system's temperature, which at around 600 fs peaks 1200 K. The abrupt increase in temperature, and as a consequence the higher thermal motion, could be the origin of the observed water's reactivity. During the two OH rupture processes the O3-Ti10 and O6-Ti8 bond lengths are decreased and few particle's Ti-O-Ti bonds originally present in the equilibrium structure are broken during the trajectory, leading to a more open structure.

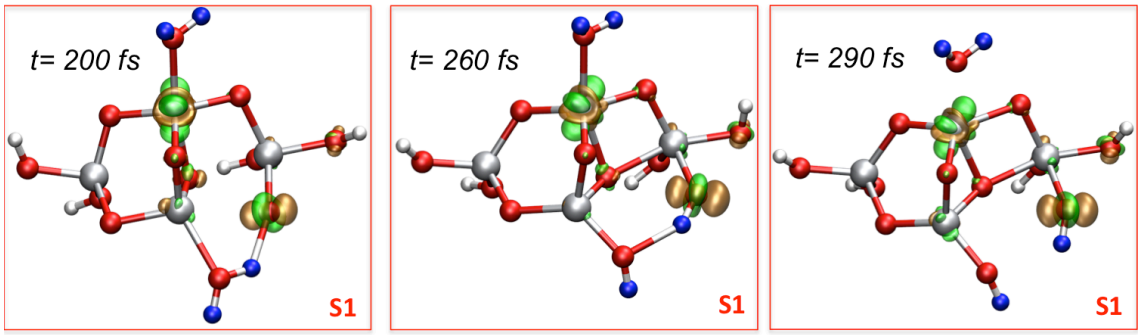

Figure 7.8 Excited state density difference plots obtained for each relevant molecular structure of the first OH rupture observed during the trajectory shown in **Figure 7.7**. The isodensity plots are calculated at a value of 0.02 a.u., where the green lobes represent regions of excess electron density, whereas the gold lobes represent regions deficient in electron density. The hydrogen atoms from the initial molecularly absorbed waters are shown as blue spheres.

Figure 7.8 illustrates the behavior of the system's excited/ground state density difference at different points along the trajectory (both electron –green and hole density –gold are shown). The three boxes in Figure 7.8 show that the overall water splitting mechanism corresponds to an heterolytic process, which involves the spatial separation of charged species (strongly localised electron/hole). Specifically, it can be observed from Figure 7.8 that the first water's OH rupture has its origin on the S1 surface and as the water's proton binds with a bridging (Ti-O-Ti) oxygen atom, the hole strongly localises on the region of the newly created bond. During this process the electron density localises on a nearby particle's titanium atom, which is in the proximity of the other molecularly absorbed water. After the system hops to the ground state (450 fs) both electron and hole densities mostly localise on a particle's Ti-O bond. Figure 7.8 highlights how in this case the water's OH bond breaking is assisted by the hole density localised on the particle (similar mechanism to the one discussed in reaction (6–1)), while the electron density does not play a role in the dissociation mechanism.

BHLYP This trajectory corresponds to one of the few BHLYP cases in which the system relaxes from S1 to S0 within the simulation's time limit of approximately 2 ps.

Specifically, in this example of trajectory (Figure 7.9), the S1-S0 surface-hop takes place at around 240 fs (green dashed line), where the energy gap between the two states is equal to 3.1 eV. In line with what previously shown in Figure 7.6, the emission energy obtained from this trajectory is red-shifted compared to the initial excitation energy of 5.0 eV and it falls in the energy range of the broad emission peak obtained as an average over all BHLYP trajectories. Once this trajectory hops from S1 to S0, it evolves on the ground state surface until the end of the simulation.

The bottom part of Figure 7.9 shows how in this case the water splitting process (H1-H2 distance is increased, leading to a rupture of one of the OH bonds in the water molecule) is observed only after the trajectory is already on the ground state surface. Before the S1-S0 surface hop the system's temperature oscillates around 300 K, and after the transition has taken place the temperature undergoes a steep increase. At 600 fs, when the system's temperature corresponds to 1100 K, one of the two molecularly absorbed waters starts reacting with the TiO_2 particle at 600 fs (detail e in Figure 7.9). The reaction proceeds until the remaining water's OH and the newly formed OH group are spatially separated. In this specific trajectory, the OH bond breaking is associated with a high temperature increase and differently from the B3LYP trajectory, no clear photochemical water splitting reaction is observed.

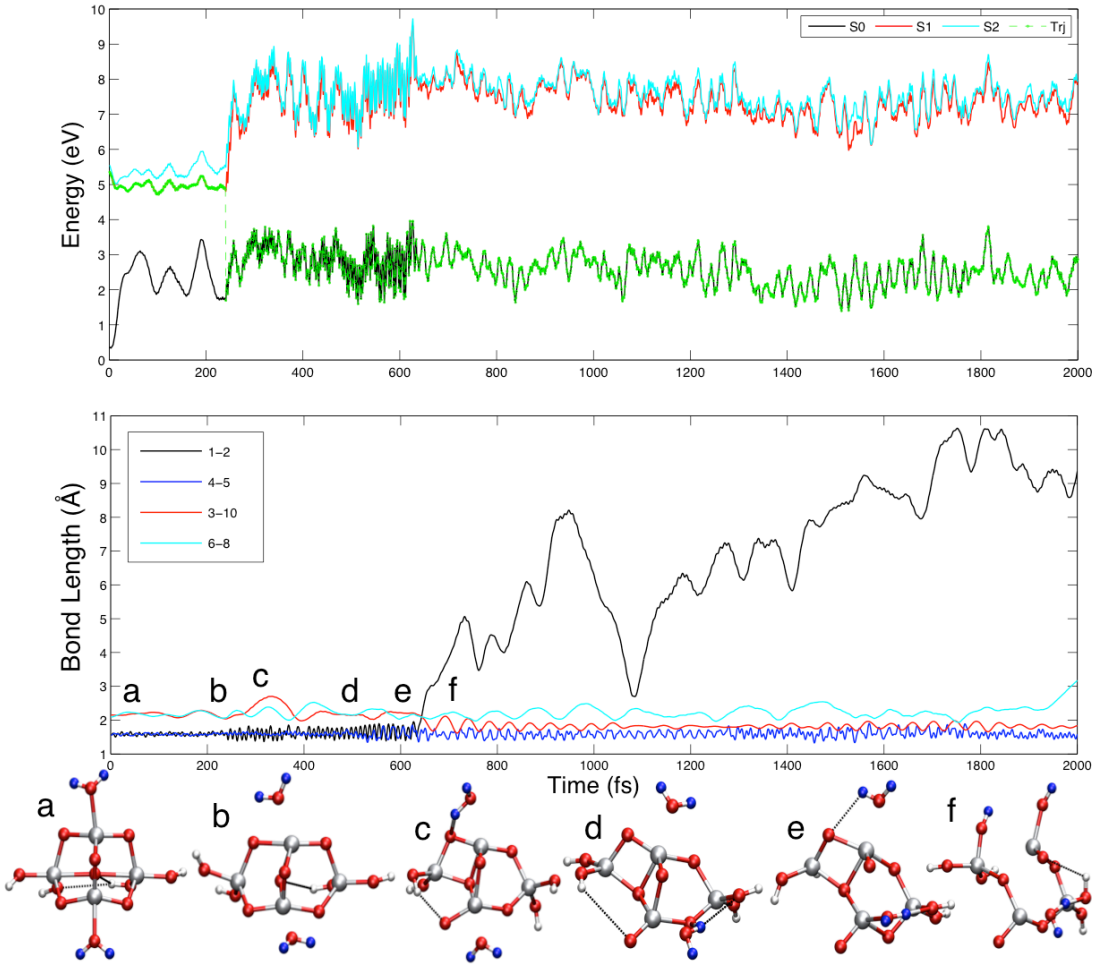

Figure 7.9 (Top) Example of BHLYP trajectory of excited state dynamics in which a –OH rupture is observed in one of the molecularly absorbed waters. Black lines represent the ground state (S0), red the lowest excited state (S1), cyan the second lowest excited state (S2), and green dots indicate the current state for which nuclear forces are calculated. Green dashed lines indicate the trajectories for which a surface hop between S1 and S0 was observed. (Bottom) Propagation of bond lengths (Å) vs time (fs) for the specific BHLYP trajectory and the molecular structures of the significant points (labeled a-f) of the trajectory.

7.4 Conclusions

This study showed how using a TD-DFT/FSSH approach it is possible to easily obtain information about excited state properties of small TiO_2 nanoparticles. In this chapter I investigated the excited state lifetimes and the photo-reactivity of a small hydrated TiO_2 particle and demonstrated that by employing different TD-DFT XC energy functionals large differences in the predictions can be expected. Specifically, I illustrated how the use of B3LYP leads to shorter *non-radiative* excited state lifetimes compared to the ones obtained with BHLYP. However, for both XC energy functionals the *non-radiative* excited state lifetimes are predicted to be in the range of the ps (0.1 – 10), much shorter than the values calculated with the Einstein equation for the bright lifetimes (~ μs). Furthermore, in line with what already discussed in earlier chapters, use of the two different XC energy functionals results in the predictions of substantially different absorption-emission spectra. For B3LYP the most intense PL peak falls in the proximity of 0 eV, and this feature of the B3LYP PL spectrum is probably connected to the XC energy functional's inability to correctly describe CXs between S1 and S0. Finally, I focused in detail on two FSSH trajectories for which a reaction between the TiO_2 particle and the initially molecularly absorbed waters was observed. For these cases I analysed the specific FSSH trajectory trying to understand which were the conditions that triggered the reaction and to describe its mechanism, which in the case of the B3LYP trajectories is found to be heterolytic in character.

This study corresponds to a first attempt of using TD-DFT/FSSH to uncover the initial steps of the photochemical water-splitting reaction catalysed by TiO_2 nanoparticles. That said there is plenty of room for future improvement, where first the complexity of the model can be increased (larger TiO_2 nanoparticle, with a larger number of water molecules in its first solvation sphere and the use of dielectric screening to reproduce the effect of bulk water), second an unrestricted reference to TD-DFT (U-KS) can be employed allowing the description of homolytic processes and finally an efficient thermostat must be employed to maintain the environment's temperature constant during the FSSH trajectory propagation. Keeping all these points in mind, I believe that in the near future NAMD simulations employing the TD-DFT/FSSH algorithm will prove extremely valuable for the interpretation of pump-probe experimental results and the prediction of the mechanism of photochemical reactions.

7.5 References

[1] Imanishi, A.; Okamura, T.; Ohashi, N.; Nakamura, R.; Nakato, Y. *J. Am. Chem. Soc* **2007**, *129*, 11569.

[2] Nakamura, R.; Okamura, T.; Ohashi, N.; Imanishi, A.; Nakato, Y. *J. Am. Chem. Soc* **2005**, *127*, 12975.

[3] Ji, Y.; Wang, B.; Luo, Y. *J. Phys. Chem. C* **2013**, *118*, 1027.

[4] Tan, S.; Feng, H.; Ji, Y.; Wang, Y.; Zhao, J.; Zhao, A.; Wang, B.; Luo, Y.; Yang, J.; Hou, J. G. *J. Am. Chem. Soc* **2012**, *134*, 9978.

[5] Norskov, J. K.; Bligaard, T.; Rossmeisl, J.; Christensen, C. H. *Nat. Chem.* **2009**, *1*, 37.

[6] Cheng, H.; Selloni, A. *Langmuir* **2010**, *26*, 11518.

[7] Sun, C.; Liu, L.-M.; Selloni, A.; Lu, G. Q.; Smith, S. C. *J. Mater. Chem.* **2010**, *20*, 10319.

[8] Chen, J.; Li, Y.-F.; Sit, P.; Selloni, A. *J. Am. Chem. Soc.* **2013**, *135*, 18774.

[9] Lee, J. H.; Selloni, A. *Phys. Rev. Lett.* **2014**, *112*.

[10] Patel, M.; Mallia, G.; Liborio, L.; Harrison, N. M. *Phys. Rev. B* **2012**, *86*, 045302.

[11] Patel, M.; Sanches, F. F.; Mallia, G.; Harrison, N. M. *Phys. Chem. Chem. Phys.* **2014**, *16*, 21002.

[12] Ji, Y.; Wang, B.; Luo, Y. *J. Phys. Chem. C* **2012**, *116*, 7863.

[13] Valdés, Á.; Kroes, G. J. *J. Phys. Chem. C* **2010**, *114*, 1701.

[14] Tritsaris, G. A.; Vinichenko, D.; Kolesov, G.; Friend, C. M.; Kaxiras, E. *J. Phys. Chem. C* **2014**, *118*, 27393.

[15] Duncan, W. R.; Prezhdo, O. V. *J. Am. Chem. Soc* **2008**, *130*, 9756.

[16] Fischer, S. A.; Duncan, W. R.; Prezhdo, O. V. *J. Am. Chem. Soc* **2009**, *131*, 15483.

[17] Guo, Z.; Prezhdo, O. V.; Hou, T.; Chen, X.; Lee, S.-T.; Li, Y. *J. Phys. Chem. Lett.* **2014**, *5*, 1642.

[18] Tapavicza, E.; Bellchambers, G. D.; Vincent, J. C.; Furche, F. *Phys. Chem. Chem. Phys.* **2013**, *15*, 18336.

[19] Tapavicza, E.; Meyer, A. M.; Furche, F. *Phys. Chem. Chem. Phys.* **2011**, *13*, 20986.

[20] Levine, B. G.; Ko, C.; Quenneville, J.; Martinez, T. J. *Mol. Phys.* **2006**, *104*, 1039.

[21] Tapavicza, E.; Tavernelli, I.; Rothlisberger, U.; Filippi, C.; Casida, M. E. *J. Chem. Phys.* **2008**, *129*.

[22] Huix-Rotllant, M.; Natarajan, B.; Ipatov, A.; Wawire, C. M.; Deutsch, T.; Casida, M. E. *Phys. Chem. Chem. Phys.* **2010**, *12*, 12811.

[23] Cordova, F.; Doriol, L. J.; Ipatov, A.; Casidaa, M. E.; Filippi, C.; Vela, A. *J. Chem. Phys.* **2007**, *127*.

[24] Tapavicza, E.; Tavernelli, I.; Rothlisberger, U. *Phys. Rev. Lett.* **2007**, *98*.

Chapter 8

Summary and perspectives

In this thesis, it was shown how the accurate prediction of excited state properties in TiO_2 nanoparticles is of pivotal importance for understanding the atomic scale processes taking place in photovoltaic and photocatalytic applications.

Coupled cluster approaches were employed in this work for the definition of accurate excited state benchmarks for small TiO_2 nanoparticles. In this study, the specific focus has been on different EOM-CC methods that include contributions of triples such as EOM-CCSDT, the approximate iterative active space EOM-CCSDt (I/II/III) method and approaches that treat triple excitations perturbatively, such as CR-EOM-CCSD(T). From those calculations, two different effects were observed with the inclusion of triple excitations: first, a downward rigid shift in the excitation energies and second, a crossing of the excited states. Whenever the systems were *well behaved*, TiO_2 monomer and dimer, only the first effect was observed when going from EOM-CCSD and EOM-CCSDT. For the most *problematic* system investigated in this study, the $(TiO_2)_3$ nanoparticle, the second effect was also observed, leading to the crossing of the two

lowest excited states when moving from EOM-CCSD to EOM-CCSDT. Furthermore, it was demonstrated that while the approximate iterative active-space EOM-CCSDt(I) method yields results that are in good agreement with EOM-CCSDT results, the cheaper EOM-CCSDt(II/III) approaches and the methods that treat triples perturbatively yield results that are not better or even worse than those obtained by EOM-CCSD.

The EOM-CCSDT benchmarks defined in Chapter 3 were then employed to evaluate the suitability of different TD-DFT XC energy functionals for the description of low-energy vertical excitations or excited state relaxation processes taking place in TiO_2 nanoparticles. My results suggest that in the case of vertical excitations TD-DFT generally provides a good qualitative and quantitative fit to excitation energies predicted by the more expensive EOM-CC methods. However, it was also shown that for specific TiO_2 nanoparticles, large deviations (underestimation) relative to EOM-CC calculated excited energies were observed when using the TD-PBE and TD-B3LYP XC energy functionals. My studies suggest that the problems arise for these systems when the relevant excitation has charge transfer (CT) character, for which the exact value is strongly underestimated by standard GGA (PBE) or hybrid (B3LYP) XC energy functionals with low HF like exchange. The same problems were completely absent for TD-CAM-B3LYP and TD-BHLYP.

In the case of excited state relaxation it was also found that TD-CAM-B3LYP and TD-BHLYP yield qualitatively similar results for all TiO_2 nanoparticles, and that they are in agreement with the EOM-CCSD predictions for the specific $(TiO_2)_2$ nanoparticle. On the other hand TD-B3LYP is shown to make rather different predictions both in PLE and excited state minimum geometries of the particles investigated. The issue with TD-B3LYP appears to be again its inherent tendency to spuriously stabilise the energy of CT states, which in this case drives the excited state optimisations towards different structures than those obtained with TD-CAM-B3LYP, TD-BHLYP and EOM-CCSD.

Following the results from these studies I would recommend the use of long-range corrected XC energy functionals (e.g. CAM-B3LYP) for the modelling of excited state processes in TiO_2 (and more generally metal oxide) nanoparticles. Whenever long-range corrected XC energy functionals are not available, I would then strongly support the use of hybrid XC energy functionals with large amounts of HFLE (e.g. BHLYP with 50%) over B3LYP or GGAs.

Following the TD-DFT benchmarking studies for small TiO_2 particles, the optical and photocatalytic properties of a larger rutile nanoparticle were investigated. With this work it was shown that the rutile nanoparticle has a larger optical gap and a stronger self-trapping energy for free charge carriers when compared to bulk rutile. These results suggest that due to the strong self-trapping of free electrons and holes, the nanoparticle is thermodynamically unable to drive the photocatalytic water splitting reaction.
As discussed in Chapter 1, a common approach to modify the material's optical and photocatalytic properties is the inclusion of ions in the metal oxide network. The presence of impurity ions within the TiO_2 nanoparticle could drive trapping processes for free charge carriers and facilitate their spatial separation. Future computational work should investigate the effect of the presence of impurity ions on the nanoparticle's excited state processes and try to understand if doping can be employed to improve the particle's thermodynamic ability to drive the water splitting reaction.

Finally, photo-dynamic properties of a small hydrated TiO_2 nanoparticle were studied with the use of TD-DFT/Fewer Switches Surface Hopping (FSSH). With this work, in line with what discussed above, I demonstrated how the employment of different XC energy functionals (e.g. B3LYP and BHLYP) leads to contrasting results for excited state lifetimes and photo-reactivity. However, both XC energy functionals predicted non-radiative excited state lifetimes to be in the range of 0.1-10 ps. Furthermore, for specific TD-B3LYP trajectories photo-induced water splitting reactions were observed. The analysis of the excited state/ground state density difference for those trajectories highlights the heterolytic character of the initial steps of the water splitting reaction.
The discussed TD-DFT/FSSH investigations employed a restricted KS reference, only allowing to the treatment of heterolytic processes during the water splitting reaction. Future work should employ an unrestricted KS reference for the TD-DFT/FSSH (recently implemented in Turbomole) simulations, leading to the correct inclusion of homolytic effects in the reaction mechanism. Furthermore, while still not implemented in Turbomole, I believe it would be interesting to repeat the TD-DFT/FSSH simulations with a long-range corrected XC energy functional (e.g. CAM-B3LYP), which could provide a more accurate prediction of the photo-dynamics of a small TiO_2 nanoparticle.

Appendix A

Excitation energies and Λ diagnostic values calculated for the hydrated nanoparticles from Chapter 4.

Table A-1 *Excitation energies and Λ values for the four lowest excited states calculated (in eV) for the $Ti(OH)_4$ cluster with S_4 symmetry.*

	TD-PBE	TD-B3LYP	TD-CAM-B3LYP	TD-BHLYP	Λ PBE	Λ B3LYP	Λ CAM-B3LYP	Λ BHLYP
2^1E	5.06	5.63	5.93	6.62	0.36	0.36	0.35	0.35
3^1E	5.06	5.63	5.93	6.62	0.36	0.36	0.35	0.35
1^1A	5.14	5.68	5.97	6.68	0.40	0.39	0.38	0.37
4^1E	5.28	5.82	6.14	6.80	0.43	0.44	0.39	0.37

	EOM-CCSD SV	EOM-CCSD TZ
2^1E	6.08	6.51
3^1E	6.08	6.51
1^1A	6.18	6.59
4^1E	6.28	6.69

Table A-2 *Excitation energies and Λ values for the four lowest excited states calculated (in eV) for the $(TiO_2)_2(H_2O)_2$ cluster with C_{2v} symmetry.*

TD-PBE		TD-B3LYP		TD-CAM-B3LYP		TD-BHLYP		Λ PBE	Λ B3LYP	Λ CAM-B3LYP	Λ BHLYP
2^1B_1	4.13	2^1B_1	4.71	2^1B_1	5.02	2^1B_1	5.63	0.30	0.30	0.31	0.31
1^1A_1	4.45	3^1B_1	5.06	3^1B_1	5.36	3^1B_1	5.86	0.32	0.42	0.43	0.42
3^1B_1	4.47	1^1A_1	5.18	1^1B_2	5.59	1^1A_1	6.27	0.42	0.32	0.40	0.33
1^1B_2	4.59	1^1B_2	5.23	1^1A_1	5.62	1^1B_2	6.28	0.40	0.40	0.33	0.41

	EOM-CCSD SV
2^1B_1	4.88
3^1B_1	5.15
1^1A_1	5.52
1^1B_2	5.54

Table A-3 *Excitation energies and Λ values for the four lowest excited states calculated (in eV) for the $(TiO_2)_2(H_2O)$ cluster with C_1 symmetry.*

	TD-PBE	TD-B3LYP	TD-CAM-B3LYP	TD-BHLYP	Λ PBE	Λ B3LYP	Λ CAM-B3LYP	Λ BHLYP
2^1A	2.87	3.19	3.35	3.84	0.35	0.34	0.34	0.33
3^1A	3.08	3.56	3.75	4.50	0.24	0.24	0.24	0.25
4^1A	3.11	3.59	3.78	4.51	0.28	0.27	0.27	0.26
5^1A	3.96	4.39	4.62	5.11	0.49	0.47	0.46	0.46

	EOM-CCSD SV
2^1A	2.90
3^1A	3.27
4^1A	3.32
5^1A	4.27

Table A-4 *Excitation energies and Λ values for the four lowest excited states calculated (in eV) for the $(TiO_2)_3(H_2O)_2$ cluster with C_1 symmetry.*

	TD-PBE	TD-B3LYP	TD-CAMB3LYP	TD-BHLYP	Λ PBE	Λ B3LYP	Λ CAM-B3LYP	Λ BHLYP
2^1A	3.91	4.46	4.76	5.35	0.31	0.30	0.30	0.30
3^1A	3.96	4.60	5.00	5.74	0.34	0.33	0.34	0.33
4^1A	4.20	4.83	5.18	5.92	0.21	0.27	0.27	0.38
5^1A	4.23	5.04	5.41	5.93	0.27	0.35	0.37	0.28

	EOM-CCSD SV
2^1A	4.56
3^1A	4.82
4^1A	--
5^1A	--

Table A-5 *Excitations energies and Λ values for the four lowest excited states calculated (in eV) for the $(TiO_2)_3(H_2O)_3$ cluster with C_1 symmetry.*

	TD-PBE	TD-B3LYP	TD-CAM-B3LYP	TD-BHLYP	Λ PBE	Λ B3LYP	Λ CAM-B3LYP	Λ BHLYP
2^1A	4.25	5.06	5.48	6.25	0.30	0.31	0.31	0.31
3^1A	4.30	5.10	5.53	6.30	0.33	0.32	0.33	0.32
4^1A	4.34	5.14	5.57	6.33	0.30	0.31	0.33	0.33
5^1A	4.38	5.26	5.71	6.43	0.30	0.31	0.35	0.36

	EOM-CCSD SV
2^1A	5.44
3^1A	5.54
4^1A	--
5^1A	--

Appendix B

Figure B-1 shows that PBE0 (with 25% of HFLE) predicts a similar trend for the calculated vertical excitation energies of small TiO_2 nanoparticles when compared to B3LYP. Specifically, it is easy to see that the trends for B3LYP and PBE0 have a clear dip of ~0.5 eV, at $(TiO_2)_3$, which is not predicted by the other XC energy functionals (CAM-B3LYP and BHLYP). The similarity in the prediction of the vertical excitation energies between PBE0 and B3LYP suggests that PBE0 could potentially underestimate CT excitations in TiO_2 nanoparticles.

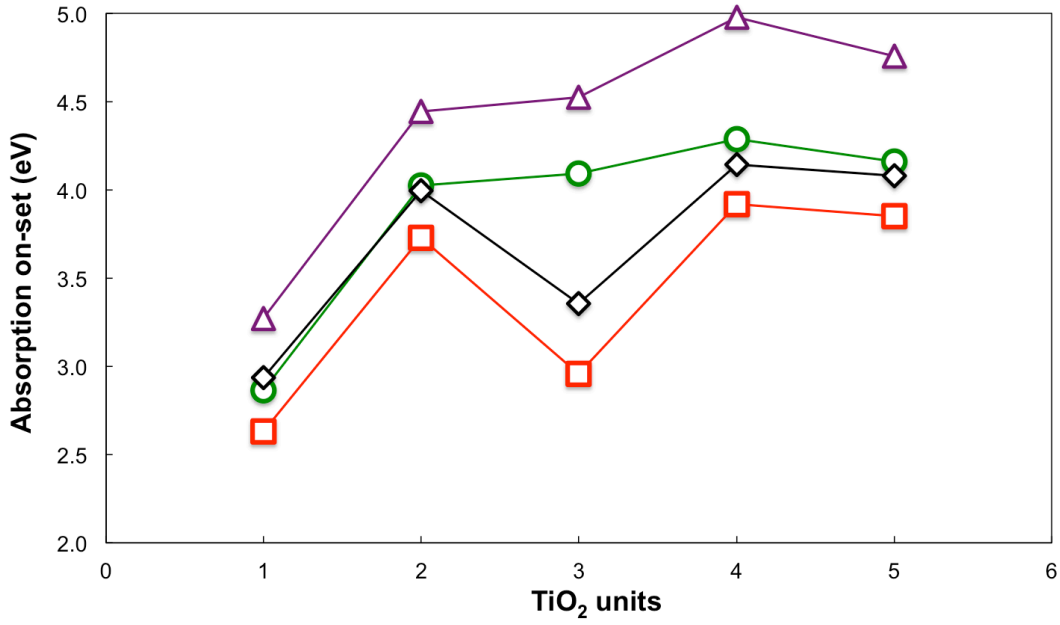

Figure B-1 Lowest singlet excitation energies calculated with different TD-DFT XC energy functionals for the B3LYP/def2-TZVP optimised ground state $(TiO_2)_n$ GM structures. B3LYP values are represented as red squares, PBE0 as black diamonds, CAMB3LYP green circles and BHLYP excitations are defined as purple triangles.

As already discussed in Chapter 5, the inability of XC energy functionals with low HFLE to correctly describe CT vertical excitations could potentially affect the excited state relaxation processes and therefore lead to large underestimations in the calculated photoluminescence energy. Figure B-2 shows that also in the case of the prediction of TD-DFT photoluminescence energies, PBE0 has a very similar behaviour to B3LYP. In PBE0, differently from B3LYP, the $(TiO_2)_2$ S1 excited state minimum optimisation does not reach a CX (PLE = 0 eV), however also in this case the excited state relaxation involves a much larger (~ 3 eV) Stokes shift if compared to CAM-B3LYP and BHLYP (~ 1.5 eV).

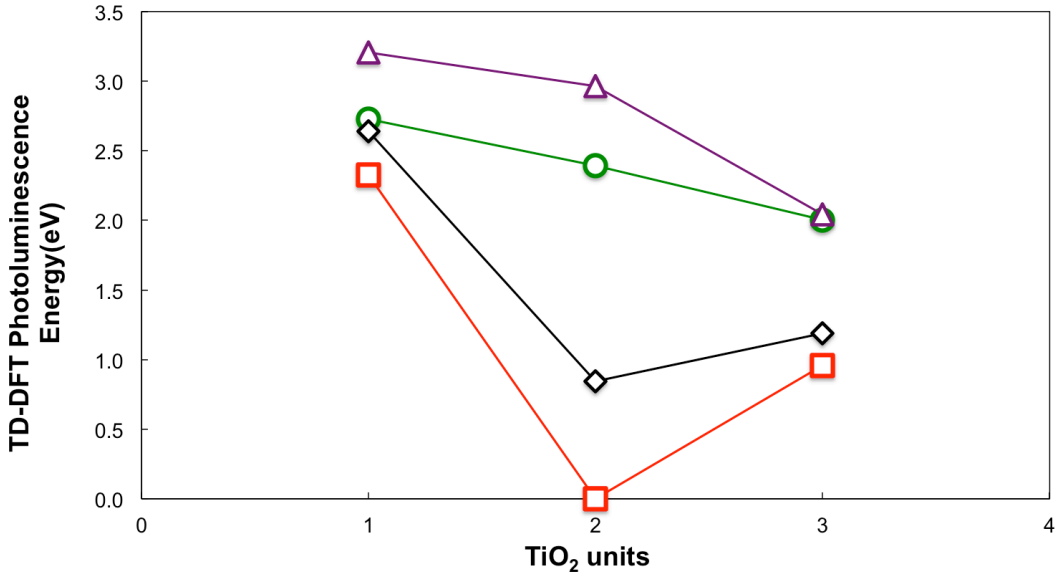

Figure B-2 TD-DFT calculated photoluminescence energies for the naked $(TiO_2)_n$ particles; B3LYP values are shown as red squares, PBE0 as black diamonds, CAM-B3LYP as green circles and BHLYP values as purple triangles. All values are in eV.

Acknowledgments

I would like to express my deepest gratitude to my supervisor, Martijn, for being such a great scientific mentor and for supporting and guiding me during the ups and downs of my PhD. This thesis owes its existence to Martijn.
I would like to thank all the members of the Zwijnenburg group for the interesting discussions and for the fun we had during our group gatherings.
I am very grateful to Prof. Filipp Furche for hosting me during my summer visit at University of California Irvine, to Dr. Enrico Tapavicza and the rest of Furche group (Brandon, Jordan and Guo) for all the endless scientific discussions and for making my visit memorable.
I would like to thank all the people that helped me in my research: first of all, Dr. Han-Shi Hu and Dr. Karol Kowalski for being great collaborators; Dr. Scott Woodley and Dr. Stephen Shevlin for fruitful discussions and for carefully proof reading all my manuscripts; Dr. Marta Corno, Dr. Massimo delle Piane, Dr. Antonio Tilocca and Prof. Piero Ugliengo for supporting me in my independent research on the modelling of bioglasses. Furthermore, I am deeply indebted to Prof. Ugliengo for introducing me to the world of computational chemistry.
My gratitude goes also to Prof. David Tozer and Prof. Nik Kaltsoyannis, who accepted to be my PhD examinors.

To Fede and Biagio for being wonderful friends; our discussions about music, science and life helped me facing the “dark days” of my PhD. To Alberto, Xavi and Giuseppe, who made me feel at home, even if in a foreign country.
I would like to thank Irwin, Cat, James and Regina for all the time spent together

talking about molecules. You guys are great fun.

Amos, Taz and Michy for always being close to me, no matter how far away I am.

To Marcia, Greg and Ben for being the best host family I could have ever asked for.

To my parents, Lucia and Enzo, I want to express my profound gratitude for all their help and support and for continuously believing in me.

Finally, I would like to thank Marta for her love. Her presence and joy of living made the last four years the most enjoyable of my life.

Enrico

List of Publications

Berardo, E.; Hu, H. S.; Kowalski, K.; Zwijnenburg, M. A. Coupled cluster calculations on TiO_2 nanoclusters. *J. Chem. Phys.* **2013**, *139*, 64313.

Berardo, E.; Hu, H. S.; Shevlin, S. A.; Woodley, S. M.; Kowalski, K.; Zwijnenburg, M. A. Modeling Excited States in TiO_2 Nanoparticles: On the Accuracy of a TD-DFT Based Description. *J. Chem. Theory Comput.* **2014**, *10*, 1189-1199.

Berardo, E.; Hu, H.-S.; van Dam, H. J. J.; Shevlin, S. A.; Woodley, S. M.; Kowalski, K.; Zwijnenburg, M. A. Describing Excited State Relaxation and Localisation in TiO_2 Nanoparticles Using TD-DFT. *J. Chem. Theory Comput.* **2014**, *10*, 5538-5548.

Berardo, E.; Zwijnenburg, M. A. Modelling the water splitting activity of a TiO_2 rutile nanoparticle. *J. Phys. Chem. C,* **2015**, 199, 13384 – 13393.

During my studies I also authored:

Berardo, E.; Pedone, A.; Ugliengo, P., Corno, M. DFT Modeling of 45S5 and 77S Soda-Lime Phospho-Silicate Glass Surfaces: Clues on Different Bioactivity Mechanism. *Langmuir*, **2013**, *29*, 5749-5759

Berardo, E.; Corno, M.; Cormack, A. N.; Ugliengo, P.; Tilocca, A. Probing the fate of interstitial water in bulk bioactive glass by ab initio simulations. *RSC Advances,* **2014**, *4*, 36425-36436